



THE HONG KONG
POLYTECHNIC UNIVERSITY

香港理工大學

Pao Yue-kong Library

包玉剛圖書館

Copyright Undertaking

This thesis is protected by copyright, with all rights reserved.

By reading and using the thesis, the reader understands and agrees to the following terms:

1. The reader will abide by the rules and legal ordinances governing copyright regarding the use of the thesis.
2. The reader will use the thesis for the purpose of research or private study only and not for distribution or further reproduction or any other purpose.
3. The reader agrees to indemnify and hold the University harmless from and against any loss, damage, cost, liability or expenses arising from copyright infringement or unauthorized usage.

IMPORTANT

If you have reasons to believe that any materials in this thesis are deemed not suitable to be distributed in this form, or a copyright owner having difficulty with the material being included in our database, please contact lbsys@polyu.edu.hk providing details. The Library will look into your claim and consider taking remedial action upon receipt of the written requests.

**FUNCTIONALIZED NANOPROBES FOR DISEASE-ASSOCIATED
NUCLEIC ACID DETECTION AND NEURODEGENERATIVE
DISEASE THERAPY**

ZHANG QIN

PhD

The Hong Kong Polytechnic University

2023

The Hong Kong Polytechnic University

Department of Biomedical Engineering

**Functionalized nanoprobe for disease-associated nucleic acid
detection and neurodegenerative disease therapy**

ZHANG Qin

**A thesis submitted in partial fulfillment of the requirements
for the degree of Doctor of Philosophy**

December 2022

Certificate of Originality

I hereby declare that this thesis is my own work and that, to the best of my knowledge and belief, it reproduces no material previously published or written, nor material that has been accepted for the award of any other degree or diploma, except where due acknowledgement has been made in the text.

_____ (Signed)

ZHANG Qin (Name of student)

Abstract

Functionalized nanoprobe have been a powerful tool for biosensing, bioimaging, and therapeutics. Förster resonance energy transfer (FRET)-based biosensors with fluorescence as the output signal have a wide range of applications in detecting viral nucleic acids and monitoring disease-associated biomarkers. To overcome the unfavorable aggregation-caused quenching (ACQ) effect of conventional organic dyes, we introduced aggregation-induced emission fluorogens (AIEgens) as donor fluorophores into the FRET sensing platform to endow fluorescent nanoprobe with optimal signal-to-noise ratio and sensitivity due to distinctive fluorescence properties of AIEgens including high brightness, large Stokes shift, strong resistance to photobleaching. Furthermore, inspired by the natural photosynthesis process, we developed a hybrid upconversion nanoparticle (UCNP)-based nanoreactor for Alzheimer's disease (AD) therapy based on the generation of photocatalytic hydrogen gas to attenuate local oxidative stress.

In the first work, we developed a FRET-based biosensor in which AIEgen-labelled oligonucleotide probes as donor fluorophores were immobilized on the surface of graphene oxide (GO) nanosheets as acceptor motif (AIEgen@GO). This biosensor was highly specific to the nucleic acid sequences of *Orflab* and *N* genes in the genome of SARS-CoV-2 virus. The sensing mechanism is based on dual fluorescence "turn-on" process in the presence of the target sequence. Here, the first-stage fluorescence recovery is due to dissociation of the AIEgen from GO surface in the presence of target viral nucleic acid. The second-stage enhancement of AIE-based fluorescent signal is caused by the formation of a nucleic acid duplex to restrict the intramolecular rotation of the AIEgen. Our work demonstrated that this AIEgen@GO nanoprobe could identify mimic *Orflab*, *N* genes, and SARS-CoV-2 plasmids with rapid detection around 1 h and good sensitivity at picomolar level without amplification. AIEgen@GO nanoprobe could be a promising tool in assisting the initial rapid detection of the SARS-CoV-2 viral sequence.

In the second work, we further developed an AIEgen/polymeric molybdenum disulfide (MoS₂)-based FRET nanoprobe for *in situ* detection of characteristic microRNA-125b (miR-125b) for early diagnosis of AD. To optimize the sensing platform for *in vivo* applications, we extended the emission wavelength of AIEgen from blue to red range to avoid autofluorescence of living systems. Accordingly, the proposed AIEgen@MoS₂ nanoprobe was highly specific to miR-125b, a promising biomarker for early AD diagnosis. In the presence of the target, AIEgen hybridized with miR-125b to form a DNA/RNA duplex, causing the donor fluorophore to

detach from the surface of MoS₂, which simultaneously activated the dual fluorescence enhancement processes. The sensing performance of AIEgen@MoS₂ was demonstrated by detecting miR-125b in both solution and a tau-based cell model *in vitro* with good sensitivity and specificity. Furthermore, the fluorescent nanoprobe also successfully demonstrated the capability of *in situ* monitoring of the endogenous miR-125b in tau-based AD mice. Therefore, AIEgen@MoS₂ could be a promising tool for *in situ* and real-time monitoring of the AD-related microRNA biomarkers and thus would provide mechanistic insight into the early diagnosis of AD.

In the third work, we designed a UCNP-based artificial nanoreactor for near-infrared (NIR) light-triggered *in situ* hydrogen gas (H₂) generation to scavenge reactive oxygen species (ROS) for AD therapy. This multi-component nanoreactor contained platinum nanoparticles (Pt NPs) and ascorbic acid encapsulated by cross-linking vesicles, which comprised two photosensitizers, chlorophyll *a* (Chl*a*) and indoline dye (Ind), absorbing the red and green luminescence from UCNP coupled on the surface. In the nanoreactor system, the excited electrons separated from Chl*a* and Ind were quickly transferred to Pt NPs to combine with protons from ascorbic acid, facilitating rapid activation of the photosynthesis of H₂, locally providing a high therapeutic concentration. Our results successfully demonstrated that the artificial nanoreactor could efficiently photosynthesize H₂ to restore ROS homeostasis, repair mitochondrial damage, and attenuate hyperphosphorylated tau in AD mice. Such an artificial nanoreactor with efficient H₂ generation has great potential to provide a new window for AD treatment.

Publications

1. **Zhang, Q.**, Yin, B., Huang, Y., Gu, Y., Yan, J., Chen, J., Li, C., Zhang, Y., Wong, S.H.D.* and Yang, M.*, 2023. A dual "turn-on" biosensor based on AIE effect and FRET for in situ detection of miR-125b biomarker in early Alzheimer's disease. *Biosensors and Bioelectronics*. 230, 115270.
2. **Zhang, Q.**, Yin, B., Hao, J., Ma, L., Huang, Y., Shao, X., Li, C., Chu, Z., Yi, C., Wong, S.H.D.* and Yang, M.*, 2022. An AIEgen/graphene oxide nanocomposite (AIEgen@GO)-based two-stage "turn-on" nucleic acid biosensor for rapid detection of SARS-CoV-2 viral sequence. *Aggregate*, p.e195.
3. Lam, C.Y.K., **Zhang, Q. (co-first author)**, Yin, B., Huang, Y., Wang, H., Yang, M.* and Wong, S.H.D.*, 2021. Recent advances in two-dimensional transition metal dichalcogenide nanocomposites biosensors for virus detection before and during COVID-19 outbreak. *Journal of Composites Science*, 5(7), p.190.

Conference Proceeding

Q. Zhang, B. Yin, J. Hao, L. Ma, Y. Huang, X. Shao, C. Li, Z. Chu, C. Yi, S. H. D. Wong*, M. Yang*. An AIEgen/graphene oxide composite based two-stage "turn-on" biosensor for rapid detection of SARS-CoV-2 nucleic acid sequence. The 31st Anniversary World Congress on Biosensors-Online. 26 July – 27 July 2021 Oral Presentation.

Academic Award

1. 2nd Runner-up of BME Research Student 3MT (Three Minute Thesis) Competition 2022
2. 2nd Runner-up of Hong Kong Medical and Healthcare Device Industries Association Student Research Award 2022

Acknowledgments

First and foremost, I would like to express my deepest appreciation to my chief supervisor, Prof. Mo YANG, for his insightful guidance and unlimited support during my Ph.D. journey. Thanks, Prof.YANG, for allowing me to do research I was interested in here. Without his assistance and dedicated involvement in every step throughout the process, this thesis would have never been accomplished.

Secondly, I wish to show my sincere gratitude to my co-supervisor, Dr.Siu Hong Dexter WONG, whose invaluable guidance and professional attitude are appreciable in completing my Ph.D. program over these past three years. Dr.Wong has taught me the methodology to carry out the research and to present the research work as clearly as possible. It was a great honor to work and study under his guidance.

Then, I am also very thankful to all the members of Prof.YANG's laboratory, Dr. YIN Bohan, Dr. SHI Jingyu, Dr. TIAN Feng, Dr. FAN Yadi, Dr. LIU Yi, Dr. LI Chuanqi, Mr. HO Kwun Hei Willis, Ms. GU Yutian, Ms. ZHANG Ruolin, Ms. HUANG Yingying, Ms. CHEN Jiareng, Mr.YAN Jiaxiangn, and Mr. LAI Huang, for their continuous supports and helpful advice on my experiments, which made my work progress smoother.

Finally, the financial support provided by the Hong Kong research grants Council is greatly acknowledged. Last but not least, I would like to thank my parents for their love and support without any reservation throughout my life.

Table of contents

Abstract.....	I
Acknowledgments.....	IV
List of figures.....	VI
List of tables.....	XIV
List of abbreviations.....	XIV
Chapter 1: Introduction.....	1
1.1 Aggregation-induced emission (AIE).....	2
1.1.1 Mechanism of AIEgen.....	3
1.1.2 AIEgen-based probes.....	4
1.1.3 Application of AIE probes for biosensing and bioimaging.....	6
1.2 Upconversion fluorescence.....	9
1.2.1 Photophysical mechanisms of upconversion fluorescence.....	10
1.2.2 Structure of UCNPs.....	11
1.2.3 Application of UCNPs for biosensing and bioimaging.....	12
1.3 Forster resonance energy transfer.....	13
1.3.1 Principle of FRET.....	14
1.3.2 Donors of FRET-based biosensors.....	15
1.3.3 Acceptor of FRET based biosensors.....	18
1.4 FRET-based nanoprobe for biosensing	21
1.4.1 Detection of virus.....	22
1.4.2 Detection of cancer biomarkers.....	24
1.4.3 Detection of AD biomarkers.....	25
1.4.4 in vivo tissue imaging.....	27
1.5 Functionalized nanoprobe for AD therapy.....	29
1.5.1 Pathogenesis of AD.....	29
1.5.2 NPs targeting A β pathology.....	31
1.5.3 NPs targeting tau pathology.....	32
1.5.4 NPs targeting ROS.....	33
1.5.5 Nanomaterials-based hydrogen therapy.....	34
1.6 Objectives of the study.....	38
Chapter 2: A dual fluorescence “turn-on” FRET biosensor based on AIEgen@GO nanoprobe for rapid detection of SARS-CoV-2 virus.....	41

2.1	Introduction.....	41
2.2	Methodology.....	44
2.2.1	Synthesis of TPE-DNA@GO nanoprobe.....	44
2.2.2	Detection of <i>N</i> and <i>Orflab</i> sequences.....	45
2.2.3	Detection of CDC-V2 plasmids.....	45
2.2.4	Agarose gel electrophoresis.....	45
2.2.5	Data analysis.....	46
2.3	Results and Discussion.....	46
2.3.1	Synthesis and characterization of AIEgen@GO nanoprobe.....	46
2.3.2	Rapid detection of SARS-CoV-2 viral sequence.....	52
2.3.3	Specificity and stability of TPE-DNA@GO nanoprobe.....	58
2.4	Summary.....	62
Chapter 3: A dual fluorescence "turn-on" biosensor based on AIEgen/MoS₂ nanocomposites for in situ detection of miR-125b in AD.....		63
3.1	Introduction.....	63
3.2	Methodology.....	65
3.2.1	Synthesis of TPET molecules and TPET-DNA.....	65
3.2.2	Synthesis of Dex-TMA.....	66
3.2.3	Preparation of TPET-DNA@Dex-MoS ₂	66
3.2.4	Detection of miR-125b in vitro.....	67
3.2.5	Cell culture and cytotoxicity of TPET-DNA@Dex-MoS ₂	67
3.2.6	Intracellular overexpression of miR-125b.....	68
3.2.7	Intracellular detection of miR-125b.....	68
3.2.8	Stereotaxic surgery and establishment of AD mouse model.....	68
3.2.9	Animal imaging in vivo.....	69
3.2.10	Histological tissue preparation and immunocytochemistry.....	69
3.2.11	Statistical analysis.....	69
3.3	Results and Discussion.....	70
3.3.1	Synthesis and characterization of TPET-DNA@Dex-MoS ₂	70
3.3.2	In vitro detection of miR-125b.....	77
3.3.3	Intracellular detection of miR-125b.....	79
3.3.4	In vivo detection of miR-125b in AD model.....	82
3.4	Summary.....	87

Chapter 4: Photosynthesis-mimic artificial nanoreactors for NIR-driven H₂ generation for AD treatment.....	89
4.1 Introduction.....	89
4.2 Methodology.....	90
4.2.1 Synthesis of UCNPs.....	91
4.2.2 Preparation of (Chl <i>a</i> +Ind) cVs.....	91
4.2.3 Preparation of (Chl <i>a</i> +Ind)cVs@Pt.....	92
4.2.4 Fabrication of (Chl <i>a</i> +Ind) NRs.....	92
4.2.5 Stability assay of (Chl <i>a</i> +Ind) NRs.....	92
4.2.6 Catalytic activity of (Chl <i>a</i> +Ind) NRs.....	93
4.2.7 Ultrasound imaging.....	93
4.2.8 Measurement of H ₂ release.....	93
4.2.9 Cytotoxicity and biocompatibility.....	93
4.2.10 Measurement of intracellular ROS levels.....	94
4.2.11 Cell apoptosis.....	94
4.2.12 Western blot.....	94
4.2.13 Animals modeling and stereotaxic injections.....	95
4.2.14 Y maze test.....	96
4.2.15 Histological tissue preparation and immunocytochemistry.....	96
4.3 Results and Discussion.....	96
4.3.1 Fabrication and characterization of (Chl <i>a</i> +Ind) NRs.....	96
4.3.2 Efficiency of photocatalytic hydrogen release by (Chl <i>a</i> +Ind) NRs.....	100
4.3.3 (Chl <i>a</i> +Ind) NRs scavenge intracellular ROS.....	101
4.3.4 (Chl <i>a</i> +Ind) NRs alleviate apoptosis and mitochondrial dysfunction.....	103
4.3.5 (Chl <i>a</i> +Ind) NRs attenuate hyperphosphorylation of tau	105
4.3.6(Chl <i>a</i> +Ind) NRs regulates apoptosis-relevant proteins and activates Akt/GSK-3 β signaling.....	105
4.3.7 (Chl <i>a</i> +Ind) NRs reduce ROS and p-tau in AD Mice.....	106
4.4 Summary.....	111
Chapter 5: Conclusions.....	113
References.....	115

List of figures

Figure 1.1 Brief introduction to fluorescence generation. (A) Jablonski diagram of absorbance, non-radiative decay and fluorescence. (B) Schematic illustration of Stokes shift	1
Figure 1.2 ACQ vs AIE phenomenon. Molecular structures and fluorescence photographs of (A) perylene and (B) hexaphenylsilole (HPS) in mixtures of acetone and water with different water fractions. The photographs were taken under 365 nm UV light irradiation	3
Figure 1.3 The mechanism of AIE phenomenon. (A) The restriction of intramolecular rotations (RIR) in Tetraphenylethene (TPE) molecules. (B) The restriction of intramolecular vibration (RIV) in cyclooctatetrathiophene (COTh) molecules	4
Figure 1.4 Molecular structure of typical AIEgens	4
Figure 1.5 Methods for the design of (A) AIEgen-based molecular robes and (B) AIE NPs	6
Figure 1.6 Representative examples of AIE probes for DNA, RNA, and protein detection. (A) Schematic illustration of TPE-DNA _p for detection of nucleic acid DNA _t . ^[1] (B) Schematic illustration of TPE-R-DNA for detection of mRNA in cancer cells. ^[2] (C) Schematic illustration of Ac-DEVDK-TPE probe and its time-dependent fluorescence intensity in the presence of caspase 3/7 proteins	9
Figure 1.7 Schematic diagram of the energy transfer mechanism of upconversion fluorescence	11
Figure 1.8 Design of core-shell UCNPs to improve upconversion efficiency	12
Figure 1.9 (A) FRET mechanism diagram (B) Diagram of Energy Transfer Efficiency (E) of FRET Assays	15
Figure 1.10 Chemical structure of (A) GO and (B) MoS ₂	20
Figure 1.11 FRET-based nanoprobe for SARS-CoV-2 detection (A) Schematic illustration of a simple SARS-CoV-2 detection method using the hACE2 mimic peptide-based molecular beacon (COVID 19-PEB) ^[3] . (B) Illustration of the FRTE assay for SARS-CoV-2 N protein showing the Eu donor-conjugated primary MAb and DL650 acceptor-conjugated primary MAb detecting of SARS-CoV-2 and enabling FRET	23
Figure 1.12 FRET nanoprobe for the detection of AD biomarkers. (A) FRET nanoprobe based on MoS ₂ with fluorescence “switch-on” for A β oligomer detection ^[4] . (B) An enzyme-free signal amplification strategy based on a FRET nanoprobe with carbon dots and GO for monitoring miR-9 in neurons and brain tissues of AD mice	27
Figure 1.13 FRET nanoprobe for in vivo imaging. (A) Schematic illustration of the synthesis and mechanism of UCNP-based FRET nanoparticles for detection of miR-122. (B) In vivo	

imaging of liver cancer mice model subcutaneously injected with different reagents. $\lambda_{ex}=980$ nm	29
Figure 1.14 The cascade of ROS, A β and tau hyperphosphorylation in AD	30
Figure 2.1 The genome structure of SARS-CoV-2 virus	43
Figure 2.2 Schematic illustration of TPE-DNA@GO nanoprobe for the detection of SARS-CoV-2 viral sequence. (A) Synthetic route to TPE-DNA. (B) Fabrication of TPE-DNA@GO nanoprobe and detection of <i>Orflab</i> and <i>N</i> genes	44
Figure 2.3 The ESI-TOF mass spectrum of (A) alkyne- <i>N_f</i> , (B) TPE- <i>N_f</i> , (C) alkyne- <i>N_r</i> , (D) TPE- <i>N_r</i> , (E) alkyne- <i>Orf_f</i> , (F) TPE- <i>Orf_f</i> , (F) alkyne- <i>Orf_r</i> , (G) TPE- <i>Orf_r</i>	47
Figure 2.4. (A) UV-vis spectra of TPE- <i>N₃</i> and TPE-DNA. (B-E) Fluorescence spectra of TPE- <i>N₃</i> , TPE-DNA probes (TPE- <i>N_f</i> , TPE- <i>N_r</i> , TPE- <i>Orf_f</i> and TPE- <i>Orf_r</i>), TPE-DNA@GO nanoprbes (TPE- <i>N_f</i> @GO, TPE- <i>N_r</i> @GO, TPE- <i>Orf_f</i> @GO, and TPE- <i>Orf_r</i> @GO). (F) Fluorescence intensity ratio (%) of TPE-DNA and TPE-DNA@GO (<i>F</i>), which are normalized to the fluorescence intensity of TPE- <i>N₃</i> (<i>F₀</i>). $\lambda_{ex}/\lambda_{em} = 320/458$ nm	48
Figure 2.5 Photoluminescence spectra and fitting curve of (A)TPE- <i>N_r</i> and (B) TPE- <i>Orf_r</i> after incubating with <i>N</i> -cDNA and <i>Orflab</i> -cDNA of a series of concentrations from 0 nM to 20 nM. $\lambda_{ex}/\lambda_{em} = 320/458$ nm	49
Figure 2.6 (A) Size distribution and (B) Zeta potential of GO and TPE-DNA@GO nanoprobe. (C)AFM images of GO, ppTPE- <i>N</i> @GOand ppTPE- <i>Orf</i> @GO nanoprbes	50
Figure 2.7 Photoluminescence spectra and quenching efficiency (<i>Q_e</i>) of (A) TPE- <i>N_f</i> , (B) TPE- <i>N_r</i> , (C) TPE- <i>Orf_f</i> , and (C) TPE- <i>Orf_r</i> incubated with GO of different concentrations (0 to 200 μ g/mL). $\lambda_{ex}/\lambda_{em} = 320/458$ nm	51
Figure 2.8 (A) Schematic illustration of TPE- <i>N_f</i> @GO and TPE- <i>N_r</i> @GO nanoprobe for the detection of mimetic <i>N</i> -cDNA sequence. Fluorescence spectra of (B) TPE- <i>N_f</i> @GO and (C)TPE- <i>N_r</i> @GO after incubated with target <i>N</i> -cDNA at increasing concentration from 0 to 20 nM. (D) Fitting logarithmic curve of the relative fluorescence intensity of TPE- <i>N_f</i> @GO (blue triangle), TPE- <i>N_r</i> @GO (red circle) against the logarithmic concentration of <i>N</i> -cDNA. $\lambda_{ex}/\lambda_{em} = 320/458$ nm	52
Figure 2.9 (A) Schematic illustration of ppTPE- <i>N</i> @GO ((TPE- <i>N_f</i> +TPE- <i>N_r</i>)@GO) probing for two binding sites of <i>N</i> -cDNA sequence. (B) Photoluminescence spectra and (C) peak fluorescence intensity at 458 nm of ppTPE- <i>N</i> @GO after incubation with <i>N</i> -cDNA. (D) The fitting curve of ppTPE- <i>N</i> @GO against logarithmic concentration of <i>N</i> -cDNA.	53
Figure 2.10 (A) The sequence of SAR-CoV-2 mimetic <i>N</i> -RNA sequence. Fluorescence spectra of nanoprbes (B) TPE- <i>N_f</i> @GO, (C) TPE- <i>N_r</i> @GO, and (D) (TPE- <i>N_f</i> +TPE- <i>N_r</i>)@GO after	

incubation with *N*-RNA. (E) Fluorescence intensity of nanoprobe (TPE- N_f @GO, TPE- N_r @GO, and (TPE- N_f +TPE- N_r)@GO) after incubation with *N*-RNA (0.2 to 20 nM). (F) Fitting curve of nanoprobe against the logarithmic concentration of *N*-RNA. $\lambda_{ex}/\lambda_{em} = 320/458$ nm

Figure 2.11 Fluorescence spectra of (A) TPE- Orf_f @GO and (B) TPE- Orf_r @GO after incubating with target *Orf*-cDNA at different concentrations. (C) Fitting logarithmic curve of the relative fluorescence intensity of TPE- Orf_f @GO (yellow triangle) and TPE- Orf_r @GO (olive circle) after incubating with *Orf*-cDNA. (D) Fluorescence spectra and (E) peak fluorescence intensity at 458 nm of ppTPE-*Orf*@GO (TPE- Orf_f +TPE- Orf_r)@GO after incubating with *Orf*-cDNA. (F) Fitting curve of (TPE- Orf_f +TPE- Orf_r)@GO against logarithmic concentration of *Orf*-cDNA. $\lambda_{ex}/\lambda_{em} = 320/458$ nm 55

Figure 2.12 (A) Scheme of the detection of CDC-V2 plasmid by ppTPE-DNA@GO nanoprobe. (B-D) Fluorescence spectra of (TPE- N_f +TPE- N_r)@GO, (TPE- Orf_f +TPE- Orf_r)@GO, and (TPE- Orf_f +TPE- N_r)@GO after incubation with denatured CDC-V2 plasmid. (E) Fluorescence intensity at 458 nm of nanoprobe after incubation with CDC-V2 plasmid 57

Figure 2.13 Fluorescence spectra of (A) TPE- N_f @GO, (B) TPE- N_r @GO, (D) TPE- Orf_f @GO and (E) TPE- Orf_r @GO after incubating with different viral sequences including target *N*-cDNA, target *Orflab*-cDNA, one base mismatch (b_1 -Mis), scrambled *N*-cDNA, scrambled *Orflab*-cDNA, and viral cDNA for InFA, HBV, HCV, and HIV-1. (C, F) Fluorescence intensity fold change of nanoprobe after incubation with different viral sequences 58

Figure 2.14 Agarose gel electrophoresis of (A) TPE- N_f @GO and TPE- N_r @GO, (B) TPE- Orf_f @GO and TPE- Orf_r @GO after incubation with target cDNA or scramble cDNA. The fluorescence intensity changes of nanoprobe (TPE- N_f @GO, TPE- N_r @GO, TPE- Orf_f @GO, and TPE- Orf_r @GO) dissolved in (C) PBS buffer with different pH values or (D) different buffers for 24 h and then incubated with corresponding target cDNA for an additional 2 h 59

Figure 3.1 (A) Schematic illustrations of the design and fabrication of TPET-DNA@Dex-MoS₂ nanoprobe. (B) Schematic diagram of TPET-DNA@Dex-MoS₂ nanoprobe for in vitro and in vivo real-time monitoring of miR-125b overexpression in neurons brain tissues of mice with AD model based on a dual fluorescence recovery mechanism 64

Figure 3.2 The synthesis and characterization of TPET. (A) Synthetic route to TPET compound. (B) MALDI-TOF mass spectrum of TPET in methanol with HCCA as the matrix. (C) ¹H NMR spectrum and (D) ¹³C NMR spectrum of TPET compound in DMSO-D₆. Molecular weight of (E) probing DNA and (F) TPET-DNA determined by ESI-MS-TOF spectrometry 69

Figure 3.3 The AIE effect of TPET molecules. (A) Fluorescence spectra of TPET in the THF/water mixtures with different water fractions. $\lambda_{ex}=480$ nm. (B) The plot of fluorescence

intensity versus the compositions of aqueous mixtures. The inset photographs were images of TPET under a UV lamp 69

Figure 3.4 The fabrication and characterization of TPE-DNA@@Dex-MoS₂. (A) UV-vis absorbance of TPET, TPET-DNA, and TPET-DNA@Dex-MoS₂ in H₂O. (B) Photoluminescence spectra of TPET, TPET-DNA, and TPET-DNA@Dex-MoS₂ in H₂O. $\lambda_{ex} = 480$ nm. (C) The fluorescence intensity percentage of TPET-DNA and TPET-DNA@Dex-MoS₂ normalized to the fluorescence intensity of TPET (F_0). (D) Size distribution, (E) Zeta potential, (F) SEM images, (G) AFM images of MoS₂, Dex-MoS₂, and TPET-DNA@Dex-MoS₂. (H) Histograms of height calculated from AFM images 72

Figure 3.5 The detection performance of TPET-DNA. (A) Photoluminescence spectra and (B) peak fluorescence intensity of TPET-DNA before and after incubating with miR-125b at a series of concentrations. (C) Fitting logarithmic curve of the relative fluorescence intensity of TPET-DNA against the increasing concentration of miR-125b. F_q : fluorescence intensity of TPET-DNA, F_r : fluorescence intensity of TPET-DNA after incubation with miR-125b. (D) Photoluminescence spectra of TPET-scrDNA after incubation with miR-125b at a concentration of 10 nM. (E) Photoluminescence spectra and (F) peak fluorescence intensity of TPET-DNA after incubation with miR-125b, scrambled miR-125b, miR-9 and miR-29a at a concentration of 10 nM 73

Figure 3.6 The synthesis and characterization of Dex-TMA. (A) Synthetic route to Dex-TMA polymer. (B) FTIR spectrum of dextran and Dex-TMA. (C) Zeta potential of dextran and Dex-TMA. The size distribution of (D) MoS₂ and (E) Dex-MoS₂ nanosheets distributed in H₂O, PBS, and cell medium(DEME) after 48 h of standing 75

Figure 3.7 The quenching efficiency of Dex-MoS₂. (A) Photoluminescence spectra and (B) peak fluorescence intensity of TPET-DNA after quenched by Dex-MoS₂ at a series of concentrations. (C) The plot of quenching efficiency (Q_e %) versus different concentrations of TMA-MoS₂ nanosheets. F_0 : fluorescence intensity of TPET. F_q : fluorescence intensity of TPET after adding Dex-MoS₂ to form TPET-DNA@Dex-MoS₂. $\lambda_{ex}/\lambda_{em} = 480/618$ nm 76

Figure 3.8 The stability of TPET-DNA@Dex-MoS₂ nanoprobe. The fluorescence intensity changes of TPET-DNA@Dex-MoS₂ nanoprobe dissolved in (A) PBS buffer with different pH values or (B) different media (TE buffer, borate buffered saline (BBS), BSA, and cell medium) for 24 h and then incubated with miR-125b for an additional 2 h. 76

Figure 3.9 Detection of miR-125b *in vitro*. (A) Schematic illustrations of the working mechanism (dual fluorescence enhancement) of TPET-DNA@Dex-MoS₂ nanoprobe. (B) Photoluminescence spectra and (C) peak fluorescence intensity of TPET-DNA@Dex-MoS₂

after incubation with increasing miR-125b ranging from 0 to 10 nM. (D) Fitting logarithmic curve of TPET-DNA@Dex-MoS₂ nanoprobe against the different concentrations of miR-125b. F_q : fluorescence intensity of TPET-DNA@Dex-MoS₂, F_r : fluorescence intensity of probes after incubation with miR-125b. (E) Photoluminescence spectra and (F) peak fluorescence intensity of TPET-DNA@Dex-MoS₂ after incubation with miR-125b, scrambled miR-125b, one base mismatched miR-125b (b₁-Mis), miR-9 and miR-29a at a concentration of 10 nM. (G) Agarose gel electrophoresis of TPET-DNA@Dex-MoS₂ nanoprobe before and after incubation with target miR-125b and scrambled miR-125b 78

Figure 3.10 The differentiation of PC12 cells. The morphology of differentiated PC12 cells was recorded from day 1 to day 9. The change of average neurite length of the differentiated PC12 cells was calculated by ImageJ 80

Figure 3.11 Intracellular detection of miR-125b. (A) Schematic illustrations of TPET-DNA@Dex-MoS₂ nanoprobe for the intracellular monitor of miR-125b. (B) The relative expression level of miR-125b in differentiated PC12 cells tested by RT-PCR assays. (C) Representative confocal images of differentiated PC12 cells pretreated with OA of different concentrations (10, 25, and 50 nM) followed by incubation with TPET-DNA@Dex-MoS₂ nanoprobe (25 μM) for 6 h. (D) Representative immunofluorescence images of differentiated PC12 cells with different treatments followed by incubation with TPET-DNA@Dex-MoS₂ nanoprobe (red fluorescence). (E) Representative histogram plots of flow cytometry to quantify the intracellular fluorescence intensity of TPET-DNA@Dex-MoS₂ nanoprobe. (F) Corresponding mean fluorescence intensity of the flow cytometric analysis in (E). (G) The fluorescence intensity of p-tau (green) and TPET-DNA@Dex-MoS₂ (red) along the profile in the labeled ROI in (D). (H) The Mander's colocalization coefficients (MCC) was calculated by ImageJ used to quantify the colocalization of p-tau and TPET-DNA@Dex-MoS₂ in the cytoplasm 80

Figure 3.12 Confocal images of differentiated PC12 cells pretreated with OA followed by incubation with scrambled probes (TPET-scrDNA@Dex-MoS₂) 81

Figure 3.13 (A) Immunofluorescence staining with anti p-tau antibody (green) of brain slices from wild-type mice and OA-induced AD mice. Scale bar: 200 μm. (B) RT-PCR to quantify the relative expression of miR-125b in the hippocampus and cortex area of brains from wild-type mice and OA-induced AD mice. 83

Figure 3.14 *In vivo* monitor miR-125b in the AD mice model. (A) Schematic illustrations of stereotaxic coordinates of the microinjection site. (B) Timeline in the animal experiments. (C) *In vivo* fluorescence images of wild-type mice (top row) and OA-induced AD mice (bottom

row) were captured after administrated with TPET-DNA@Dex-MoS₂ nanoprobe at various time points. (F) The average fluorescence intensity in the brain area in (D). (E) In vivo fluorescence images of wild-type mice and OA-induced AD mice were captured 4 h after being administrated with saline, TPET-scrDNA@Dex-MoS₂, or TPET-DNA@Dex-MoS₂ nanoprobe. (D) The fold change of fluorescence intensity in (C) was calculated by Living Imaging software. F_0 represents the signal intensity of wild-type mice in C1 group. F is the fluorescence of AD mice with different administrations. (G) *Ex vivo* fluorescence images of main organs of AD mice after being injected with TPET-DNA@Dex-MoS₂ for 24 h. (H) Quantification of fluorescence intensity in the organs by Living Image software..... 84

Figure 3.15 *Ex vivo* histological analysis. (A) hippocampus and (B) cortex regions of the brain slices from mice with different administrations were stained with p-tau antibody (green) and DAPI (blue). The white arrows labeled in the enlarged images indicated the sites of overlapping between green and red fluorescence. The regions in the merged images labeled with the white dotted lines were shown in enlarged views. The average fluorescence intensity of TPET-DNA@Dex-MoS₂ nanoprobe in the (C) hippocampal and (E) cortical areas by ImageJ. The data indicate the mean fluorescence intensity from four independent experiments. The fluorescence intensity profile of p-tau (green) and TPET-DNA@Dex-MoS₂ nanoprobe (red) along the line in the inset image of (D) hippocampus and (F) cortex was analyzed by Leica LAS X software 85

Figure 3.16 H&E staining of main organs of wild-type mice injected with saline and TPET-DNA@Dex-MoS₂ nanoprobe. Scale bar: 200 μ m for all 86

Figure 4.1 Schematic diagram illustrating the preparation of (Chla+Ind)NRs and NIR-triggered *in situ* release of H₂ from (Chla+Ind)NRs to scavenge ROS, alleviate neuronal mitochondrial damage, and reduce tau hyperphosphorylation for AD therapy 88

Figure 4.2 The fabrication and characterization of (Chla+Ind) NRs. (A) Schematic illustration of fabrication procedures of (Chla+Ind) NRs fabrication. (B) UV-Vis spectr. (C) TEM images of (Chla+Ind) cVs. (D) TEM elemental mappings of Pt, O, and S of (Chla+Ind) cVs. (E) High-resolution XPS spectra of Pt 4f in (Chla+Ind) cVs. (F) TEM images of UCNPs. (G) TEM images of (Chla+Ind) NRs. (e) UV-vis absorption spectra of Chla NPs, Ind NPs and (Chla+Ind) NRs. (f) Upconversion luminescence spectra of UCNP, Chla NRs, Ind NRs, and (Chla+Ind) NRs 95

Figure 4.3 Photocatalytic hydrogen release by (Chla+Ind) NRs. (A) Schematic illustration of photocatalytic hydrogen release by (Chla+Ind) NRs. (B) Dissolved oxygen-time course curves of H₂O₂. (C) Dependence between the elimination of H₂O₂ and concentrations of (Chla+Ind)

NRs. (D) Absorbance changes of AA in (Chla+Ind) NRs solution after various periods of laser irradiation. Background interference has been subtracted. (E) Ultrasound images of hydrogen bubble generation in the Chla NRs, Ind NRs, and (Chla+Ind) NRs solution following laser irradiation. (F) Top: The reaction mechanism of MB hydrogenation for detecting hydrogen. Bottom: UV–visible absorbance spectra of (Chla+Ind) NRs in the MB solution with laser after 10 min. (G) Quantitative analysis of reductive hydrogen release profile of Chla NRs, Ind NRs, and (Chla+Ind) NRs solution using MB as a hydrogen probe 96

Figure 4.4. (Chla+Ind) NRs scavenge intracellular ROS. (A) The confocal images of PC12 cells after incubated with Chla NRs, Ind NRs, Chla+Ind NRs. (B) The relative cell viability of PC12 cells after incubated with Chla NRs, Ind NRs and (Chla+Ind) NRs at different concentrations for 12 h. (C) The change of ROS level measured by DCFH-DA in OA-treated cells after incubated with (Chla+Ind) NRs at different concentrations with NIR laser irradiation for different time. (D) The fluorescence images of DCFH-DA to indicate intracellular ROS levels. (E) The intracellular fluorescence intensity of DCF-DA was quantified by flow cytometer. (F) The fold change of mean intracellular fluorescence intensity of DCF-DA 99

Figure 4.5 Therapeutic effect of (Chla+Ind) NRs *in vitro*. (A)The comparative cell death inhibition ability of Chla NRs, Ind NRs, (Chla+Ind) NRs was measured by a MTT assay at indicated concentrations.(B) The apoptosis results of PC12 cells after treatments stained with Annexin V-FITC/PI. (C) The quantification results of early and late apoptosis rate in (B). (D) Confocal images of PC12 cells stained with mito-tracker to display the mitochondrial morphology. (E) Confocal images of PC12 cells after treated by Chla NRs, Ind NRs, (Chla+Ind) NRs, exhibiting mitochondrial membrane potential measured using JC-1 probe. (F) Western for hyperphosphorylated tau. (G) Semi-quantification of band intensity in western blot in (F) by ImageJ..... 101

Figure 4.6. Therapeutic mechanism of (Chla+Ind) NRs *in vitro*. (A) Proposed model illustrating the mechanism underlying the efficiency of (Chla+Ind) NRs in the amelioration of ROS level and tau hyperphosphorylation in AD. (B) Western blot for Bax, cleaved-caspase-3, p-Akt, Akt, p-GSK3 β and GSK3 β in PC12 cells and OA pre-stimulated PC12 cells, followed by the treatment of different preparations. Quantification results of (C) Bax and caspase-3, (D) p-Akt, Akt, , p-GSK3 β and GSK3 β . p-Akt, p-GSK3 β were normalized to total Akt, GSK3 β , respectively 103

Figure 4.7. *In vivo* evaluation of the therapeutic effect of (Chla+Ind) NRs. (A) Schematic drawings of the Y maze test and the experimental procedures. The analysis on (B) the entries to the novel arm and (C) the duration in the novel arm during the test phase during the Y maze

test. (D) Nissl staining assay of the density and activity of neurons in the CA1 and CA3 regions of mice brains. Quantitative analysis of Nissl positive cells in the (E) CA1 and (F) CA3 regions 105

Figure 4.8 *Ex vivo* evaluation of the therapeutic effect of (Chla+Ind) NRs. (A) The staining results of ROS indicator DCFH-DA in the whole hippocampus (HP) and representative images of hippocampal CA1, CA3 and DG region of wild type mice and OA induced-AD model mice administered with saline and different NRs (Chla NRs, Ind NRs, Chla+Ind NRs) with 980 nm laser irradiation. (B) Immunostaining for anti-p tau (Ser396) in the hippocampus. (C) Quantification results of ROS level. (D) Quantification results of p-tau level. 107

Figure 4.9 The biocompatibility and biosafety of (Chla+Ind) NRs. (A) H&E-staining of major organs of mice after injection with saline, or Chla NRs, Ind NRs or (Chla+Ind) NRs. Hemolysis rate of (B) Chla NRs, (C) Ind NRs, and (D) Chla+Ind NRs. Relative rate of hemolysis in mice RBCs upon incubation with H₂O as positive control, saline as negative control and Chla NRs, Ind NRs, Chla+Ind NRs at a series of concentrations. (E) Thermal images of mice before and after laser irradiation 108

List of tables

Table 1 Comparison of the optical properties of common donors in FRET-based biosensors 16

Table 2 FRET biosensors based on AIEgens as donor fluorophores 17

Table 3 Summary of intake route and administration strategies for H₂ treatment 37

Table 4 Comparison of TPE-DNA@GO nanoprobe with RT-PCR for SARS-CoV-2 viral sequence detection 58

Table 5 The information of DNA and RNA sequences in this study.....59

Table 6 The sequence information of DNA and RNA in this study.....82

List of abbreviations

FRET	Förster resonance energy transfer
ACQ	Aggregation-caused quenching
AIE	Aggregation-induced emission
UCNP	upconversion nanoparticle
AD	Alzheimer's disease
GO	Graphene oxide

MoS ₂	molybdenum disulfide
ROS	Reactive oxygen species
QDs	Quantum dots
MB	Methylene blue
ICG	Indocyanine green
SNR	Signal-to noise ratio
AIE	Aggregation-induced emission
RIV	The restriction of intramolecular vibration
RIM	The terms “restriction of intramolecular motion
RIR	The restriction of intramolecular rotations
SNR	Signal-to-noise ratio
CuAAC	copper-catalyzed azide-alkyne cycloadditions
LoD	A limit of detection
Exo III	Exonuclease III
GFP	Green fluorescent protein
ICT	Intramolecular charge transfer
GQDs	Graphene quantum dots
TMDs	Transition metal dichalcogenides
CVD	Chemical vapor deposition
miRNA	MicroRNA
FA	Folic acid
A β	β -amyloid
NFTs	Neurofibrillary tangles
APP	The amyloid precursor protein
BACE1	By γ -secretase and cleavage enzyme
CNS	Central nervous system
RVG	Rabies virus glycoprotein
siRNAs	Several small interfering RNAs
BP	Black phosphorus
PTT	Photothermal therapy
PDT	Photodynamic therapy
RB	Rose bengal

Ru	Ruthenium
Ce	Ceria
NGF	Nerve growth factor
PCM	Phase change material
IONPs	Iron oxide nanoparticles
ROS	Reactive oxygen species
Nrf ₂	Nuclear factor erythroid-2-related factor 2
SOD	Superoxide dismutase
GSH	Glutathione
NF-kB	Nuclear factor kB
HIF-1 α	Hypoxia-inducible factor-1 α
MMP	Matrix metalloproteinases
Bcl-2	B-cell lymphoma 2
PdH	Pd hydride
NRs	Nanoreactors
Pt NPs	Platinum nanoparticles
COVID-19	Coronavirus disease 2019
SARS-CoV-2	Severe acute respiratory syndrome coronavirus 2
ORF	Open reading frame
RT-qPCR	Reverse transcription-polymerase chain reaction
LFIA	Lateral flow immunoassay
POC	Point-of-care
ssDNA	Single stranded DNA
TOFMS	Time-of-flight mass spectrometry
AFM	Atomic force microscopy
vdW	Van der Waals
TMA	Tetramethylammonium
DCM	Dichloromethane
IVIS	In vivo image system
MALDI-TOF	Matrix-assisted laser desorption/ionization coupled to time-of-flight
UV-vis	Ultraviolet-visible
BBS	Borate buffered saline

BSA	Bovine serum albumin
OA	Okadaic acid
MCC	The Manders' colocalization coefficients
cVs	Cross-linking vesicles
DLS	Dynamic light scattering
CLSM	Confocal laser scanning microscopy
CMC	The critical micelle concentration
ECL	Enhanced chemiluminescence
AA	Ascorbic acid
XPS	X-ray photoelectron spectroscopy
Chla NRs	Chla-loaded nanoreactors
Ind NRs	Ind-loaded nanoreactors
UCL	Upconversion luminescence
Bax	BCL2-associated X
HE	Hematoxylin/eosin
Dex-MoS ₂	Dextran polymer modified MoS ₂ nanosheets

Chapter 1: Introduction

Modern science is progressing toward a deeper understanding of biological networks in living subjects, which has greatly benefited from developing novel bioanalytical techniques. Since George Gabriel Stokes first used the term "fluorescence" in 1852 to describe the remarkable light phenomenon he observed in quinine solution emitting blue light when exposed to ultraviolet (UV) light, fluorescence-based imaging techniques have gradually emerged as a powerful tool to study a variety of physiological events in living systems^[5, 6]. This imaging approach has the advantages of high spatial resolution, low cost, simple operation, and good biosafety^[7, 8]. In general, fluorescence imaging relies heavily on the specific labeling by various fluorescent agents, mainly including organic fluorophores, organic fluorophores-loaded nanoparticles (NPs), inorganic nanomaterials such as quantum dots (QDs)^[9], graphene quantum dots (GQDs)^[10], carbon dots^[11], and rare earth doped upconversion nanoparticles (UCNPs)^[12]. These organic fluorophores and inorganic nanomaterials can be excited by specific wavelengths of light and absorb the energy of photons, causing their electrons to jump into an excited state. Then, the electrons release a photon with lower energy after losing some of their energy during the process of vibrational relaxation and thus emit fluorescence with a longer wavelength when they return to the ground state (Figure 1.1A)^[13]. The wavelength difference between the absorption and emission maxima is defined as Stokes shift (Figure 1.1B)^[13]. Fluorescent materials with a large Stokes shift are known to avoid re-absorption of emitted light and scattering, which is beneficial for providing high-quality fluorescence imaging by reducing autofluorescence and self-quenching.

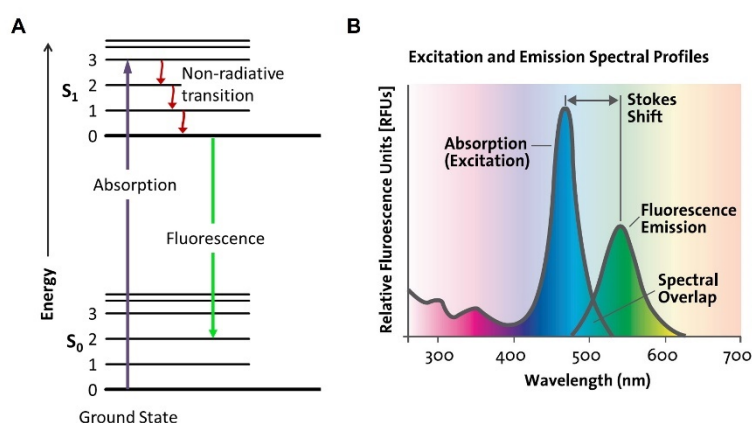


Figure 1.1 Brief introduction to fluorescence generation. (A) Jablonski diagram of absorbance, non-radiative decay and fluorescence. (B) Schematic illustration of Stokes shift^[13].

Organic dyes and dye-loaded fluorescent NPs are preferable to inorganic fluorescent materials for fluorescence bioimaging because of their inherent benefits, including good

biocompatibility, simplicity of processing, and potential biodegradability. Several organic dyes, including methylene blue (MB) and indocyanine green (ICG), have been authorized to be used in clinical applications such as the assessment of intraoperative blood flow, illustrating the great promise of organic fluorescent molecules in clinical translation ^[14, 15]. However, a great number of fluorescent dyes are hydrophobic and thus tend to aggregate in aqueous solutions and physiologic buffers due to π - π stacking interaction ^[16]. These fluorescent dyes in the aggregated state exhibit intense intermolecular π - π stacking, which greatly reduces exciton energy via non-radiative pathways and results in partial or complete fluorescence quenching. This phenomenon is known as the "aggregation-induced quenching (ACQ)" effect ^[17], which hinders the development of highly emissive fluorescent organisms for applications in biological microenvironments ^[18]. Here, we take perylene as an example to illustrate the adverse effects of ACQ on fluorescence imaging in biological applications. Perylene is a hydrophobic organic dye that exhibits strong blue emission in the well-dispersed state. Still, its emission becomes much weaker or even totally quenched in the aggregated state in the solution with a high fraction of water due to its planar structure and strong intermolecular interactions (Figure 1.2A) ^[19]. Therefore, the imaging performance of such fluorogens is heavily interrupted by the undesirable ACQ property, which restricts the concentration of fluorescent dyes used in the biological systems and causes a limited signal-to noise ratio, low potency, and photobleaching outcome.

1.1 Aggregation-induced emission (AIE)

The discovery of fluorescent molecules with aggregation-induced emission (AIE) feature offers a definitive solution to the abovementioned ACQ problem. As a new class of photophysical phenomena, AIE was first reported by Tang and colleagues in 2001 ^[20]. In contrast to the ACQ property, AIE fluorogens (AIEgens) exhibit negligible or weak emission when well-diluted in solution, but they become highly emissive in the aggregation state ^[21]. As shown in Figure 1.2B, hexaphenylsilole (HPS), a typical AIEgen, is nearly non-emissive in acetone solution where it is well-dissolved. Thus, its rotor structures trigger nonradiative decay to consume excitation energy but after adding water to form aggregates, its emission dramatically increases ^[20]. Additionally, the non-planar molecular architectures of HPS prevent tight intermolecular π - π stacking interactions during the aggregation process.

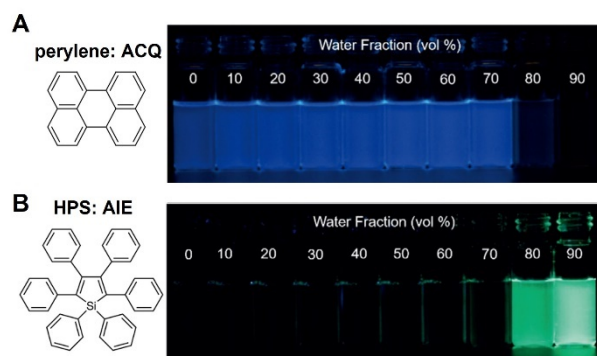


Figure 1.2 ACQ vs. AIE phenomenon. Molecular structures and fluorescence photographs of (A) perylene and (B) hexaphenylsilole (HPS) in mixtures of acetone and water with different water fractions. The photographs were taken under 365 nm UV light irradiation ^[19].

1.1.1 Mechanism of AIEgen

A better understanding of the luminescence mechanism of AIE is essential for developing new types of AIEgens and exploiting their potential applications. Through systematic investigation of different AIEgens, many researchers have successively proposed the restriction of intramolecular rotation (RIR) as the mechanism of AIEgens with rotor structures such as tetraphenylethylene (TPE) (Figure 1.3A) ^[22]. According to this mechanism, active intramolecular rotation encourages the nonradiative decay of excitons when AIEgens are dissolved in solution, which weakens their fluorescence. Instead, such intramolecular rotation is greatly restricted in the aggregated form, causing the nonradiative decay much decreased, and thus the fluorescence of AIEgens lights up. With the growing research on AIE effects, various AIEgens without rotor structures have been progressively developed and synthesized. Thus, there are also studies to reveal the luminescent mechanism for those AIEgens without rotors, such as cyclooctatetrathiophene (COTh) ^[23], which suggest that the restriction of intramolecular vibration (RIV) can be an addition of RIR since intramolecular vibration also leads to nonradiative decay of excitons in the excited state (Figure 1.3B). Altogether, the term "restricted intramolecular motility (RIM)" was coined to combine RIR and RIV as the general mechanism of AIEgens ^[24].

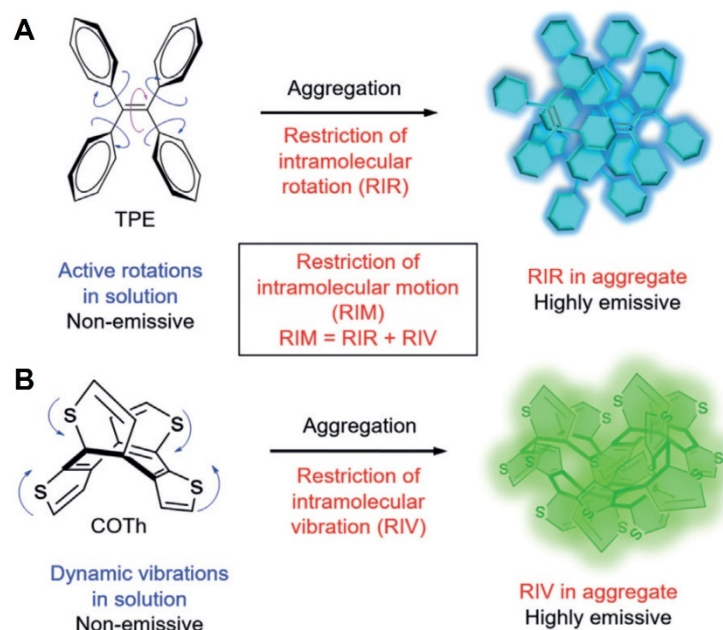


Figure 1.3 The mechanism of the AIE phenomenon. (A) The restriction of intramolecular rotations (RIR) in Tetraphenylethene (TPE) molecules. (B) The restriction of intramolecular vibration (RIV) in cyclooctatetrathiophene (COTh) molecules [22].

1.1.2 AIEgen-based probes

With recent advances in understanding the mechanism proposed to explain AIE effect, numerous AIEgens have been successfully designed and synthesized. Most of them are derived from typical AIE molecules such as tetraphenylethene (TPE), tetraphenylpyrazine (TPP), hexphenylsilole (HPS), and derivatives of 9,10-distyrylanthracene (DSA) (Figure 1.4) [25, 26]. Most of the current organic AIE molecules are hydrophobic. These molecules are inherently difficult to disperse stably and uniformly under physiological conditions, which is not conducive to extending their biological applications. Therefore, applying AIEgens in fluorescence bioimaging is achieved by developing hydrophobic AIEgens to hydrophilic molecular probes or nanoprobe.

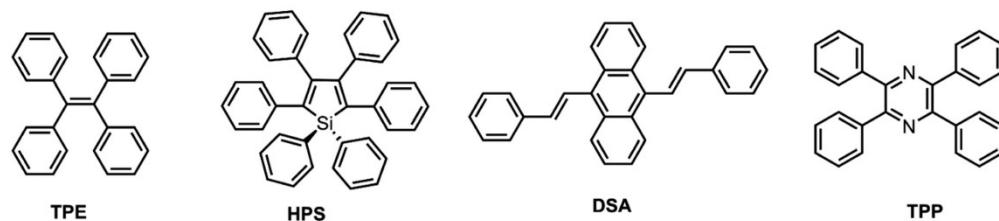


Figure 1.4 Molecular structure of typical AIEgens [26].

1.1.2.1 AIEgen-based molecular probes

Plenty of AIEgen-based molecular probes have been constructed to observe and monitor various biological species through the fluorescence enhancement caused by the binding of the AIEgen probes to the analytes. The key factor to consider while designing AIEgen-based

molecular probes is to improve their water-solubility. Initially, only cationic or anionic AIEgens-based probes could be used for imaging biomolecules and cellular organelles. In general, they bind with the analytes via hydrophobic and electrostatic interactions (Figure 1.5A). Such physical attachment of the probes to the analytes probably leads to non-specific fluorescence enhancement, which makes ionic AIEgens-based molecular probes inappropriate for applications in biological environments with many variables [27]. Accordingly, AIE molecular probes with fluorescence “turn on” properties were developed by conjugating targeting ligands or reactive groups to AIE molecules through the chemical bond to solve the specificity issue. As shown in Figure 1.5A, hydrophilic targeting ligands (e.g., DNA, RNA, peptide, and aptamer) were designed to be conjugated with AIEgens, endowing the resulting probes with good water-solubility [28]. In addition to enhancing hydrophilicity, these ligands are responsible for the specific binding of the probes to the receptors on the analytes through biomolecular interactions, such as the hybridization of oligonucleotides and recognition between antigens and antibodies. Additionally, another strategy to construct AIE molecular probes is dependent on the conjugation of cleavable quenchers with AIEgens (Figure 1.5A) [28]. The fluorescence of these AIE probes is turned on by a specific biological process that can maximize the specificity of probes by preventing any interference from other non-targeting analytes. By skillfully integrating functional groups and AIE molecules, AIE molecular probes with fluorescence "turn-on" properties have been widely employed for sensing various biomarkers of diseases and cellular imaging of organelles such as membranes, mitochondria, and lysosomes.

1.1.2.2 AIEgen-based nanoprobe

AIEgens emit strong fluorescence in the aggregated state due to restricted intramolecular motion within their structure. This property makes AIEgens more suitable than other organic fluorescent dyes for fabricating fluorescent nanoprobe (NPs). AIE NPs exhibit excellent biocompatibility due to the encapsulation of the polymer, making them more hydrophilic and stable in biological media. Moreover, AIE NPs tend to possess brighter fluorescence than their corresponding AIE molecules due to the restricted spatial scope of the nanoparticle shell. In addition, the large surface area of nanoparticles and ease of surface functionalization allows AIE NPs to show great potential in various fields of translational medicine. Several techniques have been developed for loading AIEgens into hydrophilic NPs with precise size and shape, facilitating their application in biosensing, cell imaging, therapeutic effect monitoring, and so on [29, 30]. Here are two common strategies used to fabricate AIE NPs summarized in Figure 1.5B [28]. In the first approach, AIEgens were first chemically bonded to hydrophilic polymers. The resulting AIEgen-polymer complexes were amphiphilic, so they subsequently self-assembled

to form NPs. This method requires a sophisticated design of the structure of AIE molecules, and it is challenging to tune the size of self-assembled AIE NPs. In addition, the conjugation of bulk polymers to the molecular structure of AIEgens might disrupt the non-planar conformation of AIEgens, which would cause them to lose the AIE properties.

Consequently, nanoprecipitation is a more widely used technique to prepare AIE NPs. In this strategy, AIEgens are encapsulated into amphiphilic polymeric matrices (such as the widely used DSPE-PEG and Pluronic F-127) *via* physical loading techniques such as probe sonication (Figure 1.5B) [31]. The nanoprecipitation method avoids the random nature of self-assembly and thereby provides more normalized procedures for preparing AIE NPs. Furthermore, by selecting different types of polymers and varying lengths, the shape and size of AIE NPs can be easily regulated to meet the requirements of diverse biological applications. Meanwhile, modification of functional groups (e.g., NH₂, -COOH, -SH) in the polymer matrix can provide active reaction sites for the surface functionalization of AIE NPs.

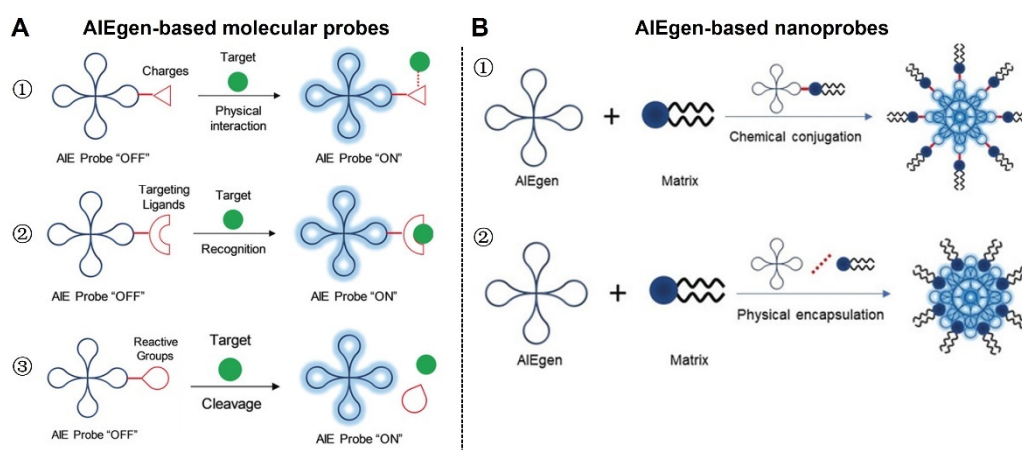


Figure 1.5 Methods for the design of (A) AIEgen-based molecular probes and (B) AIE NPs [28].

1.1.3 Application of AIE probes for biosensing and bioimaging

By the RIM mechanism, any modification that restricts intramolecular motion through molecular interaction (e.g., electrostatic, hydrophobic, and hydrogen bonding) between the recognition site of AIEgens and corresponding analytes can easily illuminate the bright emission of AIEgens. Therefore, the fluorescent signals light-up working model makes AIEgens exceptional fluorescence-based probes for achieving analytes-dependent signals output, and the light-up property is advantageous for reducing the background signal to obtain a higher signal-to-noise ratio (SNR), which would enhance the analytical sensitivity of biosensors and provide high contrast and quality for bioimaging application. Until now, AIEgens-based probes have been widely employed in the bioanalytical fields, such as biosensing and bioimaging [22].

AIE probes for biosensing. Biomolecules and biomarkers play essential roles in diagnosing and monitoring disease pathology; therefore, they must be detected and analyzed in a physiological environment. So far, different AIE-based biosensors have been employed to detect diverse biomolecules, such as DNA, RNA, and proteins. These biosensors interact with analytes to form bioprobe-analyte complexes, activating the RIM process and illuminating the sensing system. Bin Liu and co-workers demonstrated a unique sensing strategy that AIEgen (e.g., TPE) was modified with single-stranded oligonucleotides to fabricate fluorescence light-up bioprobe for the detection of complementary DNA hybridization in a homogeneous solution (Figure 1.6A) ^[1]. In this study, the probe TPE-DNA_p was designed by an azide-functionalized AIEgen (TPE-N₃) conjugated with alkyne-substituted oligonucleotide *via* copper-catalyzed azide-alkyne cycloadditions (CuAAC). The single-stranded oligonucleotide within the structure of TPE-DNA_p endows the probe with high specificity to distinguish complementary target strands from one-base and two-base mismatch sequences. The selectivity of TPE-DNA_p was much better than that of these previously reported AIEgen-based probes for DNA detection, where interaction forces between probes and target sequences were usually non-specific electrostatic and hydrophobic effects. TPE-DNA_p exhibited weak fluorescence in the solution due to the active intramolecular rotations using excitonic energy. At the same time, upon hybridization to the target DNA sequence, the formed double helix structure prevented the phenylene rings of the TPE core from freely rotating, which resulted in the fluorescence of TPE-DNA_p being significantly enhanced to indicate the target DNA. As such, the limit of detection (LoD) was measured to be 0.3 M, and the brightness of the TPE-DNA_p-target DNA complex displayed around 3-fold higher than that of the TPE-DNA_p probe alone. Fan Xia's teams then reported a similar DNA-conjugated AIE probe (TPE-R-DNA) for intracellular monitoring of mRNA expression (Figure 1.6B) ^[2]. In this work, a target recycling method assisted by exonuclease III (Exo III) was combined with a red-emitting TPE-R-DNA probe for cancer cells and tissue imaging. TPE-R-DNA comprised two sections: TPE-R-N₃, a hydrophobic AIE molecule that functioned as the fluorescence imaging agent with a long emission wavelength, and Alk-DNA, a hydrophilic single DNA strand that specifically hybridized the target mRNA fraction. Without target mRNA, TPE-R-DNA probe was completely hydrophilic, resulting in negligible fluorescence. In contrast, in the presence of target mRNA, TPE-R-DNA hybridized with target sequence to form duplex nucleic acid, following digested by Exo III to release the hydrophobic fluorogens, which eventually assembled in aqueous solution to enhance the fluorescence signals of the sensing system. As a

result, the LoD of TPE-R-DNA probe toward mRNA reached 0.6 pM, which was much more sensitive than TPE-DNA_p probe without a target recycling strategy.

Additionally, peptide-modified AIEgen probes were developed to monitor the specific enzyme activity in living cells relying on the reduced water-solubility of probes to form aggregates in the presence of analytes. For example, to detect the bio-activity of caspase 3/7 in cancer cells, Bin Liu and colleagues developed an Ac-DEVDK-TPE probe, composed of TPE core as an imaging module coupled with a peptide (Asp-Glu-Val-Asp-Lys, DEVDK) that could be specifically recognized and cleaved by caspase-3/7 (Figure 1.6C) [32]. With DEVDK peptide conjugation, the probe alone was extremely hydrophilic and almost non-fluorescent. However, once the DEVDK peptide in the probe was specifically clipped by the target caspase 3/7, the hydrophobic TPE residues aggregated in an aqueous solution and boosted the fluorescence signals in the sensing system, which was an effective strategy for caspase3/7 detection.

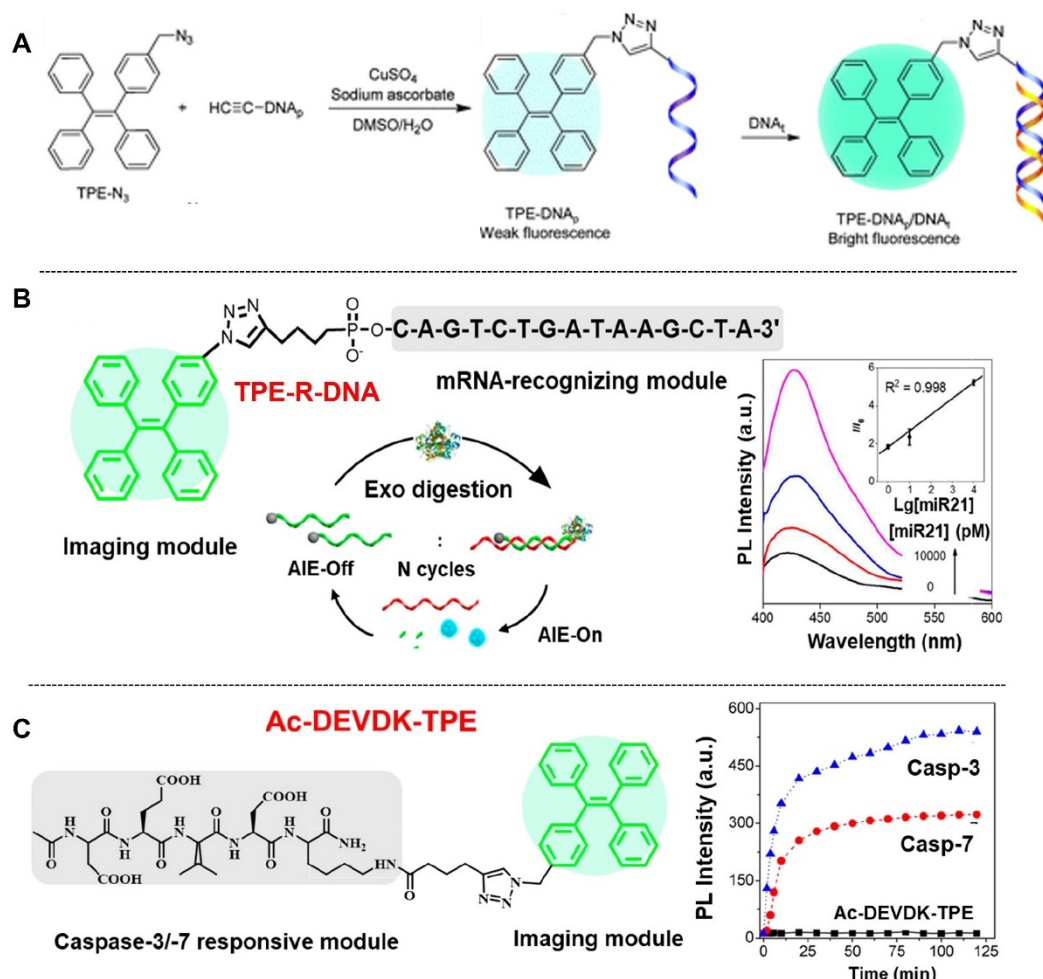


Figure 1.6 Representative examples of AIE probes for DNA, RNA, and protein detection. (A) Schematic illustration of TPE-DNA_p for detection of nucleic acid DNA_i.^[1] (B) Schematic illustration of TPE-R-DNA for detecting mRNA in cancer cells.^[2] (C) Schematic illustration of Ac-DEVDK-TPE probe and its time-dependent fluorescence intensity in the presence of caspase 3/7 proteins.^[32]

AIEgen-based probes for bioimaging. AIEgens have been attractive fluorescent materials for bioimaging applications due to their high brightness in the aggregate state and the unique property that they become stronger emitters at larger concentrations. AIEgens-based imaging systems have been superior to traditional organic dyes and QDs in terms of brightness, biocompatibility, and photobleaching resistance [27]. However, most AIEgens are only soluble in organic solvents, making them unsuitable for biological applications. Hence, AIE NPs constructed by physical nanoprecipitation using amphiphilic polymers physically encapsulated with AIE molecules are more commonly used in bioimaging. On the basis of the AIE feature, a high loading of AIE molecules is compactly encapsulated inside the nanoparticles, supporting their super brightness and good photostability [31]. In addition, AIE NPs have a high surface-to-volume ratio. They are easily adaptable to functional ligands on the surface, further expanding their application in the targeted bioimaging areas. Consequently, AIE NPs have garnered a great deal of interest due to their exceptional performance in various bioimaging applications, such as subcellular cell imaging (e.g., mitochondria and lysosome) [33, 34], in vivo imaging of tissue and vascular structure [35], imaging-guided therapy [36], and multi-modal imaging integrated with MRI, CT, etc. [37].

1.2 Upconversion fluorescence

Depending on the emission principle of fluorescent materials, fluorescence imaging techniques can be divided into two categories: downconversion fluorescence and upconversion fluorescence. The fluorescence of the majority of fluorescent agents, such as the ACQ fluorophores, AIEgen, and inorganic fluorescent quantum dots and carbon dots, is generated by the downconversion of higher energy light (typically UV to visible) to lower energy light with a longer wavelength. These fluorescent probes with downconversion emission exhibit strengths in terms of high quantum yield and long fluorescence lifetimes. However, there is a partial overlap in their excitation and emission spectra, which could lead to photobleaching issues and make it difficult for downconversion nanoprobes to meet the quality requirements for in vivo fluorescence imaging. Furthermore, endogenous fluorophores such as tryptophan and elastin, which are naturally present in biological species, exhibit significant light scattering below 700 nm, resulting in strong background autofluorescence and causing severe interference with imaging results under biological conditions [38]. These limitations have severely impeded the use of downconversion fluorescence-based probes for monitoring biological processes and detecting disease-related biomarkers in deep tissues. Here, we take the commercially available fluorescein FITC or green fluorescent protein (GFP) as examples. Both of these are down-converting fluorescent materials. Although they have been utilized extensively for cell imaging

in vitro and fluorescence imaging of superficial skin tissues for many years, few studies have employed FITC or GFP for imaging the brain or monitoring endosomal organ lesions. The discovery of upconversion fluorescence provides novel strategies for addressing this issue. Nicolaas Bloembergen originally postulated the upconversion fluorescence phenomenon in 1959, and later Porter John F. further explained upconversion as a nonlinear optical process in which low-energy light in the NIR range is transformed into high-energy light in UV and visible range [39]. Lanthanide-based UCNPs are one of the most studied upconversion materials. It possesses many desirable properties, such as easy spectrum tuning, minimal photodamage to specimens, high penetration depth, low autofluorescence, and millisecond-level lifetime, making it a promising and effective fluorescent probe for in vivo studies [40].

1.2.1 Photophysical mechanisms of upconversion fluorescence

In the structure of UCNPs, two adjacent types of lanthanide ions, known as the sensitizer and activator ions, are introduced to the crystalline host material of UCNP to accomplish the photon upconversion process [39]. Sensitizer ions, such as ytterbium (Yb^{3+}) and neodymium (Nd^{3+}), exhibit absorbance maxima in the NIR region at 980 nm and 800 nm, respectively. By absorbing a large number of low-energy photons from NIR light, the sensitizer ion is excited from its ground state to the intermediate excitation state 1 (E1), and then the ground state and E1 states of the activator ion (typically erbium Er^{3+} , thulium Tm^{3+} , and holmium Ho^{3+}) repeatedly acquire energy from the sensitizer ion. When the activator ion returns to its ground state, it generates upconversion luminescence. (Figure 1.7) [39]. Typically, UCNPs are fabricated from inorganic host materials doped with photoreceptors and activator ions. The host material is expected to be chemically stable and unrelated to excitation light or upconversion luminescence. Different host materials have been developed so far, including fluorides (NaYF_4), oxychlorides (GdOCl), oxides (Y_2O_3 and ZrO_2), oxysulfide ($\text{Y}_2\text{O}_2\text{S}$), and vanadates (YVO_4) [41]. Among them, NaYF_4 is widely used as a host lattice in UCNP-based biosensors and bioimaging due to its ultra-low cut-off phonon energy, thereby minimizing the loss in upconversion emission produced by phonon-induced non-radiative decay.

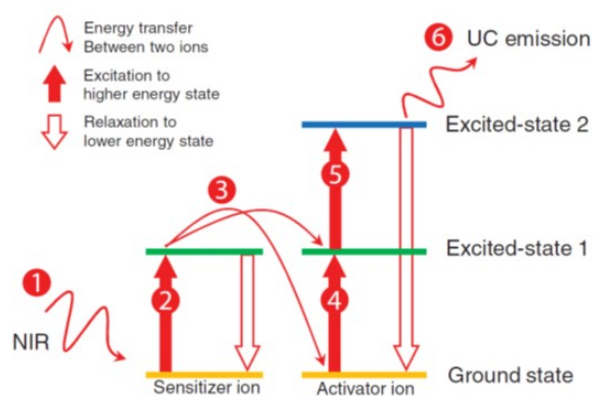


Figure 1.7 Schematic diagram of the energy transfer mechanism of upconversion fluorescence [39].

1.2.2 Structure of UCNPs

Most bare UCNPs exhibit surface quenching centers and crystal defects as a result of small-size effects, which leads to greater non-radiative energy consumption paths. This phenomenon drastically reduces the upconversion efficiency of UCNPs, as photons in both the intermediate and final excited states are capable of transferring excitation energy to the quenching centers during the upconversion process. Consequently, the primary issue with unmodified UCNPs is their low luminosity, which limits the versatility of UCNPs-based fluorescent materials in vivo applications. To achieve efficient upconversion luminescence, a laser with a fairly high power density is usually required as an excitation source. For biological applications in vivo, however, excitation powers in excess of 1 W/cm^2 may cause severe thermal damage. So far, upconversion efficiency can be improved in two primary ways: reducing the likelihood of non-radiative conversion and increasing the absorption capacity. The design of the core-shell structure of UCNPs is a highly effective strategy for achieving this goal [41]. The basic principle and common configurations of core-shell UCNPs are shown in Figure 1.8 [42]. In the core-inert shell system, the shell acts as an undoped host material devoid of activator or sensitizer ions, thereby blocking the energy transfer pathway from the activator (or sensitizer) to the surface quenching centers. This structure lowers non-radiative consumption and boosts the upconversion efficiency of core-shell UCNPs. In addition, sensitizer ions such as Yb^{3+} can be doped into the shell layer to form the core-active shell structure of UCNPs, which increases the upconversion efficiency by absorbing additional excitation photons (Figure 1.8) [42].

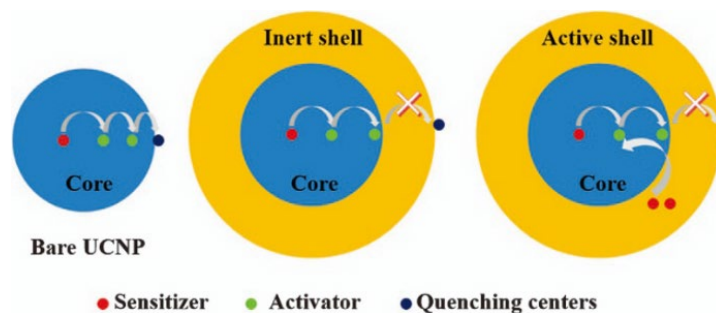


Figure 1.8 Design of core-shell UCNPs to improve upconversion efficiency ^[42].

1.2.3 Application of UCNPs for biosensing and bioimaging

UCNPs for biosensing. Biosensors enable the accurate tracking of particular physiological processes and the identification of subtle biomolecules. UCNPs are promising for biosensing applications due to their unique ability to use NIR light as an excitation source, which enables them to detect biological processes with exceptionally low background noise and adequate tissue penetration depth within living systems. In recent years, numerous UCNP-based biosensors have been reported to detect intracellular biomolecules such as DNA, RNA, and enzymes and to *in situ* monitor disease-related biomarkers in deep tissues ^[43]. In these biosensing platforms based on UCNPs, resonance energy transfer is the primary detection mechanism. In this process, UCNPs function as energy donors that bind to energy acceptors capable of altering the fluorescence intensity in response to the interaction with the analyte. However, there is no direct relationship between the fluorescence of UCNPs and any intrinsically characterized bioanalytics. Therefore, UCNPs must be designed with the proper recognition components, such as DNA, enzymes, and antibodies, in order to recognize the target analytes ^[44]. Hybridization of complementary nucleic acid base pairs frequently occurs during the process of specifically identifying DNA or RNA with UCNP-based probes. A. G. Kanaras presented a DNA biosensor based on the resonance energy transfer effect and constructed by UCNP adsorption on the surface of GO ^[45]. The monodisperse UCNP was coated with a SiO₂ shell to prevent surface quenching effects, and the SiO₂ shell with a terminal NH₂ group facilitated the modification of single-strand probing DNA. The fluorescence of ssDNA-functionalized UCNP@SiO₂ was completely quenched when it was in close proximity to the GO surface, as the fluorescence emission spectrum of UCNP@SiO₂ overlapped with the absorption spectrum of GO. In contrast, in the presence of complementary target DNA strands, the double-stranded DNA resulting from hybridization had no strong interaction with the GO quencher, resulting in the recovery of UCNP@SiO₂ luminescence. The DNA sensor exhibited a detection limit of 20 pM ^[45].

UCNPs for bioimaging. Imaging techniques utilizing conventional organic dyes, QDs and GQDs, adhere to the Stoke shift law. However, the excitation of these fluorescent materials occurs primarily in the ultraviolet-visible spectrum; as a result, they may experience problems with light penetration and autofluorescence. In addition to reinforcing the power intensity of the excitation source to allow greater light penetration, the "optical transparent window" of the tissue has little autofluorescence and light scattering in the NIR (700 to 1100 nm) range, which facilitates fluorescence imaging with high contrast and quality ^[38]. Hence, effective fluorescence materials with excitation or emission light wavelength extending to the NIR range are desirable for a wide variety of *in vivo* bioimaging applications. In contrast to downconversion fluorophores, UCNPs offer numerous advantages for bioimaging applications due to their unique optical properties, such as (1) The utilization of NIR light as an excitation source enables UCNPs to penetrate biological tissues more effectively than visible light and to avoid the auto-fluorescence. (2) The photobleaching resistance and nonblinking properties of UCNPs make them suitable for long-term bioimaging. (3) Significant anti-Stokes shift properties permit UCNP probes to emit fluorescent signals with less background noise. (4) The extended luminescence lifetime in the millisecond range enables temporal separation of the probe signals from the intense background signals by fluorescence lifetime imaging microscopy ^[40, 42-44]. Owing to these features, NIR-triggered UCNPs are growing as a new class of imaging substances for *in vivo* bioimaging, with applications in cellular imaging, whole-body photoluminescence imaging, and deep tissue imaging ^[39].

1.3 Forster resonance energy transfer

In the field of biomedical diagnostics, fluorescence imaging has been utilized extensively. During the past few decades, numerous fluorescent biosensors have been developed to monitor various biological activities and biomolecules, including nucleic acids, proteins, enzymes, antibodies, antigens, and other biological substances. These fluorescent biosensing platforms were established using two strategies: (1) direct fluorescent biosensors. One fluorophore with a single emission character was directly employed in one biosensing platform. (2) ratiometric fluorescent biosensors. The Ratiometric biosensing system was established by two fluorescent motifs with distinct emission spectra integrated into one biosensing system ^[46]. In the first strategy, the fluorescent signals of direct fluorescent biosensors are easily interrupted by different variables in the external environment (e.g., pH, temperature, and ionic strength), which makes it difficult for many direct fluorescent biosensors to accurately quantify various biomarkers and biological responses. To solve the problem, ratiometric fluorescent biosensors have been designed to detect the analytes by comparing the fluorescence intensity at two

different wavelengths simultaneously recorded. So far, intramolecular charge transfer (ICT) and Förster resonance energy transfer (FRET)-based methods are the two main ways to build ratiometric fluorescence techniques. ICT-based fluorescent probes are constructed with a single fluorophore containing electron-donating and electron-absorbing groups [47]. The electron-absorbing groups typically serve as recognition sites that specifically bind to analytes, leading to a change in the fluorescence spectrum to indicate the presence of target biomolecules. In the case of ICT, the binding of probes to analytes may enhance or inhibit the ICT interaction, resulting in a significant shift in the fluorophore absorption maximum, which would compromise the accuracy of ICT-based biosensors. In addition, it is difficult to precisely determine the ratio of two fluorescence peaks due to the extremely broad fluorescence spectrum. This problem can be partially addressed by FRET-based probes, as they produce longer emissions from a single excitation. FRET-based biosensors offer not only high sensitivity, specificity, and fast response time but also possess the advantage of homogeneous detection without washing procedures for accurate quantitative measurements in living systems [48]. Due to their multiple advantages, FRET-based biosensors have been applied to detect disease-associated biomarkers, monitor treatment results, screen drugs, and visualize biological processes.

1.3.1 Principle of FRET

FRET is a process of close-range energy transfer between two light-sensitive molecules. Within a close distance, the emission from a donor fluorophore is absorbed by an adjacent acceptor under particular excitation conditions, causing fluorescence quenching (Figure 1.9A) [49]. The key factors that affect the energy transfer efficiency (E) of FRET assay include the distance (r) between donors and acceptor pairs (typically less than 10 nm) and the overlap of emission spectrum (J) of donor and acceptor (Figure 1.9B) [50]. The energy transfer efficiency (E) can be calculated by equation (1) [51]. In a typical FRET system composed of a single pair of donor and acceptor fluorophores, the energy transfer is inversely proportional to the sixth power of the distance (r) between the donor and acceptor pairs. In this equation, R_0 represents the distance between donor and acceptor pairs at half the energy transferred. Generally, R_0 depends on the spectral overlap (J) and the quantum yield of donor fluorophores, which might range from 2 to 10 nm.

$$E = \frac{1}{1 + \left(\frac{R}{R_0}\right)^6}$$

$$R_0 = 0.0211(J\Phi k^2 n^{-4})^{1/6}$$

In equation (2), n is the refractive index of the medium between the donor and acceptor pairs, and k^2 is the orientation of the donor and acceptor transition dipole moments. As a result, the FRET assay requires extensive spectral overlap between donor and acceptor pairs. Additionally, the FRET effect can be turned on and off by the change in the distance (r) between the donor and acceptor, making FRET-based sensing platforms extremely sensitive to even minute variations in the distance [52]. Various biological processes, such as the hybridization of oligonucleotides, immunological binding reactions between antigens and antibodies, and enzyme-biocatalytic reactions, occur similarly small spatial scales in living organisms. Therefore, fluorescent biosensors based on FRET are useful tools for monitoring these biological reactions.

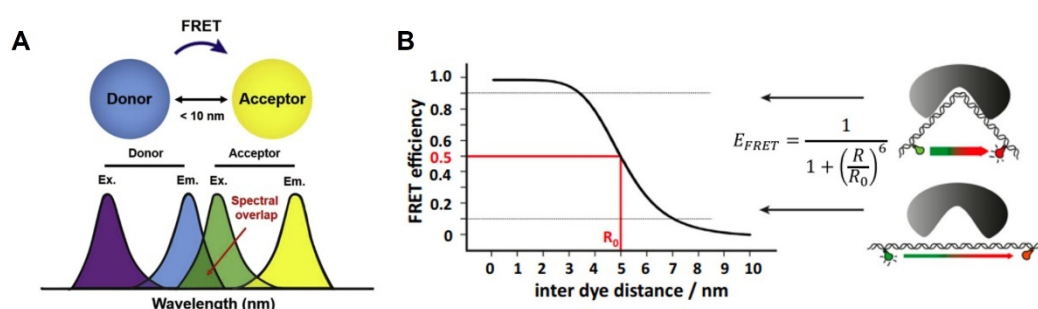


Figure 1.9 (A) FRET mechanism diagram(B) Diagram of Energy Transfer Efficiency (E) of FRET Assays [50].

1.3.2 Donors of FRET-based biosensors

The fluorescence signals for FRET-based biosensing applications are primarily determined by two variables: (1) the luminescence efficiency of donor fluorophores, as measured by quantum yield, fluorescence lifetime, etc. High luminescence efficiency causes more photons to be simultaneously excited at a given excitation power, manifesting as brighter light emission. (2) the quenching ability of the acceptor motif High quenching capacity of the acceptor motif can significantly alter the fluorescence signals resulting from biological reactions, thereby enhancing detection sensitivity [52]. To date, a variety of fluorescent materials have been used as donors in FRET sensing systems, mainly including conventional organic fluorescence dye, AIEgens, inorganic quantum dots, as well as upconversion luminescent materials[53]. Table 1 briefly summarizes the characteristics of these commonly used fluorescent agents as FRET donors.

FRET donors	traditional dyes	AIEgens	QDs	GQDs	UCNPs
FL generation	downconversion	downconversion	downconversion	downconversion	upconversion
Excitation	visible~NIR	visible~NIR	UV	UV	NIR laser
Emission	asymmetric and tailed emission bands	broad emission bands with a width of ~200 nm	tunable emission depending on size (blue to red)	tunable emission (blue to red)	tunable narrow emission bands
Stokes shift	<30 nm	>120 nm	250~400 nm		anti-stokes shift
FL lifetime	few ns	ns~ μ s	20~50 ns	ns level	μ s~ms level
Quantum yield	<0.1%	0.9%~31.5%, depending on dissolved media	40~90%, depending on buffer and surface modification	2~23%	<1%
Photostability	ACQ problem	Strong anti-photobleaching	Strong anti-photobleaching	Strong anti-photobleaching	Strong anti-photobleaching
Toxicity	low	low	high	low	low

Table 1. Comparison of the optical properties of common donors in FRET-based biosensors.

Organic fluorescence molecules are widely employed as donor fluorophores in many FRET-based biosensors. They are advantageous for developing dye-to-dye FRET systems due to their small size, a large number of modification sites, high quantum yields, and ease of bioconjugation. However, conventional organic dyes (e.g., FAM, Cy3, Cy5) are easily affected by temperature and pH during the detection process, and they are susceptible to photobleaching and blinking issues due to their inherent ACQ effect, which prevents them from being applied at high doses and further reduces the sensitivity of FRET biosensors. The application of new generations of fluorophores with AIE properties for fluorescence imaging has been briefly discussed in section 1.1. AIEgens are ideal candidates for use as donor fluorophores in the development of FRET-based sensing platforms for bioapplications due to their robust brightness, large Stokes shift, robust brightness, strong resistance to photobleaching, and good biocompatibility. Recent studies have used AIE-active molecules to construct FRET biosensors for fluorescent turn-on sensing of biomolecules. (Table 2) ^[54-60]. Most of these studies utilized cationic AIEgens with a DSA or TPE core as donor fluorophores. These cationic AIEgens possess typical AIE properties but are water-soluble and hence show minimal fluorescence in the dispersion state. To confer specific recognition sites on AIE-FRET probes, AIEgens interacted with ssDNA or aptamers via electrostatic attraction to form AIE-DNA complexes with restricted intramolecular motion, resulting in an initial fluorescence-on state. The AIE-DNA was subsequently physically coupled with graphene oxide (GO), resulting in a

fluorescence-off state. The addition of target biomolecules to AIE-DNA-GO probes led to the formation of a DNA/target complex that interacted less with GO, allowing AIEgen to detach from GO and regain fluorescence. However, labeling aptamers to AIEgens via electrostatic interactions renders AIE-FRET probes susceptible to external environmental factors and restricts their use to monitor only charged biomolecules. Consequently, there is an urgent need to develop more AIEgen-based FRET sensing platforms with improved stability and greater specificity.

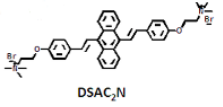
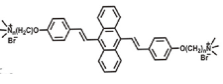
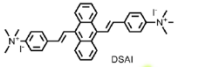
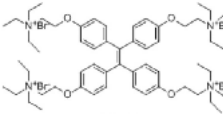
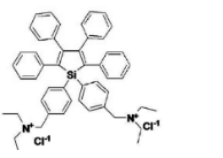
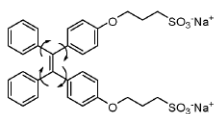
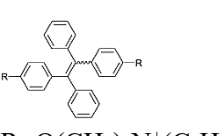
Donor/acceptor	AIEgen structure	Analytes	Detection limit	Linear range	Sample species	Ref
DSAC ₂ N/C-Apt/GO	 DSAC ₂ N	Chloramphenicol	1.26 pg/mL	5-1000 ng/mL	Tris-HCl buffer solution	[60]
DSA-DNA/GO		complementary target ssDNA	~170 pM	1-600 nM	solution	[59]
DSAI/GO		thrombin protein	3 ng/mL	10-2000 ng/mL	Thrombin solution	[58]
TTAPE-ssDNA/GO		complementary target ssDNA	2.5 nM	5-100 nM	Tris-HCl buffer solution	[57]
A2HPS/GO		BSA	2.3 µg/mL	10 to 200 µg/mL	solution	[56]
TPE-SO ₃ Na/GO		BSA	5 µg/mL	0~60 µg/mL	solution	[55]
TPE/GO	 R=O(CH ₂) ₄ N ⁺ (C ₂ H ₅) ₃	BSA	-	-	solution	[54]

Table 2. FRET biosensors based on AIEgens as donor fluorophores.

In addition to organic dyes, numerous nanoparticle types have been utilized as donors in FRET assays for diverse biological applications. Compared to conventional organic dyes, these fluorescent nanoparticles such as UCNPs, semiconductor quantum dots (QDs), and graphene

quantum dots (GQDs) usually have higher quantum yield and better photostability, making them ideal candidates as donors in FRET-based biological detection [49, 52]. QDs (e.g., InGaP, InP, CdSe, and CdTe) have been used as fluorescent markers in a variety of biological applications. QDs have several merits over conventional organic fluorescent dyes as FRET donors, including long fluorescence lifetimes and almost no photobleaching properties [52, 61]. However, it is hard to ignore the limitations of QDs as FRET-based donors. When building FRET sensors, the size of donor nanoparticles must be taken into account since the separation between the donor-acceptor pair determines the FRET efficiency. The average size of QDs is typically less than 20 nm, so employing QDs as donors will result in lower FRET efficiency than using organic dyes in sensing platforms [62]. Additionally, the manufacturing of QDs like CdSe and CdTe utilizes hazardous components, which limits their use in biological areas.

In recent years, GQDs have been used as fluorescence donors in FRET experiments. GQDs maintain some exceptional optical properties of quantum dots, such as excellent photostability, long fluorescence lifetime, high brightness, and tunable emission range [52]. Moreover, the FRET-based sensing platforms with GQDs as donors are very applicable to biological applications since GQDs have superior biocompatibility than semiconductor QDs. Additionally, the spectral overlap between donor and acceptor molecules can be optimized by modifying the surface and varying the size of the GQDs in order to enhance the energy FRET efficiency. As a new class of fluorescent materials for biosensing and imaging, UCNPs have attracted considerable attention. They offer distinct advantages over conventional organic dyes and inorganic QDs. For instance, UCNPs exhibit low toxicity, good photostability, and significant anti-Stokes shifts. Due to their exceptional properties, UCNPs are desirable as donors for FRET-based bioassays [63]. Particularly, unlike QDs and GQD excited by UV light, UCNPs utilize NIR light as excitation source, which have high penetrating capabilities and minimize photodamage to tissues. Therefore, FRET assays based on UCNPs are advantageous for biosensing applications in deep tissues.

1.3.3 Acceptor of FRET-based biosensors

High FRET efficiency requires a large overlap between the spectrum of donor emission and acceptor absorption. Therefore, materials with a broad absorption range are advantageous for quenching the fluorescence of donor fluorophores to endow FRET-based biosensors with a high signal-to-noise ratio. Furthermore, the development of nanotechnology has enabled the construction of FRET systems with multiple nanomaterial acceptors. Recently, two-dimensional (2D) nanomaterials such as graphene oxide (GO) and molybdenum disulfide (MoS₂) nanosheets have gained much attention due to their attractive optical properties [64].

1.3.3.1 GO

The structure of pristine graphene features sp^2 electronic orbitals with a high capacity for dampening fluorescence. As a derivative of graphene, GO is an oxidizing form of graphene. It is often made using Hummer's method, in which 3D graphite precursors are exfoliated into 2D GO with functional oxygen groups on their base plane and edges (Figure 1.10A) ^[65]. Due to its distinguishing heterogeneous chemical and electronic structure with functional groups for further surface modification and a high surface-to-volume ratio providing more bioreaction sites, GO has been widely utilized as acceptors for FRET-based biological applications ^[64]. The presence of the sp^3 C-O matrix and carbon atoms with sp^2 hybridization results in a distinct heterogeneous chemical and electronic structure. Such a complex structure offers a large number of chemical binding sites in addition to providing a wide absorbance spectrum ranging from 200 nm to 800 nm. Covalent interactions between biomolecules and GO are feasible due to the abundance of oxygen-containing groups like hydroxyl and carboxyl. Single-stranded DNA and single-chain polypeptides are typically readily adsorbed on GO surface through π - π stacking, whereas antibodies bind to the surface of GO via simple step coupling chemistry ^[66]. Furthermore, GO exhibits better quenching performance than other fluorescent quenchers because the FRET efficiency of GO is inversely related to the fourth power of the distance between donors and acceptors, while a six-order inversion relation is found in most of the other fluorescent quenchers ^[67], which provides GO with a substantially longer distance for efficient quenching performance. Such exceptional optical properties make GO an excellent nano-quencher when coupled with universal donor fluorophores in FRET assays for detecting various biomolecules.

One of the most widely used applications for GO-based FRET bioprobes is nucleic acid detection. The common method of detecting RNA and DNA relied on the π - π interaction between sp^2 carbon atoms on GO and oligonucleotides. The π - π stacking force between GO and DNA was affected by the length of the single-stranded (ss) DNA, with longer ssDNA resulting in a stronger interaction. Moreover, the interaction between double-stranded (ds) DNA and GO was significantly weaker than that of single-stranded DNA ^[66]. So far, numerous FRET-based biosensors have been developed to detect nucleic acid by employing GO as a fluorescent quencher and taking advantage of the differences in adsorption intensities of short ssDNA, long ssDNA, and dsDNA.

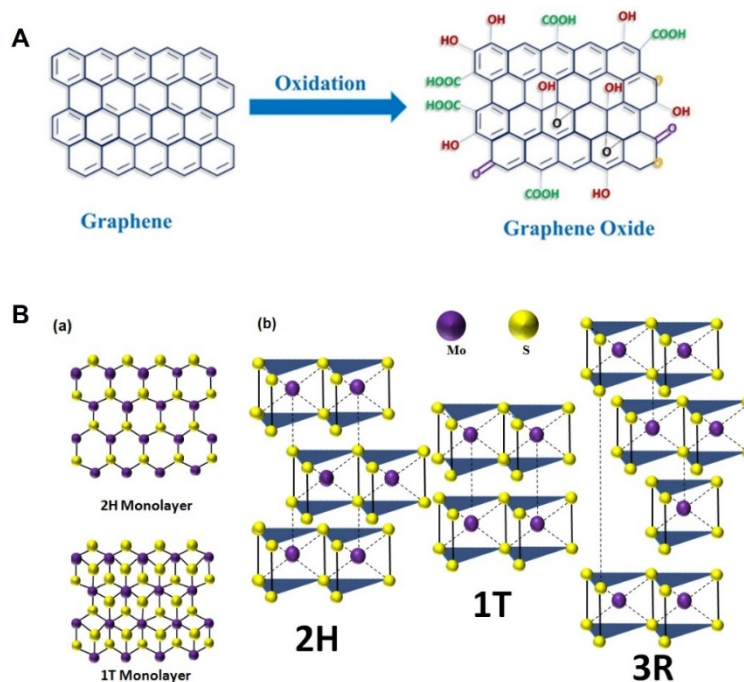


Figure 1.10 Chemical structure of (A) GO and (B) MoS₂ [66, 68].

1.3.3.2 MoS₂

The 2D transition metal dichalcogenides (TMDs) include more than 40 different types of materials. TMDs are named MX₂, where M is a transition metal (e.g., Mo, W, Ti, V, and Ta), and X is a chalcogen (e.g., S and Se) connected with the transition metal. Molybdenum disulfide (MoS₂) is the most representative member of the TMD family. Structurally, 2D MoS₂ is constructed with S-Mo-S bonding. The S and Mo atoms combined via a strong covalent bond, stabilizing the fundamental structures of the MoS₂ nanomaterial [69]. Additionally, many layers of MoS₂ are fabricated together *via* van der Waals forces. Due to the weak interaction of weak van der Waals, MoS₂ materials are easily severed by mechanical force, making MoS₂-based nanoprobe with lubricating properties suitable for a greater variety of potential bioapplications [69]. Furthermore, MoS₂ can take on a variety of structural configurations depending on the diverse alignment of S atoms. Three prototypical configurations of MoS₂ at the molecular level are shown in Figure 1.10B [68]. The most thermodynamically stable phase is 2H, in which the S atoms are arranged in a hexagonal symmetry mode. In contrast, S atoms are structured in tetragonal and rhombohedral forms in the 1T and 3R phases, respectively. MoS₂ materials in the 2H phase are the most photoluminescent, with widespread applications in biosensing and bioimaging [70]. The optical and physicochemical properties of MoS₂ materials can be tuned by varying the number of layers. For instance, the direct bandgap of 2D MoS₂ nanosheets is 1.96 eV, whereas the indirect bandgap of bulky MoS₂ is 1.2 eV due to quantum confinement [69]. Additionally, the active sites in MoS₂ are situated near the edge; therefore, an efficient strategy

to improve the performance of MoS₂ materials is to reduce the layer and thus increase the number of active sites that are exposed.

So far, the main synthesis approaches for MoS₂ nanosheets are divided into two categories: top-down and bottom-up methods. Top-down methods aim to separate single/few-layer nanosheets from bulk MoS₂ materials by destroying weak van der Waals coupling between different layers using chemical or physical pressures [70]. According to this theory, top-down methods often involve chemical, mechanical, liquid, and electrochemical exfoliation routes. These top-down exfoliation methods can produce single- or few-layer MoS₂ nanosheets with high structural crystallinity and purity, but their yield is relatively low. On the other hand, the theoretical foundation for bottom-up approaches is to synthesize the nanosheets from molybdenum and sulfur as precursors under controlled circumstances [68]. Chemical vapor deposition (CVD) is typically used to deposit MoS₂ nanosheets on the substrate. MoS₂ nanosheets with regulated size and thickness and excellent electrical characteristics can be synthesized using the CVD method. However, they are difficult to incorporate into other substrates or solutions, which has restricted their wide usage, and MoS₂ nanosheets produced by organic solvent-involved methods are not appreciated for further biomedical application. Altogether, liquid-phase exfoliation is the most common method for preparing MoS₂ nanosheets for biological applications.

MoS₂ nanosheets have garnered considerable interest in the fabrication of FRET-based biosensors due to their large absorption band, high surface area, robust photoluminescence, and bioconjugation-capable surface functionalization potential. Notably, pure MoS₂ nanosheets aggregate rapidly in physiological microenvironments such as blood and fluid, rendering MoS₂-based FRET sensing platforms relatively unstable in complex *in vivo* conditions. Therefore, many researchers have employed a surface modification strategy mainly based on the introduction of hydrophilic polymers (e.g., polyethylene glycol (PEG) and dextran) to MoS₂, which greatly improves the biostability of MoS₂ nanosheets and thereby widens their application *in vivo* biosensing assays [71].

1.4 FRET-based nanoprob es for biosensing

FRET-based biosensors are useful diagnostic and imaging tools that are widely employed in the biomedical, pharmaceutical, and toxicological fields. These biosensors emit ratiometric signals to report cellular components, significant biological processes, and biomolecular interactions. Plenty of sensing platforms based on the FRET effect have offered an opportunity to better understand the underlying processes of disease states in living cells, tissues, and organisms. In addition, the rapid development of nanotechnology in recent years provides

opportunities to develop various nanomaterials for use as donor fluorophores or quenchers in FRET-based assays for in vitro and in vivo biosensing applications. Combining these FRET-based nanoprobes with modern bioanalytical instruments enables precise and sensitive monitoring of disease-associated biomarkers, aiding in the early diagnosis, prevention, and treatment of the diseases [52, 61, 72].

1.4.1 Detection of virus

Viruses are highly infectious pathogens that must be parasitized in the host organism to reproduce and survive. Their genetic material is usually comprised of RNA or DNA, encapsulated within nucleocapsid proteins. The genomes of viruses often experience rapid genetic mutations, which cause a major difficulty in virus diagnosis and prevention. Hence, developing sensitive detection techniques with significant reliability, ease of application, and low cost are essential for the rapid screening of viruses. FRET-based nanoprobes play an important role in the field of virus detection. On the basis of nucleic acid hybridization or specific pairing of antigen and antibody, the binding of the recognizable sites in the FRET nanoprobes to the viral genomic sequence is converted into visible fluorescent signals. Up to this point, FRET-based nanoprobes have been designed to screen for a variety of viruses, including the influenza virus [73], human immunodeficiency virus (HIV) [74], as well as coronavirus disease 2019 (COVID-19) [3, 75].

In particular, after the COVID-19 outbreak, there has been much attention to coronavirus detection strategies. Here are several representative examples of FRET-based nanosensing platforms used for COVID-19 diagnostics. The COVID-19 outbreak was caused by severe acute respiratory syndrome coronavirus 2 (SARS-CoV-2), an enveloped virus with single-stranded RNA as the main genetic substance encoding four structural proteins: spike (S), envelope (E), matrix (M), and nucleocapsid (N) [76]. Currently, available FRET nanoprobes for SARS-CoV-2 sensing primarily target N and S proteins. Studies on the mechanism of SARS-CoV-2 transmission have revealed that a crucial step in the virus's entry into host cells is binding the S glycoprotein to the human angiotensin-converting enzyme 2 (hACE2) receptor. Utilizing specific binding affinity between S protein and the recognition domain of the hACE2 receptor, Byunghoon Kang et al. reported a FRET-based nanoprobe conjugated with a hACE2 receptor mimic peptide-beacon (COVID 19-PEB) for the simple detection of the S protein of SARS-CoV-2 [3]. COVID-19 PEB was made by introducing two complementary oligonucleotide sequences into the central loop stem region of a peptide sequence that mimicked hACE2. The oligonucleotide sequences were terminated with a fluorophore and a quencher, respectively. COVID 19-PEB formed a hairpin structure when SARS-CoV-2 was absent, suppressing the

fluorescent signal due to a significant FRET effect (signal "off" state). However, SARS-CoV-2 binding to COVID 19-PEB caused the hairpin structure of the probe to open, resulting in fluorescence recovery of the sensing platform (signal "on" state). Such a sensing strategy makes it simple to detect SARS-CoV-2 infection in clinical samples by mixing them with COVID 19-PEB and measuring their fluorescence intensity. With an LoD of 4×10^3 plaque-forming units per test, COVID19-PEB quickly identified SARS-CoV-2 within 50 minutes and demonstrated high fluorescence even at low virus concentrations. In addition, Kirill Gorshkov et al. designed a time-resolved FRET assay to detect SARSCoV-2 N protein generated in infected cells [75]. It utilized two types of specific anti-N monoclonal antibodies in conjunction with donor (europium cryptate, Eu) and acceptor (DyLight 650, DL650) fluorophores to generate a strong ratiometric fluorescence signal in the presence of N protein. This assay was used for high-throughput screening of a wide range of SARS-CoV-2 antivirals.

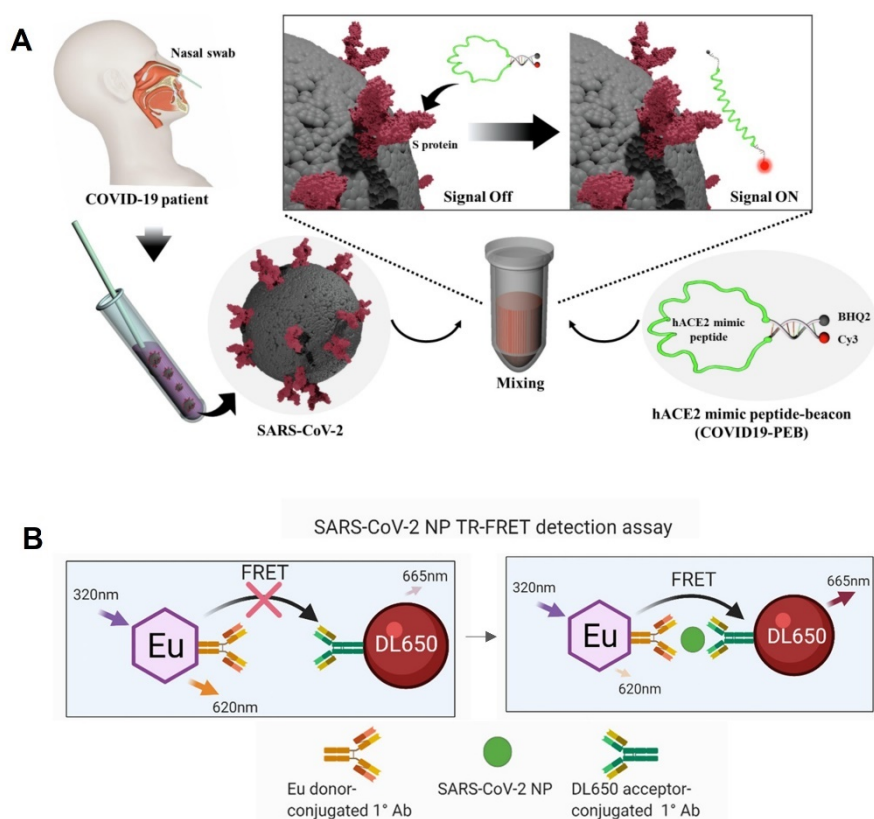


Figure 1.11 FRET-based nanoprobes for SARS-CoV-2 detection (A) Schematic illustration of a simple SARS-CoV-2 detection method using the hACE2 mimic peptide-based molecular beacon (COVID 19-PEB) [3]. (B) Illustration of the FRTE assay for SARS-CoV-2 N protein showing the Eu donor-conjugated primary MAb and DL650 acceptor-conjugated primary MAb detecting SARS-CoV-2 and enabling FRET [75].

1.4.2 Detection of cancer biomarkers

It is crucial to accurately identify cancer-related biomarkers for an early cancer diagnosis. MicroRNA (miRNA), a class of non-coding RNA with 25 nucleotides, has been found to play

pivotal roles in carcinogenesis, cancer progression, and metastasis. Therefore, the discovery of miRNAs associated with carcinogenesis offers important insights into diagnosing and preventing cancer at an early stage and promotes the development of effective therapeutic strategies. In this context, many FRET-based nanoprobe have been developed to detect cancer-related miRNA biomarkers, including miR-21^[71], miR-122^[77], miR-155^[78], miR-150^[79], etc. Compared to common approaches like northern blots and RT-PCR assays, FRET-based nanoprobe have assured sensitive detection of miRNAs *in situ*. These FRET nanoprobe are mainly based on target-probe hybridization-assisted signal enhancement for miRNA detection. That is, the specific hybridization between the ssDNA of probes and target oligonucleotides caused the detachment of donor groups from acceptors, which resulted in the recovery of fluorescence signals.

MiR-21 is highly upregulated in cancer cells and is thus an important biomarker for cancer diagnosis and prognosis monitoring. Oudeng et al. proposed a FRET nanoprobe for detecting miR-21 in HeLa and MCF-7 cancer cells^[71]. This nanoprobe employed ssDNA-FAM dye as the donor and folic acid (FA)-PEG-modified MoS₂ nanosheets as acceptors. In this study, the FRET nanoprobe was based on target-assisted signal enhancement. The specific hybridization between probes and target miR-21 caused the dissociation of FAM-labeled ssDNA from MoS₂ nanosheets, which resulted in the recovery of the green fluorescence of FAM. In addition, PEGylation on the surface aided the good biocompatibility and stability of the nanoprobe in physiological conditions, and FA conjugation with probes improved the efficiency of cancer cell internalization, allowing for the detection of intracellular miRNA in real time. However, the sensitivity of this simple one-step miRNA detection method was limited at the nanomolar level, making it difficult to meet clinically relevant requirements. Therefore, some researchers have implemented target amplification procedures to improve the sensitivity of FRET-based sensing systems. For instance, Wang et al. designed a nanoprobe based on FRET effect to detect miR-21-5p in the exosomes of HeLa cells^[80]. The stem-loop structure of Cy5-labeled probes revealed the recognition sites for AuNP-conjugated primers only after miR-21-5p hybridization. After hybridization, the AuNP-labeled primers and the Cy5-labeled probes were in close proximity, which led to FRET-on and quenched the fluorescence signal of Cy5. Then, miR-21 was released from the oligonucleotide duplex due to the strand displacement of the primers caused by enzymatic induction. Due to miRNA recycling by strand displacement, which significantly increased the fluorescence signal, this FRET-based probe demonstrated an LoD of 1.5 fM, which is significantly more sensitive than those without amplification steps^[80]. Consequently, FRET-based nanoprobe incorporating target cycling or amplification strategies

will improve sensitivity to optimize sensing performance, demonstrating the huge potential of FRET nanoprobes for monitoring miRNA tumor biomarkers in clinical specimens. Besides miRNAs, other crucial cancer biomarkers, such as sarcosine and aurora kinase A (AURKA) in prostate and epithelial malignancies, have been successfully detected using FRET-based sequencing platforms [81].

1.4.3 Detection of Alzheimer disease's biomarkers

Alzheimer's disease (AD) is a chronic neurodegenerative disorder characterized by the accumulation of extracellular β -amyloid ($A\beta$) plaques and intracellular neurofibrillary tangles, as well as neuronal loss [82]. Currently, neuropsychological testing, neuroimaging, and clinical history are the three main strategies for diagnosing AD. However, AD patients can only be identified after the onset of disease symptoms through cognitive testing and neuroimaging. Since alterations in the level of biomarkers related to A deposition and neurofibrillary tangles occur before patients exhibit spatial memory impairment and cognitive impairment, precise assessment of core AD biomarkers is critical for the early diagnosis of asymptomatic AD patients the prediction of disease progression. In this context, significant effort has been devoted to developing innovative AD biomarker-targeting sensor technologies with exceptional sensitivity and accessibility.

The oligomerization and fibrosis of $A\beta$ protein lead to $A\beta$ aggregation and plaque deposition. Yu et al. reported a FRET-based nanoprobe with fluorescence "switch-on" for the rapid and specific detection of $A\beta$ oligomers, where MoS_2 nanosheets functioned as acceptor motif, exhibiting a high quenching efficiency for donor fluorophore (FAM-ssDNA), which significantly suppressed the fluorescence of FAM and produced an initial fluorescence "off" state of the nanoprobe (Figure 1.12A) [4]. FAM-ssDNA comprised a segment of an aptamer that specifically binds to $A\beta$ oligomers, ensuring the recognition site of the probe. Selective hybridization between $A\beta$ oligomers and the nanoprobe resulted in the separation of FAM-ssDNA from the MoS_2 nanosheets, and apparent fluorescence recovery turned the fluorescence to the "on" state. The probe was demonstrated to reach an LoD of 3.1 nM for $A\beta$ oligomers. It showed feasibility for imaging $A\beta$ oligomers in hippocampal and cortical tissue samples from APP/PS1 transgenic AD mice [4]. However, there were no *in vivo* imaging results to indicate the probe's ability to visualize $A\beta$ in this study, probably since FAM fluorophore with green emission has limited light penetration and suffers from ACQ effects, which is not favorable for the probe imaging in the brain. Currently, the AD biomarkers that FRET-based nanoprobes can detect are mainly focused on the $A\beta$ pathology pathway. Since neurofibrillary tangles are also

a major pathological feature of AD, the development of nanoprobe specific for tau protein detection is particularly important for the diagnosis and prevention of AD progress.

Accumulating evidence suggests that aberrant expression of specific miRNAs affects the pathologic changes involved in the aggregation of A β plaques and neurofibrillary tangles in AD. Notably, miR-9 was found to be associated with A β oligomerization and overexpressed in neural tissues in early onset AD [83]. Therefore, there has been a study that demonstrated a fluorescent nanoprobe based on FRET for real-time detection of miR-9 in neural cells and brain tissue from APP/PS1 transgenic AD mice (Figure 1.12B) [84]. The probe consisted of azobenzene-ssDNA (DNA-Azo) labeled with red emissive carbon dots (CDs) as a donor fluorophore adsorbed onto GO. DNA-Azo exhibits a photo-responsive conformational change, displaying single-strands in UV light while forming double-strands in visible light, which can be utilized to achieve signal amplification. CDs-DNA-Azo formed a duplex structure after specifically hybridizing with target miR-9 and then fell from GO, which enabled the fluorescence CDs to recover.

Moreover, CDs-DNA-Azo presented as a duplex structure stimulated by the red fluorescence emission of CDs allowed miR-9 to be released to increase the circular fluorescence signal of the sensing platform. Such an enzyme-free amplification technique based on the photo-responsive conformational change provided a FRET nanoprobe with a low LoD of 0.57 fM, enabling extremely sensitive detection of miR-9 [84]. Therefore, *in situ* visualizations of abnormal expression of specific microRNAs using highly efficient and sensitive fluorescent nanoprobe can aid in the early diagnosis of AD. However, limited by the fact that visible light as the excitation light has only limited tissue penetration, the effectiveness of most current FRET-based fluorescent probes for monitoring AD-specific miRNAs has rarely been evaluated in the brain tissue of living models.

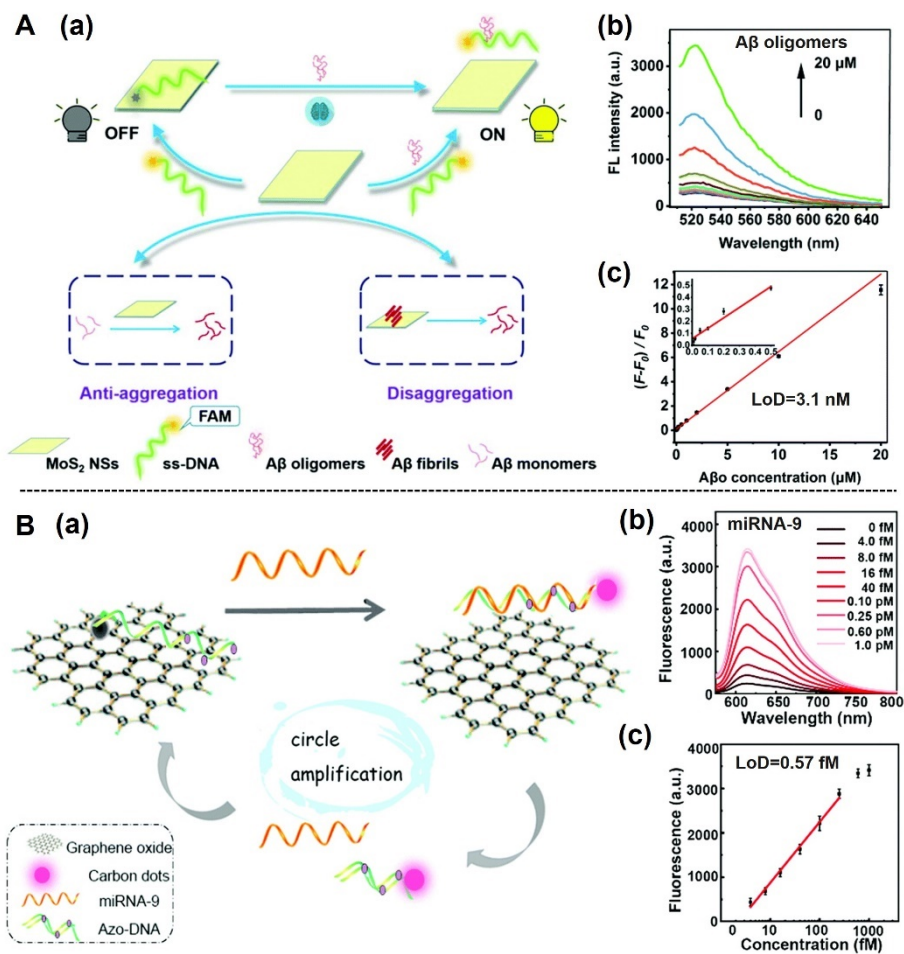


Figure 1.12 FRET nanoprobes for the detection of AD biomarkers. (A) FRET nanoprobe based on MoS₂ with fluorescence “switch-on” for Aβ oligomer detection [4]. (B) An enzyme-free signal amplification strategy based on a FRET nanoprobe with carbon dots and GO monitoring miR-9 in neurons and brain tissues of AD mice [84].

1.4.4 in vivo tissue imaging

FRET-based biosensors for *in vivo* imaging achieves multiple imaging of cellular activities and spatiotemporal viewing of biomolecules, providing opportunities to monitor intricate processes, including drug transport, targeting, and release in living systems [85]. Many *in vitro* FRET measurements primarily rely on changes in single fluorescence intensity, which would easily be impacted by a complex *in vivo* environment, such as pH fluctuations. Therefore, for *in vivo* FRET-based sensing, an internal calibration for changes in these environmental factors is made possible by pairing an emissive donor and an emissive acceptor to produce a ratiometric output. Usually, the two fluorophores are assembled into small-sized nanoparticles. Due to their close proximity, their fluorescence is quenched due to FRET. Once the nanoshells are disassembled under specific *in vivo* physiological conditions and release the fluorescent molecules, the nanoprobe fluoresces in dual colors (FRET-off). For example, Cayre et al. employed FRET-based assays to *in vivo* track the destiny of natural lipid squalene (SQ) [86].

They synthesized three SQ derivatives, including one for bioconjugation with gemcitabine (SQGem) as a prodrug and two organic dyes (SQCy5.5 and SQCy7.5) serving as donor-acceptor pairs in the FRET system. Three SQ derivatives spontaneously self-assembled in an aqueous solution through nanoprecipitation as nanoparticles. Intact nanoparticles encapsulated SQGem, SQCy5.5, and SQCy7.5 in a limited space, thus displaying a strong FRET effect and visible as the bright fluorescence of the acceptor. Still, deconstructed particles could not maintain the near closeness of two dyes, resulting in the disappearance of the FRET effect, thus allowing observation of two different fluorescences from the acceptor and donor. Thus, a dual-color FRET nanoprobe enabled *in vivo* tracking of the behavior of nanomedicine, such as nanoparticle-based drug delivery vehicles ^[86]. However, *in vivo* FRET imaging using organic dyes would be less sensitive due to the low penetration of visible light in biological tissues, which scatter and absorb visible light very strongly. Fluorescent materials with excitation and emission wavelengths in the red or near-infrared (NIR) range typically have greater tissue penetration capabilities and greatly facilitate *in vivo* FRET imaging. As an alternative, UCNPs can be used to address light penetration problems. Ren et al. developed a DNA hybridization-based FRET system by functionalizing the core-shell UCNP and TAMRA dyes with DNA sequences corresponding to different fragments of miRNA-122, which is a potential biomarker for cholesterol metabolism in liver cancers (Figure 1.13) ^[80]. The hybridization of UCNP@DNA, TAMRA-DNA with target miR-122 brought UCNP and TAMRA dyes into close proximity, which reduced the emission of UCNP at 545 nm but increased the fluorescence of TAMRA at 580 nm when excited at 980 nm. The hybridization of UCNP@DNA, TAMRA-DNA with target miR-122 brought UCNP and TAMRA dyes into close proximity, which reduced the emission of UCNP at 545 nm but increased the fluorescence of TAMRA at 580 nm when excited at 980 nm. Such a UCNP-based FRET nanoprobe successfully detected both exogenous and endogenous miRNA, demonstrating its efficacy for *in vivo* FRET biosensing. Incorporating ratiometric imaging and NIR-emitting UCNPs can enhance the applicability and efficacy of FRET-based nanoprobes for *in situ* monitoring of biological activities within living systems.

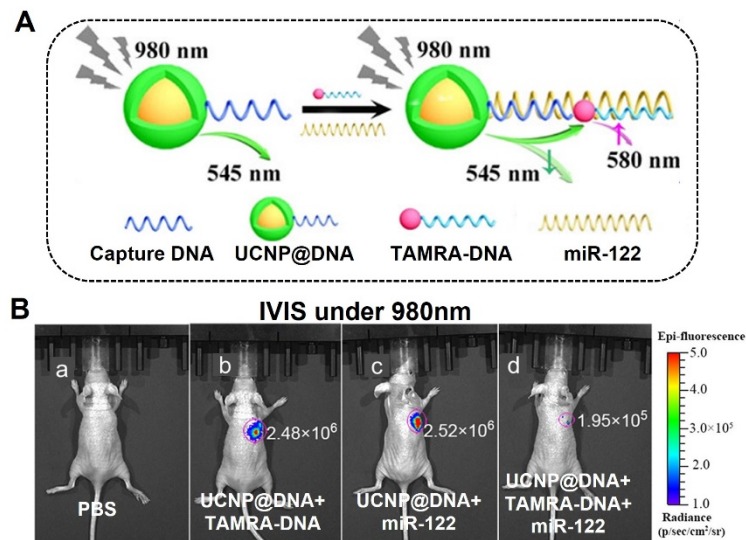


Figure 1.13 FRET nanoprobes for in vivo imaging. (A) Schematic illustration of the Synthesis and mechanism of UCNP-based FRET nanoparticles for detecting miR-122. (B) In vivo imaging of liver cancer mice subcutaneously injected with different reagents. $\lambda_e=980$ nm^[80].

1.5 Functionalized nanoprobes for AD therapy

1.5.1 Pathogenesis of AD

As the main cause of dementia in elderly people, AD is a chronic and progressive neurodegenerative disorder. The pathological changes in AD occur mainly in the hippocampus and cortex, which are highly correlated with cognitive and memory performance. Instead of a single cause, AD is caused by a combination of variables. The hallmark pathologies of AD include extracellular amyloid plaques, intracellular neurofibrillary tangles (NFTs), and neuronal loss^[82]. Native A β monomers are produced by cleaving the amyloid precursor protein (APP) by γ -secretase and cleavage enzyme (BACE1), and they promote neuronal survival and shield mature neurons from excitotoxic death. In pathogenic circumstances, excessive accumulation of monomers results in the formation of A β aggregates with low molecular weight. These aggregates are soluble, diffusible, and toxic to neurons. When oligomers reach threshold levels, plaque and insoluble cellulose/aggregates form and continue to accumulate, it has been found that soluble A β oligomers are more toxic compared to insoluble A β deposits. Particularly, A β dimers, the major soluble oligomers isolated from the AD hippocampus and cortex, are capable of directly causing neuronal degeneration and tau hyperphosphorylation, which would further induce neurofibrillary tangles (NFTs) that damage microtubules and hinders axonal transport between neurons^[87]. In addition to A β plaques and hyperphosphorylation, oxidative damage and severe neuroinflammation are also observed at the lesion sites of neurodegeneration (Figure 1.14)^[82]. Indeed, the cumulative effects of these pathogenic

conditions result in progressive neurodegeneration and cognitive deficits. It's significant to note that A β , NFTs, oxidative stress, and inflammation form a vicious cycle. Reactive oxygen species (ROS) and inflammatory factors are produced by activated microglia when A β and NFTs are present. On the other hand, inflammatory cytokines and ROS directly affect neurons, further increasing the synthesis of A β and NFTs. Therefore, it is extremely desirable to look for therapies that have several effective targets [82].

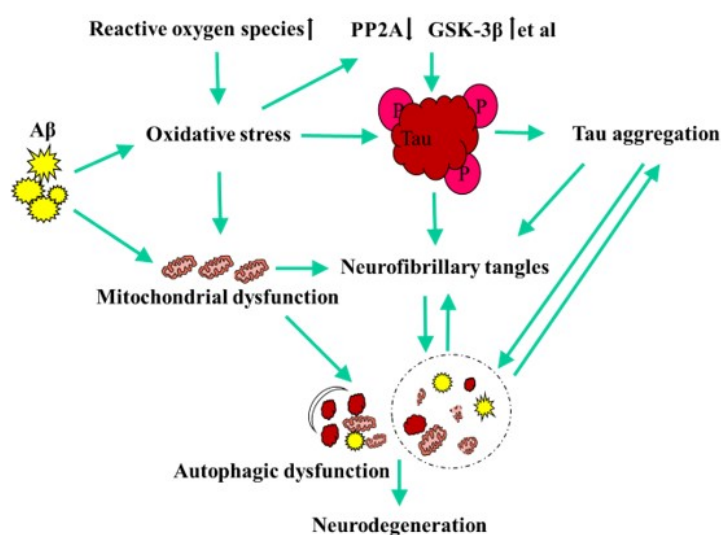


Figure 1.14 The cascade of ROS, A β , and tau hyperphosphorylation in AD [82].

The difficulty of treating AD stems not only from its unclear pathogenesis but also from the limitations of access to the lesion sites in the brain. The blood-brain barrier (BBB) is the main biological barrier that controls the entry of drugs from the peripheral circulation into the central nervous system (CNS) and hence considerably restricts medication availability. In addition to accessibility issues, therapeutic reagents delivered to the CNS must meet particular biopharmaceutical requirements that confer high bioavailability. In addition to issues of accessibility, therapeutic reagents administered to the CNS must meet specific biopharmaceutical requirements that confer high bioavailability. Many anti-AD drugs have physicochemical drawbacks, such as limited solubility, poor stability, and a large molecular weight, which dramatically lower their bioavailability and thus reduce their ultimate therapeutic effect. Over the past two decades, the rapid development of nanotechnology has revolutionized AD treatment. Various advanced nanomedicine-based approaches applied for AD treatment have been explored to compensate for the shortcomings of small molecule drugs. There are two primary benefits of nanomedicines for the treatment of AD: 1) A high surface-to-volume ratio of nanoparticles enables the encapsulation of therapeutic payloads, and 2) easy surface functionalization with different ligands is in demand. For example, several ligands, mainly peptides (e.g., rabies virus glycoprotein [RVG]) and functional polymers, have been modified

on the surface of nanoparticles to facilitate cellular uptake via the endocytosis pathway, thus promoting the ability of the nanoparticles to cross the BBB. In addition to enhancing bioavailability, nanomaterials-based therapeutic approaches have been combined with chemical medications to increase the efficacy of multimodal treatments for AD.

1.5.2 NPs targeting A β pathology

One of the most common AD therapy strategies is reducing the concentration of toxic A β aggregates, which is mainly achieved by three pathways: 1) reducing A β generation, 2) promoting A β clearance, and 3) inhibiting A β aggregation. In order to improve treatment efficacy, a single nanosystem usually contains multiple components to simultaneously interfere with more than pathways and thus attenuate A β aggregates, which is one of the areas where nanomedicines are superior to molecular drugs [88].

1.5.2.1 NPs as nanocarriers

Several small interfering RNAs (siRNAs) have been demonstrated to inhibit the generation of A β protein by knocking down β -secretase (BACE1), a key enzyme to regulate the cleavage of A β precursor protein (APP) to A β protein [89]. However, it is hard to deliver siRNAs through the BBB to exert inhibitory effects in neurons with high BACE1 expression. In addition, studies have demonstrated that siRNA circulation in the peripheral system might result in immune and inflammatory responses. The development of siRNA into nanomedicines can partially solve this problem. Wang et al. developed a nanocomplex consisting of siRNAs encapsulated by PEGylated poly (2-(N,N dimethylamino) ethyl methacrylate) modified with Tet1 and CGN peptides, applied to specifically identify neurons and improve BBB penetration capability, respectively [90]. The nanocomplex successfully knocked down half of the BACE1 mRNA level and significantly inhibited the A β plaques depositions, stimulating neurogenesis in hippocampus and cortex regions in APP/PS1 transgenic AD mice. Besides gene silence by siRNAs, nanomaterials have been designed to affect early conformational conversion and oligomerization of A β by disrupting important amyloidogenic areas to produce harmless heterooligomers. To prevent the formation of A β fibrils, Yang et al. fabricated PEG-LK7@BP by modifying PEGylated black phosphorus (BP) nanosheets with an A β inhibitor LVFFARK peptide (LK7). Through direct binding with A β species, these nanosheets stopped the fibrillization of A β , which ultimately inhibited neuron death [91].

1.5.2.2 NPs as phototherapy agents

Nanomaterials can be used not only as carriers to improve the bioavailability and biocompatibility of molecular drugs (e.g., siRNAs and peptide inhibitors) but also directly as therapeutic agents. Recently, nanomaterials-based phototherapies, including photothermal

therapy (PTT) and photodynamic therapy (PDT), have shown great potential in AD treatment. Opposed to conventional chemo- or immunotherapies, phototherapies rely on the interaction of photosensitizers or photothermal reagents with light to activate photo-drive reactions that produce ROS or heat effects that suppress A β aggregation, attenuating nerve damage. In the past several years, UCNPs have successfully achieved a number of advancements in the phototherapy of AD due to their optical merits in terms of NIR light excitation, a large anti-Stokes shift, and high photostability. For instance, Li et al. discovered that tungsten disulfide (WS₂) nanosheets could pass through BBB and selectively absorb A β ₄₀ monomers on the surface *via* van der Waals force and electrostatic interaction, thereby inhibiting A β aggregation [92]. Additionally, WS₂ nanosheets have a special capacity to absorb NIR light, which allows A β to disaggregate under NIR radiation. Furthermore, the study by Kuk et al. reported the first UCNP-based nanoplatform loaded with rose bengal (RB) as a photosensitizer to demonstrate how NIR light-induced photosensitization prevents A β aggregation. RB receives excellent energy transfer efficiency from the UCNP core upon illumination by NIR light, and then RB produces 1O₂ to denature A β ₁₋₄₂ fibrils [93]. However, the *in vivo* application of most nanomaterial-based phototherapeutic systems is limited by the lack of specificity for A β aggregates.

1.5.3 NPs targeting tau pathology

Exploration of therapeutic approaches targeting A β proteins began earlier than other mechanistic pathways. However, successive clinical trials have shown that several anti-AD drugs developed to target the A β pathway are not as effective as expected in laboratory studies. Hence, the emphasis of research on nanoprobess for AD treatment has gradually shifted towards reducing tau protein hyperphosphorylation and inhibiting tau aggregation from lessening neuronal damage. Shi et al. developed a tau-targeting nanoinhibitor (NanoTLK) by utilizing self-assembled PEG micelles to encapsulate a tau binding (D)-TLKIVW (TLK) [94]. The peptide structure of TLK is designed according to the atomic structure of the tau aggregate pattern (VQIVYK), which can bind to specific regions on tau aggregates rather than tau monomers. The fabricated nanoinhibitor can effectively identify and inhibit tau aggregation and thus prevent their seeding in neurons, dramatically reducing tau-mediated cytotoxicity. Although the inhibitory effect of NanoTLK on tau aggregates *in vivo* was not specified in this study, the discovery of TLK fragments provides new ideas for tau-targeting nanotherapeutics. In addition to TLK as a tau-targeting peptide, VQIINK, a hexapeptide derived from tau protein, can selectively catch pathological tau, which offers an opportunity to develop nanomaterials for the targeted treatment of AD. Xu et al. developed a biomimetic nanoparticle that targets

intracellular pathogenic tau via specific binding of the VQIINK peptide [95]. Through the synergistic effect of surface-sealed hydrophobic microdomains and surface-modified tau-targeting peptides, the nanoparticles can specifically catch pathological tau (e.g., tau oligomers and fibrils) and effectively inhibit the aggregation of pathological proteins. The results demonstrated that the tau-targeting nanoparticle attenuated tau aggregation-induced neurotoxicity and reduced cognitive impairment in AD mice [95].

1.5.4 NPs targeting ROS

The main cause of oxidative stress is excessive ROS generation, which results in inappropriate biomolecule oxidation and consequent protein structural alterations. Many small molecule antioxidants, both synthetic and natural, have been found to scavenge intracellular excess ROS. Flavonoids such as curcumin and anthocyanins exhibit natural antioxidant capacity due to the presence of phenolic hydroxyl groups in their structures. Nevertheless, it is still challenging to deliver flavonoids to lesion sites in the brain because of their poor stability and reduced bioavailability when exposed to physiological environments. Hence, various nano-drug delivery systems have been developed to assist small molecule antioxidants in scavenging ROS for AD therapy. A common nanomaterial-based drug delivery platform is fabricated by amphiphilic polymers like DSPE-PEG forming micelles with a hydrophobic cavity encapsulated small molecules drug in the core, and the hydrophilic terminal is distributed on the surface of nanoparticle increasing solubility as well as biocompatibility [88].

Moreover, nanomaterials possess antioxidative properties without the addition of small molecule antioxidants. For example, some small nanoparticles of metal oxides with ROS scavenging ability have been synthesized, such as ruthenium (Ru) NPs and Ceria (Ce) NPs, for AD treatment [96]. Studies on the pathogenesis of AD have pointed out that the accumulation of A β fibrils and hyperphosphorylated tau promotes the overproduction of ROS, while disruption of ROS homeostasis stimulates tau hyperphosphorylation and aggregation [82]. Therefore, nanodrugs developed for scavenging ROS are usually accompanied by inhibiting A β and tau aggregation in AD. Such multipotent nanoprobe are usually assembled by incorporating two or more materials with the ability to inhibit hyperphosphorylation and depletion of ROS through encapsulation within nanoparticles or surface modification. Zhou et al. synthesized hollow ruthenium (Ru) NPs in the form of flowers as a carrier loaded with nerve growth factor (NGF) and sealed with phase change material (PCM) tetradecyl alcohol [97]. Ru NPs exhibited strong photothermal effects under NIR irradiation, thereby facilitating nanocomposite penetration of the BBB and drug release in response to localized hyperthermia. Upon NIR triggering, the shape of NGF-PCM@Ru NPs altered under temperature stimulation to release NGF, which prevented

tau phosphorylation and attenuated oxidative stress. Ling et al. presented a tau-recognized multifunctional nanocomplex constructed by iron oxide nanoparticles (IONPs) loading with methylene blue as a tau aggregation inhibitor and ultrasmall ceria nanoparticles [98]. Ceria nanoparticles of 3~5 nm are excellent antioxidants due to their strong reactive oxygen species (ROS) scavenging capacity. For active hyperphosphorylated tau targeting, amino-T807, an amino substituent of T807, was modified onto the surface of IONPs. The nanocomplex could alleviate AD symptoms in rats by reducing oxidative stress, tau hyperphosphorylation, and neuronal death.

1.5.5 Nanomaterials-based hydrogen therapy

Hydrogen (H₂) is a colorless and odorless gas. Due to its low molecular weight, H₂ rapidly diffuses to diverse tissues and exerts a wide range of biological effects. H₂ is primarily involved in immune system regulation, anti-inflammatory, and antioxidant activities, influencing mitochondrial energy metabolism, and regulating apoptosis and autophagy to prevent cell death by reducing excessive ROS and controlling nuclear transcription factors. Several studies have been conducted using H₂ to alleviate inflammation in diseases, including pancreatitis, ischemic injury, and autoimmune diseases [99]. Therefore, H₂ shows considerable potential as a novel treatment strategy for AD.

1.5.5.1 Biological effects of hydrogen

Antioxidant effect. Oxidative stress damage is often considered the initial stage in the development of many diseases, brought about by an imbalance between the peroxide and antioxidant systems. Hydroxyl (•OH) is a highly cytotoxic ROS, and no specific enzyme is currently available to process •OH due to its rapid and non-selective interaction with surrounding nucleophilic biomolecules. H₂ is a new bioreductive agent that rapidly disperses across the cell membrane in the cytoplasm and can selectively scavenge •OH by reducing •OH to H₂O, but also retains other ROS essential for normal signaling pathways, such as antioxidant and anti-inflammatory [100]. In addition, the antioxidant effect of H₂ continued for a while even after H₂ depletion in the body, or only ultralow concentrations of H₂ present at the lesion sites, suggesting that the antioxidant mechanism of H₂ may be related to antioxidant signal regulation rather than direct scavenging of free radicals. Entry of nuclear factor erythroid-2-related factor 2 (Nrf2) into the nucleus may control the expression of genes involved in oxidative stress defense mechanisms. It has been shown that by triggering the Nrf2 signaling pathway, H₂ promotes the production of antioxidant enzymes such as superoxide dismutase (SOD) and glutathione (GSH) and inhibits the expression of NADPH oxidase, which greatly reduces intracellular ROS production [101]. An optimal antioxidant should reduce excessive oxidative

stress without interfering with redox equilibrium. H₂ may be the superior antioxidant since it quickly reaches cells through blood circulation.

Anti-inflammatory effect. Excessive intracellular ROS can trigger apoptosis by activating transcription factors involved in inflammation, including nuclear factor kB (NF-kB), hypoxia-inducible factor-1 α (HIF-1 α), p53, and matrix metalloproteinases (MMP). Thus, inflammation, apoptosis, and cell damages are concurrent and interact with each other throughout the pathology of oxidative stress. By reducing the expression of chemokines such as proinflammatory cytokines IL-1 β and TNF- α , H₂ can decrease the infiltration of neutrophils and macrophages at the early stage of inflammation, subsequently lowering the level of the inflammatory cytokines IL-6 and IFN- γ [102].

Antiapoptotic effect. Cell shrinkage, the formation of apoptotic bodies, and chromatin condensation are hallmarks of apoptosis. Signaling pathways that cause cell apoptosis are linked to both anti-apoptotic B-cell lymphoma 2 (Bcl-2) and pro-apoptotic Bax proteins. Apoptosis initiation is followed by caspase-3 activation and DNA breakage. Apoptosis initiation is followed by caspase-3 activation and DNA breakage. Studies have confirmed that H₂ may inhibit apoptosis by scavenging ROS or controlling gene transcription. In vitro studies demonstrated that an H₂-rich medium significantly inhibited intracellular ROS production and suppressed caspase-3 and caspase-9 expression [103]. In addition, H₂ rectified the disordered expression of Bax and Bcl-2. Furthermore, H₂ was shown to activate PI3K/Akt signaling pathway to protect cells from hyperoxia-induced apoptosis [99].

1.5.5.2 Conventional routes of hydrogen delivery

The conventional three forms of H₂ delivery procedures used in animal models studies and clinic research include inhaling H₂ gas, drinking H₂-dissolved water, and injecting H₂-dissolved saline (Table 3) [99, 101]. The outcomes of administration methods depend on how well H₂ dissolves in solutions like water, saline, or blood. The inhalation of H₂ gas is the most direct method of treatment. This approach ensures the duration and amount of H₂ retained in the body, but there may be an explosive hazard when the concentration of H₂ gas in the air is higher than 4.2%. Drinking water containing H₂ is a more portable and safer way to deliver H₂ for therapy. However, this method does not guarantee sufficient concentrations of H₂ in certain localized lesions because of the low solubility of H₂ in water, which reduces the bioavailability. In addition, direct injection of H₂-dissolved saline allows for rapid administration of sufficient H₂ to the affected area. However, this method is invasive and dangerous if H₂ is injected into the skin or veins. Hence, there is a great need for a delivery strategy to transport H₂ to the local

lesion sites and maintain high concentrations of H₂ for a long duration to exert optimal therapeutic effects.

Routes	advantage	disadvantage	specimens	time	Therapeutic effect	protocol	ref
inhaling H ₂ gas	ensures the intake dose	It may be explosive when the concentration is higher than 4%	Rats	120 min	Inhibits cerebral injury; antioxidant	1, 2, or 4% H ₂	[104]
			Mice	7 days	Improves COPD symptoms	66.6% H ₂ , 6-8h/d	[105]
			Human	7 days	Improves asthma symptoms;	42% H ₂ twice a day, 2 h/d	[106]
drinking H ₂ dissolved water	portable and safe	limited intake dose	Mice	10 days	anti-inflammation	0.89mM, twice a day	[107]
			human	10 days	Reduces inflammation and apoptosis of peripheral blood cells	0.753mg/L, 1,500mL/d	[108]
			Rats	90 min	Relieve retina injury; antiapoptotic	Saturated H ₂ eye drops	[109]
injecting H ₂ -dissolved saline	ensures the dose and direct application to the affected area	invasive	Mice	12 h	anti-inflammation	0.6mmol/L, 5mL/kg	[110]
			Rats	24 h	Alleviates inflammation and apoptosis in myocardial I/R injury	0.6mmol/L, 10ml/kg	[111]
nanomaterials-based H ₂ delivery	safe and higher H ₂ content	expensive, require elaborate design	rat	3~24 h	Attenuates myocardial injury, anti-inflammation and antioxidant	2×10 ¹⁰ bubbles	[112]
			mice	5 days	recover mitochondrial dysfunction, and block and neuronal apoptosis	2mg/ml, i.c.v injection	[113]

Table 3. Summary of intake route and administration strategies for H₂ treatment.

1.5.5.3 Nanomaterials-mediated hydrogen release

The development of targeted and efficient hydrogen delivery strategies is an urgent need due to the inefficiency and uncontrollability of conventional hydrogen delivery methods. The flourishing development of nanotechnology offers new perspectives on addressing this problem. As H₂ therapy is a novel therapeutic modality, there are few studies on nanomaterials with targeted hydrogen release properties. Based on the way of H₂ release, these nanoplatforms can be classified into two categories, spontaneous sustained hydrogen release, and stimuli-activated hydrogen release. They play an important role in improving the effectiveness of H₂ for the treatment of different diseases. The concentration and duration needed for hydrogen therapy vary depending on the disease. For example, chronic diseases (such as osteoarthritis) require long-term anti-inflammatory treatment, in which case nanomaterials that release hydrogen sustainably can have a better therapeutic effect. In contrast, for acute diseases requiring high concentrations of hydrogen to be maintained at specific sites, nanomaterials that release hydrogen under specific stimuli, such as NIR light, are more appropriate.

Spontaneous Sustained Release of Hydrogen. Magnesium (Mg) nanoparticles as hydrogen generators have a high hydrogen production capacity of up to 41.7 mmol/g, which is favorable for the treatment of diseases requiring long-term hydrogen supply. To alleviate osteoarthritis, Sung et al. constructed Mg@PLGA particles by encapsulating magnesium powder in poly (lactic acid- glycolic acid) polymers [114]. Mg@PLGA nanoparticles act as an in situ reservoir that continuously releases hydrogen through the activation and passivation cycles of magnesium in body fluids. The progression of osteoarthritis is arrested by the long-term hydrogen release, which reduces tissue inflammation and prevents cartilage damage. Recently, He et al. developed Pd hydride (PdH) nanoparticles in tiny sizes for large hydrogen payloads and in situ release hydrogen in the AD model [113]. Due to the catalytic hydrogenation of Pd, the hydrogen released from PdH nanoparticles showed good reducibility, supporting the effective scavenging of cytotoxic •OH in an autocatalytic pathway. By scavenging ROS and activating the cellular anti-oxidant system, released hydrogen was able to restore mitochondrial malfunction and prevent synaptic and neuronal apoptosis, therefore improving spatial memory and cognition in AD mice. Hence, multifunctional nanoparticles based on the H₂ generation technique would provide a new avenue for AD treatment.

Stimuli-activated release of hydrogen. The technique of stimuli-activated release favors the delivery of H₂ in need to increase therapeutic effectiveness and minimize side effects. It is essential to develop stimuli-responsive hydrogen nanoplatforms with high sensitivity to stimuli and good stability under physiological conditions. So far, the release of hydrogen can be

induced by a variety of external factors, like light irradiation, and endogenous factors, like acid and enzymes. Among them, nanoparticles for NIR laser irradiation-induced H₂ release have attracted great interest because NIR-response properties are particularly helpful in the treatment of deep tissue diseases due to the high penetration efficiency of NIR light. Recent developments in nanomaterials for photo-activated hydrogen release include the following representative instances. Sung et al. presented a multicomponent nanoreactor containing gold nanoparticles, ascorbic acid, and chlorophylla encapsulated in a liposomal system [115]. This liposomal nanoreactor photosynthesizes H₂ gas after absorbing photons from NIR light. The liposomal shell provides an optimal environment for photosynthetic reactions, promotes the rapid activation of H₂ gas, and releases high local concentrations of H₂ to reduce inflammatory responses. The light-driven nanoreactor reduced the levels of ROS and pro-inflammatory cytokines in the lipopolysaccharide-induced inflammation in RAW264.7 cells and mice [115]. Such a strategy of *in situ* photosynthesis of H₂ through multicomponent nanoreactors triggered by NIR light has the advantage of high selectivity. It ensures high content and efficiency of H₂ generation, providing a new idea for the development of H₂ therapeutic agents in AD.

1.6 Objectives of the study

Fluorescent nanoprobes based on the FRET working mechanism play an important role in the detection of disease biomarkers. AIEgens have intrinsic advantages in terms of bright emission, large Stokes shift, high photobleaching threshold, and fluorescence turn-on nature. The introduction of AIEgen labeled oligonucleotides probes into the FRET sensing system is expected to optimize the signal-to-noise ratio of the nanoprobe and achieve a rapid and sensitive screening of viral sequences as well as nucleic acid-based biomarkers such as miRNA in the diagnosis of diseases. Meanwhile, hydrogen has been reported to scavenge ROS as a unique antioxidant, indicating that it can treat AD by restoring ROS homeostasis. However, due to its limited solubility, the concentration of H₂ that can be delivered to the lesion site is often below its therapeutic threshold for clearing locally produced excess ROS. Therefore, the design of nanomaterials for continuous and efficient *in situ* hydrogen generation is crucial for the advancement of hydrogen therapy for AD.

Specific objectives of Chapter 2 include:

1. To develop a FRET-based biosensor with dual fluorescence "turn-on" property by integrating AIEgen-labelled oligonucleotide probes with GO nanosheets (TPE-DNA@GO) for rapid detection of SARS-CoV-2 viral sequence.
2. To characterize the AIEgen@GO nanoprobe using various techniques.
3. To investigate the sensitivity and specificity of AIEgen@GO nanoprobe for detection of

mimic SARS-CoV-2 virus sequences, including *N* gene, *Orflab* gene, and CDC-V2 plasmids.

4. To explore the advantages of the dual fluorescence-on detection strategy over the traditional single fluorescence-on strategy.

Specific objectives of Chapter 3 include:

1. To fabricate a dual fluorescence "turn-on" biosensor based on the nanocomposite of red emissive AIEgen-labeled oligonucleotide (TPET-DNA) probes immobilized on the surface of polymeric MoS₂ (TPET-DNA@Dex-MoS₂).
2. To study the quenching ability of Dex-MoS₂, the sensitivity and specificity of TPET-DNA@Dex-MoS₂ nanoprobe for the detection of miR-125b in solution.
3. To evaluate the intracellular miR-125b detection performance of TPET-DNA@Dex-MoS₂ nanoprobe in tau-based AD model cells.
4. To investigate the capability of TPET-DNA@Dex-MoS₂ nanoprobe for *in situ* monitoring of the endogenous miR-125b overexpression in a tau-based AD mice model.

Specific objectives of Chapter 4 include:

1. To construct NIR light-driven H₂ evolving nanoreactors (NRs) composed of platinum nanoparticles (Pt NPs) and ascorbic acid encapsulated by cross-linked vesicles, which includes two photosensitizers chlorophyll a (Chl_a) and indoline dye (Ind) that absorb red and green luminescence from UCNPs that act as light-harvesting antennas coupled to the surface.
2. To investigate the physical and chemical properties of (Chl_a+Ind) NRs *via* various techniques.
3. To compare the efficiency of photosynthetic H₂ gas generation by (Chl_a+Ind) NRs (dual photosensitizers loaded) with Chl_a NRs and Ind NRs (single photosensitizers loaded)
4. To assess the efficiency of (Chl_a+Ind) NRs to scavenge ROS, repair mitochondrial damage, inhibit apoptosis, and attenuate hyperphosphorylated tau protein in tau-based AD model cells.
5. To evaluate the therapeutic outcome of (Chl_a+Ind) NRs on spatial learning and memory in AD mice under tau pathology.
6. To study the effect of (Chl_a+Ind) NRs on ROS and tau phosphorylation levels in hippocampal regions of AD mice by histological analysis.

Chapter 2: A dual fluorescence “turn-on” FRET biosensor based on AIEgen@GO nanoprobe for rapid detection of SARS-CoV-2 virus

2.1 Introduction

The COVID-19 epidemic caused by SARS-CoV-2 has been spreading rapidly worldwide [116]. Even though many cases are asymptomatic, there have been over 630 million COVID-19 verified cases and over 6.5 million confirmed deaths documented globally up until the end of 2022, which poses a serious public health threat [117]. The COVID-19 epidemic has harmed the economy and social issues and harmed global public health. As a result, there is a great need for quick, effective, and affordable diagnostic techniques that distinguish infected from healthy individuals. The basic genome structure of SARS-CoV-2 is generally consistent with that of other coronaviruses. It is an enveloped virus with single-stranded RNA as the main genetic components and contains four structural proteins: spike protein (S), envelope (E), membrane (M) and nucleocapsid (N).^[76] As shown in Figure 2.1, the anterior 5' end of the genomic sequence contains Open reading frame (*Orf*) 1ab encoding *Orf1ab* polyproteins, while genes encoding structural proteins (e.g., S, E, M) are located at the 3' end of the genome^[76]. With a better understanding of the genetic composition of SARS-CoV-2, a growing number of virus-targeted diagnostic techniques are being developed to detect the *Orf*, S, and N genes. As of now, two major diagnostic assays to for screening potential SARS-CoV-2 infected individuals are divided into nucleic acid- and antigen-based tests [118]. Nucleic acid-based tests like quantitative reverse transcription-polymerase chain reaction (RT-qPCR) remain the gold-standard method for SARS-CoV-2 diagnosis. Unfortunately, there are some problems with using RT-qPCR for rapid screening of SARS-CoV-2, particularly in underdeveloped areas where access to RT-qPCR reagents, equipment, and trained operators is not readily available (Table 4). In addition, RT-qPCR assays require long and complex procedures. They also need a sterile central laboratory and a clean environment to perform nucleic acid amplification, resulting in an economic burden on society [119]. In contrast, immunodiagnostic detection kits targeting the antigen of SARS-CoV-2, such as lateral flow immunoassay (LFIA), are simple to use and enable quick screening of SARS-CoV-2 within 30 min. Still, there may be problems with false-negative results since the amount of antigen in the sample is insufficient in the early stages of virus infection onset [120]. Therefore, it is highly desirable to develop a simple and sensitive point-of-care (POC) diagnostic method for primary screening of potential positive SARS-CoV-2 cases prior to performing RT-qPCR or LFIA for secondary confirmation to efficiently prevent the rapid outbreak of COVID-19.

Fluorescent biosensors have the advantages of operational simplicity, easy portability, and high sensitivity. Among them, FRET biosensors have been widely developed in the nucleic acid detection fields ^[121]. The biosensing performance of FRET-based biosensors is primarily based on the choice of donor and acceptor pairs ^[48]. The read-out fluorescence of these FRET biosensors relies on the recovery of the donor fluorophores, which would become stronger along with the increasing concentration of the target molecules. In other words, the higher the concentration of the target, the higher the output signals of the biosensors until reaching saturation. However, traditional donor fluorophores suffer from ACQ problems at high concentrations, undermining their biosensing performance ^[9]. In contrast, AIEgens can conquer this issue via the RIR process at the aggregated state that enhances the radiative energy decay pathway as an ultra-emissive reagent ^[30]. Hence, it is feasible to optimize the sensitivity of FRET-based biosensors by introducing AIEgens as the donor fluorophores. As a typical and promising AIEgen, Tetraphenylethene (TPE) has been developed as fluorescent probes for the detection of proteins, nucleic acids, and specific small biomolecules ^[122]. Intermolecular interactions between TPE and targets are established through strong binding affinities (such as DNA hybridization and hydrophobic or charge interactions), which cause RIR processes and thus turn on the fluorescence of TPE molecules ^[122]. In particular, AIEgen-based probes fabricated by oligonucleotide-conjugated TPE (termed "TPE-DNA") would form double-stranded nucleic acid conformation or even quadruplex structure with target nucleic acid sequence, which activates RIR process and thus significantly enhance the fluorescence of the sensing system^[1, 123, 124]. However, the direct introduction of probing DNA into TPE molecules as sensing sites to synthesize TPE-DNA probes unavoidably produced partial RIR, resulting in a background signal ^[124]. As a result, we aim to design a TPE-DNA-based nanoprobe with a high signal-to-background ratio to aid in SARS-CoV-2 detection

In this work, we proposed a dual fluorescence "turn-on" FRET nanoprobe by assembling single-stranded (ss) DNA-conjugated TPE molecules with GO nanosheets (TPE-DNA@GO) for the specific detection of SARS-CoV-2 (Figure 2.2A). Here, GO (acceptor motif) is critical in minimizing the background fluorescence of TPE-DNA (donor motif), and the formation of TPE-dsDNA can contribute to the dual enhancement of read-out fluorescent signals. In the presence of the target sequence (SARS-CoV-2 virus), TPE-DNA immobilized on the GO surface would hybridize with the target viral sequence to form a double-stranded (ds) DNA/RNA structure conjugated with TPE molecules. The formed TPE-dsDNA complex separates from GO surface due to the lower adsorption affinity of GO for duplex nucleic acids, leading to the first fluorescence recovery ("OFF" to "WEAK"). Furthermore, the conformation

of duplex oligonucleotides restricts the intramolecular rotation of TPE due to the increased rigidity and mass changes from ssDNA to dsDNA, which induces further fluorescence enhancement ("WEAK" to "STRONG") (Figure 2.2B). In our TPE-DNA@GO sensing platform, a single administration of target sequence can activate a dual fluorescence enhancement process, which differs from most conventional FRET biosensors that involve only a single fluorescence recovery or a single quenching process. In this work, the feasibility of our nanoprobe for potential clinical usages is evidenced by the rapid response to target SARS-CoV-2 viral sequence and plasmid within 1 h and good sensitivity at picomolar levels without amplification steps.

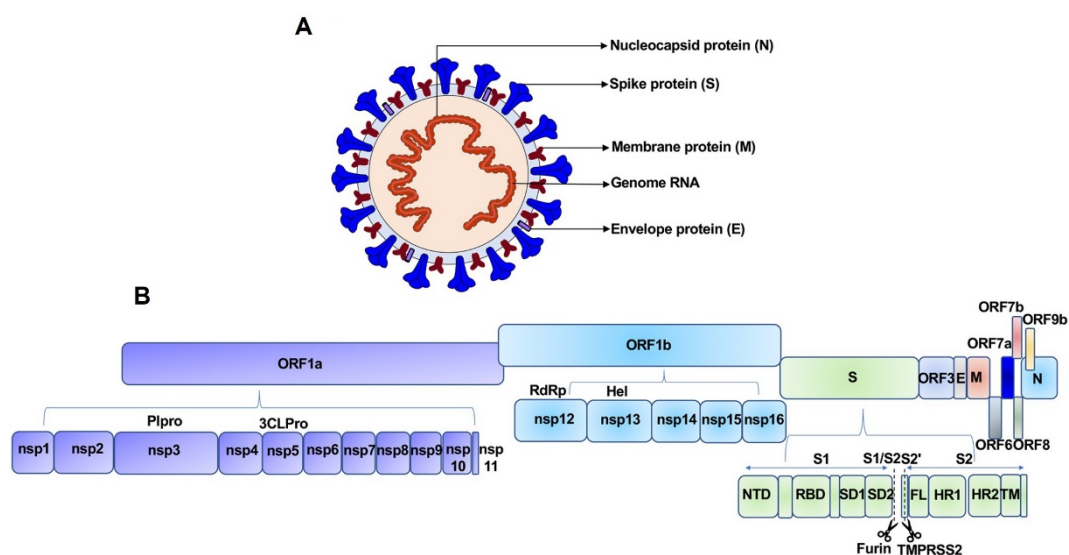


Figure 2.1 The genome structure of SARS-CoV-2 virus [76].

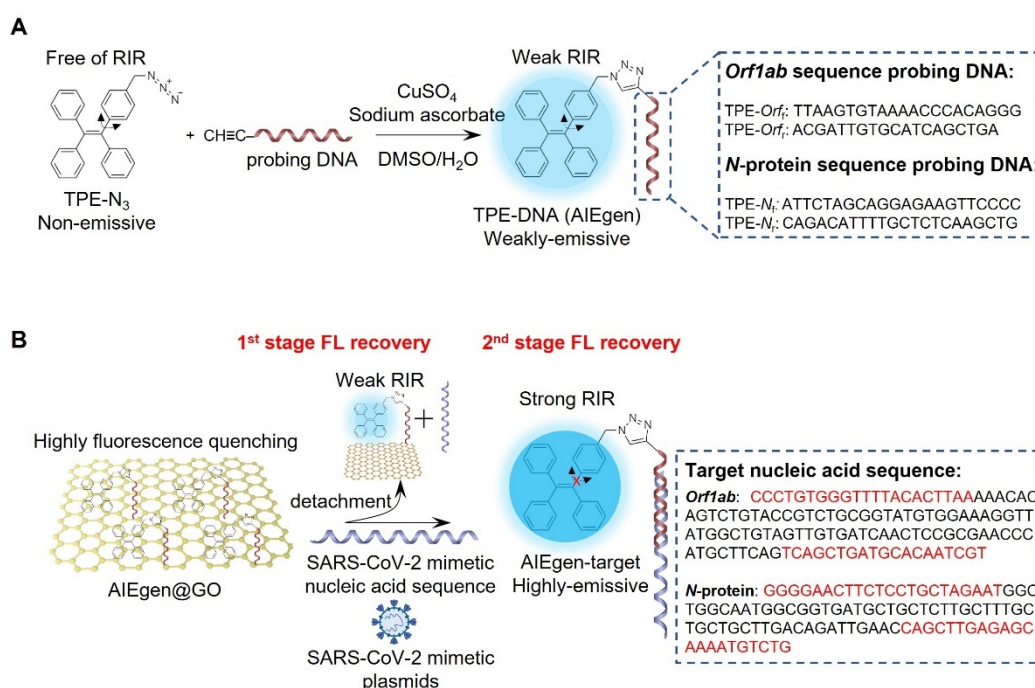


Figure 2.2 Schematic illustration of TPE-DNA@GO nanoprobe for the detection of SARS-CoV-2 viral sequence. (A) Synthetic route to TPE-DNA. (B) Fabrication of TPE-DNA@GO nanoprobe and detection of *Orflab* and *N* genes.

2.2 Methodology

2.2.1 Synthesis of TPE-DNA@GO nanoprobe

The sequence information of the DNA and RNA fragments used in this work is listed in Table 5. First, TPE-DNA was synthesized via the copper-catalyzed azide-alkyne cycloaddition (CuAAC) click reaction [1]. According to the target sequence of *Orflab* and *N* genes, four probing ssDNA were designed with an alkyne group functionalized at the 5' end (alkyne-DNA, including alkyne-*N_f*, alkyne-*N_r*, alkyne-*Orf_f*, and alkyne-*Orf_r*). For the synthesis, TPE-N₃ (1.5 μM) and alkyne-DNA (1 μM) were mixed in 1 mL of DMSO/H₂O (v/v, 1/1). Then newly made aqueous solution of sodium ascorbate aqueous solution (20 μM), CuSO₄ (10 μM), and copper ligand THPTA (20 μM) was added in sequence. After bubbling with nitrogen gas for 30 min, the reaction mixture was stirred overnight at room temperature. The obtained products (TPE-*N_f*, TPE-*N_r*, TPE-*Orf_f*, and TPE-*Orf_r*) were purified by dialysis against H₂O for 24 hours before lyophilization. Then, GO dispersion was sonicated for over 1 h to produce homogeneously distributed GO nanosheets in the aqueous phase before adsorption of TPE-DNA to fabricate TPE-DNA@GO nanoprobe. In order to explore the quenching efficiency of GO to TPE-DNA, TPE-DNA with a fixed concentration of 3 μM was incubated with GO dispersion at a final concentration of 5, 10, 20, 50, 100, 150, and 200 μg/mL for 30 min before measurement of fluorescence intensity by a spectrofluorometer. The formula $Q_e(\%) = (F_0 - F_q) / F_0$ was used to determine the quenching efficiency (Q_e) of GO, where F_0 is the fluorescence signal of 3 μM TPE-DNA and F_q represents the fluorescence intensity of TPE-DNA after adsorbed on GO at different concentrations. Three independent replications of each experiment were conducted.

2.2.2 Detection of *N* and *Orflab* sequences

Throughout the detection assays, TPE-DNA@GO nanoprobe was freshly prepared by mixing TPE-*N_f*, TPE-*N_r*, TPE-*Orf_f*, and TPE-*Orf_r* (6 μM) in DMSO/H₂O (v/v, 1/199) with GO dispersion (300 μg/mL) at an equal volume and then the mixture was co-incubated for 30 min before being adding into DNase/RNase-free TE buffer containing corresponding target sequence (*N*-cDNA, *Orflab*-cDNA, and *N*-RNA) in a range of concentrations (0~20 nM). The reaction mixture was protected from light and further incubated at 37°C for 1 h before measurement of the fluorescence spectra through a spectrofluorometer. To evaluate the specificity of TPE-DNA@GO nanoprobe towards SARS-CoV-2 viral sequence, we selected controls groups with one-base mismatched DNA sequence (b₁-Mis), full-sequence scrambled

Orflab-cDNA and *N*-cDNA sequences, scrambled *N*-RNA, and other kinds of viral DNA sequences (InFA, HBV, HCV, HIV-1). These control sequences were incubated with TPE-DNA@GO with the same operations as the target *N*-cDNA and *Orflab*-cDNA. The fluorescence spectra of all the samples were measured with excitation wavelength at 320 nm and emission wavelength from 400 nm to 600 nm. All the detection experiments were conducted with three independent samples for each group.

2.2.3 Detection of CDC-V2 plasmids

Prior to being detected by TPE-DNA@GO nanoprobe, CDC-V2 plasmid was denatured by being heated for 5 minutes in a water bath at 98°C, followed by being cooled on ice for 10 minutes. Then, denatured CDC-V2 plasmid with different concentrations was incubated with AIEgen@GO nanoprobe in TE buffer for 1 h at 37°C before measuring fluorescence intensity. Three duplicates of each group were used for testing and statistical analysis.

2.2.4 Agarose gel electrophoresis

The DNA fragments in this study, including target cDNA (*N*-cDNA and *Orflab*-cDNA), four kinds of TPE-DNA@GO nanoprobe (TPE-*N_f*@GO, TPE-*N_r*@GO, TPE-*Orf_f*@GO, and TPE-*Orf_r*@GO) as well as their corresponding probe-target cDNA complex (TPE-*N_f*@GO+*N*-cDNA, TPE-*N_r*@GO+*N*-cDNA, TPE-*Orf_f*@GO+*Orflab*-cDNA, TPE-*Orf_r*@GO+*Orflab*-cDNA) were electrophoresed on an agarose gel to analyze the band size. BlueJuice™ gel loading buffer was mixed with the DNA samples (v/v, 9/1) before being loaded onto the 5% agarose gel. In order to measure the base pair number of DNA fragments, a DNA ladder with a size range of 10 bp to 300 bp were simultaneously loaded onto the gel. After that, the agarose gels were then run in 0.5x TBE buffer at a constant voltage of 80 V for around 2 h to satisfy the maximal separation of the DNA samples, followed by being photographed using a Chemi Doc system and examined under a UV transilluminator (Bio-Rad).

2.2.5 Data analysis

The peak fluorescence intensity at 458 nm of AIEgen@GO nanoprobe after incubated with the target *N* or *Orflab* cDNA at a series of concentrations was compared through one-way ANOVA analysis and Dunnett's multiple comparison test via SPSS software (IBM SPSS 26.0). A value of $p < 0.01$ was considered to be statistically significant. Moreover, the LOD of AIEgen@GO nanoprobe was determined as the lowest tested concentration, where its peak fluorescence intensity was significantly higher than that of corresponding probes without incubation with target cDNA^[125].

2.3 Results and Discussion

2.3.1 Synthesis and characterization of AIEgen@GO nanoprobe

In this study, we selected two synthetic complementary DNA and RNA sequences of *N* and *Orflab* gene (*N*-cDNA, *N*-RNA, and *Orf*-cDNA) to mimic SARS-CoV-2 virus [126]. Accordingly, we designed two pairs of DNA fragments (N_f , N_r , Orf_f , and Orf_r) as the probing DNA to construct the TPE-DNA (TPE- N_f , TPE- N_r , TPE- Orf_f , and TPE- Orf_r) (Figure 2.2). One pair of DNA fragments were derived from the reversely complementary sequences of the 5'- and 3'-end of target cDNA, meaning that TPE-*N*@GO nanoprobe (including TPE- N_f and TPE- N_r) were used to detect *N*-cDNA while TPE-*Orf*@GO nanoprobe (including TPE- Orf_f and TPE- Orf_r) for *Orflab*-cDNA (Figure 2.2). Four TPE-DNA probes (TPE- N_f , TPE- N_r , TPE- Orf_f , and TPE- Orf_r) were synthesized through a click reaction of the azide-functionalized TPE (TPE- N_3) and alkyne-modified DNA fragments (alkyne-ssDNA). The mass spectrometry data evidenced the successful conjugation of alkyne-ssDNA and TPE- N_3 , which showed a considerable increase in molecular weight in the TPE-DNA compared to free DNA fragments (Figure 2.3). Moreover, the UV-vis spectra indicated that TPE-DNA and TPE- N_3 had an absorption peak at 320 nm, attributed to the π - π^* transition of TPE core. While only TPE-DNA showed a characteristic peak at 260 nm that demonstrated the presence of oligonucleotides within the structure of TPE-DNA probes (Figure 2.4A). More notably, at the same concentration in the aqueous solution (DMSO/H₂O, v/v=1/199), the fluorescence intensity of TPE-DNA was only 8%~9% of TPE- N_3 molecules (Figure 2.4B-C). The significantly reduced fluorescence of TPE-DNA was attributed to the increased hydrophilicity due to the introduction of probing ssDNA fragments to the structure of TPE- N_3 [124]. While bare TPE- N_3 remained hydrophobic and thus attended to aggregated states to display AIE effect in the aqueous solution. As a result, we have successfully prepared water-soluble TPE-DNA probes applicable to detect target nucleic acids in physiological environments.

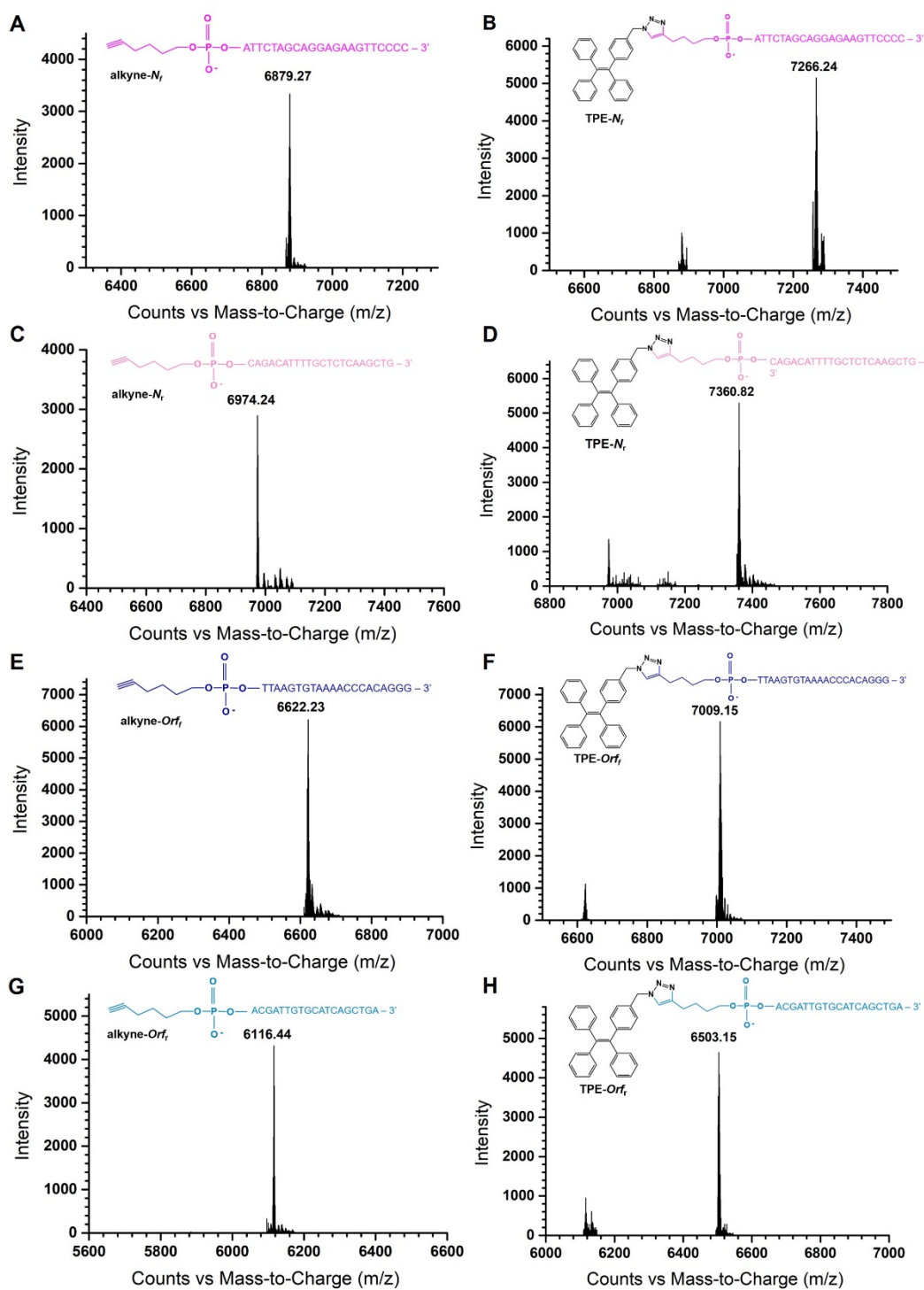


Figure 2.3 The ESI-TOF mass spectrum of (A) alkyne- N_f , (B) TPE- N_f , (C) alkyne- N_r , (D) TPE- N_r , (E) alkyne- Or_f , (F) TPE- Or_f , (G) alkyne- Or_r , (H) TPE- Or_r .

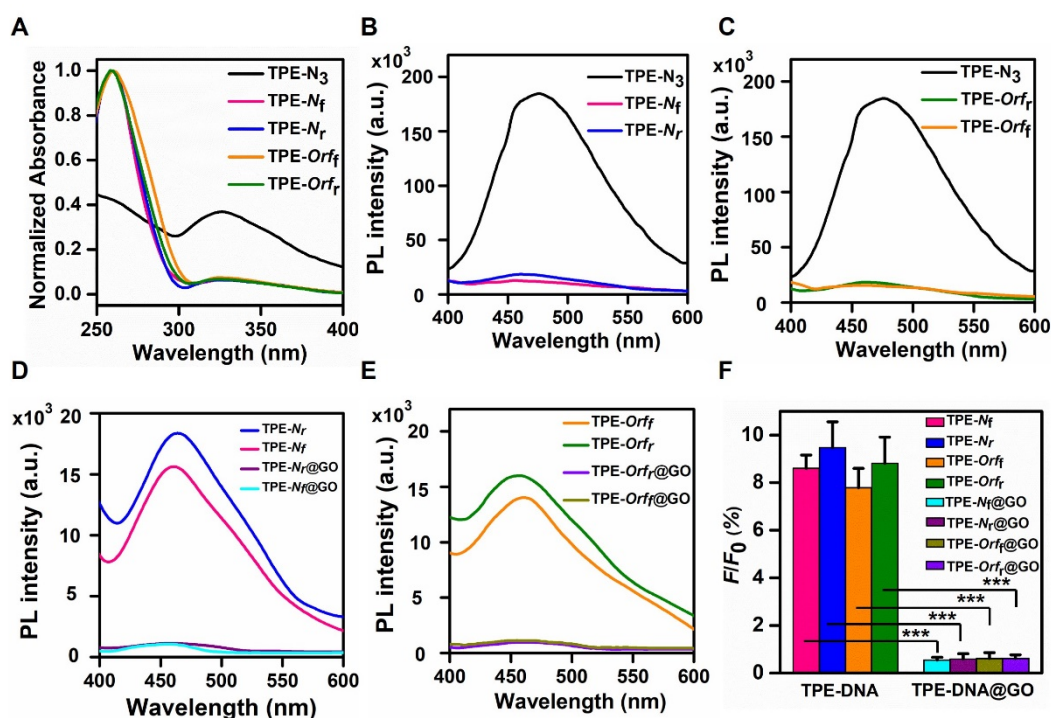


Figure 2.4. (A) UV-vis spectra of TPE-N₃ and TPE-DNA. (B-E) Fluorescence spectra of TPE-N₃, TPE-DNA probes (TPE-N_f, TPE-N_r, TPE-Orf_f and TPE-Orf_r), TPE-DNA@GO nanoprobe (TPE-N_f@GO, TPE-N_r@GO, TPE-Orf_f@GO, and TPE-Orf_r@GO). (F) Fluorescence intensity ratio (%) of TPE-DNA and TPE-DNA@GO (F/F_0), which are normalized to the fluorescence intensity of TPE-N₃ (F_0). $\lambda_{ex}/\lambda_{em} = 320/458$ nm.

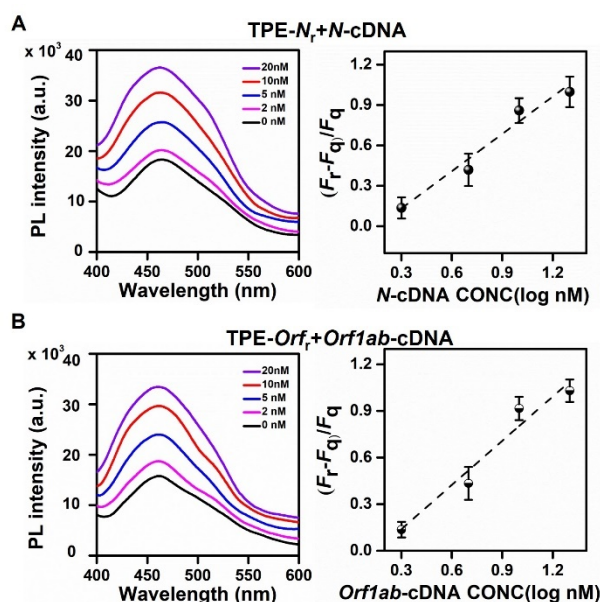


Figure 2.5 Photoluminescence spectra and fitting curve of (A) TPE-N_r and (B) TPE-Orf_r after incubating with N-cDNA and Orf1ab-cDNA of a series of concentrations from 0 nM to 20 nM. $\lambda_{ex}/\lambda_{em} = 320/458$ nm.

The complementary DNA fragments that have been inserted into TPE molecules enable TPE-DNA probes to detect N-cDNA and Orf1ab-cDNA specifically. We observed that the

fluorescence of TPE- N_r and TPE- Orf_r probes showed a recovery after incubating with the corresponding target cDNA sequence. The peak PL intensity at 458 nm increased by ~ 3 times when target cDNA was added at a high concentration of 20 nM (Figure 2.5). The limit of detection (LoD) of TPE-DNA probes for N -cDNA and $Orflab$ -cDNA was measured to be 2 nM, which is not sensitive enough to recognize SARS-CoV-2 viral sequence in clinical specimens (Figure 2.5). The partial basal fluorescence caused by a direct insert of ssDNA fragments into the structure of TPE- N_3 results in a weak signal-to-noise ratio of TPE-DNA probes, contributing to the limited sensitivity of TPE-DNA probes [124]. Therefore, we fabricated TPE-DNA@GO nanoprobe by coupling TPE-DNA with GO as a fluorescence quencher to minimize the background signals. Due to strong π - π stacking interaction, TPE-DNA was stably adsorbed on the surface of GO to minimize the basal fluorescent signals. The results showed that the peak fluorescence intensity of TPE-DNA@GO was dropped to only $\sim 7.8\%$ of the intensity in the counterpart TPE-DNA and $\sim 0.6\%$ of the intensity in TPE- N_3 at the same concentration (Figure 2.4D-F).

Furthermore, the results of physicochemical characterization demonstrated that the average hydrodynamic size of TPE-DNA@GO nanoprobe was measured to be around 30 nm larger than that of free GO in PBS buffer (Figure 2.6A). Additionally, the zeta potential of TPE-DNA@GO nanoprobe was much more negative than the GO dispersion (e.g., TPE- N_f @GO: -43.2 ± 2.3 mV and GO: -36.1 ± 1.8 mV), supporting negatively charged DNA within the sensing platform (Figure 2.6B). The observation under atomic force microscopy (AFM) also suggested the successful fabrication of TPE-DNA@GO nanoprobe since the average thickness of nanoplatform increased ~ 1 nm upon TPE-DNA adsorption (e.g., TPE- N_f @GO: 1.92 ± 0.75 nm and GO: 1.16 ± 0.20 nm), which was consistent with previous research of 2D nanosheets physically coupled with oligonucleotides (Figure 2.6C) [127]. In total, our findings showed that TPE-DNA probe was successfully adsorbed onto GO to establish a reservoir of SARS-CoV-2 sensing nanoprobes.

The FRET transfer efficiency between the donor and acceptor pairs is associated with the quenching efficiency (Q_e) of fluorescence quenchers. To investigate the optimal Q_e of GO for TPE-DNA@GO nanoplatform, we incubated TPE-DNA of a fixed concentration at 3 μ M with GO nanosheets of various concentrations. The fluorescence intensity at 458 nm gradually decreased along with the increasing concentrations of GO (Figure 2.7). When the concentration of GO in TPE-DNA@GO sensing system was 200 μ g mL $^{-1}$, the Q_e achieved the maximum at about 98% (Figure 2.7). In this study, we fabricated the TPE-DNA@GO nanoprobe for all the detection tests using GO dispersion of 150 μ g/mL with Q_e at 93% to prevent over-quenching.

So far, our results have verified the importance of incorporating TPE-DNA as an excellent donor fluorophore with GO as an efficient fluorescence quencher to increase the signal-to-background ratio of FRET-based biosensors.

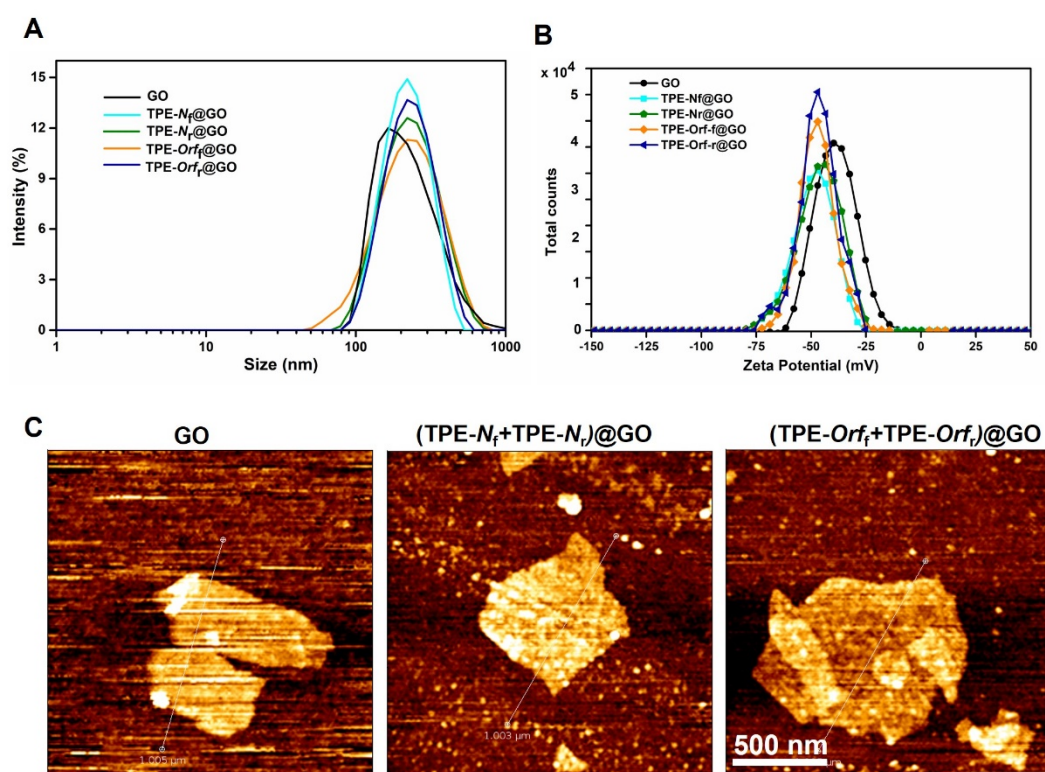


Figure 2.6 (A) Size distribution and (B) Zeta potential of GO and TPE-DNA@GO nanoprobe (TPE-N_f@GO, TPE-N_r@GO, TPE-Or_f@GO, TPE-Or_r@GO). (C) AFM images of GO, ppTPE-N@GO and ppTPE-Or_f@GO nanoprobe.

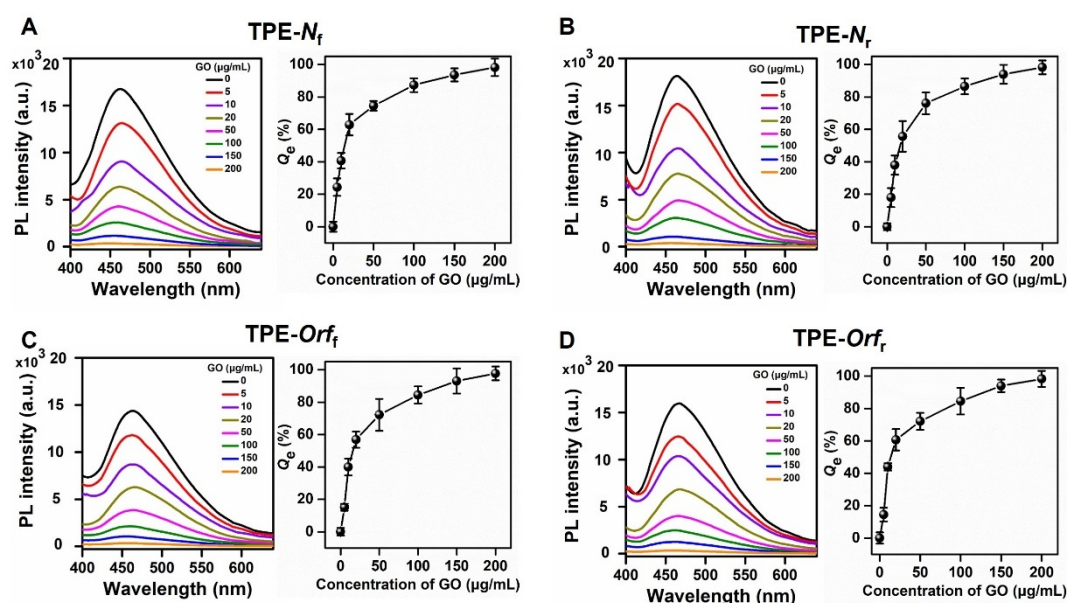


Figure 2.7 Photoluminescence spectra and quenching efficiency (Q_e) of (A) TPE-N_f, (B) TPE-N_r, (C) TPE-Or_f, and (D) TPE-Or_r incubated with GO of different concentrations (0 to 200 μg/mL). $\lambda_{ex}/\lambda_{em} = 320/458$ nm.

2.3.2 Rapid detection of SARS-CoV-2 viral sequence

2.3.2.1 Detection of *N*-cDNA sequence

We first assessed the LoD of TPE- N_f @GO and TPE- N_r @GO by hybridizing the nanoprobe with complementary target *N*-cDNA at a series of concentrations (Figure 2.8 A). In order to achieve full DNA/RNA hybridization to form duplex conformation, TPE-DNA@GO nanoprobe and target sequences were incubated at 37 °C for ~1 h before measuring fluorescence intensity, which is faster than those tests employing RT-qPCR techniques for viral identification^[119]. The results showed that the fluorescence intensity of TPE- N @GO nanoprobe (TPE- N_f @GO or TPE- N_r @GO) linearly increased *N*-cDNA concentration (Figure 2.8B-D). Strikingly, the LoD of TPE- N_f @GO and TPE- N_r @GO nanoprobe towards *N*-cDNA reached 200 pM, which is 10 times more sensitive than that of TPE- N_r probes without GO as quencher (Figure 2.5 and Figure 2.8). Compared with TPE- N_f and TPE- N_r probes, the improved sensitivity of TPE- N_f @GO and TPE- N_r @GO nanoprobe benefitted from the dual fluorescence “turn-on” strategy where the first stage of fluorescence recovery results from the TPE-DNA detached from the surface of GO quencher upon the formation of dsDNA by the hybridization of TPE-DNA and target cDNA and then the significant RIR process in the TPE core caused by duplex formation induces further fluorescence enhancement of the sensing system. Thus, the FRET-based TPE-DNA@GO biosensor integrating TPE-DNA with GO achieved an enhanced sensitivity towards SARS-CoV-2 mimetic *N*-cDNA sequence.

In addition, we proposed that GO may serve as a carrier for TPE-DNA probes bearing a pair of ssDNA fragments (e.g., N_f and N_r) that target the same nucleic acid sequence. Accordingly, we investigated whether a pair of ssDNA contained ppTPE- N @GO nanoprobe ((TPE- N_f +TPE- N_r)@GO) could detect *N*-cDNA sequences of the same concentration with higher sensitivity than the single ssDNA containing spTPE- N @GO nanoprobe (TPE- N_f @GO or TPE- N_r @GO) (Figure 2.9A). Strikingly, the results demonstrated that the LoD of (TPE- N_f +TPE- N_r)@GO nanoprobe for *N*-cDNA sequence was measured to be 100 pM, which was 2-fold more sensitive than that of TPE- N_f @GO and TPE- N_r @GO nanoprobe (Figure 2.9B-D). The higher sensitivity of ppTPE- N @GO sensing system might be related to the double DNA hybridization at the two terminals of the same target sequence for stronger signal amplification.

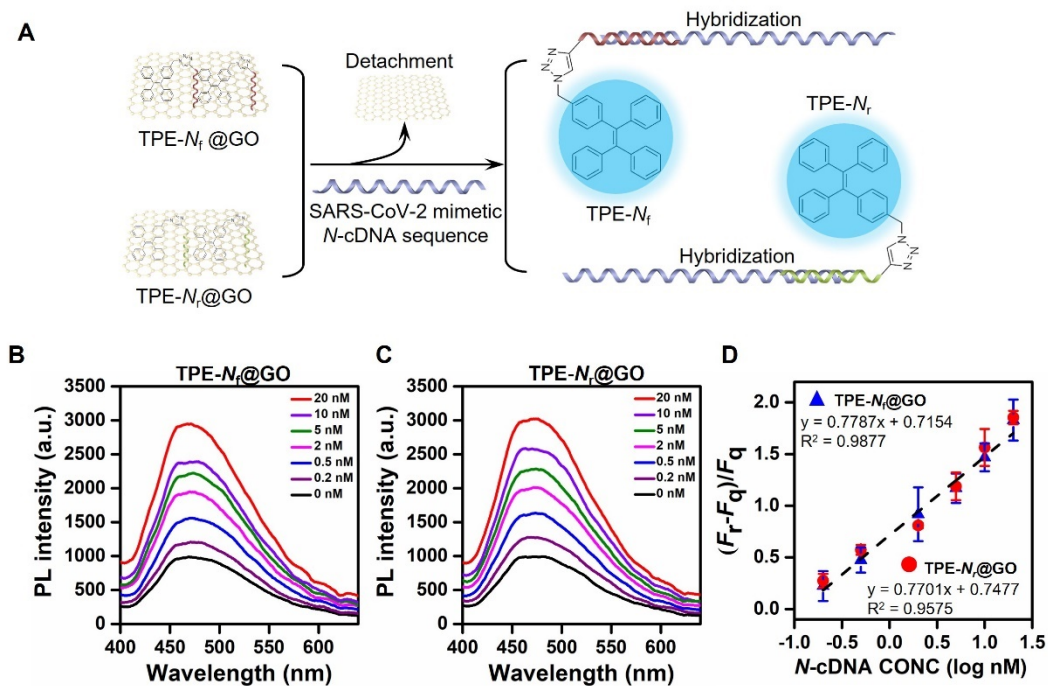


Figure 2.8 (A) Schematic illustration of TPE- N_f @GO and TPE- N_r @GO nanoprobe for the detection of mimetic N-cDNA sequence. Fluorescence spectra of (B) TPE- N_f @GO and (C) TPE- N_r @GO after incubation with target N-cDNA at an increasing concentration from 0 to 20 nM. (D) Fitting logarithmic curve of the relative fluorescence intensity of TPE- N_f @GO (blue triangle), TPE- N_r @GO (red circle) against the logarithmic concentration of N-cDNA. $\lambda_{ex}/\lambda_{em} = 320/458$ nm.

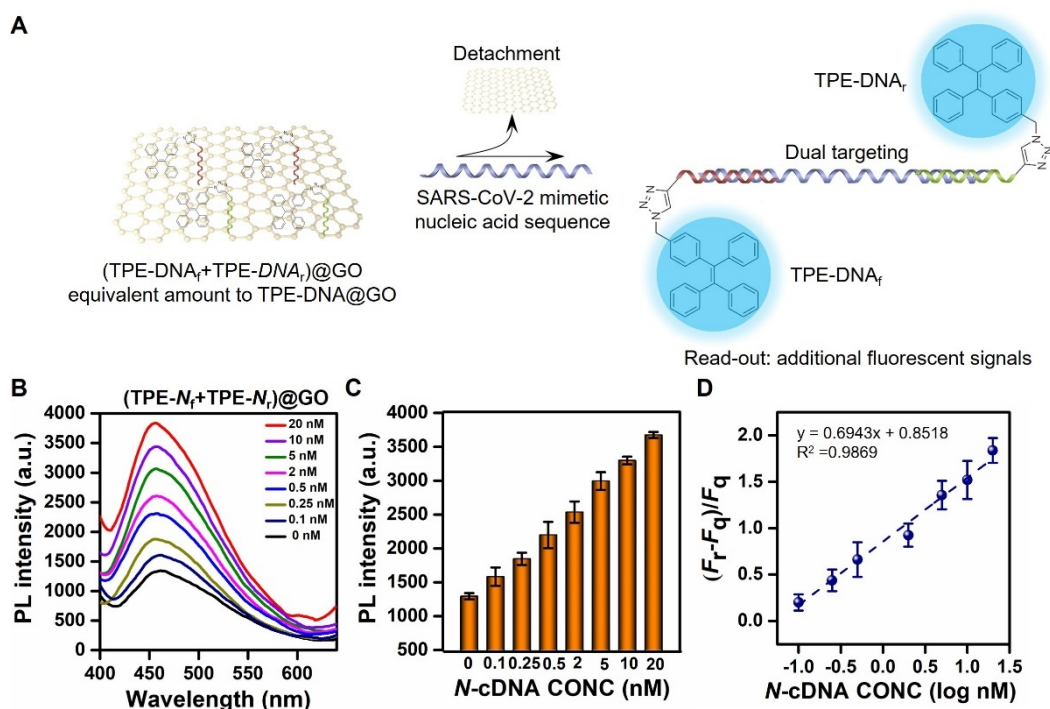


Figure 2.9 (A) Schematic illustration of ppTPE- N @GO ((TPE- N_f +TPE- N_r)@GO) probing for two binding sites of N-cDNA sequence. (B) Photoluminescence spectra and (C) peak fluorescence intensity at 458 nm of ppTPE- N @GO after incubation with N-cDNA. (D) The

fitting curve of ppTPE-*N*@GO against the logarithmic concentration of *N*-cDNA. $\lambda_{ex}/\lambda_{em} = 320/458$ nm.

2.3.2.2 Detection of *N*-RNA sequence

Considering the real SARS-CoV-2 genome sequence composed of RNA sequences, we chose synthetic *N*-RNA to mimic the viral sequence of SARS-CoV-2 to further investigate the ability of our TPE-DNA@GO for RNA detection (Figure 2.10A). Consistent with the results in *N*-cDNA detection, the fluorescent signals of both spTPE-*N*@GO and ppTPE-*N*@GO nanoprobe linearly increased as the concentration of *N*-RNA did (Figure 2.10B-D). Similarly, the LOD of ppTPE-*N*@GO ((TPE-*N_f*+TPE-*N_r*)@GO) nanoprobe and spTPE-*N*@GO (TPE-*N_f*@GO or TPE-*N_r*@GO) towards *N*-RNA was measured to be 100 pM and 200 pM, respectively (Figure 2.10B-D). These findings demonstrated the capability of our sensing platform to identify both DNA and RNA sequences, which is favorable for recognizing SARS-CoV-2 viral sequence in the clinical samples without reverse transcription.

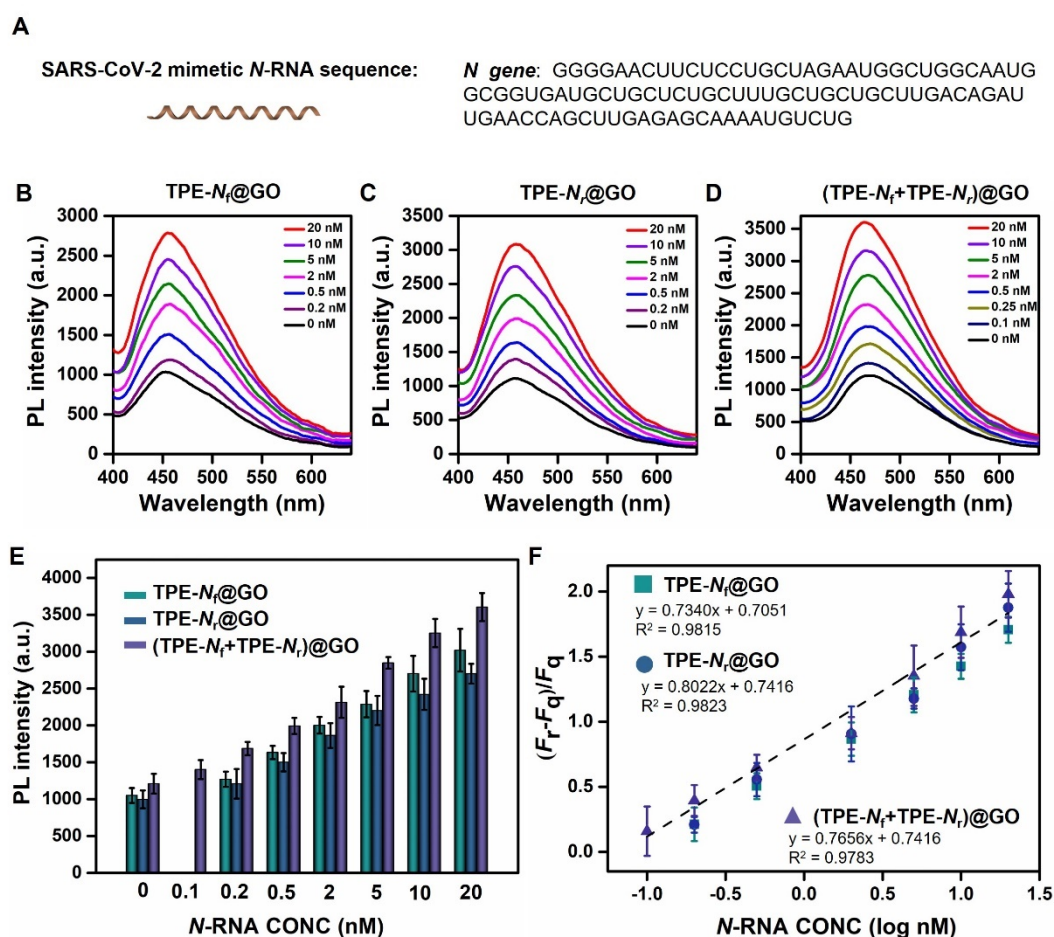


Figure 2.10 (A) The sequence of SAR-CoV-2 mimetic *N*-RNA sequence. Fluorescence spectra of nanoprobe (B) TPE-*N_f*@GO, (C) TPE-*N_r*@GO, and (D) (TPE-*N_f*+TPE-*N_r*)@GO after incubation with *N*-RNA. (E) Fluorescence intensity of nanoprobe (TPE-*N_f*@GO, TPE-*N_r*@GO, and (TPE-*N_f*+TPE-*N_r*)@GO) after incubation with *N*-RNA (0.2 to 20 nM). (F) The

fitting curve of nanoprobe against the logarithmic concentration of *N*-RNA. $\lambda_{ex}/\lambda_{em} = 320/458$ nm.

2.3.2.3 Detection of *Orf1ab*-cDNA sequence

We evaluated the capability of TPE-DNA@GO sensing platform for the detection of *Orf1ab*-cDNA sequence by incubating spTPE-*Orf*@GO (TPE-*Orf_f*@GO or TPE-*Orf_r*@GO) or ppTPE-*Orf*@GO ((TPE-*Orf_f*+TPE-*Orf_r*)@GO) nanoprobe with target *Orf1ab*-cDNA (Figure 2.11). Similarly, the results indicated that the fluorescence intensity of both spTPE-*Orf*@GO and ppTPE-*Orf*@GO nanoprobe linearly increased in the presence of *Orf1ab*-cDNA sequence with the LoD at 250 pM and 200 pM, respectively (Figure 2.11). The sensitivity of TPE-*Orf_f*@GO and TPE-*Orf_r*@GO nanoprobe for the detection of *Orf1ab*-cDNA is 8-time higher than TPE-*Orf* probes without GO adsorption, demonstrating that two-stage fluorescence recovery in TPE-DNA@GO sensing platform facilitates optimizing the sensitivity of biosensors and thus aids to identify infected samples with low viral load.

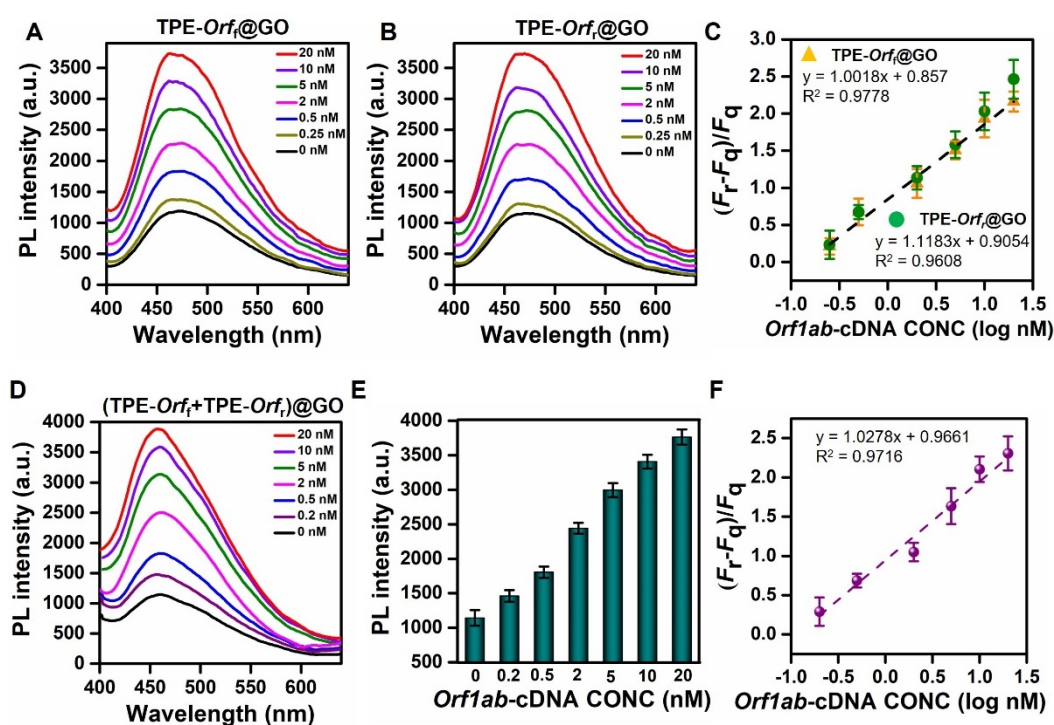


Figure 2.11 Fluorescence spectra of (A) TPE-*Orf_f*@GO and (B) TPE-*Orf_r*@GO after incubating with target *Orf*-cDNA at different concentrations. (C) Fitting logarithmic curve of the relative fluorescence intensity of TPE-*Orf_f*@GO (yellow triangle) and TPE-*Orf_r*@GO (olive circle) after incubating with *Orf*-cDNA. (D) Fluorescence spectra and (E) peak fluorescence intensity at 458 nm of ppTPE-*Orf*@GO (TPE-*Orf_f*+TPE-*Orf_r*)@GO after incubating with *Orf*-cDNA. (F) The fitting curve of (TPE-*Orf_f*+TPE-*Orf_r*)@GO against the logarithmic concentration of *Orf*-cDNA. $\lambda_{ex}/\lambda_{em} = 320/458$ nm.

2.3.2.4 Detection of SARS-CoV-2 plasmid

We chose CDC-V2 plasmid to mimic real SARS-CoV-2 samples to assess the potential application of TPE-DNA@GO nanoprobe for clinical screening of SARS-CoV-2 infected cases (Figure 2.12A). Here, CDC-V2 plasmid consists of both *N* and *Orf1ab* sequences of SARS-CoV-2 with pUC57 as the vector backbone and has been used as positive controls in the RT-PCR tests for SARS-CoV-2 diagnosis^[126, 128]. With the existing technology, the detection procedures require adding many different components, such as probes, specific primers, and amplification reagents, and take over 2 h of thermal cycles. Therefore, we attempt to investigate whether our TPE-DNA@GO nanoprobe can diagnose this positive control more easily than conventional techniques such as RT-qPCR. To assist the hybridization of CDC-V2 plasmids with our nanoprobe, CDC-V2 plasmids with double-stranded DNA were first denatured at 98 °C to form a single-stranded sequence. We assessed the detection ability of ppTPE-*N*@GO ((TPE-*N*_f+TPE-*N*_r)@GO, ppTPE-*Orf*@GO (TPE-*Orf*_f+TPE-*Orf*_r)@GO), and two different ppTPE-DNA@GO combined nanoprobe ((TPE-*Orf*+TPE-*N*)@GO) that total concentration of TPE core within these probes was kept at 3 μM (Figure 2.12). After incubated with denatured CDC-V2 plasmids, the fluorescence intensity of nanoprobe gradually increased along with the increasing concentration of CDC-V2 plasmids, which is identical to the trend of *N*-cDNA and *Orf1ab*-cDNA (Figure 2.12B-C). The resulting LoD of (TPE-*N*_f+TPE-*N*_r)@GO reached 250 pM, while that of (TPE-*Orf*_f+TPE-*Orf*_r)@GO was 400 pM (Figure 2.12B-C). Such a slightly lower sensitivity of (TPE-*Orf*_f+TPE-*Orf*_r)@GO towards CDC-V2 plasmids was probably due to more nucleotides in *Orf1ab*-cDNA fragment than *N*-cDNA which reduces the local hybridization to enhance the fluorescent signals. Furthermore, we examine the efficiency of two ppTPE-DNA@GO ((TPE-*Orf*+TPE-*N*)@GO) nanoprobe for the CDC-V2 plasmids (Figure 2.12D-E). Intriguingly, the LoD was improved by this combinatorial sensing system by up to 200 pM (Figure 2.12D-E). Altogether, these results demonstrated that our TPE-DNA@GO nanoplatform could simultaneously recognize multiple target sites that could generate additional signals for enhanced sensitivity to indicate the presence of SARS-CoV-2 virus.

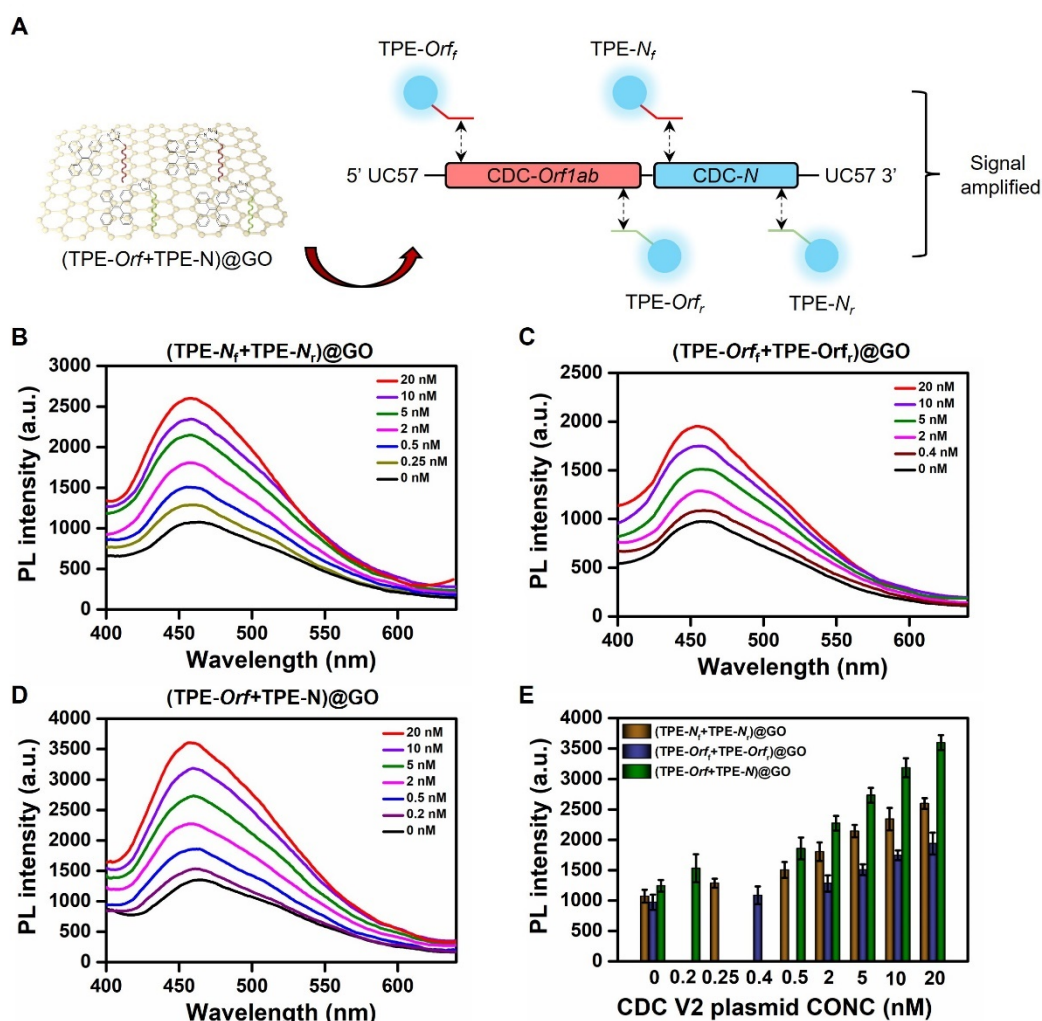


Figure 2.12 (A) Scheme of the detection of CDC-V2 plasmid by ppTPE-DNA@GO nanoprobes. (B-D) Fluorescence spectra of (TPE-N_f+TPE-N_i)@GO, (TPE-Orf_f+TPE-Orf_f)@GO, and (TPE-Orf_f+TPE-N)_i@GO after incubation with denatured CDC-V2 plasmid. (E) Fluorescence intensity at 458 nm of nanoprobes after incubation with CDC-V2 plasmid. $\lambda_{ex}/\lambda_{em} = 320/458$ nm.

2.3.3 Specificity and stability of TPE-DNA@GO nanoprobes

We investigated the specificity of our TPE-DNA@GO nanoprobes by incubating them with corresponding one base mismatch (b₁-Mis) and scrambled sequences of *N*-cDNA and *Orf1ab*-cDNA, respectively, as well as other types of viral cDNA sequences (Figure 2.13A-E). After TPE-DNA@GO nanoprobes hybridized with scrambled sequences and non-specific viral cDNA sequences (InFA, HBV, HCV, and HIV-1), even at a high concentration of 20 nM, the fluorescence intensity of corresponding nanoprobes (TPE-N_f@GO, TPE-N_i@GO, TPE-Orf_f@GO, TPE-Orf_f@GO) was measured to be ~3 times lower than the readouts of the probing entire targeted sequences, suggesting that non-specific nucleic acids minimally interfere with the signals of nanoprobes (Figure 2.13C and F). In addition, agarose gel electrophoresis results indicated that TPE-DNA@GO nanoprobes did not bind with the scrambled cDNA sequences

(Figure 2.14A and B). There was no difference in the base pair (bp) number between the scrambled cDNA alone and the complex of probe-scrambled cDNA (Figure 2.14A and B). On the contrary, the bp number for the complex of probe-target cDNA groups was significantly larger than those for the target cDNA alone (Figure 2.14A and B). The increased band size of the probe-target cDNA complex confirmed the effective DNA hybridization between TPE-DNA@GO nanoprobe and the target cDNA, demonstrating that the fluorescence enhancement of our sensing system was indeed caused by specific DNA hybridization between the nanoprobe and the target cDNA rather than the degradation of ssDNA fragments from TPE-DNA probes. In short, these results confirmed that our platform has a great specificity to SARS-CoV-2 viral *N* and *Orf1ab* sequences and minimal cross-reactivity to other non-specific viral sequences.

Meanwhile, the stability of TPE-DNA@GO sensing platform was evaluated in multiple dimensions. First, the basal fluorescence of TPE-DNA@GO nanoprobe (TPE-*N_f*@GO, TPE-*N_r*@GO, TPE-*Orf_f*@GO, TPE-*Orf_r*@GO) in PBS buffer with different pH values and various kinds of buffers (PBS, TE buffer, borate buffered saline, BSA, and cell culture medium) for 24 h did not show an obvious fluctuation (Figure 2.14C and D). Additionally, these media had little impact on the fluorescence recovery of TPE-DNA@GO nanoprobe upon the addition of corresponding target cDNA (Figure 2.14C and D). Overall, TPE-DNA@GO nanoprobe maintains detection performance without fluctuations in different physiological conditions, indicating the good stability of our sensing platform for the detection of SARS-CoV-2 viral sequences.

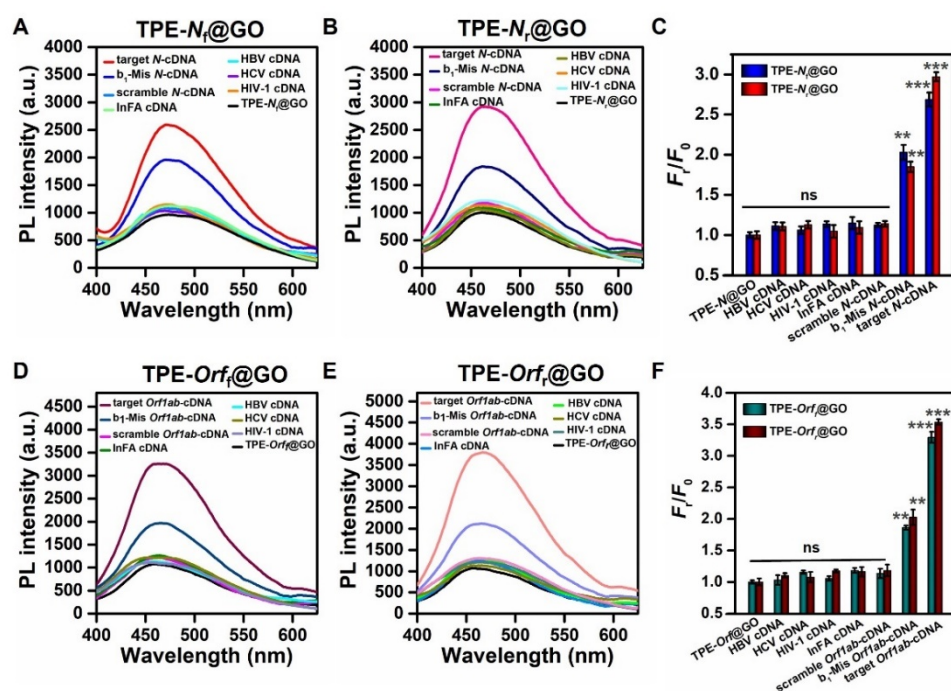


Figure 2.13 Fluorescence spectra of (A) TPE- N_f @GO, (B) TPE- N_r @GO, (D) TPE- Orf_f @GO, and (E) TPE- Orf_r @GO after incubating with different viral sequences including target N -cDNA, target $Orflab$ -cDNA, one base mismatch (b_1 -Mis), scrambled N -cDNA, scrambled $Orflab$ -cDNA, and viral cDNA for InFA, HBV, HCV, and HIV-1. (C, F) Fluorescence intensity fold change of nanoprobe after incubation with different viral sequences.

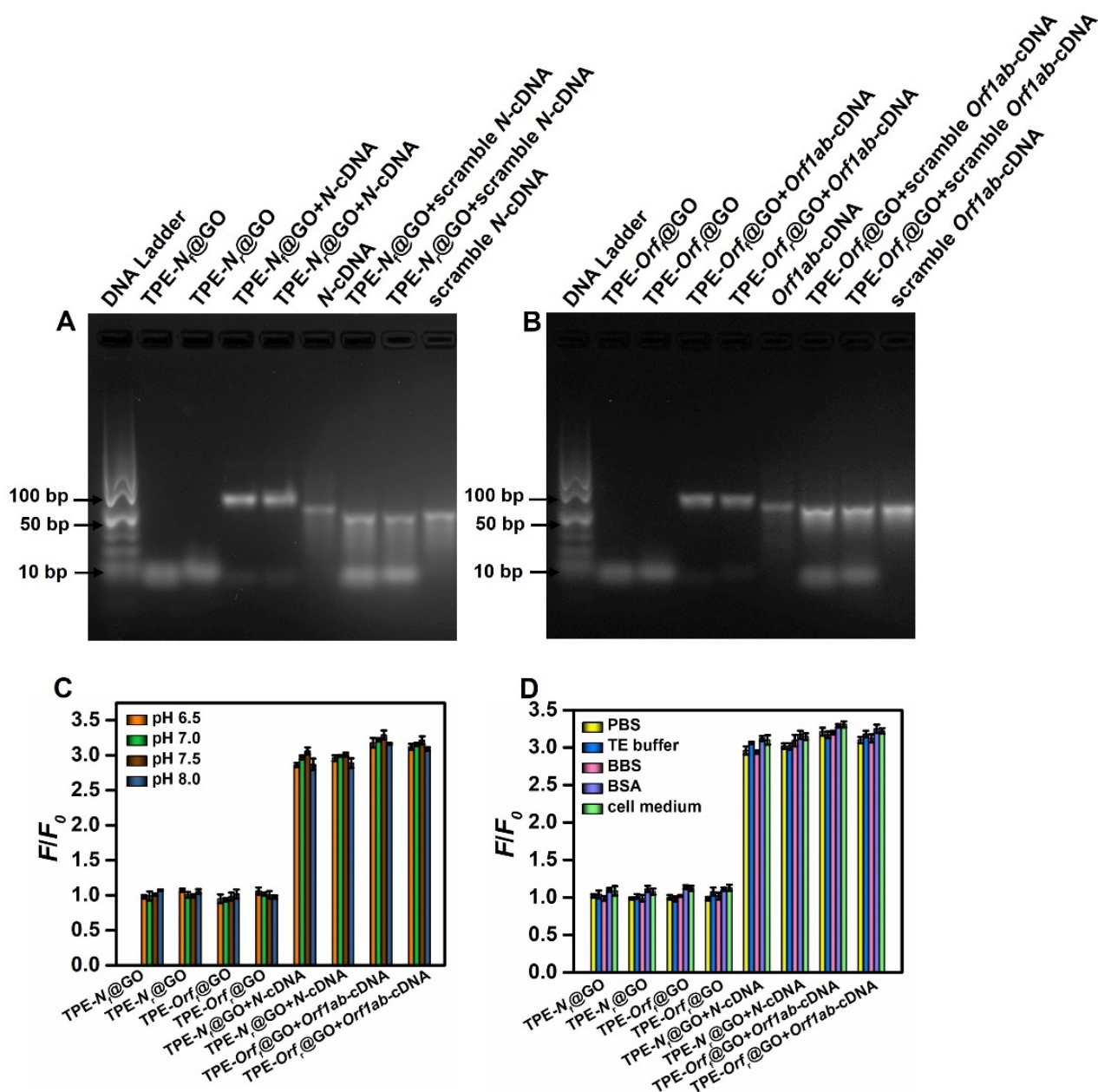


Figure 2.14 Agarose gel electrophoresis of (A) TPE- N_f @GO and TPE- N_r @GO, (B) TPE- Orf_f @GO and TPE- Orf_r @GO after incubation with target cDNA or scramble cDNA. The fluorescence intensity changes of nanoprobe (TPE- N_f @GO, TPE- N_r @GO, TPE- Orf_f @GO, and TPE- Orf_r @GO) dissolved in (C) PBS buffer with different pH values or (D) different buffers (including PBS, TE buffer, borate buffered saline, bovine serum albumin and cell culture medium) for 24 h and then incubated with corresponding target cDNA for an additional 2 h.

Parameters	AI Egen@GO probes	RT-PCR
Sensitivity	Picomolar level (Ct ~20)	~100 copies/mL (Ct~30)
Detection time	~1 h	6~8 h
Cost	Cost-effective i) low cost probe and buffer (i.e., TE buffer) ii) Fluorescence detector	Expensive i) High cost PCR kits ii) Expensive RT-PCR equipment
Experimental procedures	Easy operation	Need well-trained operators

Table 4. Comparison of TPE-DNA@GO nanoprobe with RT-PCR for SARS-CoV-2 viral sequence detection.

Name	Sequence (5' – 3')
alkyne- N_f	HC≡C-ATTCTAGCAGGAGAAGTTCCCC
alkyne- N_r	HC≡C-CAGACATTTTGCTCTCAAGCTG
alkyne- Orf_f	HC≡C-TTAAGTGTAACCCACAGGG
alkyne- Orf_r	HC≡C-ACGATTGTGCATCAGCTGA
N primer Forward	GGGGAACTTCTCCTGCTAGAAT
N primer Reverse	CAGACATTTTGCTCTCAAGCTG
$Orflab$ primer Forward	CCCTGTGGGTTTTACTTAA
$Orflab$ primer Reverse	ACGATTGTGCATCAGCTGA
N -cDNA	GGGGAACTTCTCCTGCTAGAATGGCTGGCAAT GGCGGTGATGCTGCTCTTGCTTTGCTGCTGCTT GACAGATTGAACCAGCTTGAGAGCAAAAATGTCTG CCCTGTGGGTTTTACTTAAAAACACAGTCTGTA
$Orflab$ -cDNA	CCGTCTGCGGTATGTGGAAAGGTTATGGCTGTAGT TGTGATCAACTCCGCGAACCCATGCTTCAGTCAGCT GATGCACAATCGT
N -RNA	GGGGAACUUCUCCUGCUAGAAUGGCUGGCAAUG GCGGUGAUGCUGCUCUUGCUUUGCUGCUGCUUG ACAGAUUGAACCCAGCUUGAGAGCAAAAUGUCUG

One base mismatch (b ₁ -Mis) of <i>N</i> -cDNA	GGGCAACTTCTCCTGCTAGAATGGCTGGCAA TGGCGGTGATGCTGCTCTTGCTTTGCTGCTGC TTGACAGATTGAAC CAGCTTGACAGCAAAATGTCTG CCGTGTGGGTTTTACTTAAAAACACAG
One base mismatch (b ₁ -Mis) of <i>Orflab</i> -cDNA	TCTGTACCGTCTGCGGTATGTGGAAAGGTTA TGGCTGTAGTTGTGATCAACTCCGCGAACCC ATGCTTCAG TCAGCTGATGCAGAATCGT GTTCCGTCGCTTCATACTGCTCATTCGAGCCAT
Scrambled <i>N</i> -cDNA	GGCGAAGACGGAGCGACAGTATTGGTTATGTAT TAGAGTGGACGGCTTGCATTCTTGTGGACGGAC ATAGTAGCTCGTCCTCGAGGTGGCGTATTCGGAA GATCGTCAATCTGTATTGACTGCTCCAACATTCCA AGACGTCCTAACACTGTGTGCTTGAGGATTCCG CGGAACAATCTTGGTAT
Scrambled <i>Orflab</i> -cDNA	GUUCCGUCGCUUCAUACUGCUCAUUCGAGCCAUG GCGAAGACGGAGCGACAGUAUUGGUUAUGUAUUAG AGUGGACGGCUUGCAUUCUUGUGGACGGAC
Scrambled <i>N</i> -RNA	CTGGATCCTGCGCGGGACGTCCTT
HBV cDNA	CACGCCCAAATCTCC
HCV cDNA	GCTATACATTCTTACTATTTTATTTAATCCCAG
HIV-1 cDNA	CGTGCCCAGTGAGCGAGGACTGCA
InFA cDNA	
CDC-V2 plasmid	http://www.life-biotech.com/services/imgs/20200331pdf.pdf

Table 5. The information on DNA and RNA sequences in this study.

2.4 Summary

We proposed a dual fluorescence “turn-on” sensing strategy for SARS-CoV-2 nucleic acid detection based on TPE-DNA@GO nanoprobe in this work. We have demonstrated the significance of using GO to reduce the background fluorescence of TPE-DNA to achieve a high signal-to-background ratio for the detection of viral nucleic acids. Furthermore, the results showed that TPE-DNA@GO nanoprobe is able to rapidly detect multiple SARS-CoV-2 viral sequences in the form of cDNA, RNA, and plasmid without amplification. More importantly, the preparation of our nanoprobe requires only a single-step click reaction and physical adsorption with a quencher. Thus, this sensing platform makes it possible to rapidly recognize nucleic acid from different pathogens in a simple and specific manner. In our future studies, we

may further improve the sensitivity of our sensing platform by combining TPE-DNA@GO with target cycling strategies (e.g., isothermal amplification). Thus, TPE-DNA@GO nanoprobe seems promising for translational applications and monitoring virus-associated infectious diseases.

Chapter 3: A dual fluorescence "turn-on" biosensor based on AIEgen/MoS₂ nanocomposites for *in situ* detection of miR-125b in AD

3.1 Introduction

AD is an irreversible neurodegenerative disorder characterized by progressive cognitive impairment and neuronal loss [129]. Unfortunately, the ongoing studies on AD during the last few decades have not fully elucidated its pathogenesis [130, 131]. Also, the lack of accessible and effective diagnostic tools for real-time probing initial phases of AD may lead to the failure of efficacious pharmacologic therapies. Therefore, it is critical to develop reliable diagnostic methods to detect biomarkers of AD, ideally during the initial stages. To date, a growing number of studies have revealed that pathologic changes in AD are associated with gene expression dysregulation [132-134]. MicroRNAs (miRNAs), endogenous small non-coding RNAs with 20-25 nucleotides, can regulate gene expression at the post-transcriptional level, which also plays an essential role in the pathogenesis of AD. For example, several miRNAs are associated with tau hyperphosphorylation and synaptic dysfunction in AD progression [134-136]. Among them, miR-125b has been identified to be highly expressed in brain tissues and blood of AD patients, and its upregulation could induce tau hyperphosphorylation (p-tau) and synaptic dysfunction, an early event in AD pathology [137, 138]. Therefore, miR-125b can be a promising biomarker of AD at early-stage, and its diagnostic results may provide early decisions on the therapy to halt severe neuropathological alterations associated with AD.

Several standard analytical approaches, such as northern blotting and RT-qPCR, are widely used to quantify miRNA. However, these methods are often time-consuming and require professionally trained operators to manage complicated processes. Furthermore, these techniques can only detect the extracted miRNA *in vitro* in homogenous solutions such as pure water or salt buffer, preventing them from real-time monitoring of miRNA *in situ*. Alternatively, recent advances in FRET-based fluorescence sensing systems have shown great promise in detecting oligonucleotides because of their simple operation and good stability that overcome the limitations of conventional methods [71, 139, 140]. AIEgens exhibit exceptional optical properties such as large Stokes shift, intense brightness, good photostability, and flexible molecular design and have been widely used to develop FRET probes for sensing and imaging biological analytes. With recognition site modification, AIEgens can interact with specific biomolecules such as miRNA or DNA that increase the nearby molecular bulkiness of the AIEgens to induce RIR for lighting up the AIEgens [2, 123, 140, 141]. Therefore, introducing AIEgens into FRET-based biosensing systems underpins the signal-to-noise ratio of target

biomarker-triggered fluorescent readouts for enhanced sensitivity and selectivity, especially in an extraordinarily complex microenvironment of brain tissues with AD. Nevertheless, limited studies have integrated the techniques of AIEgens and FRET for *in vivo* miRNA diagnosis.

MoS₂ nanosheets possess a larger capacity for loading ssDNA via van der Waals force, while the formation of nucleic acid duplex with the target disables this interaction [142]. Thus far, any ssDNA-labelled fluorophore, including AIEgens, can potentially form a good donor-acceptor pair with MoS₂ nanosheets. However, MoS₂ nanosheets rapidly aggregate in physiological solution [143, 144], hampering the application of MoS₂ nanosheets in the biosensing field. Herein, it is instrumental in improving the colloidal and biosensing stability of MoS₂ for *in vivo* applications.

In this work, we reported an effective and biocompatible miRNA biosensor based on the nanocomposite of AIEgens and MoS₂ nanosheets for real-time probing of the early biomarker of AD *in vitro* and *in vivo* (Figure 3.1). To achieve excellent *in vivo* imaging capability, we designed a red-emissive TPE derivative (TPET) with a large Stokes shift that can minimize cross-talk between the excitation source and the fluorescent emission for enhanced *in vitro* and *in vivo* imaging with a high signal-to-noise ratio [145-147]. TPET is conjugated with miR-125b recognizing oligonucleotide (TPET-DNA) that can achieve RIR-induced AIE for strong fluorescent signals upon detecting miR-125b. To further enhance the sensitivity, we suppress the initial fluorescent intensity of TPET-DNA by physically depositing it onto cationic dextran (Dex)-coupled MoS₂ nanosheets (Dex-MoS₂), formulating a FRET-based nanoprobe (TPET-DNA@Dex-MoS₂) to detect intracellular miR-125b with a high signal fold-change post-detection (Figure 3.1A). The cationic Dex possesses a positively charged tetramethylammonium group (TMA), thereby introducing net charges to MoS₂ nanosheets and reinforcing their physiological stability and biocompatibility for cellular uptake. Thus, we hypothesize that miR-125b can hybridize with TEPT-DNA to form a DNA/RNA duplex, causing the pre-absorbed TPET-DNA to detach from TPET-DNA@Dex-MoS₂ that simultaneously initiates "dual on" processes: (1) recovery of TPET-DNA signal and (2) RIR-induced strong fluorescent emission (Figure 3.1B). This one-step sensation mechanism triggers a dual fluorescence enhancement and potentially maximizes the miRNA sensitivity without amplification steps. This feature makes our biosensing platform unique from other existing FRET-based nanoprobe that often rely on single-stage fluorescent recovery [57, 59, 148, 149]. In our findings, the nanocomposite biosensor showed a rapid (\leq 1h) and sensitive biosensing performance (<100 pM) toward miR-125b in buffer or PC12 cells and brain tissues of mice with AD model induced by local administration of okadaic acid (OA). Moreover, our

nanoprobes showed that miR-125b was spatially associated with p-tau *in vitro* and *in vivo*. Knocking down miR-125b significantly reduced p-tau expressions in cells with the AD model. Together, our study not only demonstrates the feasibility of leveraging the techniques of FRET and AIEgen as promising nanoplatform for *in situ* and real-time monitoring of the AD-related biomarker but also provides a mechanistic insight into the early prognosis of AD.

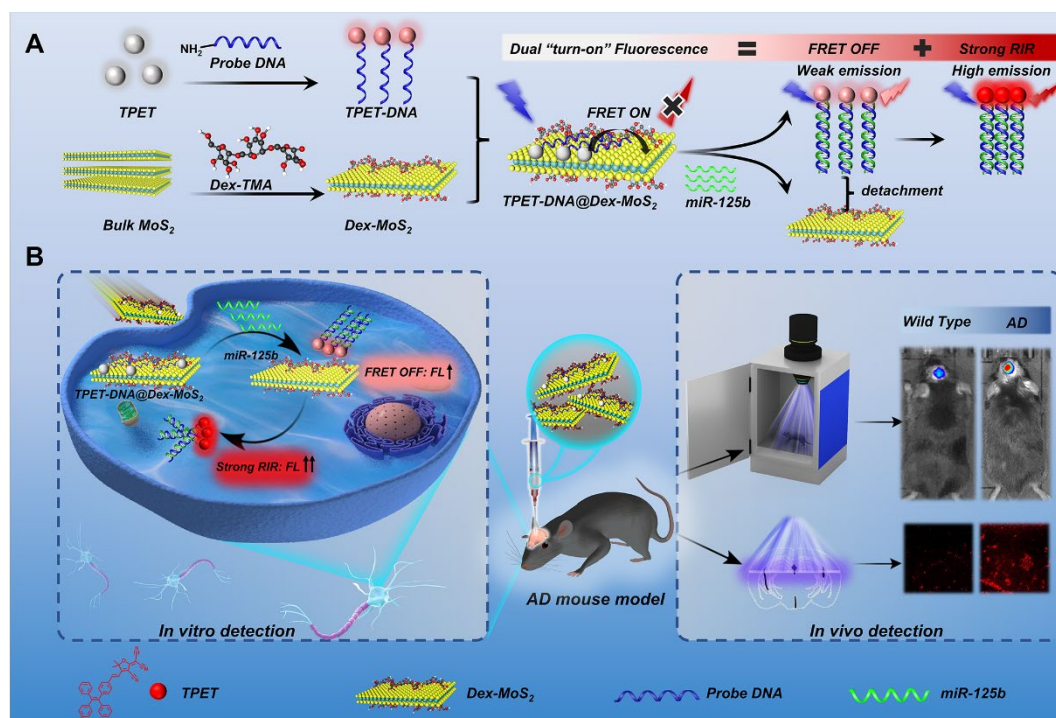


Figure 3.1 (A) Schematic illustrations of the design and fabrication of TPET-DNA@Dex-MoS₂ nanoprobe. (B) Schematic diagram of TPET-DNA@Dex-MoS₂ nanoprobe for *in vitro* and *in vivo* real-time monitoring of miR-125b overexpression in neurons brain tissues of mice with AD model based on a dual fluorescence recovery mechanism.

3.2 Methodology

3.2.1 Synthesis of TPET molecules and TPET-DNA

The AIEgen, 2-(3-cyano-4-((E)-4-((E)-2-(4-formylphenyl)-1,2-diphenylvinyl)styryl)-5,5-dimethylfuran-2(5H)-ylidene)malononitrile (TPET) was synthesized according to a previously published method ^[146]. Briefly, TPE-CHO (776 mg, 2.0 mmol), TCF (199 mg, 1 mmol), and NaOH (4.2 mg) were added to a 100 mL round-bottomed flask. The flask was evacuated and backfilled with nitrogen three times. Then, 25 mL ethanol was injected into the flask, and the reaction mixture was stirred and refluxed overnight. After the reaction, the mixture was extracted with dichloromethane (DCM). After filtration, the solvent was evaporated to give a crude residue which was then purified by silica gel column chromatography (hexane/DCM as the eluent) to yield TPET molecules (154 mg, 27.06%). ¹H NMR (400 MHz, DMSO): δ 10.01 – 9.81 (m, 1H), 7.94 – 7.59 (m, 7H), 7.33 – 6.91 (m, 11H),

5.87 – 5.66 (m, 1H), 5.49 – 5.31 (m, 1H), 1.87 – 1.57 (m, 6H). ^{13}C NMR (400 MHz, DMSO). ^{13}C NMR (400 MHz, DMSO): δ 196.74, 192.50, 168.23, 146.90, 146.64, 142.13, 141.44, 141.05, 134.32, 132.84, 131.47, 130.77, 130.35, 129.02, 128.22, 127.34, 124.97, 115.35, 112.65, 111.82, 110.82, 99.34, 54.40, 45.65, 25.04.

Then, TPET-DNA was synthesized by covalent coupling of the aldehyde group of TPET molecules to the amino group at the 5' end of the DNA sequence ^[150]. Briefly, TPET in tetrahydrofuran (THF) (150 μM , 1mL) was mixed with amine-functionalized oligonucleotides (probing DNA: 5'-NH₂-TCACAAGTTAGGGTCTCAGGGA-3', 100 μM , 1mL) in sodium borate buffer (pH 8.5). Then, the mixture was left to stir overnight at room temperature. After that, sodium borohydride dissolved in H₂O (100 μM , 0.2 mL) was added to the mixture and stirred for 2 h. In the next step, the product was purified by dialysis against deionized water in a cellulose dialysis membrane (MWCO 1kDa), followed by lyophilization to obtain TPET-DNA.

3.2.2 Synthesis of Dex-TMA

The dextran derivative with trimethylammonium groups (Dex-TMA) was synthesized according to the previous study ^[151]. First, dextran (MW=20000, 5 g) was dissolved in 25 mL of water in an ice bath, and then NaOH solution (2 M, 25 mL) was added to it. Then, a 436 μL portion of glycidyl trimethylammonium chloride was added to the reaction mixture. The temperature increased to 40 °C to start the reaction. After allowing the reaction to proceed for another 12 hours, it was quenched by cooling it down immediately in an ice bath. Afterward, 250 mL of methanol was slowly added to the reaction mixture at 25 °C to precipitate the product. Thereafter, the product was dissolved in 5 mL of water and placed on a cellulose dialysis membrane (MWCO 3500Da) for dialysis purification. After 24 hours, the Dex-TMA solution was frozen and then lyophilized.

3.2.3 Preparation of TPET-DNA@Dex-MoS₂

First, for the synthesis of Dex-MoS₂, 2 mg of Dex-TMA was dissolved in H₂O (5 mL) and then mixed with MoS₂ dispersion (2 mg/mL, 5 mL). Then, the mixture was sonicated using a probe tip sonicator pulsing at 12W with 2 sec-on and 2 sec-off for 2 h in an ice bath. Afterward, the solution was centrifuged at 3000 rpm for 1 h to collect the supernatant. Prior to the fabrication of TPET-DNA@Dex-MoS₂, Dex-MoS₂ dispersion was strongly sonicated in an ice bath for 1 h, and TPET-DNA was dissolved in DMSO/H₂O (v/v, 1/199) as a stock solution. Then, to evaluate the quenching efficiency of Dex-MoS₂ nanosheets, TPET-DNA (10 μM , 100 μL) was mixed with TMA-MoS₂ dispersion (100, 150, 200, 250, 300 $\mu\text{g}/\text{mL}$, 100 μL) in DNase/Rnase-free water for over 30 min. Then, the fluorescence intensity was determined with

excitation at 480 nm, and emission scanned from 500 nm to 750 nm. The quenching efficiency (Q_e) of Dex-MoS₂ was calculated according to the formula $Q_e (\%) = (F_0 - F_q) / F_0$, where F_0 is the fluorescence signal of TPET-DNA and F_q represents the fluorescence intensity of TPET-DNA after quenched by Dex-MoS₂. In all the following detection experiments, TPET-DNA@Dex-MoS₂ was prepared by incubating TPET-DNA with Dex-MoS₂ dispersion to a final concentration of 5 μ M and 125 μ g/mL, respectively. After incubation for 1 h at room temperature, the TPET-DNA@Dex-MoS₂ was immediately utilized in the detection assay.

3.2.4 Detection of miR-125b in vitro

TPET-DNA@Dex-MoS₂ (5 μ M) was added into Tris-EDTA buffer containing target miR-125b at a series of concentrations (0~10 nM). Then, the mixture was incubated at 37 °C for 1 h before fluorescence measurement. The limit of detection (LOD) of TPET-DNA@Dex-MoS₂ nanoprobe was calculated by the equation: $LOD = 3\sigma/k$ (where σ is the population standard deviation of the blank sample, $n = 10$, and k is the slope of the calibration curve). In addition, the fitting of a linear relationship between relatively recovered fluorescence signal $(F_r - F_q)/F_q$ (F_q : fluorescence intensity of probes, F_r : fluorescence intensity probe-cDNA complex) and logarithmic concentration of cDNA was analyzed by using Origin 9.0 software. The consequent correlation coefficient (R^2) was employed to describe the linearity. The specificity of TPET-DNA@Dex-MoS₂ nanoprobe was evaluated by incubating the probes with non-specific sequences, including one base mismatched (b₁-Mis), scrambled sequences of miR-125b, and non-specific microRNA (miR-9 and miR-29a) at the same condition as controls. Three independent experiments were performed for each measurement.

3.2.5 Cell culture and cytotoxicity of TPET-DNA@Dex-MoS₂

The neuron-like rat pheochromocytoma cell lines (PC12 cells) were used to assess the biocompatibility of TPET-DNA@Dex-MoS₂. First, PC12 cells were differentiated in Opti-MEM containing 1% FBS, 2% B27 supplement, and nerve growth factor (100 ng/ml) for 7 days [152]. Afterward, differentiated PC12 cells were seeded in a 96-well plate at the density of 1×10^4 /well for 24 h and then treated with TPET-DNA@Dex-MoS₂ nanoprobe at various concentrations (2, 5, 10, 20, 50, 100, 200 μ M). Then, cell viability was measured using an MTT assay after incubation with nanoprobe for 24 h.

3.2.6 Intracellular overexpression of miR-125b

The differentiated PC12 cells were treated with OA at different concentrations (10, 25, 50 nM) for 12 h to induce miR-125b upregulation and tau hyperphosphorylation [153, 154]. Meanwhile, the transfection of miR-125b mimics and inhibitors into cells was constructed through electroporation. Briefly, 5×10^6 cells were collected and resuspended in 0.4 mL opti-

MEM buffer containing miR-125b mimics or inhibitors (20 nM) and then incubated on ice for 15 min before being moved to an electroporation cuvette. Next, electroporation was carried out on Gene Pulser Xcell System with voltage at 250 V and capacitance at 960 μF [155]. After electroporated, the cells were further cultured for 72 h. Then, the intracellular miR-125b level was quantified by RT-PCR via a real-time microRNA qPCR kit based on SYBR green method. First, the total RNA was extracted from cells. Afterward, template cDNA was mixed with SYBR green dyes and specific primers for miR-125b, followed by amplification on CFX96 RT-PCR equipment. The sequence information for primers is listed in Table 6. The relative expression level of miR-125b was calculated using the $2^{-\Delta\Delta\text{Ct}}$ method, with U6 as an internal reference gene.

3.2.7 Intracellular detection of miR-125b

First, the differentiated PC12 cells were treated by OA for 12 h or transfected with miR-125b mimics to induce miR-125b upregulation. Then, the cells were incubated with TPET-DNA@Dex-MoS₂ (25 μM) for 6 h before being viewed and imaged under a confocal microscope ($\lambda_{\text{ex}}=488$ nm, $\lambda_{\text{em}}=550\sim 700$ nm). Then, a flow cytometer was applied to quantify the intracellular fluorescence intensity of TPET-DNA@Dex-MoS₂ with PerCP filter ($\lambda_{\text{ex}} = 488$ nm, $\lambda_{\text{em}} = 595 \pm 40$ nm). The average fluorescence intensity of the flow cytometric results was analyzed via FlowJo 10.8 software.

3.2.8 Stereotaxic surgery and establishment of the AD mouse model

The experiments were carried out with male wild-type C57BL/6 mice (25-30g, 8-12 weeks). All the animals were procured from the Centralized Animal Facilities at Hong Kong Polytechnic University. All the animal experiments were carried out in compliance with ethical approval from the Institutional Animal Ethics Committee. In this work, mice were divided into 4 groups of 4 mice each: C1 (saline + TPET-DNA@Dex-MoS₂), C2 (OA + saline), C3 (OA + TPET-scrDNA@Dex-MoS₂), and T (OA + TPET-DNA@Dex-MoS₂). Before any surgical procedure, mice were anesthetized with ketamine (100 mg/kg) and xylazine (5 mg/kg). The head of each mouse was shaved, followed by being held in a stereotaxis instrument. OA (100 ng in 2 μL saline) was then injected unilaterally to the lateral ventricle (coordinates: anterior/posterior -1.94 mm, medial/lateral -2.75mm, dorsal/ventral -2.90 mm) with an infusion rate of 100 nL/min [156]. The syringe remained for ~ 10 min after the injection to minimize backflow. The scalp wound was then sutured, and the mice were left to recover.

3.2.9 Animal imaging in vivo

After 5 days of OA injection, TPET-DNA@Dex-MoS₂ nanoprobe (50 μM in PBS, 2 μL) or scrambled probes (TPET-scrDNA@TMA-MoS₂, 50 μM in PBS, 2 μL) or saline (2 μL) was

stereotaxically administrated into the lateral ventricle (coordinates: anterior/posterior -1.94 mm, medial/lateral -2.75mm, dorsal/ventral -2.90 mm). After injection, the fluorescent signals were examined by *in vivo* image system (IVIS) at different time intervals (0, 0.5, 1, 2, 4, 6, 12, 24 h) and subjected to analysis using Living Image software. The excitation and emission filter settings in the IVIS camera were 480 nm and 620 nm, respectively.

3.2.10 Histological tissue preparation and immunocytochemistry

After imaging *in vivo*, mice were anesthetized before transcranial perfusion with 50 ml PBS and 4 % paraformaldehyde (PFA). Brains were removed from the skull and post-fixed in PFA at 4 °C for 2 days. Next, brains were dissected into 20- μ m thick coronal slices using a vibratome, and then the brain slices were immunohistochemistry-stained with the anti-p-tau antibody. Brain sections were incubated with anti-p-tau primary antibody (1:400) at 4 °C overnight and then incubated with Alex Flour 488-conjugated secondary antibody (1:1000) at 37 °C for 2 h, followed by staining with DAPI (1:1000) to label cell nuclei. Finally, brain sections were mounted on slides and cover-slipped before being imaged on the confocal microscope (DAPI: $\lambda_{ex}/\lambda_{em}$ = 405 nm/420–450 nm; Alex Flour 488: $\lambda_{ex}/\lambda_{em}$ = 488 nm/500–525 nm; TPET-DNA@Dex-MoS₂: $\lambda_{ex}/\lambda_{em}$ = 488 nm/575–700 nm). The intensity of fluorescent signals in the brain sections was analyzed by ImageJ software. The analysis of line profile intensity was obtained via Leica LAS X software.

3.2.11 Statistical analysis

Results are shown as the mean with error bars representing standard deviation. Graphpad Prism 9.0 software was used to perform statistical tests and plot results. Statistical analyses were conducted by one-way ANOVA test followed by appropriate post-hoc analyses for multiple comparisons. A value of probability $p < 0.05$ was considered statistically significant.

3.3 Results and Discussion

3.3.1 Synthesis and characterization of TPET-DNA@Dex-MoS₂

3.3.1.1 Synthesis and characterization of TPET-DNA

We first synthesized the TPET according to a previous study^[146] (Figure 3.2A). Matrix-assisted laser desorption/ionization coupled to time-of-flight (MALDI-TOF) mass spectrometry confirmed its molecular weight (MW) as 569.188 (Figure 3.2B). The chemical structure of TPET was characterized by ¹H NMR and ¹³C NMR spectroscopic techniques (Figure 3.2C and D). To investigate whether the obtained TPET possessed the inherent AIE properties of the TPE moiety, we measured the emission spectra of TPET in solvent mixtures with different fractions of THF and H₂O (Figure 3.3). Due to their limited solubility in water, the fluorescence emission

of TPET was gradually enhanced with the increased water fraction (Figure 3.3), indicating their AIE effect [146, 157]. Additionally, the excitation/emission (ex/em) peaks of TPET were 480/668 nm, which showed a huge stoke shift (~200 nm) that not only suppressed the overlap ex/em spectrum but also reduced interference from autofluorescence of brain tissues, which was substantial at emission wavelength below 600 nm [38]. Hence, we have established a high signal-to-noise red-emissive AIEgen that can be further modified to detect miRNA.

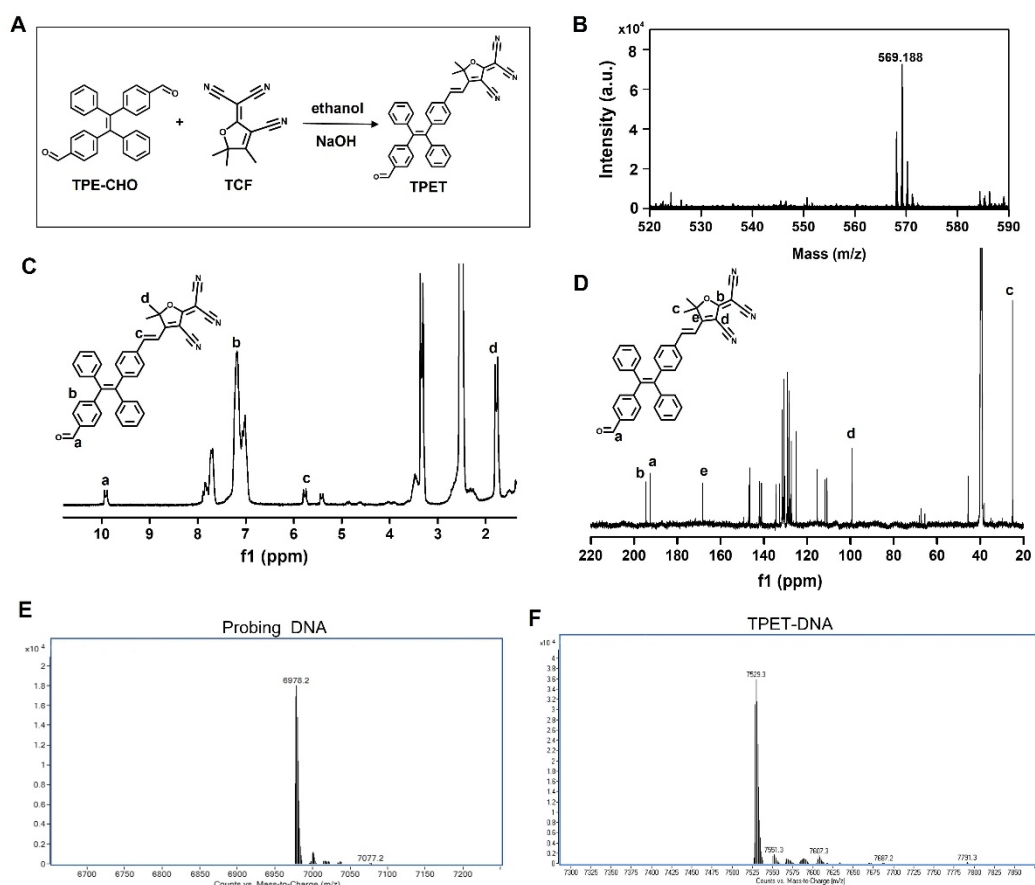


Figure 3.2 The synthesis and characterization of TPET. (A) Synthetic route to TPET compound. (B) MALDI-TOF mass spectrum of TPET in methanol with HCCA as the matrix. (C) ^1H NMR spectrum and (D) ^{13}C NMR spectrum of TPET compound in DMSO- D_6 . The molecular weight of (E) probing DNA and (F) TPET-DNA was determined by ESI-MS-TOF spectrometry.

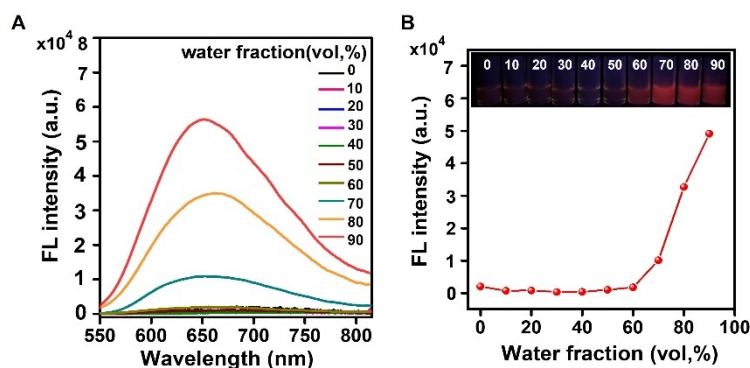


Figure 3.3 The AIE effect of TPET molecules. (A) Fluorescence spectra of TPET in the THF/water mixtures with different water fractions. $\lambda_{\text{ex}}=480$ nm. (B) The plot of fluorescence

intensity versus the compositions of aqueous mixtures. The inset photographs were images of TPET under a UV lamp.

We next conjugated TPET with an ssDNA complementary to the sequence of miR-125b (TPET-DNA) via the reaction between the aldehyde moiety of TPET and -NH₂ group of the ssDNA. The successful fabrication of TPET-DNA was confirmed by ESI-TOF mass spectrometry that showed an increase of MW from 6978.2 (TPET) to 7529.3 (TPET-DNA, Figure 3.2 E and F). Also, only TPET-DNA showed an absorption peak at 260 nm besides the two original peaks at 358 nm and 480 nm for the TPET moiety in DMSO/H₂O (v/v, 1/199), indicating the presence of oligonucleotides in TPET-DNA (Figure 3.4A). Although introducing ssDNA to TPET caused a blueshift of its emission peak from 668 nm to 618 nm, TPET-DNA remains a large Stokes shift (~138 nm) that is highly beneficial for living tissue bioimaging (Figure 3.4B). Moreover, the fluorescence intensity of TPET-DNA was only 9.33% that the TPET molecules in DMSO/H₂O (v/v, 1/199), which was attributed to the enhanced hydrophilicity of TPET-DNA that reduced AIE effect in water (Figure 3.4B and C). Before coupling TPET-DNA to Dex-MoS₂, we examine whether TPET-DNA can be "turned on" by specifically interacting with miR-125b. As expected, the peak fluorescent signals of TPET-DNA exhibited a linear increase along with increased miR-125b concentrations with a calculated limit of detection (LOD) at 416.42 pM (Figure 3.5A-C). On the other hand, TPET conjugated with scrambled ssDNA or TPET-DNA incubating with a scrambled sequence of miR-125b and non-specific sequences (miR-9 and miR-29a) did not show any incremental fluorescent signal, proving that TPET-DNA was highly specific to probe miR-125b (Figure 3.5D-E).

3.3.1.2 Synthesis and characterization of Dex-TMA

To maximize the sensitivity of TPET-DNA, we aim to suppress the intrinsic fluorescence of TPET-DNA, possibly from a basal level of RIR caused by the conjugated DNA to the TPE core [123, 124]. Hence, we adopted polymeric MoS₂ nanosheets as an effective fluorescence quencher because of the as-mentioned advantages in the introduction section. To optimize the stability and biocompatibility of the nanoplatform in biological media, we modulated the interface of MoS₂ nanosheets with a hydrophilic polymer dextran derivative bearing trimethylammonium groups (Dex-TMA), resulting in Dex-TMA/MoS₂ hybrids (Dex-MoS₂). Dex-TMA was fabricated via simple ring-opening reactions of Dex referred to a previous method (Figure 3.6A) [151]. The FTIR spectrum of Dex-TMA displayed a characteristic peak at 1595 cm⁻¹ corresponding to the C-N bond but not in the intact Dex, demonstrating the successful synthesis of Dex-TMA (Figure 3.6B). The hydrodynamic size of Dex-MoS₂ was

~167 nm, smaller than that of MoS₂, due to the coating method of single-pulse sonication (Figure 3.4D). The addition of cationic TMA groups converted the surface charge of MoS₂ nanosheets from strongly negative ($\zeta = -28.7$ mV) to slightly positive ($\zeta = +5.6$ mV) (Figure 3.6C), which facilitated the affinity between MoS₂ and Dex^[151]. This net charge can also potentially enhance the loading efficiency of TPET-DNA via electrostatic interactions apart from the single van der Waals force between MoS₂ and ssDNA^[151]. Besides, Dex-MoS₂ nanosheets were well-dispersed in water, PBS buffer, and cell culture medium with no apparent aggregation at 48 h post-incubation, and the average size of Dex-MoS₂ was measured within 150~170 nm while MoS₂ was in the micrometer range due to agglomeration, indicating high stability of Dex-MoS₂ nanosheets in various conditions (Figure 3.6D and E). So far, we have improved the performance of MoS₂ nanosheets with excellent stability, facilitating the establishment of FRET-based biosensors based on TPET-DNA and polymeric MoS₂.

FRET-based biosensors require an acceptor motif with a high quenching efficiency (Q_e). To optimize the optimum Q_e of Dex-MoS₂ nanosheets in our sensing platform, we coupled TPET-DNA with Dex-MoS₂ of varying concentrations ranging from 0 to 150 $\mu\text{g/mL}$. Significantly, the fluorescence intensity of TPET-DNA decreased along with increased TMA-MoS₂ concentrations (Figure 3.7A-B). The Q_e reached a maximum of 96.72% for 150 $\mu\text{g/mL}$ of TMA-MoS₂ (Figure 3.7C). To avoid over-quenching and achieve optimal sensing performance, we selected 125 $\mu\text{g/mL}$ of Dex-MoS₂ with a Q_e of 90.81% for fabricating TPET-DNA@Dex-MoS₂ nanoprobe in the following detection assay. Remarkably, the fluorescence intensity of TPET-DNA@Dex-MoS₂ was only ~9.19% and ~0.85% of those in TPET-DNA and TPET, respectively. These results demonstrate that Dex-MoS₂ nanosheets play a critical role in quenching the basal fluorescent signal of the TPET-DNA biosensor that can decrease the background signal for the enhanced LOD^[158].

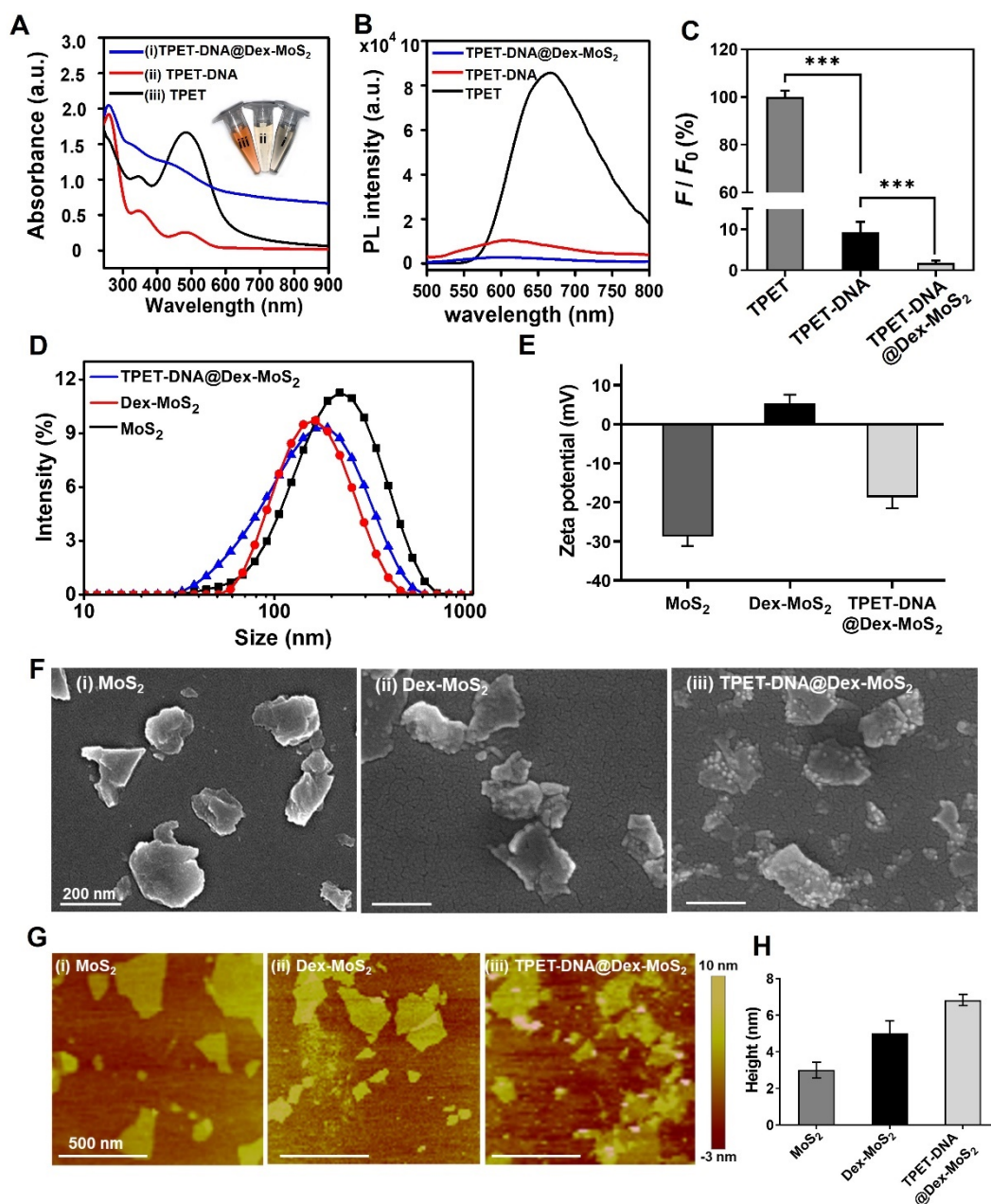


Figure 3.4 The fabrication and characterization of TPE-DNA@@Dex-MoS₂. (A) UV-vis absorbance of TPET, TPET-DNA, and TPET-DNA@Dex-MoS₂ in H₂O. (B) Photoluminescence spectra of TPET, TPET-DNA, and TPET-DNA@Dex-MoS₂ in H₂O. λ_{exc} = 480 nm. (C) The fluorescence intensity percentage of TPET-DNA and TPET-DNA@Dex-MoS₂ normalized to the fluorescence intensity of TPET (F_0). (D) Size distribution, (E) Zeta potential, (F) SEM images, (G) AFM images of MoS₂, Dex-MoS₂, and TPET-DNA@Dex-MoS₂. (H) Histograms of height calculated from AFM images.

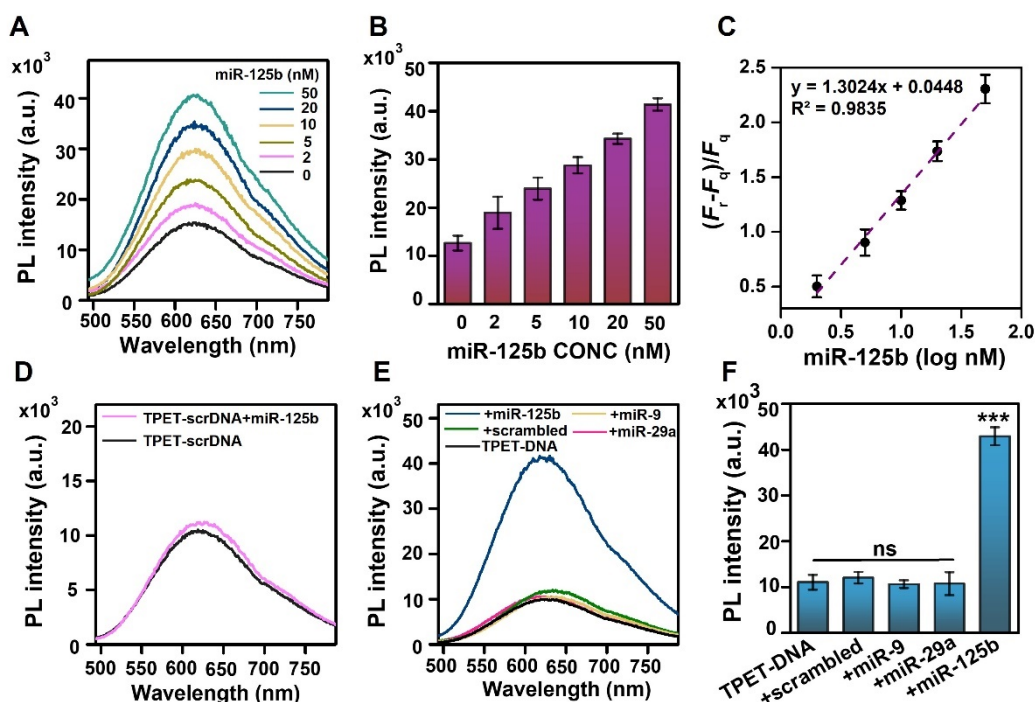


Figure 3.5 The detection performance of TPET-DNA. (A) Photoluminescence spectra and (B) peak fluorescence intensity of TPET-DNA before and after incubating with miR-125b at a series of concentrations. (C) Fitting logarithmic curve of the relative fluorescence intensity of TPET-DNA against the increasing concentration of miR-125b. F_q : fluorescence intensity of TPET-DNA, F_r : fluorescence intensity of TPET-DNA after incubation with miR-125b. (D) Photoluminescence spectra of TPET-scrDNA after incubation with miR-125b at a concentration of 10 nM. (E) Photoluminescence spectra and (F) peak fluorescence intensity of TPET-DNA after incubation with miR-125b, scrambled miR-125b, miR-9, and miR-29a at a concentration of 10 nM.

3.3.1.3 Fabrication of TPET-DNA@Dex-MoS₂

After optimizing the coupling ratio, the nanocomplex (TPET-DNA@Dex-MoS₂) was successfully fabricated, accompanied by slightly increased hydrodynamic size (~ 14 nm larger than Dex-MoS₂) and becoming negative charged ($\zeta = -18.6$ mV) due to the presence of TPET-DNA (Figure 3.4D and E). Furthermore, TPET-DNA@Dex-MoS₂ showed a rougher surface texture and thicker dimension (thickness = ~6.8 nm) than those of MoS₂ (thickness = ~3.1 nm) or Dex-MoS₂ (thickness = ~4.8 nm) (Figure 3.4F-H). Excellent stability and biocompatibility are the prerequisites for intracellular and *in vivo* biosensing applications. TPET-DNA@Dex-MoS₂ did not exhibit a strong fluorescent fluctuation in PBS buffer at various pH values (6.5, 7.0, 7.5, 8.0) and different types of media (Tris-EDTA buffer, borate buffered saline, bovine serum albumin solution, and cell culture medium) over 24 h, suggesting its excellent stability at the steady state, which is ideal for sensing targets at the physiological environment (Figure 3.8A and B). In short, we have successfully constructed TPET-DNA@Dex-MoS₂ nanocomplex

with excellent biocompatibility and stability for intracellular and *in vivo* miR-125b sensing applications.

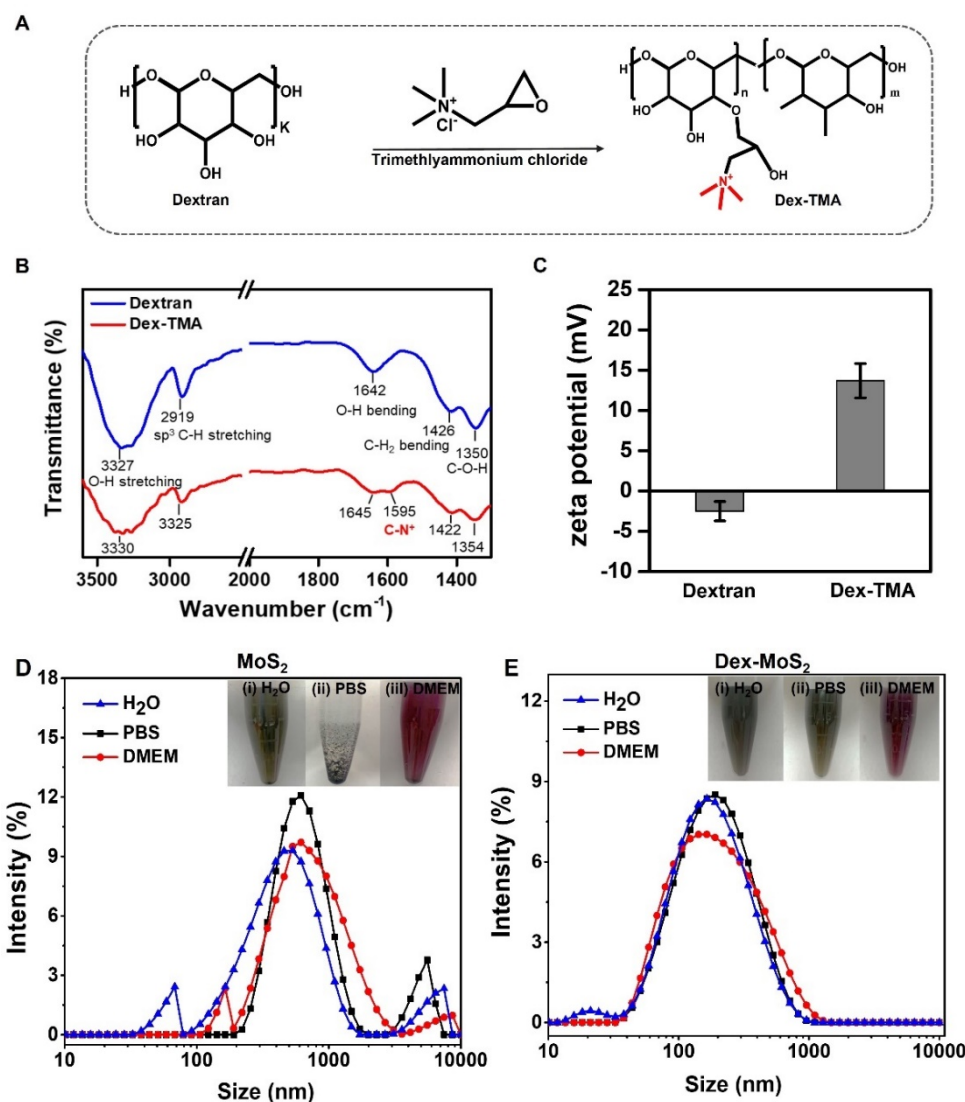


Figure 3.6 The synthesis and characterization of Dex-TMA. (A) Synthetic route to Dex-TMA polymer. (B) FTIR spectrum of dextran and Dex-TMA. (C) Zeta potential of dextran and Dex-TMA. The size distribution of (D) MoS₂ and (E) Dex-MoS₂ nanosheets distributed in H₂O, PBS, and cell medium(DEME) after 48 h of standing.

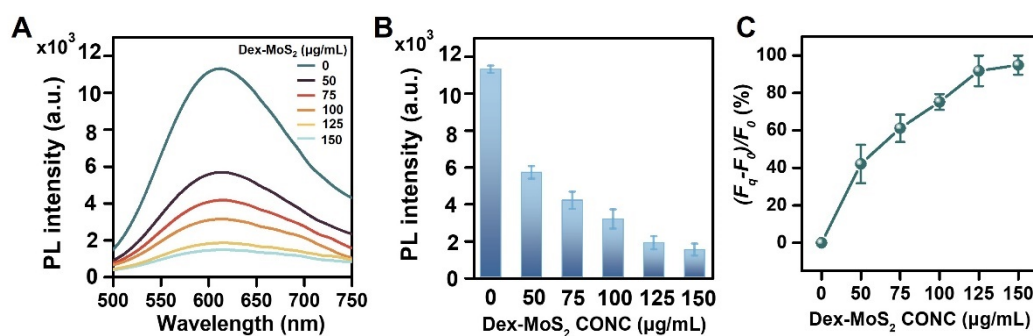


Figure 3.7 The quenching efficiency of Dex-MoS₂. (A) Photoluminescence spectra and (B) peak fluorescence intensity of TPET-DNA after quenched by Dex-MoS₂ at a series of

concentrations. (C) The plot of quenching efficiency (Q_e %) versus different concentrations of TMA-MoS₂ nanosheets. F_0 : fluorescence intensity of TPET. F_q : fluorescence intensity of TPET after adding Dex-MoS₂ to form TPET-DNA@Dex-MoS₂. $\lambda_{ex}/\lambda_{em} = 480/618$ nm.

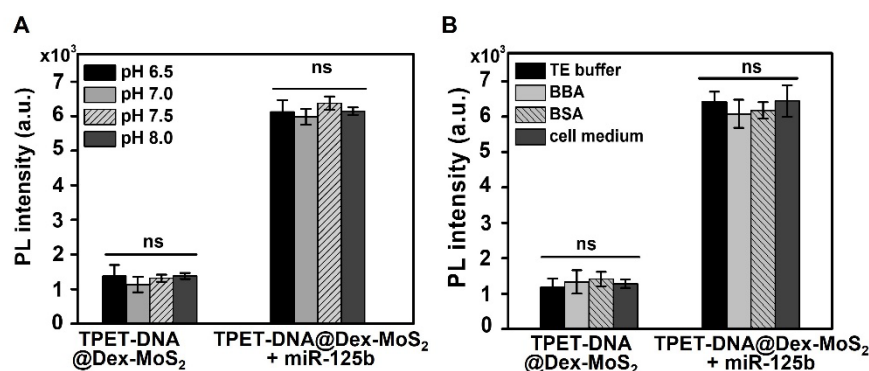


Figure 3.8 The stability of TPET-DNA@Dex-MoS₂ nanoprobe. The fluorescence intensity changes of TPET-DNA@Dex-MoS₂ nanoprobe dissolved in (A) PBS buffer with different pH values or (B) different media (TE buffer, borate buffered saline (BBS), BSA, and cell medium) for 24 h and then incubated with miR-125b for an additional 2 h. $\lambda_{ex}/\lambda_{em} = 480/618$ nm.

3.3.2 In vitro detection of miR-125b

We assessed the detection ability of the established platform against varying concentrations of the synthetic miR-125b *ex vivo*. First, we optimized that the nanoprobe reached a maximal fluorescent intensity when the incubation time with miR-125b ≥ 1 h to ensure an entire DNA-RNA hybridization process. Next, we observed that the nanoprobe at a fixed concentration showed increased fluorescent intensity with increased miR-125b concentrations, consistent with the biosensing assay results of that by TPET-DNA and also the hypothesis of signal enhancement/recovery by detaching from TPET-DNA from Dex-MoS₂ nanosheets. The peak fluorescent signals at 618 nm showed an excellent linear relationship with the logarithmic concentrations of miR-125b ($R^2 = 0.994$) with a LOD calculated at 20.82 pM (Figure 3.9A-D), which was ~ 20 times more sensitive than that achieved by TPET-DNA. Our platform entails the mechanism of "dual on" for enhanced LOD that is highly conducive to detecting miRNA detection, especially at the early stage of AD with moderate miR-125b expression [138, 153].

We next evaluated the selectivity of our nanoprobe against one-base mismatched (b₁-Mis) and scrambled miR-125b sequences, as well as two other non-specific miRNAs, miR-9 and miR-29a, both of which are aberrantly expressed in AD pathology [159]. We observed that the fluorescence of TPET-DNA@Dex-MoS₂ nanoprobe did not significantly change in the presence of scrambled miR-125b, miR-9, and miR-29a, suggesting that non-specific nucleic acids in the background did not influence the fluorescent signal of the sensing system (Figure 3.9E and F). Additionally, the agarose gel electrophoresis analysis revealed that incubating the nanoprobe with miR-125b formed a new band (~ 20 bp) with a higher base pair number than

the band of miR-125b alone (~10 bp) (Figure 3.9G). In comparison, no such band was observed when loading the probes with the scrambled sequence, confirming minimal interactions between TPET-DNA@Dex-MoS₂ and non-specific nucleic acids (Figure 3.9G). In contrast, the b₁-Mis group resulted in signals with ~2.3-fold lower than that of the intact miR-125b group, suggesting that our nanoprobe could distinguish the signal by an incomplete matching sequence of the target (Figure 3.9E and F). Altogether, these results verified that the TPET-DNA@Dex-MoS₂ is a highly sensitive and selective tool for miR-125b detection with minimal interference by non-specific miRNA species.

3.3.3 Intracellular detection of miR-125b

The AD model with miR-125b overexpression can be established through OA administration or direct transfection of miR-125b mimics into cells. We examined the biosensing performance of our nanoplatform to probe miR-125b in PC12 cells with or without the AD model. We first treated PC12 cells with nerve growth factor (NGF) to induce their differentiation into neuron-like cells, which exhibited spindle-shaped cell morphology like neuronal cells (Figure 3.10). Next, we stimulated the differentiated PC12 cells by adding okadaic acid (OA) that upregulated endogenous miR-125b expression and tau hyperphosphorylation as a preliminary cell model of AD under tau pathology^[153]. On the other hand, the cells were transfected with miR-125b mimics as a positive control, and OA pretreated cells were transfected with miR-125b inhibitor as a negative control to study the intracellular detection performance of TPET-DNA@Dex-MoS₂ nanoprobe (Figure 3.11A). Before employing the probes for the detection, we confirmed the intracellular level of miR-125b by RT-PCR. The relative expression was ~1.6-fold higher in cells treated with 50 nM OA and ~2.3-fold higher in mimic-transfected cells than that in the normal PC12 cells (Fig. 3B). In OA-treated cells, miR-125b inhibitor transfection downregulated the expression of miR-125b almost to the level of normal cells (Figure 3.11B). These results justify that miR-125b expression is regulated by the intrinsic AD pathology induced by OA.

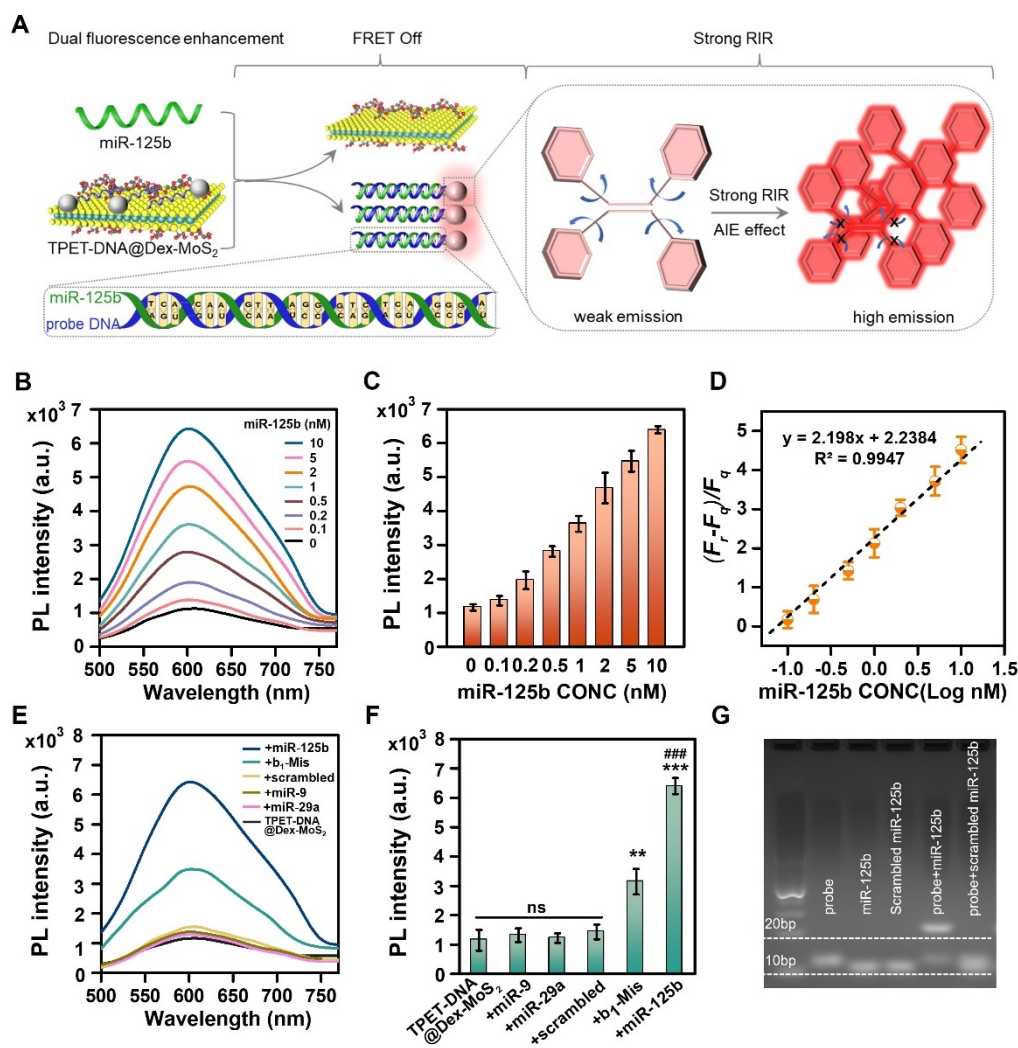


Figure 3.9 Detection of miR-125b *in vitro*. (A) Schematic illustrations of the working mechanism (dual fluorescence enhancement) of TPET-DNA@Dex-MoS₂ nanoprobe. (B) Photoluminescence spectra and (C) peak fluorescence intensity of TPET-DNA@Dex-MoS₂ after incubation with increasing miR-125b ranging from 0 to 10 nM. (D) Fitting logarithmic curve of TPET-DNA@Dex-MoS₂ nanoprobe against the different concentrations of miR-125b. F_q : fluorescence intensity of TPET-DNA@Dex-MoS₂ without adding target sequence, F_i : fluorescence intensity of probes after incubation with miR-125b. (E) Photoluminescence spectra and (F) peak fluorescence intensity of TPET-DNA@Dex-MoS₂ after incubation with miR-125b, scrambled miR-125b, one base mismatched miR-125b (b₁-Mis), miR-9 and miR-29a at a concentration of 10 nM. (G) Agarose gel electrophoresis of TPET-DNA@Dex-MoS₂ nanoprobe before and after incubation with target miR-125b and scrambled miR-125b.

In the following cellular experiments, we chose TPET-DNA@Dex-MoS₂ at 25 μ M to investigate its sensing behavior. After cellular uptake of the nanoprobe, both OA-treated cells and mimic-transfected cells showed intense cytosolic red fluorescent signals (Figure 3.11C and D). Furthermore, especially larger cytosolic punctate with a stronger signal was visualized in the cells treated with increased OA dosages, which was also validated by flow cytometric analysis (Figure 3.11E and F). These results indicated the successful detection of various levels

of endogenous miR-125b in living cells by TPET-DNA@Dex-MoS₂. Noticeably, although cells treated with OA of low-dose (10 nM) only increased their miR-125b level by 0.4-fold, the cytoplasmic fluorescence of the cells uptaking TPET-DNA@Dex-MoS₂ increased over 3.2-fold compared to the non-OA treated cells (Figure 3.11B and F). These results show that our nanoprobe can efficiently respond to low-level miR-125b aberrance, which occurs at the early stage of AD pathological progress [137, 138, 159]. Meanwhile, undetectable fluorescence signals were measured in untreated PC12 cells or miR-125b inhibitor-transfected cells with AD, where the expression of miR-125b was relatively weak (Figure 3.11D). Furthermore, replacing probing DNA with scrambled DNA in TPET-DNA@Dex-MoS₂ (TPET-scrDNA@Dex-MoS₂) also resulted in minimal cellular fluorescence signals (Figure 3.12). Thus, our miR-125b targeting nanoprobe enable sensitive and rapid detection of intracellular miR-125b with high selectivity in PC12 cells with AD progression.

Aberrant expression of miR-125b can alter tau phosphorylation to develop AD pathology. Specifically, we confirmed that p-tau was highly expressed and distributed throughout the cytoplasm of OA-treated cells and mimic-transfected cells while the transfection of miR-125b inhibitor significantly downregulated p-tau to a similar level as that in normal cells (Figure 3.11A-D). Besides, we discovered that the immunostaining signal of p-tau in these cells partially colocalized with the fluorescence of miR-125b labeled by our probes (Figure 3.11D). The line profile of cytoplasmic p-tau and miR-125b signals indicated a high spatial overlapping with the Manders' colocalization coefficients (MCC) of 0.875 (Figure 3.11G and H). Altogether, we demonstrate that TPET-DNA@Dex-MoS₂ can achieve efficient detection of miR-125b expression in the *in vitro* AD model.

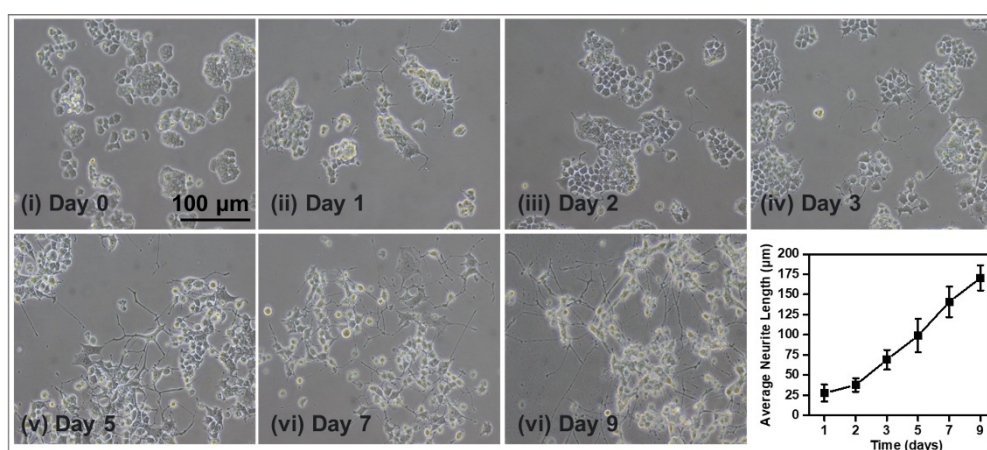


Figure 3.10 The differentiation of PC12 cells. The morphology of differentiated PC12 cells was recorded from day 1 to day 9. The change in average neurite length of the differentiated PC12 cells was calculated by ImageJ. Scale bar: 100 μm.

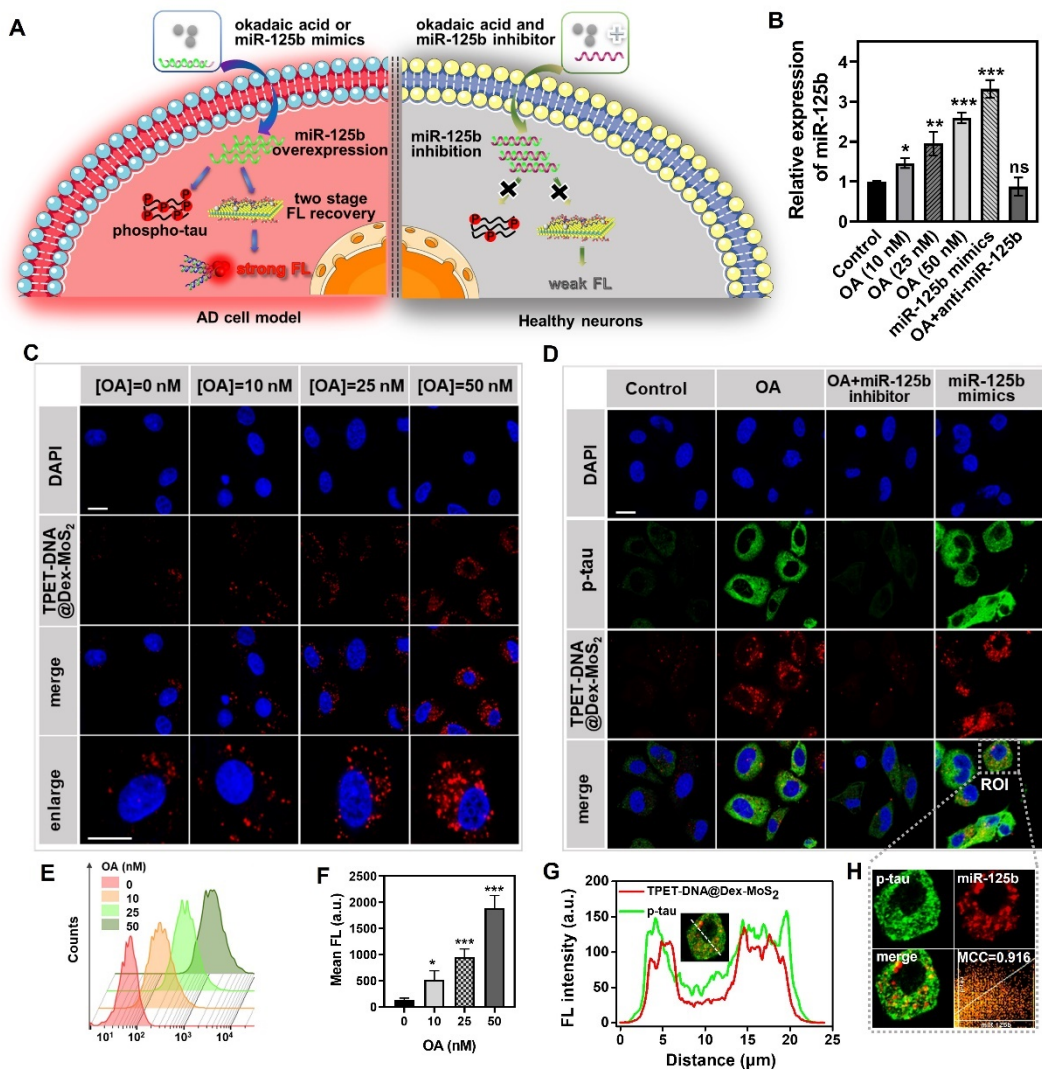


Figure 3.11 Intracellular detection of miR-125b. (A) Schematic illustrations of TPET-DNA@Dex-MoS₂ nanoprobes for the intracellular monitor of miR-125b. (B) The relative expression level of miR-125b in differentiated PC12 cells was tested by RT-PCR assays. (C) Representative confocal images of differentiated PC12 cells pretreated with OA of different concentrations (10, 25, and 50 nM) followed by incubation with TPET-DNA@Dex-MoS₂ nanoprobes (25 μM) for 6 h. (D) Representative immunofluorescence images of differentiated PC12 cells with different treatments followed by incubation with TPET-DNA@Dex-MoS₂ nanoprobes (red fluorescence). (E) Representative histogram plots of flow cytometry to quantify the intracellular fluorescence intensity of TPET-DNA@Dex-MoS₂ nanoprobes. (F) Corresponding mean fluorescence intensity of the flow cytometric analysis in (E). (G) The fluorescence intensity of p-tau (green) and TPET-DNA@Dex-MoS₂ (red) along the profile in the labeled ROI in (D). (H) The Mander's colocalization coefficients (MCC) were calculated by ImageJ used to quantify the colocalization of p-tau and TPET-DNA@Dex-MoS₂ in the cytoplasm.

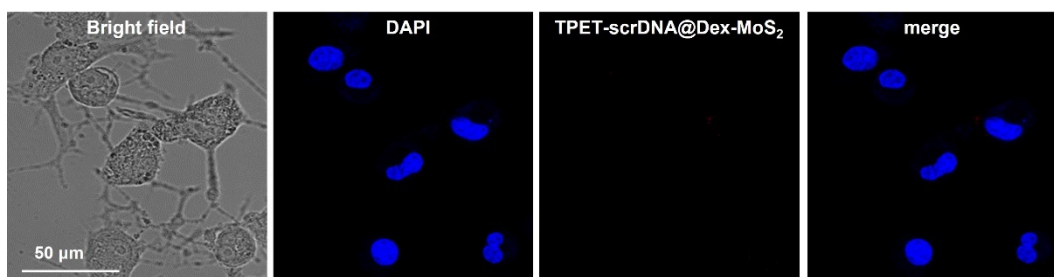


Figure 3.12 Confocal images of differentiated PC12 cells pretreated with OA followed by incubation with scrambled probes (TPET-scrDNA@Dex-MoS₂).

3.3.4 In vivo detection of miR-125b in an AD mouse model

We next investigated whether the TPET-DNA@Dex-MoS₂ nanoprobe was applicable to early AD diagnosis by monitoring miR-125b upregulation in a rodent AD model. To build this *in vivo* model, we stereotaxically injected OA into the lateral ventricle, a site involving prominent tau pathology [156]. After five days post-injection, p-tau was abundantly expressed throughout the brain, including the hippocampus and cortical layers (Figure 3.13A). Consistently, the expression of miR-125b was 1.8-fold higher in hippocampal and cortical tissues of mice with AD than those in wild-type mice (Figure 3.13B), thereby confirming the successful establishment of the *in vivo* AD model with miR-125b upregulation and tau hyperphosphorylation. Hence, we chose the time point, 5 days post AD model creation, for the following biosensing experiments.

We subsequently examined the efficacy of the nanoprobe for *in situ* and real-time detection of miR-125b in mice with AD. Thus, we performed a microinjection of TPET-DNA@Dex-MoS₂ into the same site as that with OA administration. We then evaluated the *in situ* fluorescent signals from our probes through a cranial window using an *in vivo* imaging system (IVIS). Almost all detectable signals were concentrated within the brain compartments (Figure 3.14C and E). In particular, the AD mice group exhibited a robust increase of the fluorescence intensity 0.5 h post-injection, and the signal reached the maximum at 4 h post-injection, indicating that the nanoprobe might require ~4 h for a complete diffusion to the reachable brain tissues with the signal enhancement upon detecting miR-125b (Figure 3.14C and D). Meanwhile, the fluorescent intensity slowly decreased after this time point (only ~10% drop of fluorescent signals from 4 to 24 h post-injection, suggesting a gradual clearance of the nanoprobe by circulation (Figure 3.14C and D) [160]. Although the wild-type mice group showed a similar trend of fluorescent changes to the AD mice group, its fluorescent intensity was overall ~1/6 of that in the AD mice group due to a much lower miR-125b level in the brain (Figure 3.14C and D). Furthermore, sham control (AD mice with saline injection) and AD mice with scrambled probes (TPET-scrDNA@Dex-MoS₂) illustrated negligible signals from their

brains (Figure 3.14E and F). In addition, *ex vivo* fluorescence images of major organs (brain, heart, lung, liver, kidney, and spleen) depicted the concentrated fluorescence signals in the brain area but nearly no detectable signal in our organs after 24 h post-injection, except for the liver that was responsible for the clearance and degradation of the circulated probes (Figure 3.14G and H) ^[108]. These *in vivo* imaging results confirmed the capability of TPET-DNA@Dex-MoS₂ for the effective and selective real-time detection of miR-125b with long retention in the AD model.

After *in vivo* bioimaging miR-125b expression in mice with AD, we harvested brain tissues to further validate the *in vivo* detection performance of the nanoprobes by histological analysis. Consistently, the red fluorescent signals of the nanoprobes in the hippocampus and cerebral cortex tissue slides in AD mice were 5.1-fold and 6.6-fold stronger than those in the wild-type mice, respectively (Figure 3.15). In contrast, we only observed negligible fluorescence in AD mice with saline or scrambled probes administration ((Figure 3.15A and B), verifying that the *in vivo* fluorescent signals derived from our nanoprobes upon specifically responding to miR-125b. We further question whether tau hyperphosphorylation may also spatially colocalize with the miR-125b in the brain with AD as the indirect index of their association. Hence, we measured the pixel intensities of paired fluorescent channels (green channel: p-tau, red channel: TPET-DNA@Dex-MoS₂) in the enlarged images (Figure 3.15D and F). Strikingly, the fluorescence punctate of p-tau and TPET-DNA@Dex-MoS₂ showed highly overlapping clusters according to the images, and the Manders' colocalization coefficients for the fractional overlap of p-tau with the signals of our nanoprobes were quantified to be 0.897 and 0.713 in hippocampus and cortex regions, respectively (Figure 3.15D, F, G, and H). These results are consistent with the *in vitro* study, suggesting a strong association between p-tau and miR-125b for AD progression. To the best of our knowledge, the spatial localization of miR-125b and p-tau in the *in vitro* and *in vivo* AD model has not been previously explored. Additionally, we evaluated the biosafety of TPET-DNA@Dex-MoS₂. The hemolysis assay showed that the TPET-DNA@Dex-MoS₂ nanoprobe of four concentrations (25 to 150 μ M) did not significantly cause hemolysis, supporting the satisfactory biocompatibility and biosecurity of our sensing platform (Figure 3.16).

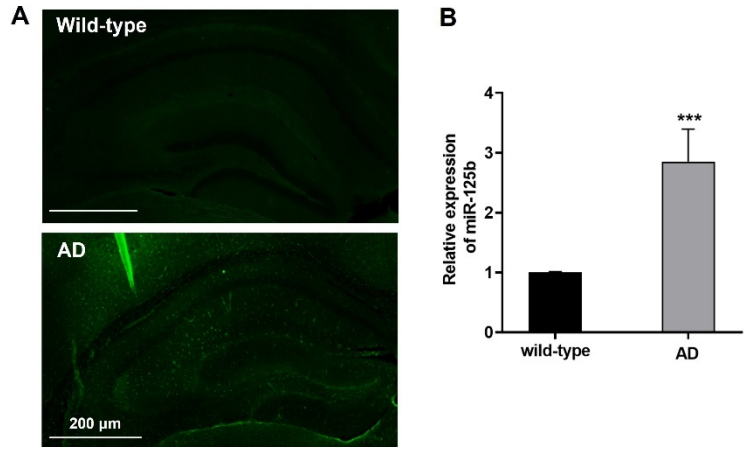


Figure 3.13 (A) Immunofluorescence staining with anti p-tau antibody (green) of brain slices from wild-type mice and OA-induced AD mice. Scale bar: 200 μ m. (B) RT-PCR to quantify the relative expression of miR-125b in the hippocampus and cortex area of brains from wild-type mice and OA-induced AD mice. Significance: *** p -value <0.001.

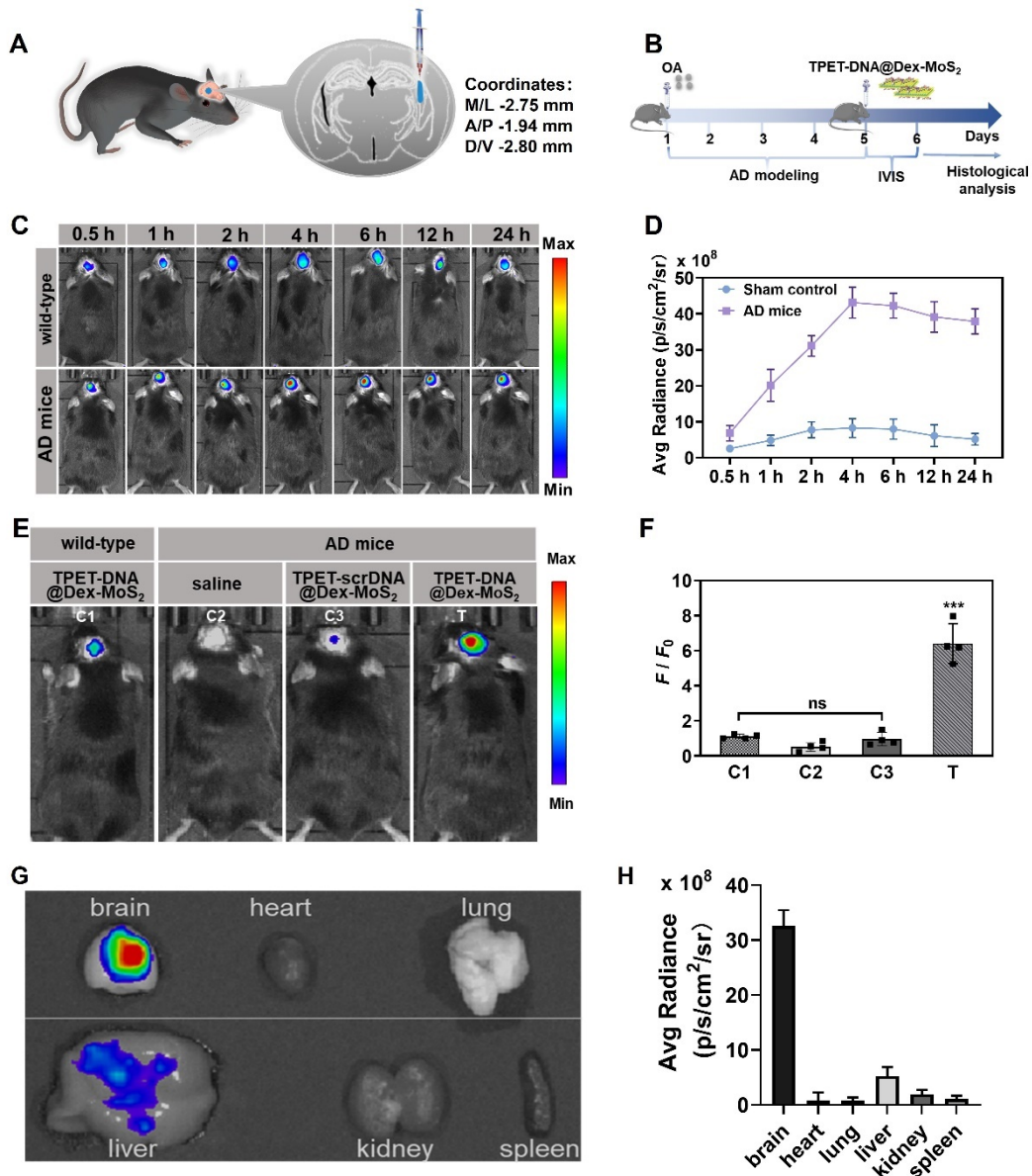


Figure 3.14 *In vivo* monitor miR-125b in the AD mice model. (A) Schematic illustrations of stereotaxic coordinates of the microinjection site. (B) Timeline in the animal experiments. (C) *In vivo* fluorescence images of wild-type mice (top row) and OA-induced AD mice (bottom row) were captured after being administrated with TPET-DNA@Dex-MoS₂ nanoprobe at various time points. (F) The average fluorescence intensity in the brain area in (D). (E) *In vivo* fluorescence images of wild-type mice and OA-induced AD mice were captured 4 h after being administrated with saline, TPET-scrDNA@Dex-MoS₂, or TPET-DNA@Dex-MoS₂ nanoprobe. (D) The fold change of fluorescence intensity in (C) was calculated by Living Imaging software. F_0 represents the signal intensity of wild-type mice in C1 group. F is the fluorescence of AD mice with different administrations. (G) *Ex vivo* fluorescence images of main organs of AD mice after being injected with TPET-DNA@Dex-MoS₂ for 24 h. (H) Quantification of fluorescence intensity in the organs by Living Image software.

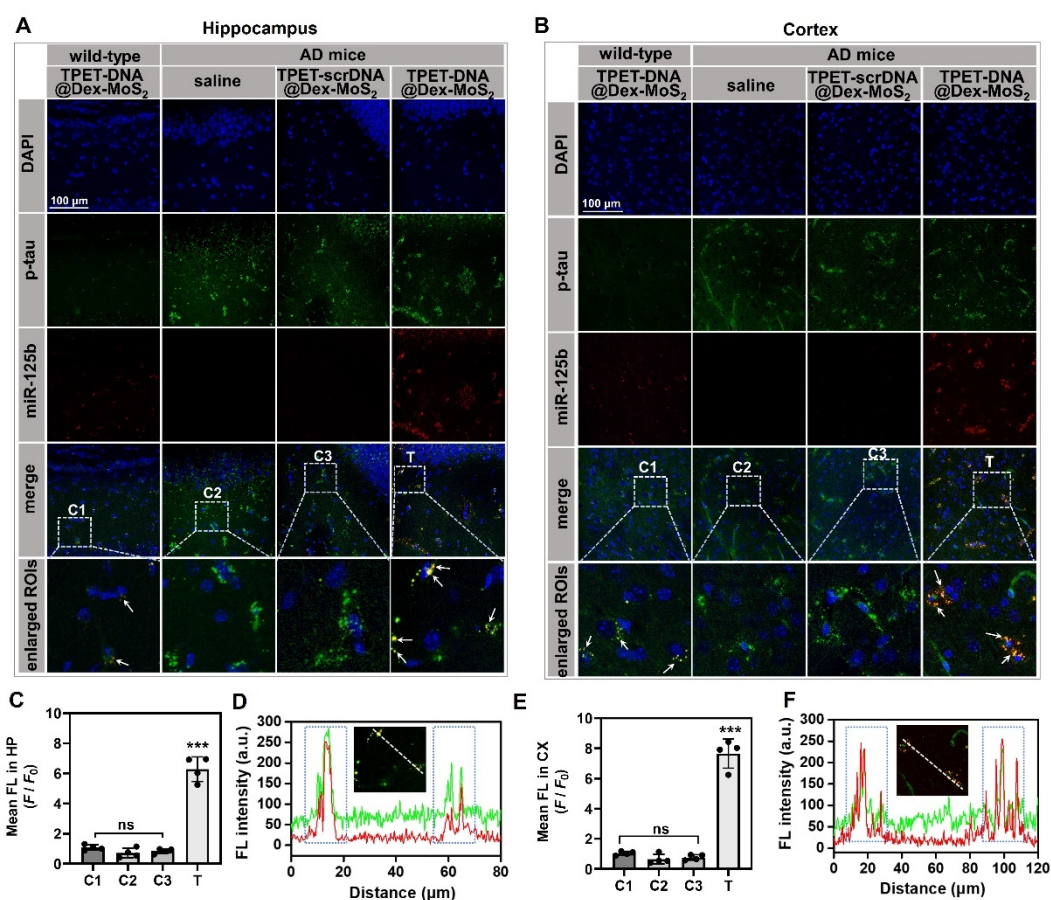


Figure 3.15 *Ex vivo* histological analysis. (A) hippocampus and (B) cortex regions of the brain slices from mice with different administrations were stained with p-tau antibody (green) and DAPI (blue). The white arrows labeled in the enlarged images indicated the sites overlapping between green and red fluorescence. The regions in the merged images labeled with the white dotted lines were shown in enlarged views. The average fluorescence intensity of TPET-DNA@Dex-MoS₂ nanoprobe in the (C) hippocampal and (E) cortical areas by ImageJ. The data indicate the mean fluorescence intensity from four independent experiments. The fluorescence intensity profile of p-tau (green) and TPET-DNA@Dex-MoS₂ nanoprobe (red) along the line in the inset image of (D) hippocampus and (F) cortex was analyzed by Leica LAS X software.

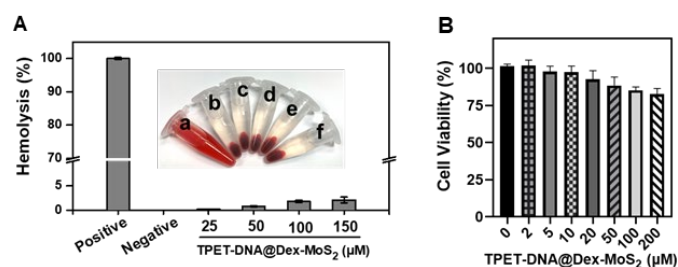


Figure 3.16 (A) Hemolysis assay of TPET-DNA@Dex-MoS₂ nanoprobe. Relative rate of hemolysis in mice RBCs upon incubation with (a) H₂O, (b) saline, and TPET-DNA@Dex-MoS₂ at a concentration of (c) 25, (d) 50, (e) 100, (f) 150 μM. (B) Relative cell viability of differentiated PC12 cells after being treated with various concentrations of TPET-DNA@Dex-MoS₂ for 24 h.

Name	Sequence (5' – 3')
probing DNA	NH ₂ -TCACAAGTTAGGGTCTCAGGGA
scrambled probing DNA	NH ₂ -GACGCTAAGTTACGCGGTTAAG
target miR-125b	UCCCUGAGACCCUAACUUGUGA
scrambled miR-125b	AUUGCCGCCAUAGUUGCCAACU
One base mismatched miR-125b	UCCCUGAGAGCCUAACUUGUGA
miR-9	TCATACAGCTAGATAACCAAAGA
miR-29a	TAACCGATTCAGATGGTGCTA
miR-125b primer	TCCCTGAGACCCTAACTTGTGA
U6 primer forward	GCTTCGGCAGCACATATACTAAAAT
U6 primer reverse	CGC TTC ACG AAT TTG CGT GTC AT

Table 6. The sequence information of DNA and RNA in this study.

3.4 Summary

In this work, we presented a biocompatible and efficient nanoplatfrom based on the combination of an AIEgen with a large stokes shift and effective 2D quencher, Dex-MoS₂, for *in situ* detection of the biomarker of OA-induced AD model, miR-125b *in vitro* and *in vivo*. We unravel the low sensitivity of single TPET-DNA for nucleic acid detection by introducing the concept of "dual on" fluorescent enhancement. The developed nanoprobe show excellent stability and selectivity to real-time detect the miR-125b sequence at picomolar levels in a complex environment of the AD model. In our future study, we aim to optimize this nanosensor for overcoming brain-blood barriers with a high tissue-penetrating ex/em spectrum for a more non-invasive diagnosis. Conceptually, we believe that our design provides a novel insight into the rapid detection of AD progression at the initial stage.

Chapter 4: Photosynthesis-mimic artificial nanoreactors for NIR-driven H₂ generation for AD treatment

4.1 Introduction

It is well-known that intracellular neurofibrillary tangles caused by hyperphosphorylation of tau protein are one of the most important pathological hallmarks of AD. Furthermore, oxidative stress and mitochondrial dysfunction are key factors in AD pathology. Hence, combinational nanotherapeutics that can scavenge excess ROS and inhibit tau hyperphosphorylation represent a promising therapeutic strategy for AD.

Since Dole and colleagues reported for the first time that hydrogen gas (H₂) as a therapeutic agent could slow down the proliferation of cancer cells in 1975, a large number of studies on the application of H₂ for antioxidant, anti-inflammatory, anti-apoptotic, anti-tumor, anti-atherosclerotic, and systemic immune responses have gradually appeared^[99, 161]. Hydrogen therapy has many benefits compared to conventional chemical drugs, including low cost, good biosafety, no significant side effects, and strong bio-diffusion across biological membranes due to its tiny size and non-polar nature^[162]. As of now, the three main methods of administering hydrogen therapy are inhalation of hydrogen, injection of hydrogen-rich saline, oral administration of hydrogen-rich water, and hydrogen prodrugs^[99, 101]. Among them, hydrogen prodrugs exert their therapeutic effect by releasing hydrogen in the body, which ensures the concentration of hydrogen to improve the therapeutic effect. However, most common hydrogen prodrugs, such as calcium hydride and magnesium, are unstable in the physiological buffer, making it difficult to regulate the targeted release of hydrogen at the site of the lesion^[163, 164]. Therefore, it is urgent and essential, but still challenging, to achieve *in situ* continuous generations of H₂ to improve the therapeutic outcome. In recent reports, photocatalytic hydrogen production is emerging as a new therapeutic strategy^[115, 165, 166]. Compared with the chemical decomposition of hydrogen, the therapeutic approach based on photocatalytic hydrogen production has some incomparable advantages, such as the high efficiency of *in situ* hydrogen yield and the ease of controlling the rate of hydrogen release, which facilitate the application of hydrogen for the treatment of chronic diseases such as AD.

Inspired by natural photosynthesis, we report herein an artificial nanoreactor that mimics the structure and light-harvesting function of a natural photosynthetic system for hydrogen evolution. The photo-responsive nanoreactor, named as (Chl a +Ind) NRs, contains platinum nanoparticles (Pt NPs) as catalysts and ascorbic acid as sacrificial agent protected by robust cross-linking vesicles (cVs), which comprise two photosensitizers chlorophyll *a* (Chl a) and

indoline dye (Ind) and is coupled to the surface of upconversion nanoparticles (UCNPs) (Figure 4.1) [115, 167, 168]. Near-infrared (NIR) light has higher tissue penetration and lower phototoxicity than UV or visible light. In this work, we choose NIR-excited UCNP as a donor fluorophore and two photosensitizers as acceptor fluorophores for photosynthesizing hydrogen. Upon NIR laser irradiation (980 nm), the red and green upconversion luminescence was absorbed by Chla and Ind, respectively. The excited electrons separated from Chla* and Ind* were quickly transferred to Pt NPs to combine with the proton from ascorbic acid to generate hydrogen.

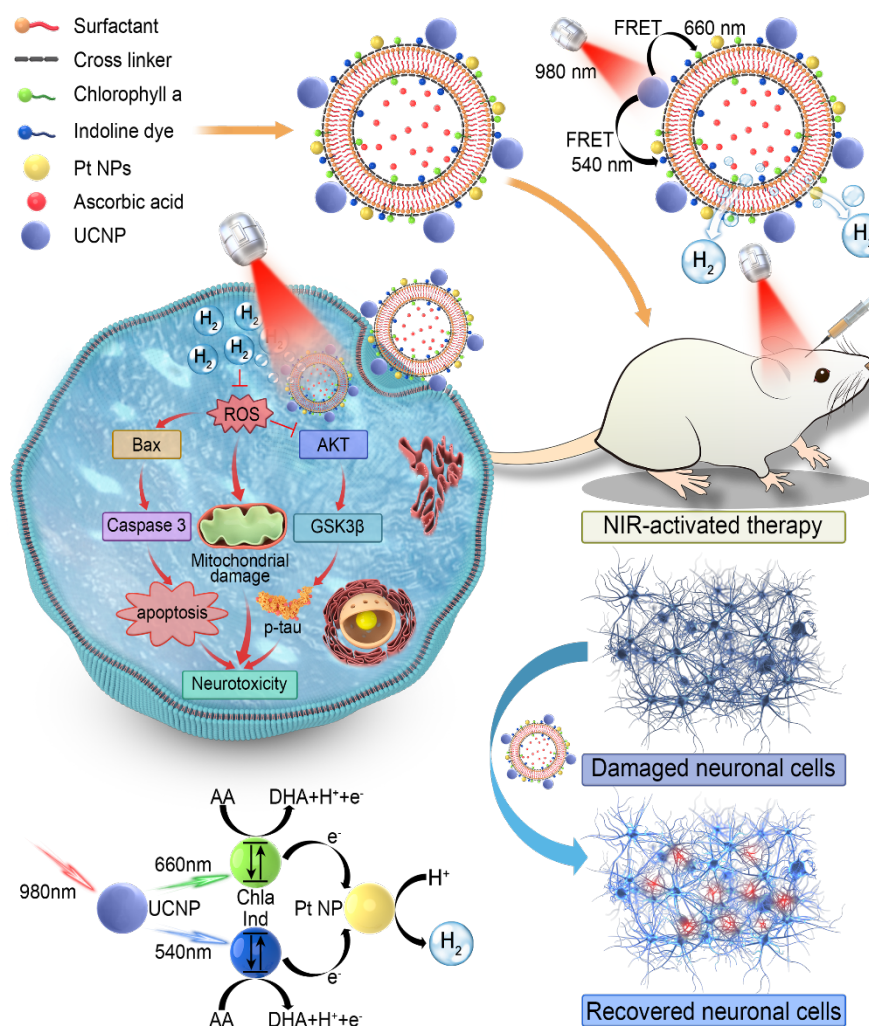


Figure 4.1 Schematic diagram illustrating the preparation of (Chla+Ind)NRs and NIR-triggered *in situ* release of H₂ from (Chla+Ind)NRs to scavenge ROS, alleviate mitochondria damage, and reduce tau hyperphosphorylation for AD therapy.

4.2 Methodology

4.2.1 Synthesis of UCNPs

To synthesize UCNPs (NaYF₄:Er/Yb), YCl₃·6H₂O (1.56 mmol), YbCl₃·6H₂O (0.4 mmol), ErCl₃·6H₂O (0.04 mmol), oleic acid (15 mL) and 1-octadecene (30 mL) were successively added to a 100 mL three-necked flask and then kept it at room temperature for 1 h before being

gradually heated to 120 °C under the protection of the nitrogen. Then, the mixture solution was kept at 156 °C for ~1 h while stirring. After a uniform translucent yellow solution was observed, the nitrogen was pumped into the system, and the reactants were gradually cooled to ambient temperature. After that, NH₄F (8 mmol) and NaOH (5 mmol) were prepared in 10 ml of methanol solution, immediately injected into the reaction solution from the previous step, and stirred for 2 h at room temperature. Subsequently stirring for 2 h at room temperature, the mixture was slowly heated to evaporate methanol and then maintained at 290 °C for 1.5 h, then slowly cooling down to room temperature. The reaction solution was then transferred from the flask to a centrifuge tube containing 20 ml of ethanol and centrifuged at 8000 rpm/min for 10 min. The product was obtained by collecting and resuspending the precipitate in cyclohexane for storage.

The UCNPs obtained from the above step with oleic acid capped were dispersed in 5 mL of cyclohexane and mixed with 5 mL of an aqueous solution. Then, hydrochloric acid solution (HCl, 0.5 M) was added to the mixture to maintain the pH value at 3 and stirred at room temperature for 12 h. After the reaction, the water-dispersible fraction was recovered by centrifugation after precipitation with acetone. Finally, the product was redispersed in acetone, and oleate-free UCNPs were reacquired by centrifugation and dispersed in H₂O.

4.2.2 Preparation of (Chla+Ind) cVs

First, the synthetic routes to the surfactant and crosslinker used to prepare cross-linked vesicles followed the previous report [168]. Then crosslinker 1 (16.0 mg, 0.02 mmol) and lauryl amine (3.6 mg, 0.02 mmol) were mixed into 50.0 μL of dimethyl sulfoxide (DMSO) at room temperature. After waiting for 12 h for the counterion to stabilize, photosensitizers Chla (0.004 mmol) and Ind (0.004 mmol) were added, followed by dropwise addition to the aqueous solution containing ascorbic acid (100 mM) under the vortex at room temperature to form vesicles. After the addition of excess crosslinker 2 (0.08 mmol) and 2-Hydroxy-4'-(2-hydroxyethoxy)-2-methylpropiophenone (PI 2959, 2.24 mg/mL in CH₃OH, 20 μL, 0.0002 mmol), cross-linked vesicles were obtained under irradiated in a rayonet photoreactor for 30 min until most alkyne groups were consumed. Meanwhile, the excessive cross-linker agent will enrich sulfhydryl groups on the surface of cross-linked vesicles. The reactants were then dialyzed against Millipore water using 2 kDa MWCO tubes to obtain (Chla+Ind) cVs. The other two single photosensitizer-loaded cVs, Chla cVs, and Ind cVs were prepared by the same method except for added Chla or Ind, respectively

To determine the loading content of ascorbic acid (AA), Chla, and Ind, an aliquot of AA-containing vesicle solution was dissolved in acetone for UV-Vis spectroscopy measurement.

The loading content of the vesicles was determined as the following equation: loading content (%) = $(W_{AA}/W_{AA\text{-loaded vesicles}}) \times 100$. According to the standard calibration curves, the loading content of the AA, Chla, and Ind was calculated as ~15.3%, ~3.5%, and ~3.6%, respectively.

4.2.3 Preparation of (Chla+Ind)cVs@Pt

Chloroplatinic acid (H_2PtCl_6 , 1.6 mg, 0.004 mmol) and sodium borohydride ($NaBH_4$, 3 mg, 0.08 mmol) were added to the above cross-linked vesicle solution, and the Pt NPs generated by continuous stirred 2 h to obtain stable dispersion of Pt NPs to attach the surface of cross-linked vesicles. The resulting solution was then dialyzed against Millipore water using 2 kDa tubes to obtain (Chla+Ind) cVs@Pt as a brownish transparent solution. The prepared (Chla+Ind) cVs@Pt was characterized by various techniques, including dynamic light scattering (DLS), transmission electron microscopy (TEM), elemental mappings, confocal laser scanning microscopy (CLSM), and UV-Vis absorption measurements.

4.2.4 Fabrication of (Chla+Ind) NRs

Briefly, (Chla +Ind) cVs@Pt (10 mg) was mixed with UCNPs (1 mg). Briefly, (CHI+Ind)cVs@Pt (10 mg) was mixed with UCNPs (1 mg), and then the mixture was stirred overnight at room temperature to obtain (Chla +Ind) cVs@Pt@UCNPs (named as “(CHI+Ind) NRs”). The extra UCNPs were then separated by centrifugation at 3000 rpm for 10 min. Finally, the purified (CHI+Ind)NRs were redispersed in PBS for the following assays.

4.2.5 Stability assay of (Chla+Ind) NRs

The critical micelle concentration (CMC) of surfactants was determined to be 57 μ M. Hence, (Chla +Ind) NRs were diluted to 57 μ M to evaluate colloidal stability. Briefly, DLS measurement was performed to continuously monitor the size of (Chla+Ind) NRs at a concentration of 57 μ M to determine their stability. Furthermore, we also investigated the stability of (Chla +Ind) NRs by incubating them with 10% FBS. First, FBS (1 mL) was mixed with (Chla +Ind) NRs (10 mM, 9.0 mL) and incubated at 37°C. Then, DLS was used to record the size of nanoreactors after 0 h, 12 h, and more than 24 h.

4.2.6 Catalytic activity of (Chla+Ind) NRs

A solution in 10 ml PBS buffer containing H_2O_2 (30 μ M) and various concentrations of (Chla+Ind) NRs was incubated for 20 min at room temperature. Then 5 ml of molybdate solution (2.5 mM) was added to the mixture, reacting with H_2O_2 to form a substrate-stabilized complex. The relative activity of catalase was estimated by the absorbance of the complex at 400 nm. The H_2O_2 elimination rate was calculated according to the following formula: H_2O_2

elimination (%) = $[(A_0 - A)/A_0] \times 100$, where A_0 is the absorbance of the [H₂O₂+ammonium molybdate], and A is the absorbance of the [nanoreactors+H₂O₂+ammonium molybdate]. The dissolved O₂ concentration was detected with a dissolved oxygen meter.

4.2.7 Ultrasound imaging of (Chla+Ind) NRs

The photo-responsive characteristics of Chla NRs, Ind NRs, and (Chla+Ind) NRs solution in glassware were studied by observing their effectiveness in photosynthesizing H₂ gas bubbles in the presence of laser irradiation (980 nm, 1 W/cm²). The H₂ gas bubbles were observed by an ultrasound imaging system with a 5 MHz linear array transducer (Z-one, Zonare, Mountain View, CA, USA).

4.2.8 Measurement of H₂ release from (Chla+Ind) NRs

Methylene blue (MB) was used as an indicator to *in vitro* indirectly detect H₂ generated from the Chla NRs, Ind NRs, and (Chla+Ind) NRs. According to Beer's law, the absorbance peak of MB at 665 nm shows a linear decrease in relation to the amount of hydrogen produced. First, (Chla+Ind) NRs (final 100 µg/mL) were prepared and added to MB solution (final 10 µg/mL) in the quartz glassware, then start laser irradiation (980 nm, 1 W/cm²). The absorbance at 665 nm was monitored every few minutes by a UV-Vis spectrophotometer. Then, the standard curve of MB solutions at a series of concentrations was measured to quantify the generation of hydrogen based on the decrease of absorbance at 665 nm.

4.2.9 Cytotoxicity and biocompatibility of (Chla+Ind) NRs

The neuron-like rat pheochromocytoma cell lines (PC12) were used to assess the biocompatibility of Chla NRs, Ind NRs, and (Chla+Ind) NRs. Firstly, PC12 cells were seeded in 96-well plates at the density of 1×10^4 /well for 24 h and then incubated with Chla NRs, Ind NRs, and (Chla+Ind) NRs at various concentrations (10, 20, 50, 100, 200, 500 µg/mL). After further 24 h culture, cell viability was measured using an MTT assay. For cellular uptake assay, PC12 cells were seeded in confocal dishes at a density of 1×10^5 before being incubated with nanoreactors (Chla NRs, Ind NRs, (Chla+Ind) NRs, 100 µg/mL) for 12 h. Next, the cells were stained with DAPI to label the cell nuclei, followed by observing under the Leica SP8 confocal microscope (green UCL: $\lambda_{ex}/\lambda_{em} = 980/540$ nm, red UCL: $\lambda_{ex}/\lambda_{em} = 980/660$ nm).

4.2.10 Measurement of intracellular ROS levels

PC12 cells were seeded in confocal dishes for 24 h and then treated with OA (100 nM) for 12 h before being incubated with nanoreactors (100 µg/mL) for a further 12 h, followed by 980 nm laser irradiation (0.5W/cm², 20 min). At the end of the cell culture, the cells were then incubated with DCFH-DA (5 µM) in Opti-MEM medium at 37 °C for 15 min before being

observed under the confocal microscope ($\lambda_{ex} = 488 \text{ nm}$, $\lambda_{em} = 500\text{-}530 \text{ nm}$). The flow cytometry was also applied to quantify the intracellular fluorescence intensity of DCFH-DA ($\lambda_{ex}/\lambda_{em} = 488/530 \text{ nm}$). All the flow cytometry data were analyzed with FlowJo V10.8 (FlowJo, USA).

4.2.11 Cell apoptosis

PC12 cells were firstly cultured in 6-well plates overnight and then replaced with a full medium containing okadaic acid (OA) at a concentration of 100 nM for a further 12 h, followed by incubation with Chla NRs, Ind NRs, or (Chla+Ind) NRs (100 $\mu\text{g}/\text{mL}$) for 12 h followed by 980 nm laser irradiation (0.5W/cm², 20 min). Then the treated cells in each group were collected to stain with Annexin V-FITC and PI to evaluate the early apoptosis rate (Annexin V-FITC⁺/PI⁻) and late apoptosis rate (Annexin V-FITC⁺/PI⁺). The fluorescence intensity of Annexin V-FITC and PI was measured by an Accuri C6 flow cytometer.

4.2.12 Western blot

Following completion of the different treatments for each setting, total protein was extracted by lysing cells with 0.5 ml of RIPA buffer containing 1% protease inhibitor for 30 min on ice. The concentration of proteins in each group was then measured with the BCA assay kit and adjusted to 4 $\mu\text{g}/\mu\text{l}$. Then, proteins were heated with SDS-PAGE denaturing buffer at 95°C for 10 min. For the western blotting, the deformed protein was separated on 10% SDS-PAGE gel and then transferred to a PVDF membrane. The membrane was blocked with 1% BSA buffer for 1 h at room temperature before incubating with primary antibodies at 4 °C overnight. The dilution of primary antibodies (e.g., p-tau, Bax, cleaved-Caspase 3, AKT, p-AKT, GSK3 β , and p-GSK3 β) was 1:1,000, except 1:5,000 of β -actin. Next, the membrane was incubated with horseradish peroxidase-conjugated secondary antibodies for 2 h at room temperature, then visualized using enhanced chemiluminescence (ECL) reagents.

4.2.13 Animals modeling and stereotaxic injections

All the animal experiments were performed in compliance with ethical approval from the institutional animal ethics committee of the Hong Kong Polytechnic University. An AD mouse model was created by administering okadaic acid to wild-type C57BL/6 mice simulating for 2 weeks. Before the surgical procedure, mice were anesthetized by intraperitoneal injection of ketamine and xylazine and held on a stereotaxis instrument with ear bars. OA (100 ng in 2 μL saline) was then microinjected into the hippocampus (coordinates: AP -2.18 mm, ML -2.20 mm, DV -2.50 mm) with an infusion rate of 150 nL/min^[156]. The scalp wound was then sutured with surgical silk and intraperitoneally injected with penicillin for 3 days to prevent infection.

Mice with OA and saline injection were regarded as AD model and sham control groups, respectively. In this study, all the mice were divided into 8 groups of 4 mice each: sham, OA, OA+NIR, OA+CVs-Pt-UCNP, OA+(Chl α +Ind) NRs, OA+Chl α NRs+NIR, OA+Ind NRs+NIR, OA+(Chl α +Ind) NRs+NIR. After 10 days of OA injection, the AD mouse model was successfully established. The nanoreactors (0.5 mg/mL, 2 μ L) were then microinjected into the intracerebral according to the previous coordinates. After 2 h of injection, the laser irradiation groups were exposed to 980 nm laser at 0.5 W/cm² for 20 min (3 min-on and 2 min-off), which would not cause undesirable thermal damage. The laser irradiation was implemented twice each day. During laser irradiation, the eyes of mice were covered with aluminum foil to avoid interference from the visible guide light. In addition, the distance between the laser tip and the mice's scalp was appropriately adjusted to prevent cortical damage caused by excessive heat.

To track the retention in the brain after nanoreactors administration, the nanoreactors were labeled with IR780 to offer strong fluorescent signals for *in vivo* imaging. The images were collected at different time points by *in vivo* fluorescence imaging system (IVIS® Spectrum III PerkinElmer) ($\lambda_{ex}/\lambda_{em} = 780/810$ nm). After *in vivo* imaging for 3 days, the major organs (brain, kidney, heart, liver, spleen, and lung) were collected for *ex vivo* fluorescence imaging. Imaging data were analyzed with IVIS Living Image 2.0 software (PerkinElmer).

4.2.14 Y maze test

After completing all the treatments, mice were subjected to a Y-maze test. The Y-maze consists of three identical arms, artificially defined as the starting arm, the novel arm, and another arm. The Y-maze test was divided into a training phase and a testing phase. During the training phase, the novel arm was kept closed, and mice were allowed to explore freely in the starting arm and the other arm. Two days after training, mice participated in a test phase in which they were allowed to explore freely in all three arms. The spatial memory ability of mice was assessed by analyzing parameters such as the number of entries into the novel arm, the duration in the novel arm, and routes in the Y maze.

4.2.15 Histological tissue preparation and immunocytochemistry

The mice were sacrificed for *ex vivo* experiments. They were perfused with PBS and fixed in 4% PFA for 2 days. Then, the brain tissues were dissected into 20- μ m thick coronal slices using a vibratome. The brain sections were stained with DCFH-DA to indicate the ROS level and analyzed by immunohistochemistry using the p-tau-specific antibody. Briefly, brain sections were incubated with anti-p-tau antibody (Ser396 1:500) at 4 °C overnight, followed by Alex Flour 635-conjugated secondary antibody (1:500) at 37 °C for 2 h. Finally, after being

stained with DCFH-DA and DAPI, brain slices were cover-slipped for observation under the fluorescence microscope. The positive signal in each section was analyzed by ImageJ software.

4.3 Results and Discussion

4.3.1 Fabrication and characterization of (Chl*a*+Ind) NRs

The preparation process of the (Chl*a*+Ind) NRs is illustrated in Figure 4.2A. First, Chl*a* and Ind were introduced as photosensitizers into the surfactants solution and then dropped into an aqueous solution containing ascorbic acid (AA) to form vesicles by self-assembly. The hydrophobic photosensitizer was embedded in the shell layer of the vesicles, while the water-soluble AA was encapsulated inside the hydrophilic cavity of the vesicles. After adding a thiol-bearing cross-linker and a micrphotoinitiator (PI 2959), cross-linked vesicles (Chl*a*+Ind) cVs were obtained by the reaction between alkynyl groups on the vesicles' surface with the thiol groups of the cross-linker under UV illumination. Then, the platinum nanoparticles (Pt NPs) generated by the reduction of chloroplatinic acid were attached to the surface of (Chl*a*+Ind) cVs to fabricate (Chl*a*+Ind) cVs@Pt depending on the interaction of Pt and O. The DLS measurement showed (Chl*a*+Ind) cVs@Pt with an average hydrodynamic diameter of ~180 nm, which was a little larger than the particle size observed by TEM images at ~110 nm (Figure 4.2 B-C). The black nanodots on (Chl*a*+Ind) cVs@Pt in the TEM images were suggested as protected Pt NPs (Figure 4.2C). For further confirmation, the element mapping analysis of (Chl*a*+Ind) cVs@Pt indicated the distribution of Pt element throughout the whole vesicles (Figure 4.2D). In addition, X-ray photoelectron spectroscopy (XPS) spectra revealed that the Pt 4f7/2 and 4f5/2 doublet with binding energies of 72.1 and 76.2 eV were regarded as zerovalent Pt (Figure 4.2E).

As a photosynthesis-mimic artificial nanoreacting system, (Chl*a*+Ind) NRs employed NIR-excited UNCPS as the light source to achieve photocatalytic hydrogen generation. In this study, to avoid surface quenching effects, we used core-shell structures UNCPS conjugated on the surface of cVs through strong thiol-metal interactions to construct (Chl*a*+Ind) NRs. The TEM images demonstrated the successful attachment of UNCPS onto the surface of nanoreactors (Figure 4.2F-G).

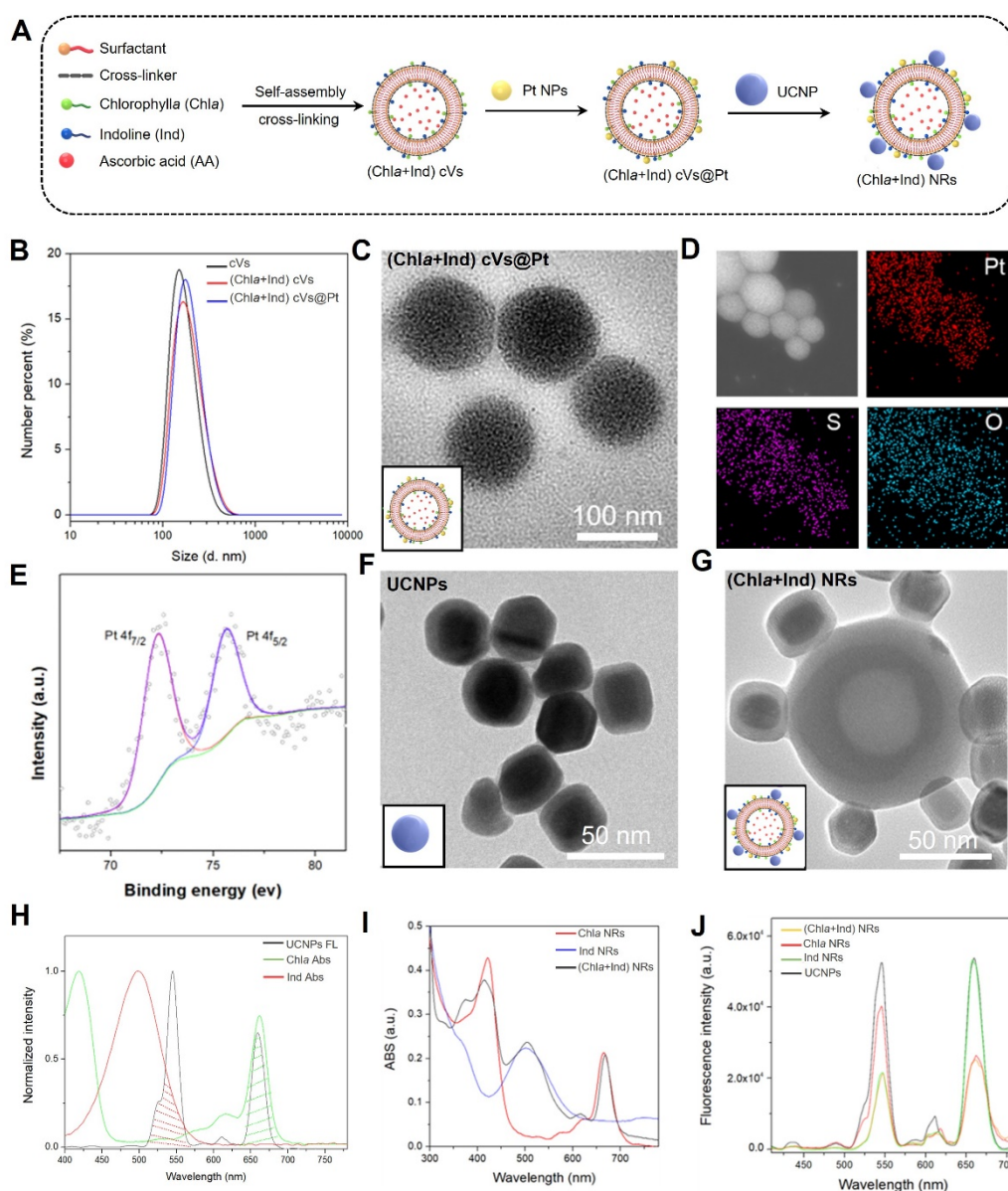


Figure 4.2 The fabrication and characterization of (Chla+Ind) NRs. (A) Schematic illustration of fabrication procedures of (Chla+Ind) NRs fabrication. (B) Size distribution of cVs, (Chla+Ind) cVs, (Chla+Ind) cVs@Pt. (C) TEM images of (Chla+Ind) cVs. (D) TEM elemental mappings of Pt, O, and S of (Chla+Ind) cVs. (E) High-resolution XPS spectra of Pt 4f in (Chla+Ind) cVs. (F) TEM images of UCNPs. (G) TEM images of (Chla+Ind) NRs. (H) Normalized UV-vis absorption spectra of Chl and Ind with upconversion luminescence spectra of UCNP under NIR excitation. (I) UV-Vis spectra of Chla NRs, Ind NRs, and (Chla+Ind) NRs. (J) Upconversion luminescence spectra of UCNP, Chla NRs, Ind NRs, and (Chla+Ind) NRs under NIR excitation.

The UCNP emitted green and red upconversion fluorescence under 980 nm laser irradiation, extensively overlapping with the absorption spectrum of Ind and Chla, respectively (Figure 4.2H). In order to compare the efficiency of light harvesting and conversion, we also prepared Chla-loaded nanoreactors (Chla NRs) and Ind-loaded nanoreactors (Ind NRs). The UV-Vis absorbance spectra of Chla NRs, Ind NRs, and (Chla+Ind) NRs were recorded (Figure

4.2I). As expected, the absorption peaks of Chla NRs were located at 660 nm and 410 nm, absorbing the red fluorescence of UCNP and Ind NRs exhibited an absorption peak at 540 nm, corresponding to the green fluorescence of UCNP. While the dual photosensitizers loaded nanoreactors (Chla+Ind), NRs had these three absorption peaks, which would support their higher efficiency of light harvesting (Figure 4.2I). The capability of three types of nanoreactors to capture light was compared by measuring the upconversion luminescence spectrum of the UCNP, Chla NRs, Ind NRs, and (Chla+Ind) NRs under excitation with 980 nm laser (Figure 4.2J). The results showed that Chla NRs and Ind NRs exhibited a significantly decreased fluorescence intensity at 660 nm and 540 nm compared with the emission spectrum of pure UCNP, indicating the efficient energy transfer from UCNP to Chla NRs and Ind NPs. Remarkably, the fluorescence intensity of (Chla+Ind) NRs was more drastically reduced in red and green regions, suggesting a simultaneous capture of energy from UCNP to both Chla and Ind.

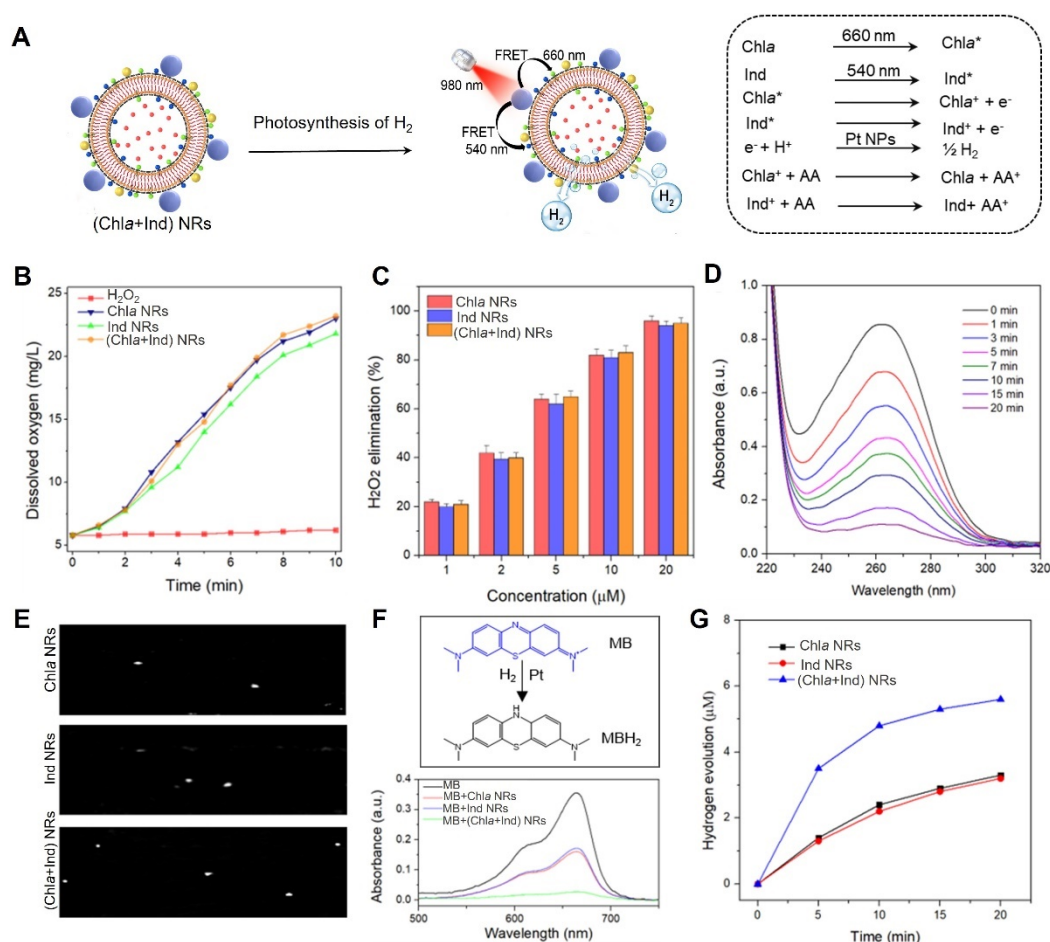


Figure 4.3 Photocatalytic hydrogen release by (Chla+Ind) NRs. (A) Schematic illustration of photocatalytic hydrogen release by (Chla+Ind) NRs. (B) Dissolved oxygen-time course curves of H₂O₂. (C) Dependence between the elimination of H₂O₂ and concentrations of (Chla+Ind) NRs. (D) Absorbance changes of AA in (Chla+Ind) NRs solution after various periods of laser irradiation. Background interference has been subtracted. (E) Ultrasound images of hydrogen

bubble generation in the *Chla* NRs, Ind NRs, and (*Chla*+Ind) NRs solution following laser irradiation. (F) Top: The reaction mechanism of MB hydrogenation for detecting hydrogen. Bottom: UV–visible absorbance spectra of (*Chla*+Ind) NRs in the MB solution with laser after 10 min. (G) Quantitative analysis of reductive hydrogen release profile of *Chla* NRs, Ind NRs, and (*Chla*+Ind) NRs solution using MB as a hydrogen probe.

4.3.2 Efficiency of photocatalytic hydrogen release by (*Chla*+Ind) NRs

The reaction process for NIR-triggered photocatalytic hydrogen release by (*Chla*+Ind) NRs is illustrated in Figure 4.3A. To confirm the catalytic activity of the vesicle-protected Pt NPs, we investigated the elimination of H_2O_2 by the nanoreactors by monitoring the dissolved oxygen in an aqueous solution (Figure 4.3B). The results revealed that the dissolved oxygen gradually increased after the addition of *Chla* NRs, Ind NRs, and (*Chla*+Ind) NRs, indicating that vesicle-protected Pt NPs could catalyze H_2O_2 to produce oxygen. As shown in Figure 4.3C, the catalytic activity of *Chla* NRs, Ind NRs, and (*Chla*+Ind) NRs for H_2O_2 consumption was in a dose-dependent manner, and 97% of the H_2O_2 was cleared when the concentration of three nanoreactors reached at 20 μM , suggesting the excellent catalytic performance of Pt NPs in the artificial nanoreacting system. Depletion of AA is an essential procedure for photocatalytic H_2 production by our nanoreactors (Figure 4.3A). Hence, we monitored the consumption of AA during photosynthesis by measuring the change in UV-vis absorption spectra of (*Chla*+Ind) NRs during NIR laser irradiation. The results exhibited a progressive drop of the absorption band at 260 nm with longer irradiation time, confirming that AA was depleted in photosynthetic hydrogen production (Figure 4.3D). In addition, photocatalytic hydrogen bubbles could be viewed by the ultrasound imaging system (Figure 4.3E). After laser irradiation for 3 min, H_2 gas bubbles were observed in the *Chla* NRs, Ind NRs, and (*Chla*+Ind) NRs solution, and (*Chla*+Ind) NRs produced more gas bubbles (Figure 4.3E). Furthermore, the efficiency of the three nanoreactors to produce hydrogen was confirmed by a methylene blue (MB) probe. Here, blue MB can be reduced to colorless MBH_2 by hydrogen gas in the presence of Pt NPs as catalysts. Therefore, the absorbance of the MB probe at 665 nm could indirectly indicate the efficiency of H_2 generation. As depicted in Figure 4.3F, the addition of *Chla* NRs, Ind NRs, and (*Chla*+Ind) NRs to MB solution resulted in a significant decrease in the absorbance of the MB probe at 665 nm under NIR laser irradiation. We measured the standard curves according to different concentrations of MB versus their absorbance at 665 nm and further quantified the hydrogen release from *Chla* NRs, Ind NRs, and (*Chla*+Ind) NRs with different laser irradiation duration. The results confirmed that the hydrogen release of (*CHI*+Ind) NPs was higher than that of *Chla* NRs and Ind NRs and approached the maximum after being irradiated for 20 min (Figure 4.3G).

4.3.3 (Chla+Ind) NRs scavenge intracellular ROS

To verify whether (Chla+Ind) NRs could scavenge the ROS at the cellular level, the rat neuroendocrine cell line PC12 was selected in this study to establish the AD cell model. We first examined the cellular uptake behavior of the nanoreactors. The fluorescence images showed that the green and red upconversion luminescence (UCL) of UCNP in Chla NRs, Ind NRs, and (Chla+Ind) NRs was strongly distributed in the cytoplasm, which indicates that the NRs were largely endocytosed into cells after 6 h co-incubation (Figure 4.4A). Efficient cellular uptake and internalization of the NRs would be favorable for their therapeutic effects. We then explored the cytotoxicity of Chla NRs, Ind NRs, and (Chla+Ind) NRs. Relative viability higher than 85% was found in PC12 cells after being treated by our nanoreactors at different concentrations, indicating that the as-prepared NIR photocatalytic nanoreactors were nearly no toxic effect on cell activity (Figure 4.4B).

Moreover, we investigated the effect of the (Chla+Ind) NRs on the intracellular ROS levels and mitochondria functions in the presence of NIR irradiation. First, okadaic acid (OA) was used to treat PC12 cells for a tauopathy cell model accompanied by hyperphosphorylation of tau and overproduction of intracellular ROS levels^[98]. PC12 cells were treated with okadaic acid (OA) at 100 nM for 12 h to induce the aberrant ROS upregulation^[169]. Then, continuous ROS monitoring demonstrated that our nanoreactors under NIR irradiation rapidly caused the visible fall of intracellular ROS level in a power density- and dosage-dependent way. In contrast, the absence of NIR irradiation had no discernible effect on ROS level (Figure 4.4C). Notably, the intracellular ROS level continued to decline even after NIR irradiation was stopped, showing that the removal of cytotoxic $\cdot\text{OH}$ by the bioactive H_2 generated by photocatalytic nanoreactors lasted a long period of up to 4 h (Figure 4.4C). We also observed that the intracellular ROS, indicated by the green fluorescence of DCFH-DA, was much lower in the cells with (Chla+Ind) NRs treatment under NIR irradiation than that with Chla NRs and Ind NRs under the condition, suggesting that the ROS scavenging capacity of nanoreactors loaded with dual light absorbers was stronger than single light absorber functioned nanoreactors might attribute to higher efficiency to utilize both the green and red UCL in the system of (Chla+Ind) NRs (Figure 4.4D). Consistently, the flow cytometry analysis revealed that almost 20 folds elevated the intracellular ROS level in OA-pretreated cells. At the same time, the nanoreactors (Chla NRs, Ind NRs, and (Chla+Ind) NRs) with NIR irradiation reduced the ROS to only 4 times compared to the normal cells (Figure 4.4E-F). These findings support that our photocatalytic nanoreactors contribute to restoring intracellular redox homeostasis by scavenging ROS.

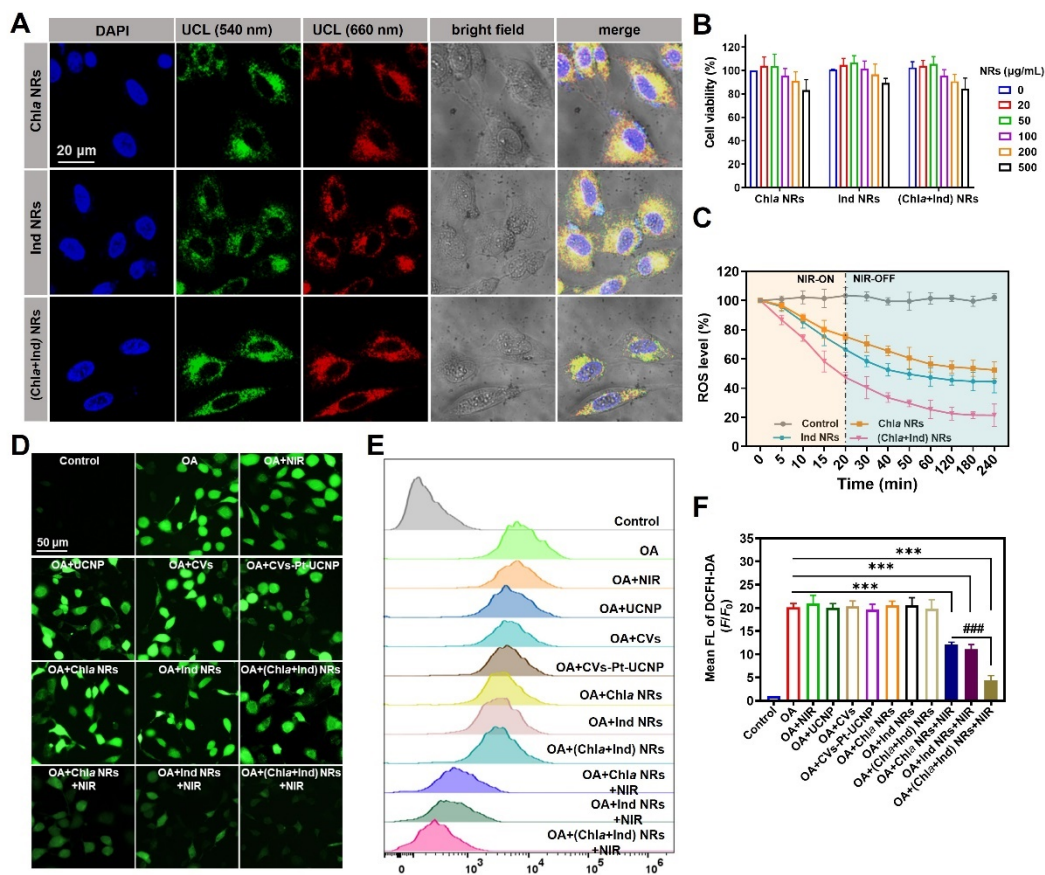


Figure 4.4. (Chla+Ind) NRs scavenge intracellular ROS. (A) The confocal images of PC12 cells after incubation with Chla NRs, Ind NRs, and Chla+Ind NRs. The images of green upconversion luminescence (UCL) and red UCL were captured under excitation at 980 nm with an emission peak at 540 nm and 660 nm, respectively. The cell nuclei were stained with DAPI and imaged with excitation at 405 nm. (B) The relative cell viability of PC12 cells after incubation with Chla NRs, Ind NRs, and (Chla+Ind) NRs at different concentrations for 12 h. (C) The change of ROS level measured by DCFH-DA in OA-treated cells after incubation with (Chla+Ind) NRs at different concentrations with NIR laser irradiation for a different time. (D) The fluorescence images of DCFH-DA indicate intracellular ROS levels. PC12 cells were incubated with OA to induce ROS overproduction, followed by treatment with NRs (Chla NRs, Ind NRs, Chla+Ind NRs, 0.1 mg/mL) with/without 980nm laser irradiation ($0.5W/cm^2$, 20 min). (E) The intracellular fluorescence intensity of DCF-DA was quantified by a flow cytometer. (F) The fold change of mean intracellular fluorescence intensity of DCF-DA.

4.3.4 (Chla+Ind) NRs alleviate apoptosis and mitochondrial dysfunction

ROS accumulation can stimulate tau hyperphosphorylation and lead to neuronal apoptosis [170, 171]. Therefore, clearance of ROS can prevent cell death to rescue tau pathology. Hence, we evaluated the cell viability of OA-pretreated PC12 cells upon exposure to Chla NRs, Ind NRs, and (Chla+Ind) NRs with NIR irradiation (Figure 4.5A). The cell viability was merely 51.22% for the OA-damaged cells, and the vehicular controls (including UCNP, CVs, and CVs-Pt-UCNP groups) did not improve the survival rate of the cells (Figure 4.5A). In comparison, significant inhibition of cell death was seen in Chla NRs, Ind NRs, and (Chla+Ind) NRs with

NIR irradiation, with corresponding cell viability rising to 70.70%, 74.09%, and 82.17% as a result (Figure 4.5A). Compared with Chl*a* NRs and Ind NRs, (Chl*a*+Ind) NRs exhibited better therapeutic performance on OA-induced AD model cells due to more H₂ released from (Chl*a*+Ind) NRs to clear the cytotoxic ·OH. Additionally, the cell apoptosis was assessed by Annexin V-PI staining and further quantified by flow cytometric analysis, which revealed the capability of our NIR irradiation-catalyzed nanoreactors to prevent OA-induced neuronal apoptosis (Figure 4.5B and C). Upon stimulation with OA, the apoptosis rate was around 44.76% but dramatically reduced to 14.84% after being treated by (Chl*a*+Ind) NRs in the presence of NIR irradiation, significantly lower than Chl*a* NRs treatment (23.82%) and Ind NRs treatment (21.67%) under the same condition (Figure 4.5B and C). All the above results proved that our nanoreactors are highly effective in rescuing neurons from apoptosis. Optimizing the nanosystem by encapsulating dual light absorbers, the resultant (Chl*a*+Ind) NRs showed a better capability to protect the neurons because more H₂ was released to exert reinforced therapeutic efficacy.

Such a remarkable recovery of ROS homeostasis caused by the nanoreactors could be beneficial to repair mitochondrial dysfunction, commonly manifested as mitochondrial morphology defects and a loss of mitochondrial membrane potential. Thereby, it was observed that the mitochondrial morphology deteriorated in OA-induced cells. Still, it was restored almost entirely upon treatment by Chl*a* NRs, Ind NRs, and (Chl*a*+Ind) NRs under NIR irradiation (Figure 4.5D). On the other hand, mitochondrial damage was initially characterized by a decrease in membrane potential, which can be assessed by the JC-1 probe that forms green-fluorescent monomers at low membrane potential while it aggregates and emits red fluorescence at high potential^[172]. When PC12 cells were damaged by OA to cause intracellular ROS overproduction, the mitochondrial membrane potential depolarized and thus decreased, where JC-1 existed as monomers and emitted green fluorescence (Figure 4.5E). However, in cells under repair by NIR-activated Chl*a* NRs, Ind NRs, and (Chl*a*+Ind) NRs, JC-1 exhibited more red-fluorescent aggregates, suggesting an increased mitochondrial membrane potential of these cells (Figure 4.5E). Altogether, our as-developed photocatalytic nanoreactors can alleviate oxidative damage by scavenging intracellular ROS and thereby repair impaired mitochondria.

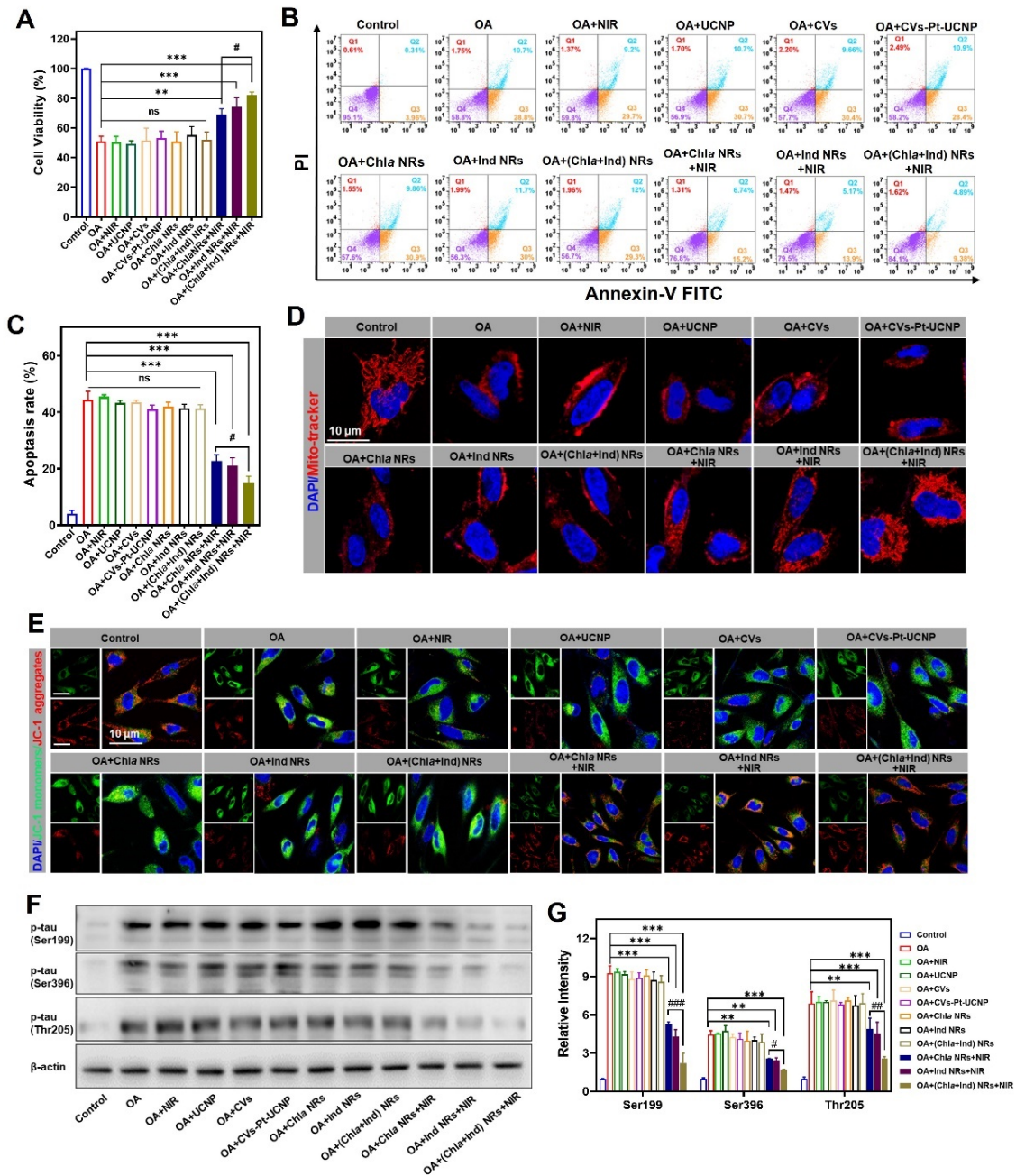


Figure 4.5 Therapeutic effect of (Chla+Ind) NRs *in vitro*. (A) Inhibition of OA-induced cell death of PC12 cells after exposure to 100 nM OA for 12 h and then treated with NRs for another 12 h following NIR irradiation. The comparative cell death inhibition ability of Chla NRs, Ind NRs, and (Chla+Ind) NRs was measured by an MTT assay at indicated concentrations. (B) The apoptosis results of PC12 cells after incubation with Chla NRs, Ind NRs, and (Chla+Ind) NRs with/without 980 nm laser irradiation were measured by flow cytometry. After different treatments, PC12 cells were stained with Annexin V-FITC/PI. (C) The quantification results of early and late apoptosis rate in (B). (D) Confocal images of PC12 cells stained with mito-tracker to display the mitochondrial morphology. (E) Confocal images of PC12 cells after being treated by Chla NRs, Ind NRs, (Chla+Ind) NRs, exhibiting mitochondrial membrane potential measured using JC-1 probe. (F) Western for hyperphosphorylated tau at serine 199, 396 epitopes, and threonine 205 epitopes in PC12 cells after different treatments. (G) Semi-quantification of band intensity in western blot in (F) by ImageJ.

4.3.5 (Chla+Ind) NRs attenuate hyperphosphorylation of tau

To verify whether the nanoreactors could decrease the tau hyperphosphorylation in OA-treated PC12 cells, we performed the western blot assay to measure the phosphor-tau (p-tau) level at multiple sites, including Ser199, Ser396, and Thr205. Among these sites, phosphorylation of the tau protein at Ser396 is one of the initial signs of AD pathology [173]. Hence, eliminating hyperphosphorylated tau will assist with AD treatment. Our results demonstrated that Chla NRs, Ind NRs, and (Chla+Ind) NRs under NIR laser irradiation can significantly down-regulate the OA-stimulated tau hyperphosphorylation at the site of Ser199, Ser396, and Thr205 (Figure 4.5F). Strikingly, (Chla+Ind) NRs showed enhanced inhibition to Ser199, Ser396, and Thr205 compared with Chla NRs and Ind NRs (Figure 4.5 G). These findings revealed that our nanoreactors could rescue tau pathology by clearance of overproduced ROS through NIR laser-triggered H₂ generation.

4.3.6 (Chla+Ind) NRs Regulate Apoptosis-Relevant Proteins and Activates Akt/GSK-3 β Signaling

We further explored the underlying mechanism of (Chla+Ind) NRs to prevent neurons from apoptosis and tau hyperphosphorylation. It is known that oxidative stress can induce apoptosis by activation of pro-apoptotic protein Bcl2-associated X (Bax) and downstream protein caspase-3 [174]. Consequently, the relative level of Bax and Caspase 3 can indicate whether the cells have launched the apoptotic caspase cascade (Figure 4.6A). In this study, the expression of Bax and Caspase 3 was determined by western blot analysis. The results showed that the level of Bax and cleaved caspase 3 (c-Caspase 3) was increased in OA-treated cells, consistent with previous studies (Figure 4.6B) [98]. However, in the presence of NIR laser, (Chla+Ind) NRs treatment remarkably reduced both Bax and c-caspase 3 levels, demonstrating that our nanoreactors can block the pro-apoptotic pathway by clearance of ROS (Figure 4.6B-D).

In addition, tau pathogenesis in AD involves two central kinases, protein kinase B (AKT) and its downstream kinase glycogen synthase kinase 3 β (GSK3 β) [170]. In the normal physiological condition, GSK3 β could be inactivated, accompanied by residue Ser9 phosphorylated into p-Ser9 by the upregulation of phosphorylated AKT (p-Ser473) [171] (Figure 4.6A). Our results confirmed that OA treatment down-regulated the expression of both p-Akt and p-GSK3 β , causing the hyperphosphorylation of Tau into p-Tau, suggesting the successful establishment of the AD cell model under tau pathology (Figure 4.6B-D). Notably, after being treated by (Chla+Ind) NRs with NIR irradiation, both the expression of p-Akt and p-GSK3 β were recovered, indicating our nanosystem attenuated tau pathology through activating Akt/GSK3 β signaling pathway (Figure 4.6B-D). Taken together, our nanoreactors protect

neuronal cells against apoptosis by regulating pro-apoptotic proteins and inhibiting intracellular tau hyperphosphorylation by activating the Akt/GSK3 β signaling pathway.

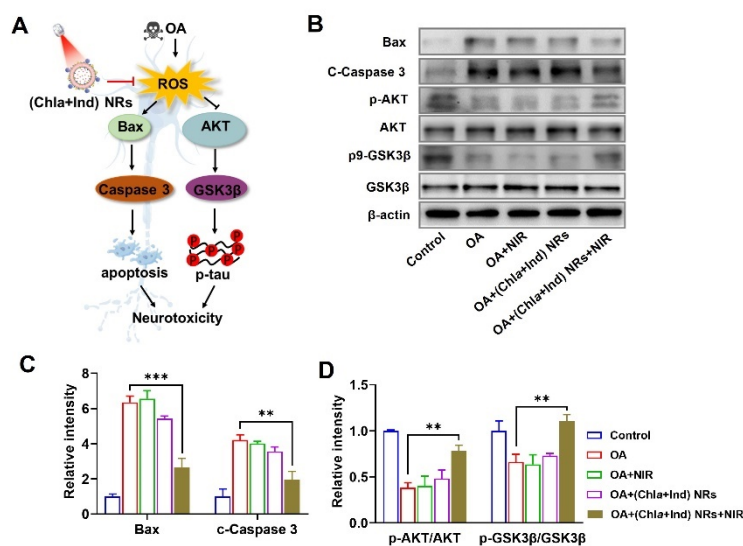


Figure 4.6. The therapeutic mechanism of (Chla+Ind) NRs *in vitro*. (A) The proposed model illustrates the mechanism underlying the efficiency of (Chla+Ind) NRs in ameliorating ROS level and tau hyperphosphorylation in AD. (B) Western blot for Bax, cleaved-caspase-3, p-Akt, Akt, p-GSK3 β , and GSK3 β in PC12 cells and OA pre-stimulated PC12 cells, followed by the treatment of different preparations. Quantification results of (C) Bax and caspase-3, (D) p-Akt, Akt, p-GSK3 β , and GSK3 β . p-Akt, p-GSK3 β were normalized to total Akt, GSK3 β , respectively.

4.3.7 (Chla+Ind) NRs reduce ROS and p-tau in AD Mice

To evaluate the therapeutic efficiency of our nanoreactors *in vivo*, our nanoreactors (Chla NRs and Ind NRs, (Chla+Ind) NRs) were microinjected into the unilateral hippocampus two weeks after the establishment of AD model mice through intracerebral administration of OA to induce tau pathology^[154]. A 980 nm laser was used as the light source and vertically irradiated the skull of AD mice to trigger the release of H₂ *in situ*.

The capability of the nanoreactors to remain in the brain for a long time after administration would maximize their therapeutic effect at the lesion site. Therefore, to inspire the nanoreactors to *in situ* release H₂, 980 nm laser irradiation with power at 0.5W/cm² was performed on the skull of mice 2 h post-injection for 20 min cycling with 3 min-on and 2 min-off. The laser irradiation was conducted twice daily at a 12 h interval for 3 days to optimize ROS scavenging efficiency. Progressive cognitive deficits and memory loss are considered to be the primary symptoms of AD. Accordingly, we introduced the spontaneous Y-maze test to explore the short-time spatial learning and memory in the OA-induced AD model mice after being treated with the Chla NRs, Ind NRs, and (Chla+Ind) NRs (Figure 4.7A). Compared with the wild-type mice, there was less path density for AD mice in the novel arm during the test period, indicating impaired short-term memory and disrupted exploratory activity upon OA exposure. However,

after being treated by photocatalytic nanoreactors, the mice spent more time in the novel arm, suggesting a recovery of spatial memory (Figure 4.7B and C).

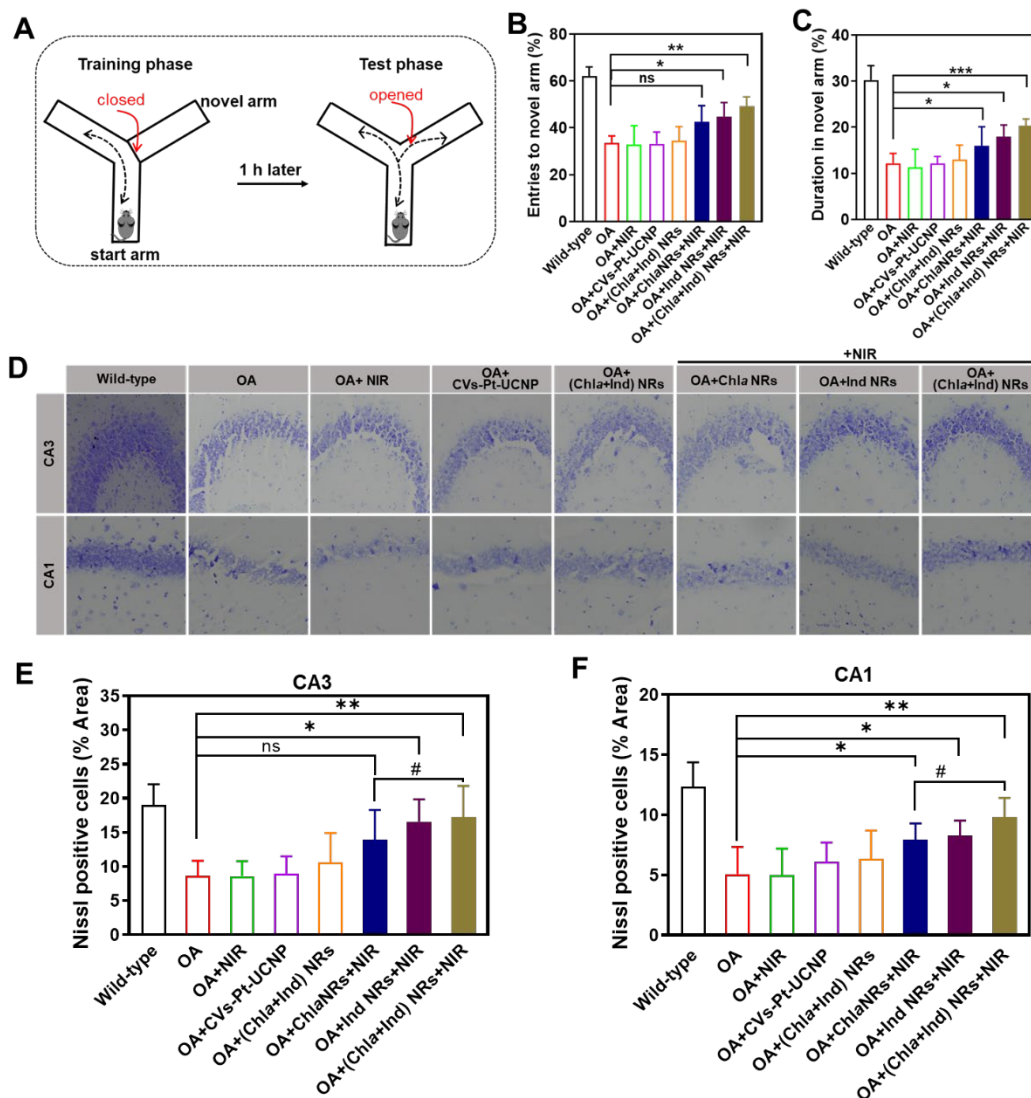


Figure 4.7. *In vivo* evaluation of the therapeutic effect of (Chla+Ind) NRs. (A) Schematic drawings of the Y maze test and the experimental procedures. The analysis on (B) the entries to the novel arm and (C) the duration in the novel arm during the test phase during the Y maze test. (D) Nissl staining assay of the density and activity of neurons in the CA1 and CA3 regions of mice brains. Quantitative analysis of Nissl positive cells in the (E) CA1 and (F) CA3 regions.

All the mice were sacrificed for histological studies following the behavioral test. First, Nissl staining was used to stain Nissl bodies in the hippocampus to evaluate the functional state of neurons after treatment with Chla NRs, Ind NRs, and (Chla+Ind) NRs. The results demonstrated that compared with the OA-induced AD group, NRs-treated brain slices exhibited more nissl-positive cells, indicating the neuron density in the hippocampus region was increased after treatment (Figure 4.7D-F). Moreover, the brain slices were stained with a DCFH-DA probe to evaluate the level of ROS in the hippocampus, including sub-regions of the cornu ammonis 1 (CA1), cornu ammonis 3 (CA3), and dentate gyrus (DG), which encode

spatial memory and tau pathogenesis in AD pathology. Consistent with previous studies, the green fluorescence intensity of ROS in the hippocampus of OA-induced AD mice was much stronger than in wild-type mice, and the ROS level was not affected by treatment with CVs-Pt-UCNP and (Chla+Ind) NRs without NIR (Figure 4.8A and C). While a significant down-regulation of ROS intensity only occurred in nanoreactors treatment groups (Chla NRs, Ind NRs, and (Chla+Ind) NRs) in the presence of NIR irradiation, which further demonstrated that our photocatalytic nanoreactors could scavenge ROS *in vivo* (Figure 4.8A and C). Remarkably, (Chla+Ind) NRs exhibited a higher efficacy for *in vivo* ROS scavenging than Chla NRs and Ind NRs (Figure 4.8A and C). In addition, we performed the immunofluorescence assay to detect the expression of phosphate tau (p-tau) in the hippocampal region. As shown in Figure 4.8B, negligible red fluorescence of p-tau was shown in the wild-type mice group. In contrast, OA administration induced the expression of p-tau to be increased in the hippocampus (Figure 4.8B). After AD mice were microinjected with our nanoreactors followed by NIR laser inspiration, the p-tau in the hippocampus was decreased by ~1.46-, 1.58- and 2.47-fold lower than that in AD mice treated with CVs-Pt-UCNP and (Chla+Ind) NRs treatment but without NIR laser (Figure 4.8B and D). These histological analysis results strongly suggest that our nanoreactors could effectively assist in restoring ROS hemostasis in AD pathology by clearance of ROS and decreasing the level of p-tau in the hippocampus to fight against tau hyperphosphorylation in AD.

To evaluate the *in vivo* biocompatibility of our nanoreactors, hematoxylin/eosin (HE) staining was carried out on the main organs (heart, liver, spleen, lungs, and kidneys) of mice administrated with Chla NRs, Ind NRs and (Chla+Ind) NRs (Figure 4.9A). Compared to the wild-type mice, no distinct histopathological lesions were observed in the tissues of the mice injected with nanoreactors under NIR irradiation. Additionally, a hemolysis assay was performed to investigate whether the nanoreactors influence red blood cell membranes. No hemolysis phenomenon occurred in the negative control groups and nanoreactors co-incubation groups. In contrast, the positive control group showed significant hemolysis, indicating the excellent blood biocompatibility of three types of NRs (Figure 4.9B-D). Altogether, these results support that our as-developed photo-inspired nanoreactors had good biosafety for *in vivo* applications. However, in this study, the nanoreactors were administrated in an intracerebral injection manner, failing to meet the requirements for non-invasive surgery in clinical practice. To improve the potential of translational applications, we would further optimize the (Chla+Ind) NRs with a capacity to penetrate the brain-blood barriers and *in situ* generate bioactive H₂ at the pathological sites in the brain for further therapy.

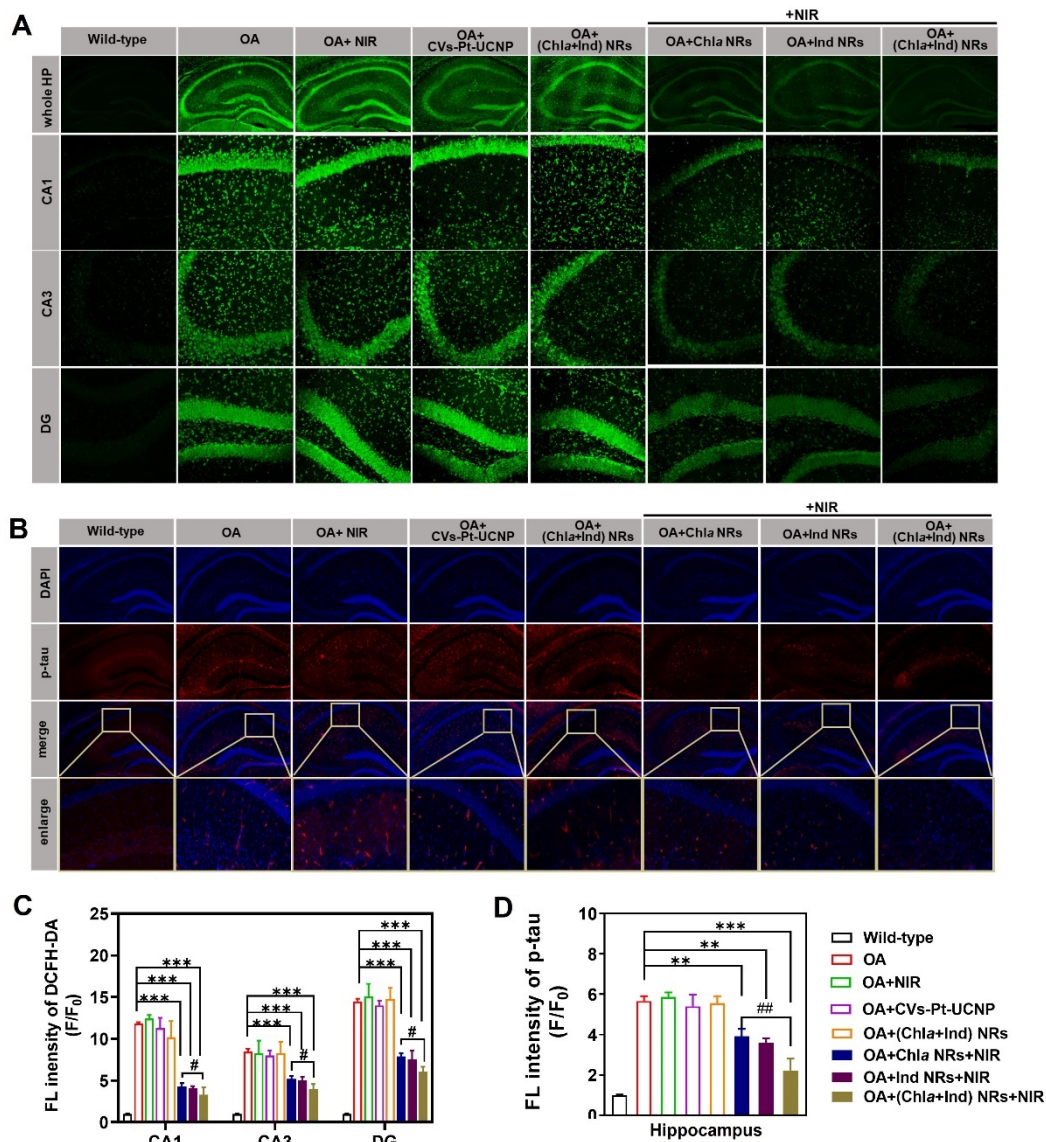


Figure 4.8 *Ex vivo* evaluation of the therapeutic effect of (Chla+Ind) NRs. (A) The staining results of ROS indicator DCFH-DA in the whole hippocampus (HP) and representative images of hippocampal CA1, CA3, and DG region of wild-type mice and OA induced-AD model mice administered with saline and different NRs (Chla NRs, Ind NRs, Chla+Ind NRs) with 980 nm laser irradiation. (B) Immunostaining for anti-p tau (Ser396) in the hippocampus. (C) Quantification results of ROS level. (D) Quantification results of p-tau level. Data were presented as mean \pm SD. * $p < 0.05$, ** $p < 0.01$ and *** $p < 0.001$, compare with OA group. Scale bar: 20 μ m.

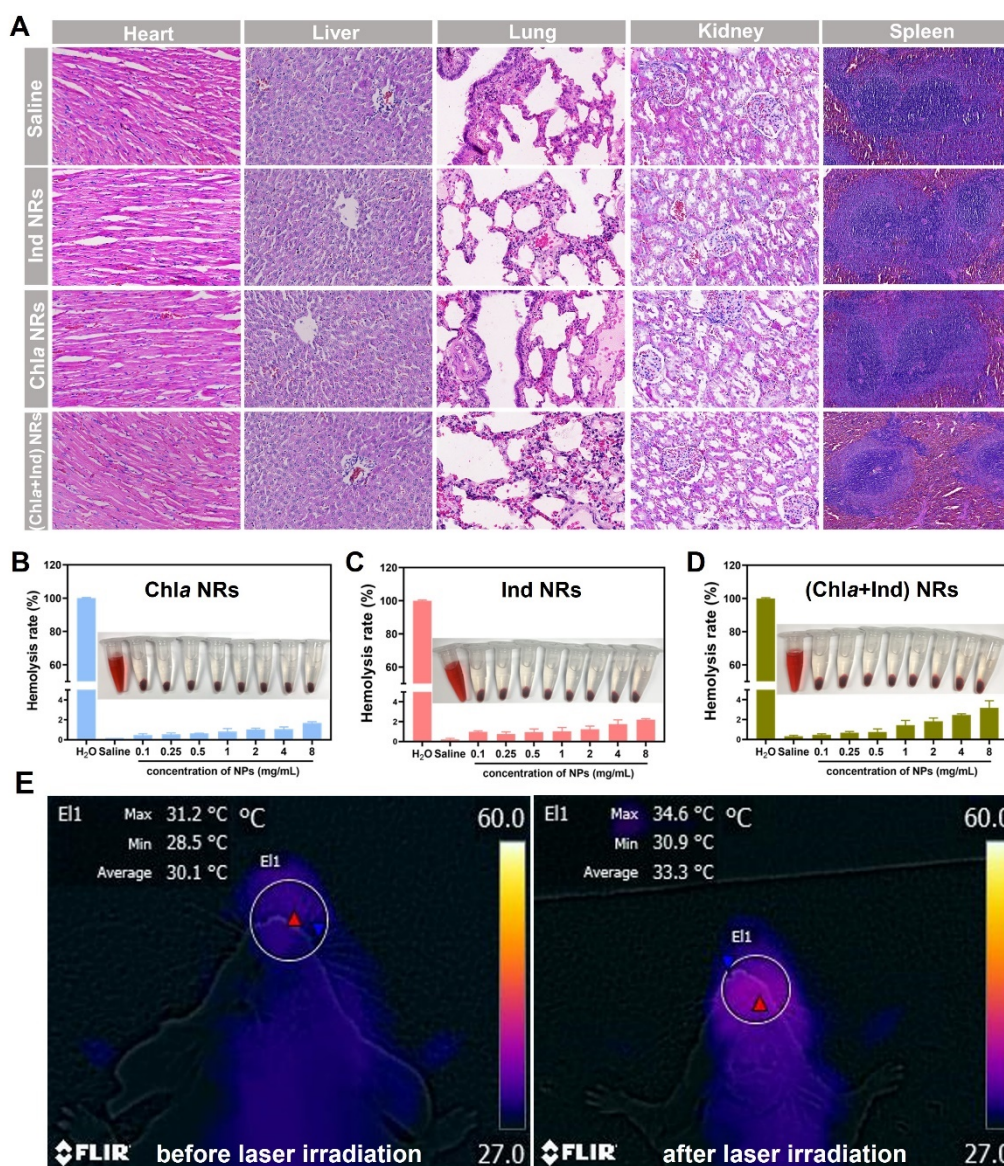


Figure 4.9 The biocompatibility and biosafety of (Chla+Ind) NRs. (A) H&E-staining of major organs of mice after injection with saline, or Chla NRs, Ind NRs, or (Chla+Ind) NRs. Hemolysis rate of (B) Chla NRs, (C) Ind NRs, and (D) Chla+Ind NRs. Relative hemolysis rate in mice RBCs upon incubation with H₂O as a positive control, saline as a negative control, and Chla NRs, Ind NRs, and Chla+Ind NRs at a series of concentrations. (E) Thermal images of mice before and after laser irradiation at 0.5W/cm² for 20 min.

4.4 Summary

The cascades of events comparing oxidative stress damage, mitochondrial dysfunction, and subsequent tau hyperphosphorylation play important roles in the etiology of AD. As a common non-toxic medical gas, hydrogen has been proven to be anti-inflammatory, anti-oxidant, and anti-apoptotic and regulate autophagic signaling pathways in many studies. In this work, we developed the photo-driven nanoreactor (Chla+Ind) NRs to mimic the light-harvesting capabilities of a natural photosynthetic system to achieve in situ controlled release

of hydrogen gas for AD treatment. The (Chl a +Ind) NRs were composed of cross-linked vesicles encapsulated with ascorbic acid, Chl a , and Ind in the hydrophobic center, while Pt NPs as catalysts and UCNPs as a light source was conjugated on the surface of the cross-linked vesicles. The (Chl a +Ind)NRs consist of cross-linked vesicles that encapsulate ascorbic acid, Chl a , and the hydrophobic center of Ind, while Pt NPs as catalysts and UCNP as light sources are conjugated on the surface of the cross-linked vesicles. These cVs-based artificial nanoreactors guarantee excellent biocompatibility and stability during the photosynthesis process in biological systems. Furthermore, NIR laser irradiation-triggered photosynthesis initiation ensures lower photodamage and deeper tissue penetration of the light source, which is extremely beneficial for photo-responsive *in situ* hydrogen release of nanoreactors in hippocampal and cortical regions. Moreover, integrating two photosensitizers in the artificial nanoreaction system endows (Chl a +Ind) NRs with the ability to harvest both the green and red upconversion luminescence of UCNPs, allowing them to produce hydrogen with higher efficiency than single photosensitizer-loaded Chl a NRs and Ind NRs. Therefore, (Chl a +Ind) NRs perform better than Chl a NRs and Ind NRs in scavenging ROS, rescuing mitochondrial dysfunction, and mitigating tau hyperphosphorylation in AD cells and mice models induced by OA administration. In addition, the symptoms of impaired learning memory capacity and neuronal loss in AD mice were significantly alleviated by nanoreactors treatment. Such an artificial nanoreaction system with hydrogen release by photocatalysis will provide a new approach to AD treatment.

Chapter 5: Conclusions

We first proposed a FRET-based biosensor (TPE-DNA@GO) for specifically detecting nucleic acid sequences of *N* and *Orflab* fragments. TPE-DNA@GO nanoprobe was fabricated by TPE-labelled oligonucleotide probes as donor fluorophores adsorbed on the surface of GO nanosheets as an acceptor motif. Here, GO is critical in minimizing the background fluorescence of TPE-DNA to improve the signal-to-noise ratio of the sensing platform. Moreover, TPE-DNA immobilized on the GO surface would hybridize with the target sequence to form a double-stranded DNA/RNA complex conjugated with TPE molecules. Due to the decreased adsorption affinity of GO for duplex nucleic acids, TPE-dsDNA complex dissociates from the GO surface, resulting in the first-stage fluorescence recovery ("OFF" to "WEAK"). In addition, the conformation of duplex oligonucleotides hinders the intramolecular rotation of TPE due to the increased stiffness and mass shifts from ssDNA to dsDNA, resulting in an increase in fluorescence ("WEAK" to "STRONG"). Furthermore, we designed a ppTPE-DNA@GO nanoprobe where GO served as a carrier for the TPE-DNA probe bearing a pair of ssDNA fragments (e.g., N_f and N_r) that target the same nucleic acid sequence, which showed improved sensitivity than the single ssDNA contained spTPE-*N*@GO nanoprobe. This strategy provides new insights into the application of FRET biosensors for nucleic acid detection. In chapter 2, our work demonstrates that TPE-DNA@GO nanoprobe could identify both *N* and *Orflab* genes with rapid detection around 1 h and good sensitivity at the picomolar level without amplification. TPE-DNA@GO nanoprobe shows great promise in assisting the initial rapid detection of the SARS-CoV-2 nucleic acid sequence.

To achieve *in situ* detecting miR-125 in the AD model, we further developed a FRET nanoprobe (TPET-DNA@Dex-MoS₂), constructed by TPET compounds conjugated with probing-ssDNA as donor fluorophores adsorbed on the cationic Dextran polymer modified MoS₂ nanosheets (Dex-MoS₂). With red emission and a large Stokes shift, TPET molecules can minimize cross-talk between the excitation source and the fluorescent emission for enhanced *in vitro* and *in vivo* imaging with a high signal-to-noise ratio. In addition, the introduction of Dextran polymer-modified nanosheets facilitated the physiological stability and biocompatibility of TPET-DNA@Dex-MoS₂ nanoprobe for intracellular and *in vivo* sensing applications. Our TPET-DNA@Dex-MoS₂ nanoprobe hybridized with miR-125b to form a DNA/RNA duplex, causing the pre-absorbed TPET-DNA to detach from TPET-DNA@Dex-MoS₂ that simultaneously initiates "dual on" processes: (1) recovery of TPET-DNA signal and (2) RIR-induced strong emission. In chapter 3, the sensing performance of TPET-DNA@Dex-

MoS₂ was demonstrated by detecting miR-125b in the OA-induced AD cell model *in vitro* with good sensitivity and specificity. Moreover, TPET-DNA@Dex-MoS₂ nanoprobe was also successfully applied to *in situ* monitoring of the endogenous miR-125b in a tau-based AD mice model established by OA administration. Therefore, TPET-DNA@Dex-MoS₂ nanoprobe could be a promising tool for *in situ* and real-time monitoring of AD-related microRNA biomarkers, providing mechanistic insight into the early diagnosis of AD.

Finally, we designed a multicomponent nanoreactor for NIR light-triggered *in situ* H₂ generation to scavenge ROS for the treatment of AD. Inspired by the natural photosynthesis process, we constructed the nanoreactor platform by encapsulating ascorbic acid as sacrificial agents and two photosensitizers, Chl a and Ind, into the cVs. Meanwhile, Pt NPs as catalysts and NIR-excited UCNPs as a light source were attached to the surface of cVs. cVs offer excellent stability, biocompatibility, and biodegradability for (Chl a +Ind) NRs. Moreover, upon NIR laser irradiation (980 nm), the red and green upconversion luminescence of UCNPs was absorbed by Chl a and Ind, respectively. The excited electrons separated from Chl a * and Ind* were quickly transferred to Pt NPs to combine with the proton from ascorbic acid, facilitating rapid activation of the photosynthesis of H₂ gas, locally providing a high therapeutic concentration thereof. In chapter 4, our results successfully demonstrated that (Chl a +Ind) NRs could efficiently release H₂ as an efficient antioxidant to restore ROS homeostasis, repair mitochondrial damage, and attenuate hyperphosphorylated tau in AD mice. Such NIR-driven nanoreactors with *in situ* H₂ production have great potential to provide new directions for AD treatment.

In summary, in this thesis, a dual "turn on" sensing strategy was proposed by integrating the strengths of AIEgens and FRET-based biosensors. Based on the dual "turn on" sensing mechanism, oligonucleotide-modified AIEgens immobilized on 2D nanosheets to form nanoprobe demonstrated excellent stability and selectivity to detect disease-relative nucleic acids with a rapid response and sound sensitivity. In the future study, we aim to optimize this nanobiosensor for overcoming brain-blood barriers for a more non-invasive diagnosis with a deeper tissue-penetrating imaging platform for real-time monitoring of disease-relative nucleic acids. Furthermore, in order to further improve the efficiency in the photosynthetic systems AIEgens will be utilized as photosensitizers to fabricate artificial nanoreactors with higher efficiency to generate H₂ to exert multiple therapeutic functions.

References

1. Zhang J, Campbell RE, Ting AY, Tsien RY: Creating new fluorescent probes for cell biology. *Nat. Rev. Mol. Cell Biol.* 2002, 3(12):906-918.
2. Lavis LD, Raines RT: Bright ideas for chemical biology. *ACS Chem. Biol.* 2008, 3(3):142-155.
3. Guo Z, Park S, Yoon J, Shin I: Recent progress in the development of near-infrared fluorescent probes for bioimaging applications. *Chem. Soc. Rev.* 2014, 43(1):16-29.
4. Wolfbeis OS: An overview of nanoparticles commonly used in fluorescent bioimaging. *Chem. Soc. Rev.* 2015, 44(14):4743-4768.
5. Resch-Genger U, Grabolle M, Cavaliere-Jaricot S, Nitschke R, Nann T: Quantum dots versus organic dyes as fluorescent labels. *Nat. Methods* 2008, 5(9):763-775.
6. Rakovich A, Rakovich T: Semiconductor versus graphene quantum dots as fluorescent probes for cancer diagnosis and therapy applications. *J. Mater. Chem. B* 2018, 6(18):2690-2712.
7. Li XC, Zhao SJ, Li BL, Yang K, Lan MH, Zeng LT: Advances and perspectives in carbon dot-based fluorescent probes: Mechanism, and application. *Coordin. Chem. Rev.* 2021, 431.
8. Loo JFC, Chien YH, Yin F, Kong SK, Ho HP, Yong KT: Upconversion and downconversion nanoparticles for biophotonics and nanomedicine. *Coordin. Chem. Rev.* 2019, 400.
9. Jablonski A: Efficiency of Anti-Stokes Fluorescence in Dyes. *Nature* 1933, 131(3319):839-840.
10. Cwalinski T, Polom W, Marano L, Roviello G, D'Angelo A, Cwalina N, Matuszewski M, Roviello F, Jaskiewicz J, Polom K: Methylene Blue-Current Knowledge, Fluorescent Properties, and Its Future Use. *J. Clin. Med.* 2020, 9(11).
11. Zhang C, Li Y, Wang X, Zhang M, Jiang W, Ou J: Clinical study of combined application of indocyanine green and methylene blue for sentinel lymph node biopsy in breast cancer. *Medicine (Baltimore)* 2021, 100(15):e25365.
12. Zhelev Z, Ohba H, Bakalova R: Single quantum dot-micelles coated with silica shell as potentially non-cytotoxic fluorescent cell tracers. *J. Am. Chem. Soc.* 2006, 128(19):6324-6325.
13. Bünau Gv: J. B. Birks: *Photophysics of Aromatic Molecules*. Wiley-Interscience, London 1970. 704 Seiten. Preis: 210s. In: 1970.

14. Weiss J: FLUORESCENCE OF ORGANIC MOLECULES*. Nature 1943, 152(3850):176-178.
15. Zhao Z, Zhang HK, Lam JWY, Tang BZ: Aggregation-Induced Emission: New Vistas at the Aggregate Level. Angew Chem. Int. Edit 2020, 59(25):9888-9907.
16. Luo JD, Xie ZL, Lam JWY, Cheng L, Chen HY, Qiu CF, Kwok HS, Zhan XW, Liu YQ, Zhu DB et al: Aggregation-induced emission of 1-methyl-1,2,3,4,5-pentaphenylsilole. Chem. Commun. 2001(18):1740-1741.
17. Qi J, Chen C, Ding D, Tang BZ: Aggregation-Induced Emission Luminogens: Union Is Strength, Gathering Illuminates Healthcare. Adv. Healthc. Mater. 2018, 7(20).
18. Mei J, Hong YN, Lam JWY, Qin AJ, Tang YH, Tang BZ: Aggregation-Induced Emission: The Whole Is More Brilliant than the Parts. Adv. Mater. 2014, 26(31):5429-5479.
19. Tripathi A, Kumar V, Chetti P: Stability, optical and charge transport properties of saddle-shaped cyclooctatetrathiophene (COTh) isomers: a theoretical study. J. Sulfur. Chem. 2022, 43(2):180-192.
20. Zhang JY, Zhang HK, Lam JWY, Tang BZ: Restriction of Intramolecular Motion(RIM): Investigating AIE Mechanism from Experimental and Theoretical Studies. Chem. Res. Chinese U 2021, 37(1):1-15.
21. Chen M, Qin AJ, Lam JWY, Tang BZ: Multifaceted functionalities constructed from pyrazine-based AIEgen system. Coordin. Chem. Rev. 2020, 422.
22. Xu WH, Lee MMS, Zhang ZH, Sung HHH, Williams ID, Kwok RTK, Lam JWY, Wang D, Tang BZ: Facile synthesis of AIEgens with wide color tunability for cellular imaging and therapy. Chem. Sci. 2019, 10(12):3494-3501.
23. Kwok RTK, Leung CWT, Lam JWY, Tang BZ: Biosensing by luminogens with aggregation-induced emission characteristics. Chem. Soc. Rev. 2015, 44(13):4228-4238.
24. Cai XL, Liu B: Aggregation-Induced Emission: Recent Advances in Materials and Biomedical Applications. Angew Chem. Int. Edit 2020, 59(25):9868-9886.
25. Wan Q, Huang Q, Liu MY, Xu DZ, Huang HY, Zhang XY, Wei Y: Aggregation-induced emission active luminescent polymeric nanoparticles: Non-covalent fabrication methodologies and biomedical applications. Appl. Mater. Today 2017, 9:145-160.
26. Wang YF, Zhang YX, Wang JJ, Liang XJ: Aggregation-induced emission (AIE) fluorophores as imaging tools to trace the biological fate of nano-based drug delivery systems. Adv. Drug Deliver. Rev. 2019, 143:161-176.

27. Chen SJ, Wang H, Hong YN, Tang BZ: Fabrication of fluorescent nanoparticles based on AIE luminogens (AIE dots) and their applications in bioimaging. *Mater. Horiz.* 2016, 3(4):283-293.
28. Li YQ, Kwok RTK, Tang BZ, Liu B: Specific nucleic acid detection based on fluorescent light-up probe from fluorogens with aggregation-induced emission characteristics. *RSC Adv.* 2013, 3(26):10135-10138.
29. Wang XD, Dai J, Min XH, Yu ZH, Cheng Y, Huang KX, Yang JL, Yi XQ, Lou XD, Xia F: DNA-Conjugated Amphiphilic Aggregation-Induced Emission Probe for Cancer Tissue Imaging and Prognosis Analysis. *Anal. Chem.* 2018, 90(13):8162-8169.
30. Shi HB, Kwok RTK, Liu JZ, Xing BG, Tang BZ, Liu B: Real-Time Monitoring of Cell Apoptosis and Drug Screening Using Fluorescent Light-Up Probe with Aggregation-Induced Emission Characteristics. *J. Am. Chem. Soc.* 2012, 134(43):17972-17981.
31. Liu ZX, Wang Q, Zhu ZR, Liu M, Zhao XL, Zhu WH: AIE-based nanoaggregate tracker: high-fidelity visualization of lysosomal movement and drug-escaping processes. *Chem. Sci.* 2020, 11(47):12755-12763.
32. Li HD, Kim H, Zhang C, Zeng S, Chen QX, Jia LY, Wang JY, Peng XJ, Yoon J: Mitochondria-targeted smart AIEgens: Imaging and therapeutics. *Coordin. Chem. Rev.* 2022, 473.
33. Li YX, Hu DH, Sheng ZH, Min TL, Zha ML, Ni JS, Zheng HR, Li K: Self-assembled AIEgen nanoparticles for multiscale NIR-II vascular imaging. *Biomaterials* 2021, 264.
34. Li RT, Chen M, Yang ZC, Chen YJ, Huang NH, Chen WH, Chen J, Chen JX: AIE-based gold nanostar-berberine dimer nanocomposites for PDT and PTT combination therapy toward breast cancer. *Nanoscale* 2022, 14(27):9818-9831.
35. Wen HF, Zhang ZJ, Kang MM, Li HX, Xu WH, Guo H, Li YM, Tan YH, Wen ZY, Wu Q et al: One-for-all phototheranostics: Single component AIE dots as multi-modality theranostic agent for fluorescence-photoacoustic imaging-guided synergistic cancer therapy. *Biomaterials* 2021, 274.
36. Moreno MJ, Ling BB, Stanimirovic DB: In vivo near-infrared fluorescent optical imaging for CNS drug discovery. *Expert Opin. Drug Dis.* 2020, 15(8):903-915.
37. Tan GR, Wang MH, Hsu CY, Chen NG, Zhang Y: Small Upconverting Fluorescent Nanoparticles for Biosensing and Bioimaging. *Adv. Opt. Mater.* 2016, 4(7):984-997.
38. Chen GY, Qju HL, Prasad PN, Chen XY: Upconversion Nanoparticles: Design, Nanochemistry, and Applications in Theranostics. *Chem. Rev.* 2014, 114(10):5161-5214.

39. Fan Y, Liu L, Zhang F: Exploiting lanthanide-doped upconversion nanoparticles with core/shell structures. *Nano Today* 2019, 25:68-84.
40. Feng W, Zhu XJ, Li FY: Recent advances in the optimization and functionalization of upconversion nanomaterials for in vivo bioapplications. *Npg Asia Mater.* 2013, 5.
41. Xin N, Wei D, Zhu Y, Yang M, Ramakrishna S, Lee O, Luo H, Fan H: Upconversion nanomaterials: a platform for biosensing, theranostic and photoregulation. *Mater Today Chem* 2020, 17.
42. Gu B, Zhang QC: Recent Advances on Functionalized Upconversion Nanoparticles for Detection of Small Molecules and Ions in Biosystems. *Adv. Sci.* 2018, 5(3).
43. Alonso-Cristobal P, Vilela P, El-Sagheer A, Lopez-Cabarcos E, Brown T, Muskens OL, Rubio-Retama J, Kanaras AG: Highly Sensitive DNA Sensor Based on Upconversion Nanoparticles and Graphene Oxide. *ACS Appl. Mater. Inter.* 2015, 7(23):12422-12429.
44. Zhang XJ, Hu Y, Yang XT, Tang YY, Han SY, Kang A, Deng HS, Chi YM, Zhu D, Lu Y: FOrster resonance energy transfer (FRET)-based biosensors for biological applications. *Biosens. Bioelectron.* 2019, 138.
45. Ma YX, Chen QH, Pan XY, Zhang J: Insight into Fluorescence Imaging and Bioorthogonal Reactions in Biological Analysis. *Topics Curr. Chem.* 2021, 379(2).
46. Tian F, Lyu J, Shi JY, Yang M: Graphene and graphene-like two-denominational materials based fluorescence resonance energy transfer (FRET) assays for biological applications. *Biosens. Bioelectron.* 2017, 89:123-135.
47. Kikuchi K, Takakusa H, Nagano T: Recent advances in the design of small molecule-based FRET sensors for cell biology. *Trac-Trend Anal. Chem.* 2004, 23(6):407-415.
48. Gust A, Zander A, Gietl A, Holzmeister P, Schulz S, Lalkens B, Tinnefeld P, Grohmann D: A Starting Point for Fluorescence-Based Single-Molecule Measurements in Biomolecular Research. *Molecules* 2014, 19(10):15824-15865.
49. Berney C, Danuser G: FRET or no FRET: A quantitative comparison. *Biophys J* 2003, 84(6):3992-4010.
50. Shi JY, Tian F, Lyu J, Yang M: Nanoparticle based fluorescence resonance energy transfer (FRET) for biosensing applications. *J. Mater. Chem. B* 2015, 3(35):6989-7005.
51. He XW, Xiong LH, Huang YL, Zhao Z, Wang ZY, Lam JWY, Kwok RTK, Tang BZ: AIE-based energy transfer systems for biosensing, imaging, and therapeutics. *Trac-Trend Anal. Chem.* 2020, 122.

52. Tong H, Hong YN, Dong YQ, Haussler M, Lam JWY, Li Z, Guo ZF, Guo ZH, Tang BZ: Fluorescent "light-up" bioprobes based on tetraphenylethylene derivatives with aggregation-induced emission characteristics. *Chem. Commun.* 2006(35):3705-3707.
53. Xu XJ, Huang J, Li JJ, Yan JW, Qin JH, Li Z: A graphene oxide-based AIE biosensor with high selectivity toward bovine serum albumin. *Chem. Commun.* 2011, 47(45):12385-12387.
54. Xu XJ, Li JJ, Li QQ, Huang J, Dong YQ, Hong YN, Yan JW, Qin JG, Li Z, Tang BZ: A Strategy for Dramatically Enhancing the Selectivity of Molecules Showing Aggregation-Induced Emission towards Biomacromolecules with the Aid of Graphene Oxide. *Chem. Eur. J.* 2012, 18(23):7278-7286.
55. Tyagi A, Chu KL, Abidi IH, Cagang AA, Zhang Q, Leung NLC, Zhao E, Tang BZ, Luo Z: Single-probe multistate detection of DNA via aggregation-induced emission on a graphene oxide platform. *Acta Biomater.* 2017, 50:334-343.
56. Li X, Ma K, Zhu SJ, Yao SY, Liu ZY, Xu B, Yang B, Tian WJ: Fluorescent Aptasensor Based on Aggregation-Induced Emission Probe and Graphene Oxide. *Anal. Chem.* 2014, 86(1):298-303.
57. Wang H, Ma K, Xu B, Tian WJ: Tunable Supramolecular Interactions of Aggregation-Induced Emission Probe and Graphene Oxide with Biomolecules: An Approach toward Ultrasensitive Label-Free and "Turn-On" DNA Sensing. *Small* 2016, 12(47):6613-6622.
58. Zhang S, Ma L, Ma K, Xu B, Liu LJ, Tian WJ: Label-Free Aptamer-Based Biosensor for Specific Detection of Chloramphenicol Using AIE Probe and Graphene Oxide. *ACS Omega* 2018, 3(10):12886-12892.
59. Stanisavljevic M, Krizkova S, Vaculovicova M, Kizek R, Adam V: Quantum dots-fluorescence resonance energy transfer-based nanosensors and their application. *Biosens. Bioelectron.* 2015, 74:562-574.
60. Jethi L, Mack TG, Kambhampati P: Extending Semiconductor Nanocrystals from the Quantum Dot Regime to the Molecular Cluster Regime. *J. Phys. Chem. C* 2017, 121(46):26102-26107.
61. Wang J, Sheng T, Zhu XH, Li Q, Wu YH, Zhang J, Liu JL, Zhang Y: Spectral engineering of lanthanide-doped upconversion nanoparticles and their biosensing applications. *Mater. Chem. Front.* 2021, 5(4):1743-1770.
62. Zhou J, Chen JJ, Ge YQ, Shao YH: Two-dimensional nanomaterials for Forster resonance energy transfer-based sensing applications. *Nanophotonics-Berlin* 2020, 9(7):1855-1875.

63. Ricci A, Cataldi A, Zara S, Gallorini M: Graphene-Oxide-Enriched Biomaterials: A Focus on Osteo and Chondroinductive Properties and Immunomodulation. *Materials* 2022, 15(6).
64. Shahriari S, Sastry M, Panjekar S, Raman RKS: Graphene and Graphene Oxide as a Support for Biomolecules in the Development of Biosensors. *Nanotechnol Sci. Appl.* 2021, 14:197-220.
65. Vogel SS, van der Meer BW, Blank PS: Estimating the distance separating fluorescent protein FRET pairs. *Methods* 2014, 66(2):131-138.
66. Mouloua D, Kotbi A, Deokar G, Kaja K, El Marssi M, El Khakani MA, Jouiad M: Recent Progress in the Synthesis of MoS(2) Thin Films for Sensing, Photovoltaic and Plasmonic Applications: A Review. *Materials (Basel)* 2021, 14(12).
67. Gong LB, Feng L, Zheng YW, Luo Y, Zhu D, Chao J, Su S, Wang LH: Molybdenum Disulfide-Based Nanoprobes: Preparation and Sensing Application. *Biosensors-Basel* 2022, 12(2).
68. Backes C, Berner NC, Chen X, Lafargue P, LaPlace P, Freeley M, Duesberg GS, Coleman JN, McDonald AR: Functionalization of Liquid-Exfoliated Two-Dimensional 2H-MoS₂. *Angew Chem. Int. Edit* 2015, 54(9):2638-2642.
69. Oudeng G, Au MT, Shi JY, Wen CY, Yang M: One-Step in Situ Detection of miRNA-21 Expression in Single Cancer Cells Based on Biofunctionalized MoS₂ Nanosheets. *ACS Appl. Mater. Inter.* 2018, 10(1):350-360.
70. Kaur A, Dhakal S: Recent applications of FRET-based multiplexed techniques. *Trac-Trend Anal. Chem.* 2020, 123.
71. Ye WW, Tsang MK, Liu X, Yang M, Hao JH: Upconversion Luminescence Resonance Energy Transfer (LRET)-Based Biosensor for Rapid and Ultrasensitive Detection of Avian Influenza Virus H7 Subtype. *Small* 2014, 10(12):2390-2397.
72. Oudeng G, Benz M, Popova AA, Zhang Y, Yi CQ, Levkin PA, Yang M: Droplet Microarray Based on Nanosensing Probe Patterns for Simultaneous Detection of Multiple HIV Retroviral Nucleic Acids. *ACS Appl. Mater. Inter.* 2020, 12(50):55614-55623.
73. Kang B, Lee Y, Lim J, Yong D, Choi YK, Yoon SW, Seo S, Jang S, Son SU, Kang T et al: FRET-based hACE2 receptor mimic peptide conjugated nanoprobe for simple detection of SARS-CoV-2. *Chem. Eng. J.* 2022, 442.
74. Gorshkov K, Vasquez DM, Chiem K, Ye CJ, Tran BN, de la Torre JC, Moran T, Chen CZ, Martinez-Sobrido L, Zheng W: SARS-CoV-2 Nucleocapsid Protein TR-FRET Assay Amenable to High Throughput Screening. *ACS Pharmacol. Transl.* 2022, 5(1):8-19.

75. Zhang QQ, Xiang R, Huo SS, Zhou YJ, Jiang SB, Wang Q, Yu F: Molecular mechanism of interaction between SARS-CoV-2 and host cells and interventional therapy. *Signal. Transduct. Tar.* 2021, 6(1).
76. Wang B, You Z, Ren DH: Target-assisted FRET signal amplification for ultrasensitive detection of microRNA. *Analyst* 2019, 144(7):2304-2311.
77. Borghei YS, Hosseini M, Ganjali MR: Fluorometric determination of microRNA via FRET between silver nanoclusters and CdTe quantum dots. *Microchim Acta* 2017, 184(12):4713-4721.
78. Tian HY, Yuan CJ, Liu Y, Li Z, Xia K, Li MY, Xie FX, Chen QH, Chen M, Fu WL et al: A novel quantification platform for point-of-care testing of circulating MicroRNAs based on allosteric spherical nanoprobe. *J. Nanobiotechnol.* 2020, 18(1).
79. Ren H, Long Z, Shen XT, Zhang Y, Sun JH, Ouyang J, Na N: Sandwich DNA Hybridization Fluorescence Resonance Energy-Transfer Strategy for miR-122 Detection by Core-Shell Upconversion Nanoparticles. *ACS Appl. Mater. Inter.* 2018, 10(30):25621-25628.
80. Imani M, Mohajeri N, Rastegar M, Zarghami N: Recent advances in FRET-Based biosensors for biomedical applications. *Anal. Biochem.* 2021, 630.
81. Liu ZZ, Li T, Li P, Wei NN, Zhao ZQ, Liang HM, Ji XY, Chen WW, Xue MZ, Wei JS: The Ambiguous Relationship of Oxidative Stress, Tau Hyperphosphorylation, and Autophagy Dysfunction in Alzheimer's Disease. *Oxid. Med. Cell Longev.* 2015, 2015.
82. Kong L, Zhou X, Shi G, Yu Y: Molybdenum disulfide nanosheets-based fluorescent "off-to-on" probe for targeted monitoring and inhibition of beta-amyloid oligomers. *Analyst* 2020, 145(19):6369-6377.
83. Kim K, Lee CH, Park CB: Chemical sensing platforms for detecting trace-level Alzheimer's core biomarkers. *Chem. Soc. Rev.* 2020, 49(15):5446-5472.
84. Wu W, Zheng T, Tian Y: An enzyme-free amplification strategy based on two-photon fluorescent carbon dots for monitoring miR-9 in live neurons and brain tissues of Alzheimer's disease mice. *Chem. Commun.* 2020, 56(58):8083-8086.
85. Bhuckory S, Kays JC, Dennis AM: In Vivo Biosensing Using Resonance Energy Transfer. *Biosensors-Basel* 2019, 9(2).
86. Cayre F, Mura S, Andreiuk B, Sobot D, Gouazou S, Desmaele D, Klymchenko AS, Couvreur P: In Vivo FRET Imaging to Predict the Risk Associated with Hepatic Accumulation of Squalene-Based Prodrug Nanoparticles. *Adv. Healthc. Mater.* 2018, 7(3).

87. Dhapola R, Hota SS, Sarma P, Bhattacharyya A, Medhi B, Reddy DH: Recent advances in molecular pathways and therapeutic implications targeting neuroinflammation for Alzheimer's disease. *Inflammopharmacology* 2021, 29(6):1669-1681.
88. Li TZ, Hou XY, Qi Y, Duan XH, Yan PC, Zhu HR, Xie ZJ, Zhang H: Nanomaterials for neurodegenerative diseases: Molecular mechanisms guided design and applications. *Nano Res.* 2022, 15(4):3299-3322.
89. Singer O, Marr RA, Rockenstein E, Crews L, Coufal NG, Gage FH, Verma IM, Masliah E: Targeting BACE1 with siRNAs ameliorates Alzheimer disease neuropathology in a transgenic model. *Nat. Neurosci.* 2005, 8(10):1343-1349.
90. Wang PZ, Zheng XY, Guo Q, Yang P, Pang XY, Qian K, Lu W, Zhang QZ, Jiang XG: Systemic delivery of BACE1 siRNA through neuron-targeted nanocomplexes for treatment of Alzheimer's disease. *J. Control Release* 2018, 279:220-233.
91. Yang JN, Liu W, Sun Y, Dong XY: LVFFARK-PEG-Stabilized Black Phosphorus Nanosheets Potently Inhibit Amyloid-beta Fibrillogenesis. *Langmuir* 2020, 36(7):1804-1812.
92. Li M, Zhao AD, Dong K, Li W, Ren JS, Qu XG: Chemically exfoliated WS₂ nanosheets efficiently inhibit amyloid beta-peptide aggregation and can be used for photothermal treatment of Alzheimer's disease. *Nano Res.* 2015, 8(10):3216-3227.
93. Zhang ZM, Wang J, Song YX, Wang ZK, Dong MD, Liu L: Disassembly of Alzheimer's amyloid fibrils by functional upconversion nanoparticles under near-infrared light irradiation. *Colloid Surface B* 2019, 181:341-348.
94. Zhu L, Xu LL, Wu XH, Deng F, Ma RJ, Liu Y, Huang F, Shi LQ: Tau-Targeted Multifunctional Nanoinhibitor for Alzheimer's Disease. *ACS Appl. Mater. Inter.* 2021, 13(20):23328-23338.
95. Xu LL, Ding YX, Ma FH, Chen Y, Chen GD, Zhu L, Long JF, Ma RJ, Liu Y, Liu JF et al: Engineering a pathological tau-targeted nanochaperone for selective and synergetic inhibition of tau pathology in Alzheimer's Disease. *Nano Today* 2022, 43.
96. Sun H, Zhong Y, Zhu XD, Liao HW, Lee JY, Chen Y, Ma LJ, Ren JF, Zhao M, Tu MJ et al: A Tauopathy-Homing and Autophagy-Activating Nanoassembly for Specific Clearance of Pathogenic Tau in Alzheimer's Disease. *Acs Nano* 2021, 15(3):5263-5275.
97. Zhou H, Gong YC, Liu YN, Huang AL, Zhu XF, Liu JW, Yuan GL, Zhang L, Wei JA, Liu J: Intelligently thermoresponsive flower-like hollow nano-ruthenium system for sustained release of nerve growth factor to inhibit hyperphosphorylation of tau and neuronal damage for the treatment of Alzheimer's disease. *Biomaterials* 2020, 237.

98. Chen L, Du Y, Zhang K, Liang ZY, Li JQ, Yu H, Ren R, Feng J, Jin ZM, Li FY et al: Tau-Targeted Multifunctional Nanocomposite for Combinational Therapy of Alzheimer's Disease. *ACS Nano* 2018, 12(2):1321-1338.
99. Tian Y, Zhang YF, Wang Y, Chen YX, Fan WP, Zhou JJ, Qiao J, Wei YZ: Hydrogen, a Novel Therapeutic Molecule, Regulates Oxidative Stress, Inflammation, and Apoptosis. *Front. Physiol.* 2021, 12.
100. Ostojic SM, Vukomanovic B, Calleja-Gonzalez J, Hoffman JR: Effectiveness of Oral and Topical Hydrogen for Sports-Related Soft Tissue Injuries. *Postgrad. Med.* 2014, 126(5):188-196.
101. Zhou GX, Goshi E, He QJ: Micro/Nanomaterials-Augmented Hydrogen Therapy. *Adv. Healthc. Mater.* 2019, 8(16).
102. Wang XJ, Yu P, YongYang, Liu XC, Jiang JH, Liu DG, Xue G: Hydrogen-rich saline resuscitation alleviates inflammation induced by severe burn with delayed resuscitation. *Burns* 2015, 41(2):379-385.
103. Qiu XC, Dong KS, Guan JZ, He JM: Hydrogen attenuates radiation-induced intestinal damage by reducing oxidative stress and inflammatory response. *Int. Immunopharmacol.* 2020, 84.
104. Ohsawa I, Ishikawa M, Takahashi K, Watanabe M, Nishimaki K, Yamagata K, Katsura K, Katayama Y, Asoh S, Ohta S: Hydrogen acts as a therapeutic antioxidant by selectively reducing cytotoxic oxygen radicals. *Nature Medicine* 2007, 13(6):688-694.
105. Huang PK, Wei SS, Huang WH, Wu PH, Chen SY, Tao AL, Wang HY, Liang ZY, Chen RC, Yan J et al: Hydrogen gas inhalation enhances alveolar macrophage phagocytosis in an ovalbumin-induced asthma model. *Int. Immunopharmacol* 2019, 74.
106. Zheng ZG, Sun WZ, Hu JY, Jie ZJ, Xu JF, Cao J, Song YL, Wang CH, Wang J, Zhao H et al: Hydrogen/oxygen therapy for the treatment of an acute exacerbation of chronic obstructive pulmonary disease: results of a multicenter, randomized, double-blind, parallel-group controlled trial. *Resp. Res.* 2021, 22(1).
107. Zhao M, Liu MD, Pu YY, Wang D, Xie Y, Xue GC, Jiang Y, Yang QQ, Sun XJ, Cao L: Hydrogen-rich water improves neurological functional recovery in experimental autoimmune encephalomyelitis mice. *J. Neuroimmunol.* 2016, 294:6-13.
108. Guo Q, Xu ST, Yang P, Wang PZ, Lu S, Sheng DY, Qian K, Cao JX, Lu W, Zhang QZ: A dual-ligand fusion peptide improves the brain-neuron targeting of nanocarriers in Alzheimer's disease mice. *J. Control Release* 2020, 320:347-362.

109. Oharazawa H, Igarashi T, Yokota T, Fujii H, Suzuki H, Machide M, Takahashi H, Ohta S, Ohsawa I: Protection of the Retina by Rapid Diffusion of Hydrogen: Administration of Hydrogen-Loaded Eye Drops in Retinal Ischemia-Reperfusion Injury. *Invest. Ophthalm. Vis. Sci.* 2010, 51(1):487-492.
110. Xie KL, Zhang Y, Wang YQ, Meng XY, Wang YZ, Yu YH, Chen HG: Hydrogen attenuates sepsis-associated encephalopathy by NRF2 mediated NLRP3 pathway inactivation. *Inflamm. Res.* 2020, 69(7):697-710.
111. Yao WF, Guo AS, Han X, Wu S, Chen CJ, Luo CF, Li HB, Li SR, Hei ZQ: Aerosol inhalation of a hydrogen-rich solution restored septic renal function. *Aging-U.S.* 2019, 11(24):12097-12113.
112. Zou R, Wang MH, Chen Y, Fan X, Yang B, Du J, Wang XB, Liu KX, Zhou J: Hydrogen-Rich Saline Attenuates Acute Lung Injury Induced by Limb Ischemia/ Reperfusion Via down-Regulating Chemerin and Nlrp3 in Rats. *Shock* 2019, 52(1):134-141.
113. Zhang L, Zhao PH, Yue CP, Jin ZK, Liu Q, Du XB, He QJ: Sustained release of bioactive hydrogen by Pd hydride nanoparticles overcomes Alzheimer's disease. *Biomaterials* 2019, 197:393-404.
114. Zan R, Wang H, Cai WJ, Ni JH, Luthringer-Feyerabend BJC, Wang WH, Peng HZ, Ji WP, Yan J, Xia JZ et al: Controlled release of hydrogen by implantation of magnesium induces P53-mediated tumor cells apoptosis. *Bioact. Mater.* 2022, 9:385-396.
115. Wan WL, Lin YJ, Chen HL, Huang CC, Shih PC, Bow YR, Chia WT, Sung HW: In Situ Nanoreactor for Photosynthesizing H₂ Gas To Mitigate Oxidative Stress in Tissue Inflammation. *J. Am. Chem. Soc.* 2017, 139(37):12923-12926.
116. Hu B, Guo H, Zhou P, Shi ZL: Characteristics of SARS-CoV-2 and COVID-19. *Nat. Rev. Microbiol.* 2021, 19(3):141-154.
117. Irons NJ, Raftery AE: Estimating SARS-CoV-2 infections from deaths, confirmed cases, tests, and random surveys. *P Natl Acad Sci USA* 2021, 118(31).
118. Maddali H, Miles CE, Kohn J, O'Carroll DM: Optical Biosensors for Virus Detection: Prospects for SARS-CoV-2/COVID-19. *Chembiochem* 2021, 22(7):1176-1189.
119. Broughton JP, Deng XD, Yu GX, Fasching CL, Servellita V, Singh J, Miao X, Streithorst JA, Granados A, Sotomayor-Gonzalez A et al: CRISPR-Cas12-based detection of SARS-CoV-2. *Nat. Biotechnol.* 2020, 38(7):870-+.
120. Fu Y, Pan YB, Li ZQ, Li YR: The Utility of Specific Antibodies Against SARS-CoV-2 in Laboratory Diagnosis. *Front. Microbiol.* 2021, 11.

121. Quan K, Yi CP, Yang XH, He XX, Huang J, Wang KM: FRET-based nucleic acid probes: Basic designs and applications in bioimaging. *Trac-Trend Anal. Chem.* 2020, 124.
122. Mai DK, Lee J, Min I, Vales TP, Choi KH, Park BJ, Cho S, Kim HJ: Aggregation-Induced Emission of Tetraphenylethene-Conjugated Phenanthrene Derivatives and Their Bio-Imaging Applications. *Nanomaterials-Basel* 2018, 8(9).
123. Zhu LY, Zhou J, Xu GH, Li CG, Ling PH, Liu B, Ju HX, Lei JP: DNA quadruplexes as molecular scaffolds for controlled assembly of fluorogens with aggregation-induced emission. *Chem. Sci.* 2018, 9(9):2559-2566.
124. Zhang RY, Kwok RTK, Tang BZ, Liu B: Hybridization induced fluorescence turn-on of AIEgen-oligonucleotide conjugates for specific DNA detection. *RSC Adv.* 2015, 5(36):28332-28337.
125. Arias-Barreiro CR, Okazaki K, Koutsaftis A, Inayat-Hussain SH, Tani A, Katsuhara M, Kimbara K, Mori IC: A Bacterial Biosensor for Oxidative Stress Using the Constitutively Expressed Redox-Sensitive Protein roGFP2. *Sensors-Basel* 2010, 10(7):6290-6306.
126. Li DD, Zhang JW, Li JM: Primer design for quantitative real-time PCR for the emerging Coronavirus SARS-CoV-2. *Theranostics* 2020, 10(16):7150-7162.
127. Kundu S, Pyne A, Dutta R, Sarkar N: Unveiling the Interaction of Duplex DNA with Graphene Oxide in the Presence of Two Diverse Binders: A Detailed Photophysical Study. *J. Phys. Chem. C* 2018, 122(12):6876-6888.
128. Xie XP, Lokugamage KG, Zhang XW, Vu MN, Muruato AE, Menachery VD, Shi PY: Engineering SARS-CoV-2 using a reverse genetic system. *Nat. Protoc.* 2021, 16(3):1761-1784.
129. Scheltens P, De Strooper B, Kivipelto M, Holstege H, Chetelat G, Teunissen CE, Cummings J, van der Flier WM: Alzheimer's disease. *Lancet* 2021, 397(10284):1577-1590.
130. Hipp MS, Kasturi P, Hartl FU: The proteostasis network and its decline in ageing. *Nat. Rev. Mol. Cell Biol.* 2019, 20(7):421-435.
131. Forman HJ, Zhang H: Targeting oxidative stress in disease: promise and limitations of antioxidant therapy. *Nat. Rev. Drug. Discov.* 2021, 20(9):689-709.
132. Walgrave H, Balusu S, Snoeck S, Vanden Eynden E, Craessaerts K, Thrupp N, Wolfs L, Horre K, Fourne Y, Ronisz A et al: Restoring miR-132 expression rescues adult hippocampal neurogenesis and memory deficits in Alzheimer's disease. *Cell Stem Cell* 2021, 28(10):1805-1821 e1808.
133. Kim K, Lee CH, Park CB: Chemical sensing platforms for detecting trace-level Alzheimer's core biomarkers. *Chem. Soc. Rev.* 2020, 49(15):5446-5472.

134. Seyedaghamiri F, Rajabi M, Mohaddes G: Targeting Novel microRNAs in Developing Novel Alzheimer's Disease Treatments. *Neurochem. Res.* 2022.
135. Wang L, Shui X, Mei Y, Xia Y, Lan G, Hu L, Zhang M, Gan CL, Li R, Tian Y et al: miR-143-3p Inhibits Aberrant Tau Phosphorylation and Amyloidogenic Processing of APP by Directly Targeting DAPK1 in Alzheimer's Disease. *Int. J. Mol. Sci.* 2022, 23(14).
136. Jiang H, Liu J, Guo S, Zeng L, Cai Z, Zhang J, Wang L, Li Z, Liu R: miR-23b-3p rescues cognition in Alzheimer's disease by reducing tau phosphorylation and apoptosis via GSK-3beta signaling pathways. *Mol. Ther. Nucleic Acids* 2022, 28:539-557.
137. Banzhaf-Strathmann J, Benito E, May S, Arzberger T, Tahirovic S, Kretschmar H, Fischer A, Edbauer D: MicroRNA-125b induces tau hyperphosphorylation and cognitive deficits in Alzheimer's disease. *Embo J.* 2014, 33(15):1667-1680.
138. Ma XH, Liu LL, Meng J: MicroRNA-125b promotes neurons cell apoptosis and Tau phosphorylation in Alzheimer's disease (Publication with Expression of Concern. See vol. 769, 2022) (Retracted article. See vol. 783, 2022). *Neurosci. Lett.* 2017, 661:57-62.
139. Shi J, Chan C, Pang Y, Ye W, Tian F, Lyu J, Zhang Y, Yang M: A fluorescence resonance energy transfer (FRET) biosensor based on graphene quantum dots (GQDs) and gold nanoparticles (AuNPs) for the detection of mecA gene sequence of *Staphylococcus aureus*. *Biosens. Bioelectron.* 2015, 67:595-600.
140. Zhang Q, Yin BH, Hao JH, Ma LJ, Huang YY, Shao XY, Li CQ, Chu ZQ, Yi CQ, Wong SHD et al: An AIEgen/graphene oxide nanocomposite (AIEgen@GO)-based two-stage "turn-on" nucleic acid biosensor for rapid detection of SARS-CoV-2 viral sequence. *Aggregate* 2022.
141. Xia F, Wu J, Wu X, Hu Q, Dai J, Lou X: Modular Design of Peptide- or DNA-Modified AIEgen Probes for Biosensing Applications. *Acc. Chem. Res.* 2019, 52(11):3064-3074.
142. Lu C, Liu YB, Ying YB, Liu JW: Comparison of MoS₂, WS₂, and Graphene Oxide for DNA Adsorption and Sensing. *Langmuir* 2017, 33(2):630-637.
143. Zhu XB, Ji XY, Kong N, Chen YH, Mahmoudi M, Xu XD, Ding L, Tao W, Cai T, Li YJ et al: Intracellular Mechanistic Understanding of 2D MoS₂ Nanosheets for Anti-Exocytosis-Enhanced Synergistic Cancer Therapy. *ACS Nano* 2018, 12(3):2922-2938.
144. Liu T, Wang C, Gu X, Gong H, Cheng L, Shi XZ, Feng LZ, Sun BQ, Liu Z: Drug Delivery with PEGylated MoS₂ Nano-sheets for Combined Photothermal and Chemotherapy of Cancer. *Adv. Mater.* 2014, 26(21):3433-3440.

145. Li YY, Cai ZC, Liu SJ, Zhang HK, Wong STH, Lam JWY, Kwok RTK, Qian J, Tang BZ: Design of AIEgens for near-infrared IIb imaging through structural modulation at molecular and morphological levels. *Nat. Commun.* 2020, 11(1).
146. Wang YJ, Shi Y, Wang ZY, Zhu ZF, Zhao XY, Nie H, Qian J, Qin AJ, Sun JZ, Tang BZ: A Red to Near-IR Fluorogen: Aggregation-Induced Emission, Large Stokes Shift, High Solid Efficiency and Application in Cell-Imaging. *Chem. Eur. J.* 2016, 22(28):9784-9791.
147. Santos EM, Sheng W, Salmani RE, Nick ST, Ghanbarpour A, Gholami H, Vasileiou C, Geiger JH, Borhan B: Design of Large Stokes Shift Fluorescent Proteins Based on Excited State Proton Transfer of an Engineered Photobase. *J. Am. Chem. Soc.* 2021, 143(37):15091-15102.
148. Min XH, Zhang MS, Huang FJ, Lou XD, Xia F: Live Cell MicroRNA Imaging Using Exonuclease III-Aided Recycling Amplification Based on Aggregation-Induced Emission Luminogens. *ACS Appl. Mater. Inter.* 2016, 8(14):8998-9003.
149. Zou D, Wu WJ, Zhang JP, Ma Q, Fan SS, Cheng J, Li D, Niu JQ, Qian XQ, Li WW et al: Multiplex detection of miRNAs based on aggregation-induced emission luminogen encoded microspheres. *RSC Adv.* 2019, 9(68):39976-39985.
150. Yuen J, Chai J, Ding Y: Condensation of DNA-Conjugated Imines with Homophthalic Anhydride for the Synthesis of Isoquinolones on DNA. *Bioconjugate Chem.* 2020, 31(12):2712-2718.
151. Kim HI, Yim D, Jeon SJ, Kang TW, Hwang IJ, Lee S, Yang JK, Ju JM, So Y, Kim JH: Modulation of oligonucleotide-binding dynamics on WS2 nanosheet interfaces for detection of Alzheimer's disease biomarkers. *Biosens. Bioelectron.* 2020, 165.
152. Vaudry D, Stork PJ, Lazarovici P, Eiden LE: Signaling pathways for PC12 cell differentiation: making the right connections. *Science* 2002, 296(5573):1648-1649.
153. Zhang LY, Dong H, Si YW, Wu N, Cao H, Mei B, Meng B: miR-125b promotes tau phosphorylation by targeting the neural cell adhesion molecule in neuropathological progression. *Neurobiol. Aging* 2019, 73:41-49.
154. Baker S, Gotz J: A local insult of okadaic acid in wild-type mice induces tau phosphorylation and protein aggregation in anatomically distinct brain regions. *Acta Neuropathol Com.* 2016, 4.
155. Covello G, Siva K, Adami V, Denti MA: An electroporation protocol for efficient DNA transfection in PC12 cells. *Cytotechnology* 2014, 66(4):543-553.
156. Broetto N, Hansen F, Brolese G, Batassini C, Lirio F, Galland F, dos Santos JPA, Dutra MF, Goncalves CA: Intracerebroventricular administration of okadaic acid induces

- hippocampal glucose uptake dysfunction and tau phosphorylation. *Brain Res. Bull.* 2016, 124:136-143.
157. Kang MM, Zhang ZJ, Xu WH, Wen HF, Zhu W, Wu Q, Wu HZ, Gong JY, Wang ZJ, Wang D et al: Good Steel Used in the Blade: Well-Tailored Type-I Photosensitizers with Aggregation-Induced Emission Characteristics for Precise Nuclear Targeting Photodynamic Therapy. *Adv. Sci.* 2021, 8(14).
158. Galievsky VA, Stasheuski AS, Krylov SN: Improvement of LOD in Fluorescence Detection with Spectrally Nonuniform Background by Optimization of Emission Filtering. *Anal. Chem.* 2017, 89(20):11122-11128.
159. Zhao YH, Jaber V, Alexandrov PN, Vergallo A, Lista S, Hampel H, Lukiw WJ: microRNA-Based Biomarkers in Alzheimer's Disease (AD). *Front. Neurosci.* 2020, 14.
160. Zhang HY, Hao CL, Qu AH, Sun MZ, Xu LG, Xu CL, Kuang H: Light-Induced Chiral Iron Copper Selenide Nanoparticles Prevent beta-Amyloidopathy In Vivo. *Angew Chem. Int. Edit* 2020, 59(18):7131-7138.
161. Dole M, Wilson FR, Fife WP: Hyperbaric hydrogen therapy: a possible treatment for cancer. *Science* 1975, 190(4210):152-154.
162. Wu Y, Yuan M, Song JB, Chen XY, Yang HH: Hydrogen Gas from Inflammation Treatment to Cancer Therapy. *ACS Nano* 2019, 13(8):8505-8511.
163. Xu C, Wang SH, Wang H, Liu K, Zhang SY, Chen B, Liu H, Tong F, Peng F, Tu YF et al: Magnesium-Based Micromotors as Hydrogen Generators for Precise Rheumatoid Arthritis Therapy. *Nano Lett.* 2021, 21(5):1982-1991.
164. Yuan GL, Cen JQ, Liao JM, Huang YQ, Jie L: In situ hydrogen nanogenerator for bimodal imaging guided synergistic photothermal/hydrogen therapies. *Nanoscale* 2021, 13(37):15576-15589.
165. Wan WL, Tian B, Lin YJ, Korupalli C, Lu MY, Cui QH, Wan DH, Chang Y, Sung HW: Photosynthesis-inspired H₂ generation using a chlorophyll-loaded liposomal nanoplatfrom to detect and scavenge excess ROS. *Nat. Commun.* 2020, 11(1).
166. Xu YS, Fan MJ, Yang WJ, Xiao YH, Zeng LT, Wu X, Xu QH, Su CL, He QJ: Homogeneous Carbon/Potassium-Incorporation Strategy for Synthesizing Red Polymeric Carbon Nitride Capable of Near-Infrared Photocatalytic H₂ Production. *Adv. Mater.* 2021, 33(39).
167. Liu JN, Bu WB, Pan LM, Zhang S, Chen F, Zhou LP, Zhao KL, Peng WJ, Shi JL: Simultaneous nuclear imaging and intranuclear drug delivery by nuclear-targeted multifunctional upconversion nanoprob. *Biomaterials* 2012, 33(29):7282-7290.

168. Li CQ, Zhang SY, Pang J, Wu Y, Gu ZW: Facile Fabrication of Robust Organic Counterion-Induced Vesicles: Reversible Thermal Behavior for Optical Temperature Sensor and Synergistic Catalyst upon Removal of Amine. *Adv. Funct. Mater.* 2015, 25(24):3764-3774.
169. Jiang W, Duan WB, Li S, Shen XY, Zhou Y, Luo T, He F, Xu J, Wang HQ: Jatrorrhizine Protects Against Okadaic Acid Induced Oxidative Toxicity Through Inhibiting the Mitogen-Activated Protein Kinases Pathways in HT22 Hippocampal Neurons. *CNS Neurol. Disord.* 2015, 14(10):1334-1342.
170. Kitagishi Y, Nakanishi A, Ogura Y, Matsuda S: Dietary regulation of PI3K/AKT/GSK-3beta pathway in Alzheimer's disease. *Alzheimers Res. Ther.* 2014, 6(3):35.
171. Han G, Bai K, Yang X, Sun C, Ji Y, Zhou J, Zhang H, Ding Y: "Drug-Carrier" Synergy Therapy for Amyloid-beta Clearance and Inhibition of Tau Phosphorylation via Biomimetic Lipid Nanocomposite Assembly. *Adv. Sci.* 2022, 9(14):e2106072.
172. Zhang W, Hu X, Shen Q, Xing D: Mitochondria-specific drug release and reactive oxygen species burst induced by polyprodrug nanoreactors can enhance chemotherapy. *Nat. Commun.* 2019, 10(1):1704.
173. Mondragon-Rodriguez S, Perry G, Luna-Munoz J, Acevedo-Aquino MC, Williams S: Phosphorylation of tau protein at sites Ser(396-404) is one of the earliest events in Alzheimer's disease and Down syndrome. *Neuropathol. Appl. Neurobiol.* 2014, 40(2):121-135.
174. D'Amelio M, Cavallucci V, Cecconi F: Neuronal caspase-3 signaling: not only cell death. *Cell Death. Differ.* 2010, 17(7):1104-1114.